uOttawa

L'Université canadienne
Canada's university

FACULTÉ DES ÉTUDES SUPÉRIEURES ET POSTOCTORALES

uOttawa

L'Université canadienne
Canada's university

FACULTY OF GRADUATE AND POSDOCTORAL STUDIES

Anne-Marie Boulanger
AUTEUR DE LA THÈSE / AUTHOR OF THESIS

Ph.D. (Chemistry)
GRADE / DEGREE

Department of Chemistry
FACULTÉ, ÉCOLE, DÉPARTEMENT / FACULTY, SCHOOL, DEPARTMENT

Unimolecular Chemistry of Gas-phase Hydrazine Ions

TITRE DE LA THÈSE / TITLE OF THESIS

Paul M. Mayer
DIRECTEUR (DIRECTRICE) DE LA THÈSE / THESIS SUPERVISOR

CO-DIRECTEUR (CO-DIRECTRICE) DE LA THÈSE / THESIS CO-SUPERVISOR

EXAMINATEURS (EXAMINATRICES) DE LA THÈSE / THESIS EXAMINERS

Hans Terlouw

Javier Giorgi

Robert Burke

Tom Woo

Gary W. Slater
Le Doyen de la Faculté des études supérieures et postdoctorales / Dean of the Faculty of Graduate and Postdoctoral Studies

UNIMOLECULAR CHEMISTRY OF GAS-PHASE HYDRAZINE IONS

ANNE-MARIE BOULANGER

Thesis submitted to the
Faculty of Graduate and Postdoctoral Studies
University of Ottawa
In partial fulfillment of the requirements for
the degree of Doctor of Philosophy in the
Ottawa-Carleton Chemistry Institute

July 2008

Thèse soumise à la
Faculté des études supérieures et postdoctorales
Université d'Ottawa
en vue de l'obtention du doctorat
à l'institut de chimie d'Ottawa-Carleton

Juillet 2008

Candidate	Supervisor /Superviseur
Anne-Marie Boulanger	Dr. Paul M. Mayer

Your file Votre référence
ISBN: 978-0-494-48388-6
Our file Notre référence
ISBN: 978-0-494-48388-6

À mes parents qui m'ont aimée
et soutenue dans tous mes projets

Solum certum nihil esse certi.
Caius Plinius Secundus, Natural History

Abstract

The unimolecular dissociation reactions of ionized methylhydrazine, $CH_3NHNH_2^{+\bullet}$, 1,1-dimethylhydrazine, $(CH_3)_2NNH_2^{+\bullet}$, and tetramethylhydrazine, $(CH_3)_2NN(CH_3)_2^{+\bullet}$, were investigated using tandem mass spectrometry, threshold photoelectron photoion coincidence spectroscopy and variational transition state theory. The modelled thresholds for the ion dissociation yielded new thermochemistry for these N_2-containing ions.

The low energy dissociation pathways of the methyl-substituted hydrazine radical cations correspond to the losses of a hydrogen atom, a methyl radical and/or a rearrangement process leading to the loss of methane. The three fragment ions of $MH^{+\bullet}$ are ion *m/z* 45, $CH_2NHNH_2^+$, ion *m/z* 31, $NHNH_2^+$, and ion *m/z* 30, $N_2H_2^{+\bullet}$. The two fragment ions of $DMH^{+\bullet}$ are ion *m/z* 59, $(CH_3)(CH_2)NNH_2^+$, and ion *m/z* 45, $CH_3N{=}NH_2^+$. The two fragment ions of $TMH^{+\bullet}$ are ion *m/z* 73, $(CH_3)_2NNCH_3^+$, and ion *m/z* 72, $C_3H_8N_2^{+\bullet}$.

Product ion structures were determined from MIKE, CID, KER and deuterium exchange experiments performed on a modified VG ZAB mass spectrometer of BEE geometry. The TPEPICO experiments were performed at the Daresbury Laboratory Synchrotron Radiation Source. The breakdown diagrams in the threshold region for each ion were modelled. The potential energy curve of each dissociation reaction was calculated at the B3-LYP/6-31+G(d) level of theory. The molecular configuration corresponding to the minimum sum-of-states was located and used as the transition state in the RRKM calculation of *k(*E*)*. The *k(*E*)* data was convoluted with the internal energy distribution of the

ion, the electron transmission function of the electron analyser and the monochromator band-pass width to simulate the experimental breakdown curves.

The effects of the entropy of activation on simple dissociation reactions were also investigated. Several transition states were identified with increasing ion internal energy for the methyl radical loss and the hydrogen atom loss channels. The variation in the $\Delta S^{\ddagger}$ values was found to affect largely the shape of the breakdown curves and the dissociation reactions.

Enthalpies of formation of the fragment ions, determined from the theoretical fits of the experimental breakdown curves, were found to be in excellent agreement with the calculated values. The proton affinities of several NN-containing neutral molecules and the N–C and H–C bond dissociation enthalpies were also determined.

Résumé

Les réactions de dissociation unimoléculaire des ions du méthylhydrazine, $CH_3NHNH_2^{+\bullet}$, du 1,1-diméthylhydrazine, $(CH_3)_2NNH_2^{+\bullet}$, et du tétraméthylhydrazine, $(CH_3)_2NN(CH_3)_2^{+\bullet}$, ont été étudiées par spectrométrie de masse en tandem, par spectroscopie TPEPICO et avec la théorie de l'état de transition variationel. Des valeurs thermochimiques ont été déterminées à partir de la modélisation des seuils de dissociation des ions fragmentaires.

Les dissociations de plus basse énergie des trois cations radicaux étudiés correspondent aux pertes d'un atome d'hydrogène, d'un radical méthyle et/ou d'une molécule de méthane. Les ions fragmentaires du $MH^{+\bullet}$ sont l'ion *m/z* 45, $CH_2NHNH_2^+$, l'ion *m/z* 31, $NHNH_2^+$, et l'ion *m/z* 30, $N_2H_2^{+\bullet}$; ceux du $DMH^{+\bullet}$ sont l'ion *m/z* 59, $(CH_3)(CH_2)NNH_2^+$, et l'ion *m/z* 45, $CH_3NNH_2^+$, et ceux du $TMH^{+\bullet}$ sont l'ion *m/z* 73, $(CH_3)_2NNCH_3^+$, et l'ion *m/z* 72, $C_3H_8N_2^{+\bullet}$.

Des expériences MIKE, CID, KER et de marquage au deutérium ont été menées avec un spectromètre de masse en tandem modifié VG ZAB de géométrie BEE. Les expériences de spectroscopie TPEPICO ont été menées au Daresbury Laboratory Synchrotron Radiation Source. La courbe d'énergie potentielle de chaque réaction de dissociation a été calculée au niveau de théorie B3-LYP/6-31+G(d). Les configurations moléculaires correspondant au minimum de la somme des états ont été utilisées comme états de transition dans les calculs RRKM de $k(E)$. Les courbes de dissociation de chaque ion parent ont été modélisées en convoluant l'ensemble des $k(E)$ avec la distribution de l'énergie

interne de l'ion parent, la fonction de transmission électronique de l'analyseur électronique et la largeur de la bande passante du monochromateur.

Plusieurs états de transition ont été identifiés en fonction de l'augmentation de l'énergie interne de l'ion parent pour les dissociations menant aux pertes d'un radical méthyle et d'un atome d'hydrogène. Il a été trouvé que la variation de $\Delta S^{\ddagger}$ affecte grandement l'aspect des courbes de dissociation et les réactions de dissociation.

Les enthalpies de formation des ions fragmentaires, déterminées à partir de la modélisation des courbes expérimentales de dissociation, concordent avec les valeurs calculées. L'affinité protonique et les enthalpies de dissociation des liaisons N–C et H–C ont également été déterminées.

Acknowledgements

I wish to thank my supervior, Dr Paul M. Mayer, for the past five years spent in his laboratory, first as an honours student and then as a graduate student. I had great and diverse opportunities as a student: I went three times on training periods at the Daresbury Laboratory Synchrotron Radiation Source and I attended many national and international conferences. My supervisor guided and supported me in my research as well as in the various aspects of the Ph. D. studies. I will always be grateful to him for all the trust and patience he has demonstrated towards me throughout the years.

This thesis would not have been possible without the collaboration of two British scientists, Dr David M. P. Holland and Dr David A. Shaw. I thank them for their great help during the beamtime periods at the synchrotron, for their generous and constant contribution to the data analysis and for their precious advice throughout my studies.

I also want to thank Dr Emma E. Rennie who was a postdoc in the laboratory at the beginning of my studies. She helped greatly with my research, particularly with the data analysis from the Daresbury Laboratory, and I thank her for her availability and constant support.

Many people embellished my years in the Mass Spectrometry Center at the University of Ottawa and they are Dr John L. Holmes, Dr Clement Kazakoff and Dr Sander Mommers. I thank them all for their support and their presence during my studies. I met many students during those years and I want to thank them all for their help, support, friendship and encouragement. I will always remember the good time we had joking, teasing

each other and laughing together. Thanks to Annick, Clement, Abdul, Xian, Julie, Annie, Mohammad, Brandon, WeiWei, Yawei, Madlena and Éric.

My warm thanks go to my family, especially my parents who supported me throughout all my projects, and my friends. Thanks to my mother Lise, my father Jean-Simon, my sister Maude, my uncle Michel and my friends Jennifer, Anik, Sébastien, Patrick, Luc, Marie-Christine and Lauren.

Finally, I thank the Natural Sciences and Engineering Research Council of Canada (NSERC) and the University of Ottawa for scholarships.

Remerciements

Je tiens à remercier sincèrement mon directeur de thèse, le Dr Paul M. Mayer, pour les cinq magnifiques années passées dans son laboratoire à titre d'étudiante de spécialisation et ensuite comme étudiante graduée. J'ai eu la chance de vivre des expériences aussi diverses qu'enrichissantes en effectuant des stages d'études au Daresbury Laboratory Synchrotron Radiation Source et en participant à plusieurs conférences nationales et internationales. Il a su me guider et m'appuyer dans ma recherche ainsi que dans les divers aspects de mes études doctorales. Je serai toujours reconnaissante de la confiance et de la patience qu'il m'a démontrées au cours des années passées dans son laboratoire.

Cette thèse a été rendue possible grâce à la collaboration de deux scientifiques britanniques du Daresbury Laboratory Synchrotron Radiatio Source au Royaume-Uni, le Dr David M. P. Holland et le Dr David A. Shaw. Je les remercie de leur aide immense lors des longues périodes de travail au synchrotron, de leur apport constant et généreux dans l'analyse des données et de leurs précieux conseils tout au long de mes études.

Je tiens également à remercier la Dre Emma E. Rennie qui a effectué un stage postdoctoral dans notre laboratoire au début de mes études. Elle m'a grandement aidée avec ma recherche, en particulier avec l'analyse des données obtenues au Daresbury Laboratory. Je la remercie pour sa disponibilité et son appui constant.

Plusieurs personnes ont également enrichi et embelli mes années au centre de spectrométrie de masse de l'Université d'Ottawa et j'ai nommé le Dr John L. Holmes, le Dr Clement Kazakoff et le Dr Sander Mommers. Je les remercie tous profondément de leur appui et leur présence pendant mes études. Les nombreux étudiants que j'ai croisés et avec

qui j'ai partagé d'excellents moments ont tous contribué à rendre mes années au laboratoire mémorables. Je les remercie pour leur soutien, leur aide, leur encouragement et leur amitié, et aussi pour les blagues, les taquineries et les bons moments partagés au laboratoire et lors des conférences auxquelles nous avons participé ensemble. Merci à Annick, Clement, Abdul, Xian, Julie, Annie, Mohammad, Brandon, WeiWei, Yawei, Madlena et Éric.

Je termine en remerciant chaleureusement ma famille, en particulier mes parents qui m'ont appuyée et soutenue dans tous mes projets, et mes ami(e)s. Je leur suis reconnaissante de m'avoir écoutée et encouragée aux différentes étapes de mon doctorat. Sans eux, les dernières années auraient été beaucoup plus difficiles à traverser. Je suis choyée d'être aussi bien entourée et je tiens à le souligner. Merci à ma mère Lise, mon père Jean-Simon, ma sœur Maude, mon oncle Michel et à mes ami(e)s Jennifer, Anik, Sébastien, Patrick, Luc, Marie-Christine et Lauren.

Je remercie finalement le conseil de recherches en sciences naturelles et en génie du Canada (CRSNG) et l'Université d'Ottawa pour les bourses d'études que j'ai reçues pendant mes études.

Table of Contents

List of Tables

List of Figures and Schemes

List of Abbreviations

$IE_a(AB)$	Adiabatic ionization energy of neutral molecule AB
AE	Appearance energy
N_A	Avogadro's number
$R_1N{=}NR_2$	Azo compound with $R_{i,\ i=1,2}$ = H or alkyl group
B3-LYP	Becke 3 term, Lee, Yang, Parr: a hybrid density functional method
k_B	Boltzmann constant, equal to 1.380×10^{-23} J K^{-1}
DH	Bond dissociation enthalpy
$R^{\ddagger}$	Bond distance at which is located the transition state of a unimolecular dissociation reaction
$k(T)$	Canonical rate constant
CID	Collision-induced dissociation
G2, G3	Composite methods, high level quantum mechanical calculations
A^+	Daughter ion and/or fragment ion
$\rho(E)$	Density of states at a particular energy E
HN=NH	Diazene
DMH	1,1-Dimethylhydrazine
$P(E,T)$	Distribution of internal energies at a particular temperature T
$e^-/AB^{+\bullet}$	Electron-ion pair created by photoionization
EI	Electron ionization
ESA	Electrostatic energy analyzer
$\Delta_f H_0$, $\Delta_f H_{298}$	Enthalpy of formation at 0 K or 298 K
$\Delta H_0^{\ddagger}$	Enthalpy of activation
$\Delta S^{\ddagger}$	Entropy of activation
E_0	Energy of activation
FFR	Field-free region
FR	Free rotor model for entropy calculations
s	Harmonic oscillator in RRK and RRKM theories
HO	Harmonic oscillator model for entropy calculations

HF	Hartree-Fock *ab initio* method
IUPAC	International Union of Pure and Applied Chemistry
$E_{int}(AB^{+\bullet})$	Internal energy of the radical cation $AB^{+\bullet}$
E or E_{int}	Internal energy
$KE(e^-)$	Kinetic energy of electron
KER	Kinetic energy release
MIKE	Mass-analyzed ion kinetic energy
m/z	Mass-to-charge ratio
MH	Methylhydrazine
$k(E)$	Microcanonical rate constant
$k(E, J)$	Vibrational and rotational microcanonical rate constant
R	Molar gas constant, equal to 8.314 J K^{-1} mol^{-1}
MP2	Moller-Plesset second-order perturbation theory
AB	Neutral molecule
$B^{\bullet}$	Neutral fragment
$AB^{+\bullet}$	Parent ion and/or a radical cation
X_i	Particular internal energy of an ion $AB^{+\bullet}$
Q_i	Partition function (rotational and/or vibrational)
hv	Photon and/or photon energy
PEPICO	Photoelectron-photoion coincidence spectroscopy
h	Planck constant, equal to 6.626×10^{-34} J s
$V(R)$	Potential energy as a function of the reaction coordinate R
PA	Proton affinity
QET	Quasi-equilibrium theory
R or R–X	Reaction coordinate (e.g. dissociating bond in ion)
σ	Reaction degeneracy in RRKM theory or molecular symmetry number
RRK	Rice-Ramsperger-Kassel theory
RRKM	Rice-Ramsperger-Kassel-Marcus theory
R_1R_2N–NR_3R_4	Substituted hydrazine compound with R_i = H, CH_3 or alkyl group

$N^{\ddagger}(E - E_0)$	Sum of states
$N^{\ddagger}_{min}$	Minimum in the sum of states
T	Temperature
TMH	Tetramethylhydrazine
TPEPICO	Threshold photoelectron-photoion coincidence spectroscopy
TOF	Time-of-flight
TS	Transition state
VUV	Vacuum ultraviolet light
VTST	Variational transition state theory
ω_i or ν_i	i^{th} Vibrational frequency

Chapter 1

INTRODUCTION

1.1 Objectives

The work presented in this thesis is part of a larger investigation of NN-containing molecules and ions. The main goal of this study was to examine the impact that the entropy of activation ($\Delta S^{\ddagger}$) can have on an otherwise simple unimolecular dissociation reaction: a bond cleavage. Three methyl-substituted hydrazine ions, R_1R_2N–NR_3R_4, R_i = CH_3 or H, were chosen because, as will be evident from the experimental data obtained for these ions, the reactions leading to the loss of a hydrogen atom and a methyl group exhibit significant entropy effects. In addition, we set out to determine reliable enthalpies of formation for the observed NN-containing fragment ions.

1.2 The properties of N_2-containing molecules and ions

Cations containing two nitrogen atoms in their backbone have been the subject of only a few experimental and theoretical studies [1-4]. Most of the investigations, carried out in the 1970s, concerned the photoelectron spectroscopy of the azo compounds (R_1N=NR_2) and some hydrazine derivatives (R_1R_2N–NR_3R_4) [5-20].

One of the simplest N_2-containing molecules, the short-lived diazene molecule (HN=NH), has been the subject of many spectroscopic and theoretical investigations [11, 12, 21-24]. The interest in this molecule arises from its reactive and spectroscopic properties. Because of its small size, it has also been extensively studied by theoreticians. This molecule is an isoelectronic analogue [11] of important species such as molecular

oxygen (O_2, $^1\Delta_g$), formaldehyde ($H_2C{=}O$) and ethylene ($H_2C{=}CH_2$). Ionised diazene produces a known constituent of interstellar clouds, the N_2H^+ cation, in its lowest energy fragmentation channel [22]. HN=NH has two configurations [11, 12, 23, 25], trans or cis, the lower one being the trans singlet ground state (C_{2h} symmetry). The cis configuration (C_{2v} symmetry), separated by a barrier of 230 kJ mol^{-1} from the trans configuration, is only 24.3 kJ mol^{-1} higher in energy. A third isomer of diazene is postulated to exist, the iso-diazene or 1,1-dihydrodiazene, H_2NN [12]. It probably has a triplet ground state and a pyramidal geometry [12, 25]. Its singlet state should have a planar geometry and be higher in energy by just 8.4–12.6 kJ mol^{-1} [25]. Diazene is also a well known selective reducing agent in solution. It acts as a multiple bond hydrogenation catalyst with functional and stereo selectivity [11, 26].

Diazene is believed to be one of the intermediates in the reduction of nitrogen to ammonia by the enzyme nitrogenase [27, 28]. Many studies have been done on nitrogenase in order to elucidate the reaction intermediates during the N_2 reduction and to determine the mechanism of this reduction. A proposed nitrogenase reaction mechanism for N_2 reduction involves intermediates in which the FeMo-cofactor binds N_2-derived species at the levels of reduction of diazene and hydrazine as shown in Scheme 1.1. Barney et al. [27], in 2005, published the first report of high-population intermediates trapped at the various stages (early, middle and late) of the N_2 reduction.

Even if the diazene molecule has been the subject of many studies, its derivatives, the azo compounds and their saturated analogues, the hydrazine derivatives, have received little attention. These compounds are interesting because of their high-energy content, their versatility and reactivity. The properties of the azo and hydrazine compounds depend on the

nature of the substituent R groups [6]. The azo dyes have been traditionally extremely important to industry due to their high stability and to their electronic transitions that occur in the visible region. When R is a relatively stable alkyl radical, the azo dyes become thermally labile and constitute an important class of polymerisation initiators [6, 29, 30]. The practical properties of these azo compounds rest mainly on their electronic structure and thermochemistry.

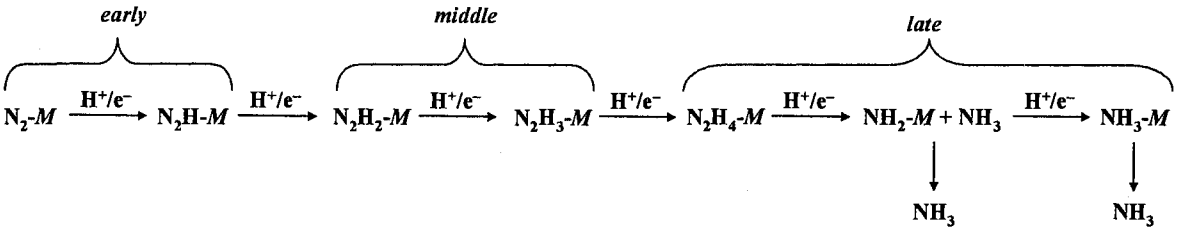

Scheme 1.1 – Proposed N_2 reduction mechanism by the FeMo-cofactor (denoted as *M*) of the enzyme nitrogenase through 2-electron/2-proton, semi-reduced intermediates (adapted from reference [27]).

1.3 The uses and applications of the hydrazine derivatives

The hydrazine derivatives are very energetic compounds that have many industrial and analytical applications. Hydrazine is used as a corrosion inhibitor [31] for steel structures in contact with hot water. These uses arise from the fact that it is an endothermic compound ($\Delta_f H°_{298} = 95.3 \pm 0.8$ kJ mol^{-1} [32]) and its reaction with oxygen in the gas phase is largely exothermic ($\Delta H_{rxn} = 580$ kJ mol^{-1}) [31]:

$$N_2H_4(g) + O_2(g) \longrightarrow N_2(g) + H_2O(g) \qquad (1.1)$$

Protonated hydrazine, $H_2N–NH_3^+$, was also found to be a very effective corrosion inhibitor in the aqueous systems of nuclear reactors [31]. Under irradiation conditions, the principal

radical species produced are the solvated electron and the hydroxyl radical. Protonated hydrazine reacts with the solvated electron [31]:

$$e_{(aq)}^- + H_2NNH_3^+ \rightarrow N_2H_4 + H^\bullet,\ \Delta G_{rxn} = -10\ kJ\ mol^{-1} \qquad (1.2)$$

The hydrazine derivatives have long been known to react uniquely with carbonyl compounds in solution as reported by Emil Fischer and A. Purgotti in 1884 and 1894, respectively [33]. 2,4-Dinitrophenylhydrazine is widely used for sensitive measurements of carbonyl compounds in aqueous solutions and in extracted air samples. The carbonyl derivatisation reaction is shown in Scheme 1.2. The addition process is catalyzed by acid to produce formaldehyde hydrazone and water. The resulting hydrazones are readily detected by the strong absorption of visible light by the nitrophenyl chromophore [33].

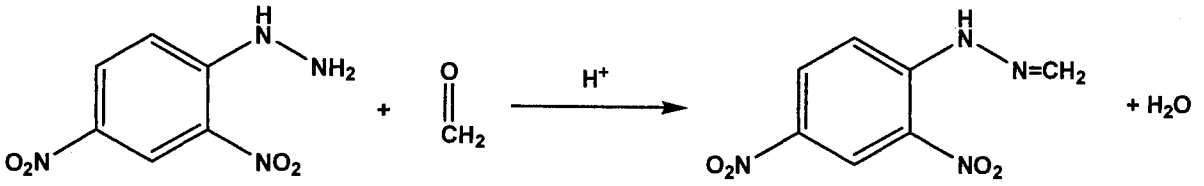

2,4-dinitrophenyl hydrazine formaldehyde dinitrophenylhydrazine

Scheme 1.2 – Acid-catalyzed hydrazone formation in solution (adapted from reference [33]).

Methylhydrazine has many applications in synthesis [34] like in material synthesis by chemical vapour deposition (CVD) processes. In inorganic synthesis, it has been used as a nitrogen precursor to replace ammonia for the organometallic vapour-phase epitaxy growth of the group III nitride [35]. MH is also a nitrogen source in the metal organic molecular beam epitaxy growth of GaN [36] and for the vapour-phase epitaxial growth of InN [37].

Hydrazine and its derivatives are also used as propellant fuels in rocket and satellite thrusters [31, 34, 38-45]. Most of the studies performed on the hydrazines are related to combustion chemistry or their use as a fuel. Only a few studies [31, 38, 46-48] have been performed on the gas-phase chemistry of the hydrazine ion and its derivatives. Methyl-substituted hydrazines are attractive as mono- and bipropellant fuels for thrusters [45] because they are storable liquids. As monopropellants, the hydrazine derivatives decompose exothermically upon contact with a catalyst or a hot surface and generate hot gas in a controlled manner for thrust or pneumatic power. The methylhydrazine (fuel) and nitrogen tetraoxide (oxidizer) bipropellant formulation is widely used for satellites propulsion. At present, it is used for space shuttles, for many satellites and for the launcher Ariane 5 [34, 44]. This bipropellant formulation is hypergolic which means that the two compounds ignite spontaneously upon contact at low temperature ($T \leq 298$ K). The initiation reactions, in the gas phase, were found important for ignition when the two compounds come into contact in the liquid state [34]:

$$CH_3NHNH_2 + NO_2 \rightarrow C^{\bullet}H_2NHNH_2 + HONO \qquad (1.3.a)$$

$$CH_3NHNH_2 + NO_2 \rightarrow CH_3N^{\bullet}NH_2 + HONO \qquad (1.3.b)$$

$$CH_3NHNH_2 + NO_2 \rightarrow CH_3NHNH^{\bullet} + HONO \qquad (1.3.c)$$

Methyl- and 1,1-dimethylhydrazine are also components of some advanced propellant systems including gelled fuels (with inhibited red-fuming nitric acid (IRFNA)) and metalized gelled propellants [40, 41].

A knowledge of the decomposition, spectroscopy and chemical dynamics of the hydrazine compounds is not only valuable in predicting the storability and possible precombustion reactions but is vital to properly interpret and model the dynamics of the

thrusters whose efficiency depends strongly on the extent of dissociation and electron-ion and atom-atom recombination [38, 39, 45].

Interest in hydrazine and its derivatives is not only directed towards their combustion chemistry applied to propulsion but also to their fate once they are released into the atmosphere [34, 49]. Although most of the hydrazine fuel aboard spacecraft is combusted, appreciable amounts are released in an unburned state as the engine is shut down. The reactions of the hydrazines with high-altitude atmospheric species have to be considered to assess the importance of fuel products as potential contaminants in the spacecraft environment. Different examples of important atmospheric oxidation of methylhydrazine with high-altitude species are explained below. The first type of reaction expected in the atmosphere is the tropospheric oxidation of neutral methylhydrazine with hydroxyl radicals, as reaction with OH radicals is the major atmospheric process for most chemical species with available hydrogen atoms [34]:

$$CH_3NHNH_2 + OH^{\bullet} \rightarrow C^{\bullet}H_2NHNH_2 + H_2O \qquad (1.4.a)$$

$$CH_3NHNH_2 + OH^{\bullet} \rightarrow CH_3N^{\bullet}NH_2 + H_2O \qquad (1.4.b)$$

$$CH_3NHNH_2 + OH^{\bullet} \rightarrow CH_3NHNH^{\bullet} + H_2O \qquad (1.4.c)$$

The reaction generates methylhydrazyl radicals that can undergo further reactions with molecular oxygen to form peroxy radicals. Another type of reactions is the low-Earth orbital altitude oxidation of methylhydrazine. At these altitudes (250 km above the Earth's surface), the most prominent species found is the oxygen cation. The ion density is approximately 10^5 cm^{-3} and roughly 98% is O^+ [49]. The oxygen cation will undergo a charge transfer reaction with neutral methylhydrazine to generate the methylhydrazine ion [34]:

$$CH_3NHNH_2 + O^{+\bullet} \rightarrow CH_3NHNH_2^{+\bullet} + O \qquad (1.5)$$

This MH ion can then fragment to form smaller fragments through N–N, N–C and C–H bond breaking [49]. Gardner et al. [49] have studied the fragmentation reactions of neutral methylhydrazine with the oxygen cation and other small cations such as NO^+, Ar^+, CO^+ and CO_2^+ and found that the product ions for the $[X^+ + CH_3NHNH_2]$ reactions fell into three mass ranges, (a) *m/z* 15–18, (b) *m/z* 27–31 and (c) *m/z* 44–47, corresponding to compounds containing a single carbon or nitrogen atom.

A better knowledge of all these processes can be acquired by modeling all the chemistries happening in the atmosphere. In order to do this modeling, considerable thermodynamic and kinetic data are required as input to the models. This is where the importance of having reliable thermochemistry of H/C/N species comes into play. The thermodynamic and chemical kinetic data of many species likely to be present in the atmospheric chemical reactions mentioned above are not available in the literature [34]. Their enthalpy of formation could be estimated from group additivity methods to avoid computational expense of *ab initio* calculations. However, these estimation methods cannot be used for many of these species due to lack of group data for the groups and molecules considered here. The best way to obtain reliable thermochemical data (e.g., enthalpy of formation, bond dissociation enthalpy, etc.) is by performing high-level *ab initio* calculations when experimental data is not available.

1.4 Threshold photoelectron-photoion coincidence spectroscopy

Photoelectron-photoion (PEPICO) and threshold photoelectron-photoion (TPEPICO) coincidence spectroscopy studies provide the most detailed information about the dissociations of state selected ions, the dependence of their decomposition rates upon parent

ion internal energy and the study of fragment ion translational energies [50, 51]. In both methods, a molecule, AB, is ionized through the absorption of a photon ($h\nu$) having a well defined energy [50, 51]:

$$AB + h\nu \rightarrow AB^{+\bullet} + e^{-} \qquad (1.6.a)$$

$$AB^{+\bullet} \rightarrow A^{+} + B^{\bullet} \qquad (1.6.b)$$

The ionization process creates an electron-ion pair ($e^{-}/AB^{+\bullet}$) and the experiment concerns the detection of the electron in coincidence with its associated ion (parent ion, $AB^{+\bullet}$, or daughter ion, A^{+}). If the internal energy of the parent ion is sufficient, it can fragment to produce a daughter ion A^{+} and a neutral fragment $B^{\bullet}$. The ionization process can be written energetically as [50-52]:

$$h\nu = IE_a(AB) + E_{int}(AB^{+\bullet}) + KE(e^{-}) \qquad (1.7)$$

where $E_{int}(AB^{+\bullet})$ is the parent ion internal energy, $KE(e^{-})$ is the kinetic energy of the electron, $h\nu$ is the photon energy and $IE_a(AB)$ is the adiabatic ionization energy of the neutral molecule. The parent ion internal energy can be determined by a measurement of the kinetic energy of the ejected electron, which corresponds to the excess energy, since the photon and the ionization energies are known precisely. The ionization process is bound to a continuum transition, so the ion $AB^{+\bullet}$ can have a range of internal energies, from the ground state up to an energy [$h\nu - IE_a$]. The relation of the electron kinetic energy and the ion internal energy is depicted in Figure 1.1 [51].

In the PEPICO technique [50-52], a photon source having a fixed excitation energy, normally the HeI resonance line at 21.2 eV, is used to photoionize a molecule and the ions are detected in coincidence with electrons of selected energies. These electrons are measured with a dispersive electrostatic energy analyser. As explained above, the parent

ions generated in this type of experiment can be formed in various electronic and vibrational states within the limitations imposed by vertical ionization and non-vanishing Franck-Condon factors [50].

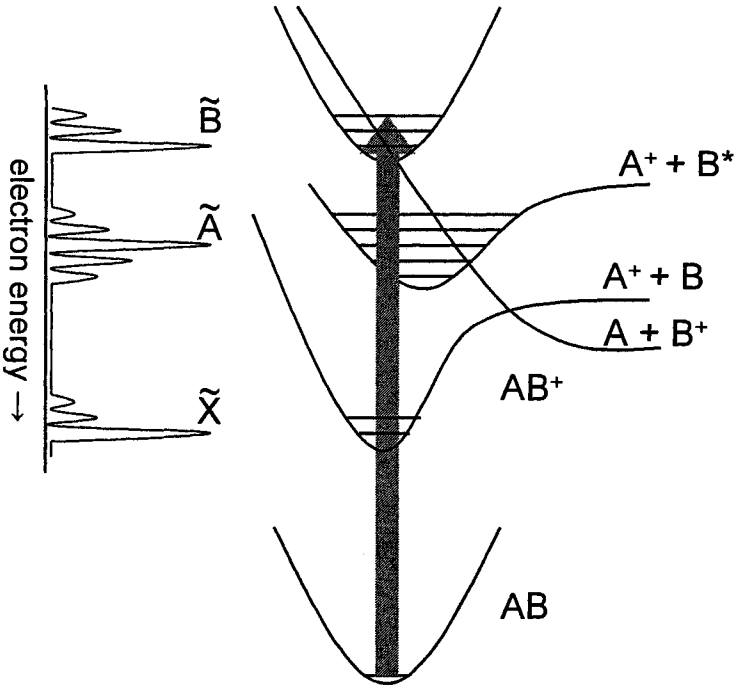

Figure 1.1 – Distribution of the ion states produced by photoionization. The photoelectron spectrum is shown on the left (adapted from reference [51]).

In the TPEPICO approach, a continuously tunable photon source is used and only threshold electrons (i.e. electrons having initially zero kinetic energy) are detected with their associated ions. There are two main advantages [50, 52] of the TPEPICO technique over the conventional PEPICO method. First, the detection efficiency of threshold electrons is nearly 100% whereas the detection of energetic electrons is only a few percent because these electrons are scattered in all directions [51]. Secondly, degenerate autoionization allows ions to be formed even in the Franck-Condon gaps. The only disadvantage of the TPEPICO

technique is the requirement of a tunable photon source. This has been overcome through the use of synchrotron radiation.

A molecular ion will decompose according to its internal energy as shown in Figure 1.2. It is thus of fundamental importance to accurately determine this parameter in the TPEPICO approach. In order to have a high electron energy resolution, a low extraction field is necessary in the instrument. On the other hand, to have a high ion mass resolution, a high extraction field is needed. This limitation was overcome by Stockbauer [53, 54] who devised a pulse extraction field method. After the creation of electron-ion pair, a low electric field is applied across the interaction region of the TPEPICO instrument to extract the threshold electrons. Once the electrons are detected, the ion extraction field is applied. This high voltage pulse will draw the ions towards the drift tube and the ions are then detected in coincidence with their electrons. This method provides an advantage in that a delay between the detection of the electron and the application of the ion extraction field can be introduced and thus the parent ion residence time in the interaction region can be varied. The observed fragmentation depends on the residence time because as the ion spends more time in the source region, the probability that sufficient energy is accumulated in a particular vibrational mode for decomposition to occur increases. Breakdown curves can be determined as a function of residence time and their kinetic shift can be measured [50].

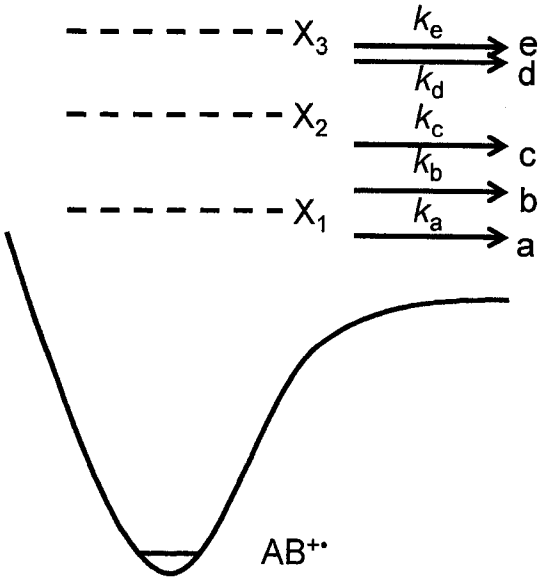

Figure 1.2 – Three possible internal energies ($X_1 < X_2 < X_3$) of an ion $AB^{+\bullet}$ with five different dissociation pathways (a, b, c, d and e). Depending on its internal energy X_i, the ion will have access to more or fewer fragmentation pathways.

The IUPAC [55] definition of synchrotron radiation is: "a radiation which results from the acceleration of charged particles in circular orbits by strong electric and magnetic fields." The charged particles are usually electrons, created by an electron gun, which are firstly accelerated by the linear accelerator. This electron beam is then injected in the booster ring where it is further accelerated. Once the electrons have reached the desired energy, they are transferred in the storage ring where the synchrotron radiation is emitted and transmitted toward the experimental stations as shown in Figure 1.3.

In the early 1990s, the high-resolution monochromatized third-generation VUV synchrotron sources became available. The major advantage of synchrotron radiation is its tunability. Third-generation synchrotron sources have a higher brightness due to a tighter focusing of the orbiting electron bunches [56].

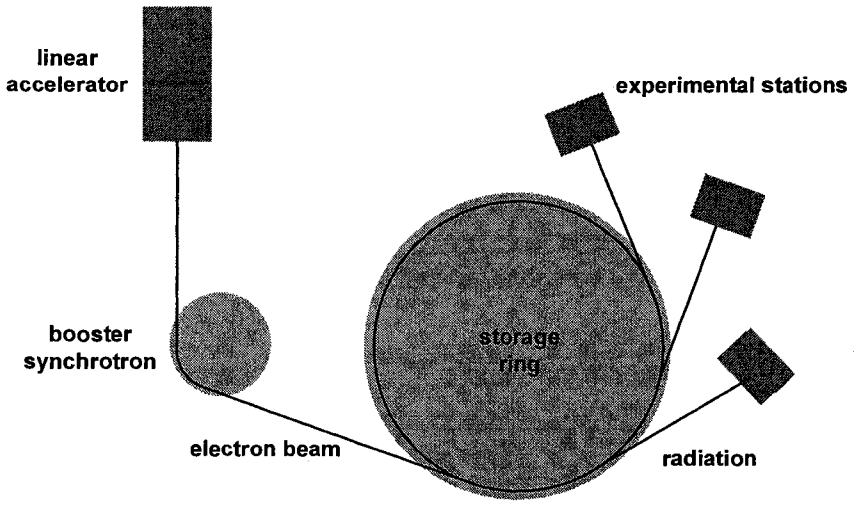

Figure 1.3 – A typical synchrotron storage ring (adapted from reference [57]).

Synchrotron radiation [58] was first observed at the General Electrics 70 MeV synchrotron. When electrons traveling at relativistic speeds are accelerated, electromagnetic radiation is emitted. Synchrotron radiation ranges from vacuum ultraviolet to hard X-rays. In a synchrotron radiation facility, the electrons are stored in a circular accelerator – the electron storage ring. The synchrotron radiation is generated in bending magnets or in other insertion devices like wigglers and undulators placed into linear sections in the storage ring. The circulating electrons are subjected to centripetal acceleration of Lorentz forces and they emit radiation. The synchrotron radiation is highly collimated because the radiation emission pattern is pushed dramatically into a forward direction due to the relativistic velocity of the moving electrons. The circulating electrons have longitudinal and transverse oscillations. Thus, the energy spectrum of the emitted synchrotron radiation has a continuous distribution. An important property of synchrotron radiation is its polarizability characteristics. The polarization depends on the direction of the circulating electron beam and the direction of the photon emission. The polarization can be calculated exactly and the synchrotron radiation can be used for radiometric purposes. Synchrotron radiation from the

electron storage ring offers a clean and stable radiation source with a significant lifetime. The light intensity decreases with time due to collisions between the traveling electrons with residual gas in the storage ring.

Since synchrotron radiation has a continuous distribution, the radiation must be monochromatized [58]. Air is opaque for photons with energy greater than 6 eV. Therefore, the monochromators operating at energies above 6 eV must be evacuated.

1.5 Statistical theories of dissociation rates

Statistical theories like the Rice-Ramsperger-Kassel-Marcus (RRKM) theory and the quasi-equilibrium theory (QET) were developed more than sixty years ago to explain and understand unimolecular reactions. Some of these theories will be reviewed in this section.

1.5.1 RRK theory

A unimolecular reaction (as written in equation 1.8) is defined as any system evolving in time as a result of prior excitation [52]. Dissociation and isomerisation are both unimolecular processes. A unimolecular reaction follows an exponential decay as written in equation 1.9 and from the very beginning, it was recognized that the dissociation rate k depended on the internal energy of the molecule, $k(E)$ [52]:

$$AB \rightarrow products \tag{1.8}$$

$$-\frac{d[AB]}{dt} = k[AB] \tag{1.9}$$

The canonical rate constant $k(T)$ is related to the microcanonical rate constant $k(E)$ by averaging $k(E)$ over the energy distribution [52, 59]:

$$k(T) = \int_{E_0}^{\infty} P(E,T)k(E)dE \tag{1.10}$$

where E_0 is the activation energy and $P(E,T)$ is the distribution of internal energies at a given temperature T. In the 1920s, Lindemann and Hinshelwood [60] developed a mechanism for thermally activated unimolecular reactions [52, 61, 62]:

activation (k_1)–deactivation (k_{-1}) steps: $AB + M \leftrightarrow AB^* + M$ (1.11.a)

unimolecular dissociation (k_2): $AB^* \rightarrow A + B$ (1.11.b)

where AB^* represents an excited molecule and M is any molecule in the vessel. If the steady-state is assumed for the production of AB^*, the overall rate of product formation is given by [52, 61, 62]:

$$rate = k_2[AB^*] = \frac{k_1 k_2 [AB][M]}{k_{-1}[M] + k_2} = k_{uni}[AB] \tag{1.12}$$

This mechanism differentiates the activation and dissociation steps and accounts for the transition of the unimolecular rate constant k_{uni} from the second order at low pressures to first order at high pressures [52, 63].

Rice, Ramsperger and Kassel were the first to develop a conceptual framework for understanding unimolecular reactions [51, 52, 63]. They proposed that the dissociating system was composed of an ensemble of s identical harmonic oscillators with one oscillator, the critical oscillator, truncated at an energy E_0, the activation energy for the dissociation. The critical oscillator is thus the reaction coordinate. A fundamental assumption in this theory is that the energy flows statistically among all the oscillators. The probability of the molecule to be in a dissociative state is given by the following equation [52, 63]:

$$probability = \frac{(n-m+s-1)!n!}{(n-m)!(n+s-1)!} \tag{1.13}$$

where n is the total number of vibrational quanta and m is the number of quanta in the critical coordinate. This probability equation can be converted into a rate constant expression by its multiplication with a frequency of passing through the transition state. This gives the classical RRK rate constant expression [51, 52, 63]:

$$k(E) \approx \nu\left(\frac{n-m}{n}\right)^{s-1} = \nu\left(\frac{E-E_0}{E}\right)^{s-1} \tag{1.14}$$

Unfortunately, the RRK expression is incapable of giving a correct rate even within an order of magnitude [52] due to several reasons. First, it assumes a collection of classical oscillators with $(n - m) >> s$ which is inappropriate for most chemical systems. Second, the RRK theory neglects the zero point energy. Other quantum theories were developed through the years and eliminated the problems associated with the RRK expression by treating the vibrational and rotational degrees of freedom in detail. These theories are known as the RRKM and QET theories.

1.5.2 RRKM/QET

The RRKM/QET expression gives the rate constant for a molecule or an ion at a given energy E and with an activation energy E_0 and is given by [51, 52, 59, 63]:

$$k(E) = \frac{\sigma N^{\ddagger}(E-E_0)}{h\rho(E)} \tag{1.15}$$

where σ is the reaction degeneracy, $N^{\ddagger}(E - E_0)$ is the transition state sum of states from 0 to $E - E_0$, and $\rho(E)$ is the parent ion density of states at an energy E. Two approaches [52, 64] have been proposed for the evaluation of the reaction degeneracy and both should lead to the correct answer. The preferred approach evaluates the reaction degeneracy with the symmetry numbers according to the following equation [52, 64]:

$$\sigma = \sigma_r / \sigma^{\ddagger} \tag{1.16}$$

where σ_r and $\sigma^{\ddagger}$ are the symmetry numbers of the reactant and the transition states structures, respectively. The RRKM/QET theory depends strongly on the values of the vibrational frequencies unlike the RRK theory. To use this expression it is crucial to properly understand the concept of sum and density of states.

The sum and density of states, if the ion's rotational energy is ignored, refer only to the vibrational degrees of freedom [63]. If the ion has s vibrational degrees of freedom and an internal energy E, the sum of states of that ion will represent all the possibilities of distributing the energy among the s oscillators such that the total energy is equal to or less than E. In the RRKM/QET approach, each oscillator has a unique vibrational frequency and thus a distinct energy content. Hence, $N(E)$ is the total number of states and is unitless. The density of states at an energy E represents the number of vibrational configurations with energy content between E and $E + \delta E$. Qualitatively, the sum of states can be interpreted as the number of ways to pass through the transition state that has a total energy of $E - E_0$, while the density of states at an energy E represents the number of ways to get lost in the molecular ion phase space [51, 63]. The sum of states is the numerator and the density of states is the denominator of the RRKM/QET expression because at the transition state, a portion of the ion's total energy has been channeled into the critical oscillator (i.e., the dissociating R–X bond in a simple bond cleavage reaction). The energy in the critical oscillator is at least E_0 and so the remaining energy, $E - E_0$, can be distributed in the other (s – 1) oscillators. The reaction could also pass through the transition state with an energy ε_i above the required minimum energy of E_0 as shown in Figure 1.4 and thus the remaining

internal energy $E - E_0 - \varepsilon_i$ would be partitioned among the other vibrational modes of the ion [63].

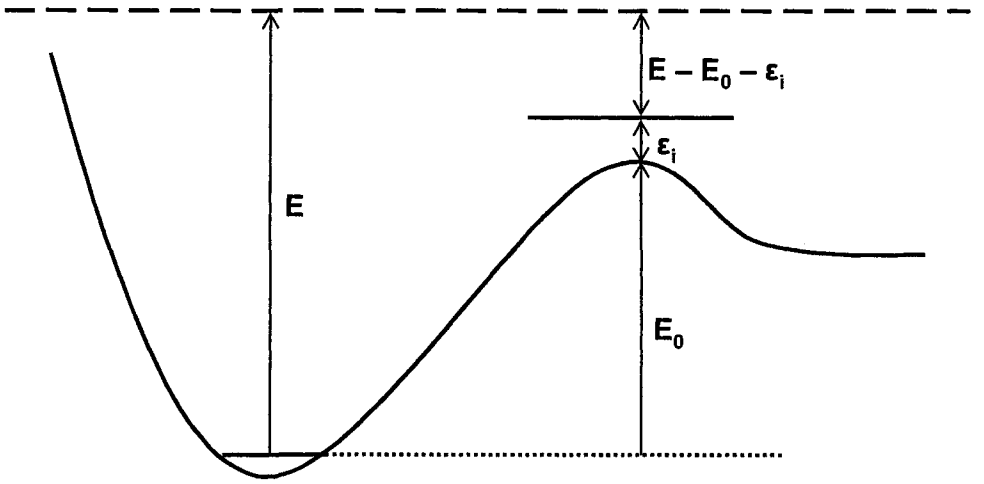

Figure 1.4 – Potential energy surface for a unimolecular dissociation with a real barrier (adapted from references [63, 65]).

To evaluate the RRKM/QET expression 1.15, the activation energy E_0 and the vibrational frequencies of the reactant ion and transition state must be known. These two parameters (E_0 and ω_i) can be treated as adjustable parameters in the fitting procedure of experimentally determined rate constants [52].

1.5.3 Treatments of the transition state

The characterization of the transition state in statistical theories is a major problem. In the case of low angular momentum and moderately attractive potential for the dissociation of a diatomic molecule, no obvious internuclear distance can be associated with the structure of a transition state [52]. This is also true for simple bond cleavage reactions in polyatomic molecules. Often, the transition state structure is only vaguely known which

makes the choice of vibrational frequencies difficult. In many cases, it is not possible to identify a single structure of the transition state because it changes with the internal energy of the ion [52]. In 1938, Wigner suggested that the transition state structure corresponded to the configuration through which the reaction trajectory passed once and only once [59, 63-66]. This is the fundamental assumption of transition state theory [65, 67]. Many years later, Miller [68] and Chesnavich et al. [69] suggested that two transition state structures could exist. In this switching TS model [52, 68, 69], the first transition state is located on the potential energy surface at a long bond distance R–X (R–X being the dissociating bond in the ion) and corresponds to an orbiting TS while the second transition state is found at a shorter R–X bond distance and is the vibrator (or tight) TS. The switch between the two is sudden. This model has been used to calculate dissociation rates of various ionic fragmentations; however the quality of the experimental data was often not sufficient to notice or confirm the presence of the two transition states [52]. Other methods [52] have been developed to treat the transition states in more details. For example, in the adiabatic channel theory, the "interesting" aspects of the reaction (e.g., R–X stretch and R–X bends) are treated in detail and the statistical approach is used for the remaining vibrational modes.

To apply any statistical theory, the structure and vibrational frequencies of the reactants, products and transition states must be known. However, the vibrational frequencies have only been measured for neutral molecules usually in their ground states. In the past, the measurement of ionic vibrational frequencies was difficult if not impossible. With the advent of multiphoton dissociation experiments, the measurement of ions' vibrational frequencies is becoming easier [70, 71]. In studies on halobenzene ions ($C_6H_5X^{+\bullet}$, X = Cl, Br, I) [72, 73], the dissociation rates were calculated assuming that the

vibrational frequencies of the transition state were approximatively the same as those of the reactant ion. It was also assumed that these vibrational frequencies (i.e., reactant ion and TS) could be estimated by scaling the vibrational frequencies of the neutral reactant molecule.

1.5.4 Variational transition state theory

By convention, the transition state is considered as the surface in configuration space dividing the reactant from the products and at which the phase space is minimum [52, 59, 64]. For reactions with a considerable energy barrier as shown in Figure 1.4, the transition state or dividing surface is located at the saddle point which is the highest energy point on the minimum energy path from the reactant to products [59]. In the case of a bond cleavage reaction, the potential energy curve, $V(R)$, as shown in Figure 1.5, does not present a maximum between the reactant and products. Thus, the location of the transition state is not properly defined and the calculation of $\Delta S^{\ddagger}$ is difficult. In this situation, the transition state is referred to as a "generalized" transition state which does not necessarily pass through a saddle point [59]. The generalized TS is defined as being perpendicular to the minimum energy path and intersecting it at a certain bond distance $R^{\ddagger}$ (see Figure 1.5). The position of the dividing surface in simple bond cleavage reactions can be determined using the variational criterion. As suggested by Lifshitz in 1978 [65, 74], ionic systems are well described by the variational criterion since many ionic dissociations have an insignificant reverse activation energy.

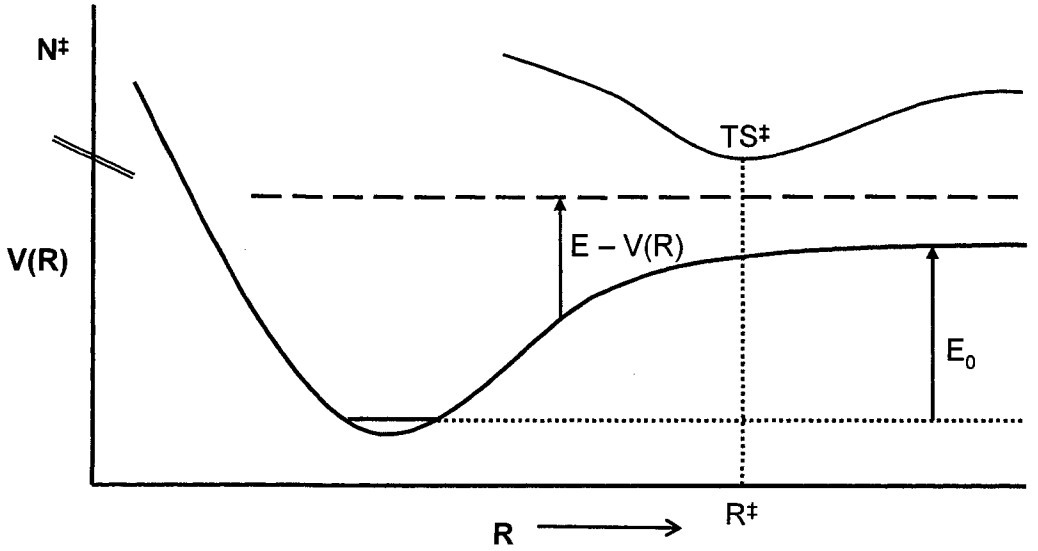

Figure 1.5 – The variation of the sum of states $N^{\ddagger}$ with the bond distance R for a dissociation reaction with no saddle point. The transition state is located at $R = R^{\ddagger}$ at a given total energy E (adapted from reference [52]).

In the variational transition state theory (VTST), the rate constant $k(E,J)$ is calculated as a function of the reaction coordinate R [52]. Figure 1.5 shows the potential energy curve, $V(R)$, as a function of the reaction coordinate R. The variational approach provides an upper limit to the true rate constant for a given potential energy surface. Thus, the best choice of transition state is the dividing surface between the reactant and products that correspond to the smallest rate constant. This corresponds to a local minimum in the sum-of-states ($N^{\ddagger}_{min}$) and is called an entropic bottleneck [52, 65, 74]. The location of the transition state is found by solving the following equation [65]:

$$\frac{\partial}{\partial R} N_{s-1}\left(E - V(R); R\right) = 0 \qquad (1.17)$$

where $N_{s-1}(E - V(R); R)$ is the sum of states of the $(s - 1)$ degrees of freedom perpendicular to R at an energy less than or equal to $E - V(R)$. The rate constant can then be determined from the minimum $N^{\ddagger}$ using the RRKM/QET expression 1.15. Some VTST studies have also been performed by calculating the configuration phase space integrals with a Monte

Carlo integration technique [75-80]. Bimolecular reactions such as collinear and recombination reactions have also been studied with VTST [59, 64, 81-83].

The location of the transition state will shift as the ion's internal energy is increased and this is expected from theory [52, 84]. As the dissociating bond (i.e., the reaction coordinate R) is elongated, two factors come into play: the increase in the potential energy $V(R)$ and the decrease in the vibrational frequencies of the transitional modes which evolve into product rotations and translations. As the reaction proceeds, the potential energy $V(R)$ is constantly increasing and this reduces the available energy $[E - V(R)]$ which in turn reduces the sum of states, while the decrease in the transitional vibrational frequencies increases the sum of states. These two opposing forces will result in a minimum in the sum of states at some bond distance $R^{\ddagger}$ [52, 84] where the transition state is thus located. At low internal energies, the first factor (the available energy) dominates and the transition state occurs at large R values. As the internal energy increases, the two factors become important and transition state switching is expected [84].

1.5.5 Entropy of activation

In the thermodynamic version of transition state theory, the canonical rate constant $k(T)$ is defined in terms of the activation entropy ($\Delta S^{\ddagger}$) and the activation enthalpy ($\Delta H_0^{\ddagger}$) [52, 57]:

$$k(T) = \frac{k_B T}{h} e^{\Delta S^{\ddagger}/R} e^{-\Delta H_0^{\ddagger}/RT} \qquad (1.18)$$

The entropy of activation is a convenient way of describing the nature of a reaction. It is simply the difference in entropy between the reactant ion and its transition state and is calculated using their vibrational frequencies (and rotational constants). A loose transition

state, typically corresponding to simple bond cleavage, has a positive entropy of activation ($\Delta S^{\ddagger} > 0$) because the transition state is less ordered than the reactant ion. Conversely, a tight transition state typically corresponds to a rearrangement process and has a negative entropy of activation ($\Delta S^{\ddagger} < 0$) because it is more ordered than the reactant ion. When $\Delta S^{\ddagger} = 0$, the vibrational frequencies are identical in the transition state and in the reactant ion. Calculating the entropy of activation is also a convenient method for reducing the large number of vibrational frequencies of the reactant ion (3N – 6) and its transition state (3N – 7) into a single parameter. The entropy of activation is determined from the molecular vibrational and rotational partition functions (Q_i) and the internal energies (E_{int}) at a temperature T [57, 63]:

$$\Delta S^{\ddagger} = k_B \ln \frac{\prod Q_i^{\ddagger}}{\prod Q_i} + \frac{E_{int}{}^{\ddagger} - E_{int}}{T} \qquad (1.19)$$

By convention, the entropies of activation are reported at 600 or 1000 K.

The activation energy E_0 and the entropy of activation $\Delta S^{\ddagger}$ both have an impact on the rate constant as a function of internal energy [63]. The magnitude of $k(E)$ is mainly due to E_0 whereas the slope of $k(E)$ is largely due to $\Delta S^{\ddagger}$. The transition state of a reaction is preferably calculated by *ab initio* calculations and so are its vibrational frequencies. Otherwise, the transition state frequencies may be estimated. This is done by using the vibrational frequencies of the reactant ion less one corresponding to the reaction coordinate. The transition state may then by tightened or loosened by scaling the five lowest vibrational frequencies by a common factor (less than 1 will increase $\Delta S^{\ddagger}$ while greater than 1 will decrease $\Delta S^{\ddagger}$) [63].

Chapter 2

EXPERIMENTAL AND COMPUTATIONAL PROCEDURES

2.1 Introduction

The unimolecular dissociation pathways of the methyl-substituted hydrazine ions have been studied with various experimental and theoretical approaches: tandem mass spectrometry, threshold photoelectron-photoion coincidence spectroscopy and variational transition state theory. The instruments used and the procedures behind each approach will be discussed in details in this chapter.

2.2 The modified VG ZAB mass spectrometer

The VG ZAB mass spectrometer [85], found in the University of Ottawa Mass Spectrometry Center, was used mainly to perform structure characterization experiments on the observed fragment ions. The instrument will be described as well as the different types of experiments carried out and the underlying theory.

2.2.1 Description of the instrument

The instrument is a modified three sector VG ZAB mass spectrometer [85] of reverse-geometry with a BEE configuration where B refers to magnet and E to electrostatic analyzer. The instrument is depicted in Figure 2.1 showing the ion source, the magnet, the two electrostatic analyzers and the three field-free regions (FFR).

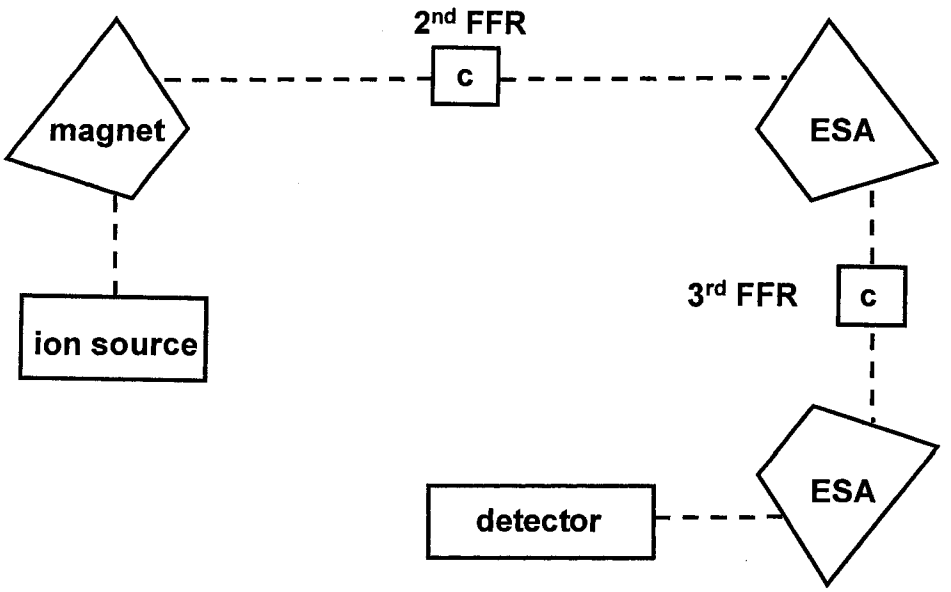

Figure 2.1 – The modified three sector VG ZAB mass spectrometer.

2.2.1.1 Ion source

The ions are created in the ion source by electron ionization (EI) [86]. The electrons, generated from a helical filament heated above 2000 °C, are accelerated towards the ionization chamber by a potential energy difference of 70 eV between the filament and the ionization chamber. The electrons traverse the ionization chamber at a constant velocity, because it is essentially free of electric fields, and are trapped by an electrode, located at the far end of the ionization chamber, which is at a potential slightly higher than that of the ionization chamber. The ion source temperature is usually around 100–150 °C due to the high emission temperature of the filament. The liquid samples are introduced in the ion source via a liquid septum inlet. The liquid is first volatilized in a reservoir and the vapour then leaks into the source via a small capillary. All the experiments were performed using a "low-pressure" ion source. The pressure inside the ion source was kept at ~ 1.0×10^{-5} Torr as measured with an ionization gauge located above the ion source diffusion pump.

After their creation in the ionization chamber, the ions are repelled by a very small electric field of ~ 1 eV. Outside the ionization chamber, they are then submitted to a strong electric field of several thousand volts (in this instrument, the accelerating voltage is 8 kV). The kinetic energy of the ions of mass m and charge ze, z is the number of charges of the ion and e is the fundamental charge of an electron, leaving the ion source with an accelerating voltage of V_{acc} = 8 kV is given by the following equation [86]:

$$\frac{1}{2} mv^2 = zeV_{acc} \qquad (2.1)$$

The main ion beam is the beam of ions having a kinetic energy equal to the full accelerating energy. According the equation 2.1, all the ions thus leave the ion source with essentially the same kinetic energy.

2.2.1.2 Magnetic sector

The ions are analyzed according to their mass-to-charge ratios (m/z). It is thus necessary to separate out the various ions produced in the ion source according to their respective m/z ratios by the use of a magnetic field B perpendicular to the ion motion. An ion of mass m, charge ze and velocity v in a magnetic field will follow a circular path of radius r [86]:

$$r = \frac{mv}{Bze} \qquad (2.2)$$

By rearranging equation 2.1 to $v = (2zeV_{acc}/m)^{1/2}$ and equation 2.2 to $mv = rBze$ and by combining them together, the following relationship is obtained [86]:

$$\frac{m}{z} = \frac{B^2 r^2 e}{2V_{acc}} \qquad (2.3)$$

A particular ion with a mass-to-charge ratio *m/z* can thus be selected to pass through the magnetic sector by the appropriate choice of voltage V (which is held constant) and magnetic field B.

2.2.1.3 Electrostatic energy analyzers

The electrostatic energy analyzers (ESA) are composed of two curved parallel plates between which is applied a potential difference producing an electric field of strength E. The ions will be transmitted through the ESA if their kinetic energy is such that the electrostatic force on them is exactly balanced by the centrifugal force [86]:

$$\frac{1}{2}mv^2 = zeV_{acc} = \frac{1}{2}zeEr \qquad (2.4.a)$$

$$r = \frac{2V_{acc}}{E} \qquad (2.4.b)$$

The potential difference across the two ESA plates can be adjusted to allow ions of selected translational kinetic energy to pass through and be focussed.

2.2.1.4 Field-free regions

There are three field-free regions in the VG ZAB mass spectrometer: the first one is between the ion source and the magnet, the second one is between the magnet and the first ESA and the third one in between the two ESAs. The second and third FFRs are the main experimental regions of the instrument where mass-analyzed ion kinetic energy (MIKE) and collision-induced dissociation (CID) experiments are performed. The second and third field-free regions contain collision cells (identified as "c" in Figure 2.1) which are used to perform CID experiments.

2.2.2 Experiments performed on mass-selected ions

Four different types of experiments were performed on the mass spectrometer and will be explained in more detail.

2.2.2.1 Mass-analyzed ion kinetic energy (MIKE)

All the singly charged (z = 1) ions that leave the ion source will have the same translational kinetic energy, independent of their mass [87]:

$$eV_{acc} = \tfrac{1}{2} m_1 v_1^2 = \tfrac{1}{2} m_2 v_2^2 = \tfrac{1}{2} m_n v_n^2 \qquad (2.5)$$

As explained previously, the ions are separated according to their mass-to-charge ratio m/z as they pass through the magnetic sector. A metastable ion of mass m_1^+ can fragment during its flight in the second FFR and produce a fragment ion of mass m_2^+. The metastable ion m_1^+ will be transmitted through the ESA at an electrostatic potential E_1 onward to the detector and then lower electrostatic potentials (E_2, E_3, ...) will be needed to transmit its fragment ions (m_2^+, m_3^+, ...) [87]:

$$\frac{E_1}{E_2} = \frac{m_1^+}{m_2^+} \qquad (2.6)$$

A MIKE mass spectrum is recorded by sweeping the voltage from E_1 to zero to transmit all fragment ions produced by the metastable ion m_1^+.

2.2.2.2 Collision induced dissociation (CID)

CID experiments were performed in the 2nd and 3rd FFRs using helium as the target gas. The helium pressure in the collision cell was approximately 8.0×10^{-8} Torr to 1.0×10^{-7}

Torr corresponding to a beam reduction of 10% (i.e., the ions suffer on average only single collisions under these conditions) [87].

2.2.2.3 Kinetic energy release (KER)

As the metastable ion m_1^+ dissociates in the second FFR, kinetic energy will be released and this will cause a broadening of the fragment ion peak in the MIKE mass spectrum. The translational kinetic energy ($T_{0.5}$) released in the fragmentation is derived from the peak width at half-height ($W_{0.5}$) and it is convenient to report in order to characterize the peak [87]:

$$T_{0.5} = \frac{(m_1^2)\left(W_{0.5}^2(m_2^+) - W_{0.5}^2(m_1^+)\right)}{16 m_2 m_3 E_1} \qquad (2.7)$$

where $W_{0.5}$ is the half-height width of the m_2^+ fragment ion peak and of the m_1^+ ion beam and m_2 and m_3 are the product masses. For Gaussian-type peaks, $T_{0.5}$ values are of the order of 0.1–75 meV [87]. The KER experiments are conducted under conditions of high resolution by narrowing y-axis beam collimating slits throughout the instrument. The widths of the fragment ion peaks are thus indicative of the kinetic energy release [86]. The peak widths at half-height for the parent ions were 4.022 V for MH, 7.306 V for DMH and 11.872 V for TMH.

2.2.2.4 Deuterium labeling

Deuterium exchange experiments were done with D_2O (MSD Isotopes, 99.9% D, used without further purification). The glass capillary inlet was flushed four times with 10

μL of deuterium oxide prior to the introduction of the sample. A peak with a higher mass-to-charge ratio was observed corresponding to the deuterated methyl-substituted hydrazine ion:

$$CH_3NHNH_2^{+\bullet}\ (m/z\ 46) + D_2O_{excess} \rightarrow CH_3N\mathbf{D}N\mathbf{D}_2^{+\bullet}\ (m/z\ 49) \qquad (2.8)$$

$$(CH_3)_2NNH_2^{+\bullet}\ (m/z\ 60) + D_2O_{excess} \rightarrow (CH_3)_2NN\mathbf{D}_2^{+\bullet}\ (m/z\ 62) \qquad (2.9)$$

MIKE and CID experiments were then performed on the ions of interest.

2.3 The TPEPICO mass spectrometer

The threshold photoelectron-photoion coincidence (TPEPICO) experiments have been carried out at the Daresbury Laboratory Synchrotron Radiation Source (SRS) in Daresbury, Cheshire, UK. The TPEPICO mass spectrometer [50], connected to a 5m normal incidence monochromator [88], is described in this section.

2.3.1 Description of the instrument

The TPEPICO mass spectrometer [50] is shown in Figure 2.2 and consists of a hemispherical electrostatic energy analyzer to detect threshold electrons and a TOF mass spectrometer to detect the associated ions. The instrument, kept inside a stainless steel vacuum chamber and pumped by both a cryopump and a turbomolecular pump, is shielded by two layers of high permeability alloy to attenuate the effect of the earth's magnetic field inside the chamber [50].

2.3.1.1 5m Normal incidence monochromator

The 5m, vertically dispersing, normal incidence monochromator was designed according to specific parameters of the Daresbury Laboratory and has been described in details by Holland et al. [88].

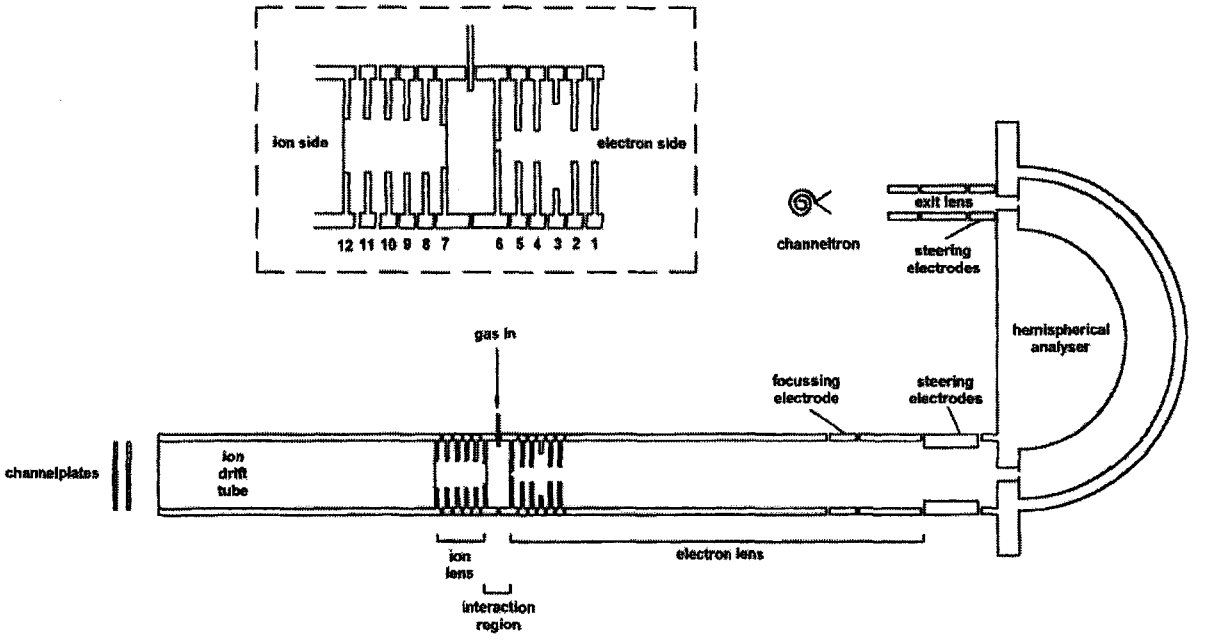

Figure 2.2 – A schematic representation of the TPEPICO apparatus showing the main components consisting of the electron analyzer and the ion TOF mass spectrometer (reproduced with permission from reference [50]).

2.3.1.2 Hemispherical electrostatic energy analyzer

The 100 mm mean radius hemispherical electrostatic threshold electron analyzer [50] comprises a series of entrance lens. Plate 3, shown in the inset of Figure 2.2, acts as a focusing element by reducing the off-axis aberration. A second focusing element, positioned about two-thirds of the distance from the ionization source to the hemispherical analyzer entrance, has magnification purposes. The last component of the entrance lens incorporates split sections which provide additional electric fields that can be used to steer the electrons.

The exit lens is constituted of a three-element cylinder lens. All the electron and ion lens components, including the two hemispheres and the base plate, have been manufactured from aluminium and coated with graphite to obtain a uniform surface potential to minimize any disturbances to the electric fields through which the electrons pass [50]. The electron lens and analyser system have been design to strongly discriminate against the energetic electrons.

2.3.1.3 TOF mass spectrometer

The two-field TOF mass spectrometer [50] is used to mass analyze and detect the ions. The mass spectrometer incorporates the spatial focusing conditions formulated by Wiley and McLaren [89]. The plates 7-12, in the ion lens, are equally spaced over a distance of 35 mm. The interaction region, found between plates 6 and 7, has a width of 18 mm. It is in the interaction region that the photoionisation takes place. Plate 12 forms the entrance to the drift tube which has a length of 224.7 mm [50]. The ends of the drift tube are covered in graphite coated copper mesh to block field penetration. The source and acceleration electric fields, respectively of 400 and 800 V/cm, are applied across plates 6, 7 and 8 and across plates 8 to 12, respectively [50]. The internal diameter of the drift tube is 50 mm which matches that of the channelplates used to detect the ions. The voltage on plate 8 is nominally zero [50].

2.3.2 Pulsed extraction method

In a TPEPICO experiment, a threshold electron is detected in coincidence with its ion. A pulse extraction method has been developed by Stockbauer [53, 54] in which an

initial low electric field is applied across the interaction region to extract the threshold electron and collect it with high energy resolution and high efficiency. The detection of the electron triggers the application of a high voltage pulse across the interaction region to draw the ion inside the TOF mass spectrometer where it is detected in coincidence with its threshold electron with a high ion mass resolution.

A pulsed extraction technique provides another advantage by allowing the breakdown curve to be recorded as a function of parent ion residence time in the interaction region by changing the time between the detection of the threshold electron and the application of the ion drawout field [50, 90]. The residence time is defined as the period between the creation of the electron-ion pair and the application of the pulse, and is given by the transit time of the electron added to the electronic signal processing time. The minimum residence time in the current apparatus has been measured as 1.116 ± 0.050 μs using the experimental procedure described in Holland et al. [50].

The breakdown curves of methylhydrazine [91] and 1,1-dimethylhydrazine [92] in the first cross-over region (between $h\nu \approx 9.64$ and 11.04 eV for MH and between $h\nu \approx 9.4$ and 10.4 eV for DMH) have been measured for four ion residence times, t_{res} = 1.116, 3.116, 5.116 and 7.116 μs, while the breakdown curve of tetramethylhydrazine [91] in the first cross-over region (between $h\nu \approx 8.62$ and 11.02 eV) has been measured for three ion residence times, t_{res} = 1.116, 3.116 and 5.116 μs. The electron transmission function used in the convolution of the calculated breakdown curves was derived from a threshold electron spectrum obtained from the photoionisation of krypton in the region of the $^2P_{1/2}$ ionization limit under the conditions used in the TPEPICO measurements [50].

The photoionisation volume inside the TPEPICO instrument is defined as the intersection between the cylindrical gas jet of 2 mm diameter and the photon beam of 1.5 mm diameter. Thus, the coincidence ions are considered as those formed in the interaction region defined above. The ions formed outside that region will emit photoelectrons which will not be able to move across the electron analyzer system, and consequently the ion extraction field will not be triggered [50].

2.3.3 The spectrometer control and data acquisition system

The spectrometer control and data acquisition system uses standard CAMAC instrumentation interfaced to a PC. The signal processing is done with NIM modules. The time interval between the electron (start) and the ion (stop) pulses is measured with a Le Croy 4208 time-to-digital converter operated in multihit mode. The accumulation of many such events constitutes a TOF spectrum [50]. The delay and blanking circuitry is similar to that described by Butler et al. [93].

2.3.4 Data analysis procedure

The TOF mass spectra of a parent ion (MH, DMH or TMH parent ion) were recorded at various photon energies and parent ion residence times. In the threshold region ($h\nu \approx 9.0$–11.0 eV for the hydrazine ions), the TOF mass spectra are recorded every 50 meV. As the photon energy increases, the acquisition step increases as well. The TOF mass spectra are used to generate the breakdown curves. The breakdown curve plots the normalized abundance of all observed (fragment) ions as a function of energy (photon or internal energy). The cross-over point is defined as the energy at which the parent and

fragment ions are produced with equal intensity [90]. If the cross-over point shifts to lower energy as the residence time increases, it indicates that the ion breakdown curve exhibits a kinetic shift [94]. Figure 2.3 shows the experimental breakdown curve of the methylhydrazine ion in the first cross-over region.

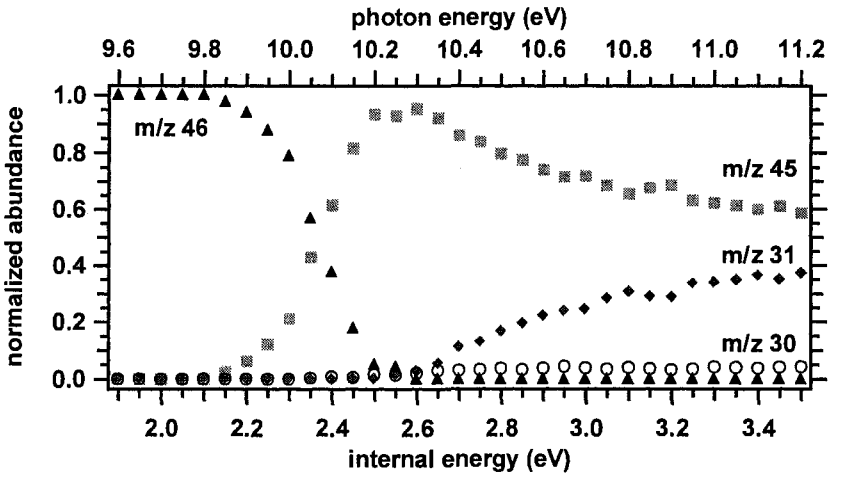

Figure 2.3 – First cross-over region of the experimental breakdown curve of methylhydrazine ion at a parent ion residence time of 1.116 μs.

The detection of the threshold electron and of its associated ion is based on the pulsed extraction method described above in Section 2.3.2. Thus, the observed spectrum, denoted as "true + random", contains contributions from true coincidences and random events. The random events arise from processes in which the ion providing the stop is not the ion associated with the threshold electron providing the start [50]. In order to obtain a spectrum solely due to true coincidences, it is necessary to subtract the random contributions from the "true + random" spectrum. A "random" TOF spectrum is measured using a clock generator that triggers the extraction pulse and initiates the TOF measurement. The stop is provided by the ion signal in the usual manner. Both spectra ("true + random" and "random") are then normalized and the normalized "random" spectrum is subtracted from the "true + random" spectrum to obtain the "true" coincidence spectrum [50]. The "true"

spectrum contains the final data that is compared with the theoretical predictions. Figure 2.4 shows an example of the three types of TOF spectra for methylhydrazine ion at a photon energy of 10.55 eV.

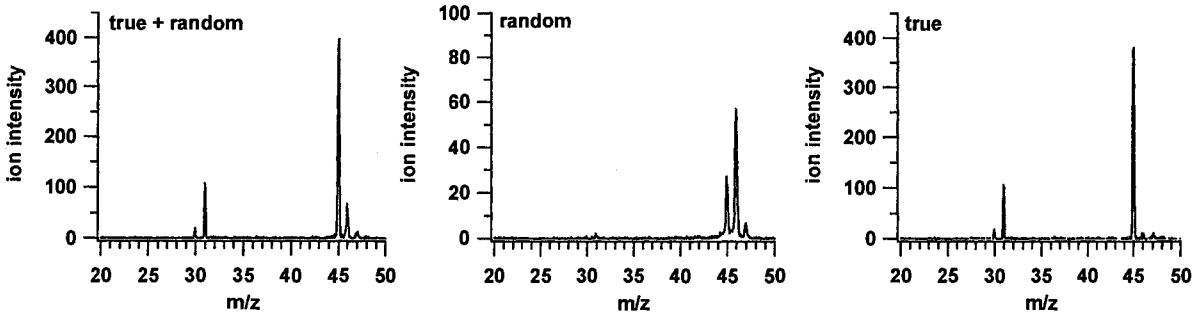

Figure 2.4 – An example of "true + random", "random" and "true" ion TOF spectra for methylhydrazine ion at a photon energy of 10.55 eV.

In a typical experiment, a "true + random" TOF spectrum is recorded for 270 s, followed by the accumulation of a "random" spectrum for 30 s. This process is then repeated until reasonable statistics have been obtained [50]. In the threshold region ($h\nu \approx 9$–11 eV), the process is usually repeated five times.

2.3.5 Materials

1,1-Dimethylhydrazine (Lancaster, 98%), methylhydrazine, tetramethylhydrazine (Aldrich, > 97%) and deuterium oxide (MSD Isotopes, 99.9% D) were used without further purification for the MIKE, CID and KER experiments. For the TPEPICO experiments, all three hydrazine compounds were obtained form Aldrich with a purity > 97%. The samples were subjected to three freeze-pump-thaw cycles to remove air.

2.4 Computational Approaches

To correctly interpret the experimental results, calculations were necessary. In this section, the optimization and assessment steps are explained in details as well as the complete fitting procedure of the breakdown curves and the entropy calculations.

2.4.1 Optimization of neutral and ion structures

Ab initio molecular orbital calculations were performed using the Gaussian 98 [95] suite of programs. The methylhydrazine [91], 1,1-dimethylhydrazine [92] and tetramethylhydrazine [91] ions and all their fragment ions and neutrals were optimized at the B3-LYP/6-31+G(d) level of theory in accordance with an assessment carried out for 1,1-dimethylhydrazine ions [92].

2.4.2 Assessment of the levels of theory and basis sets

The combination of B3-LYP level of theory with the 6-31+G(d) basis set was chosen because it adequately described the geometry and vibrational frequencies of the 1,1-dimethylhydrazine ion when compared to larger basis sets. The optimized geometric parameters of neutral and ionic 1,1-dimethylhydrazine are listed in Table 2.1 and shown in Figure 2.5.

The neutral molecule has been optimized at three different levels of theory (HF, MP2 and B3-LYP) with eight different basis sets, from 6-31G(d) up to 6-311+G(2df,p), except at the B3-LYP level of theory where four basis sets were used. Ionized 1,1-dimethylhydrazine was optimized at the same three levels of theory with basis sets ranging from 6-31G(d) up to 6-311+G(d,p). Similar geometrical parameters were obtained at the MP2 and B3-LYP levels

of theory. The HF bond lengths were always shorter than those calculated using the MP2 or B3-LYP methods. As the basis set size was increased from 6-31G(d) to 6-311+G(2df,p), we observed that the geometries of both neutral and ionic 1,1-dimethylhydrazine did not vary significantly. From these observations, we concluded that it was not necessary to use a large basis set, such as 6-311+G(2df,p), to perform our calculations since the results were similar to those obtained using 6-31+G(d). The MP2 treatment was discarded in this theoretical study because it gave results for the dissociation energies that were contrary to the experimental results. The two possible dissociation channels resulting in hydrogen atom loss, either $[(CH_3)(CH_2)NNH_2^+ + H^\bullet]$ or $[(CH_3)_2NNH^+ + H^\bullet]$, were much lower in energy at the MP2 level of theory than the methyl loss channel, $[CH_3NNH_2^+ + CH_3^\bullet]$. In the B3-LYP treatment, the relative energies of the fragments were more consistent with the MIKE and CID experimental results. Table 2.2 lists the absolute and relative energies of the 1,1-dimethylhydrazine ion and its dissociation products at the three different levels of theory mentioned previously with the five different basis sets.

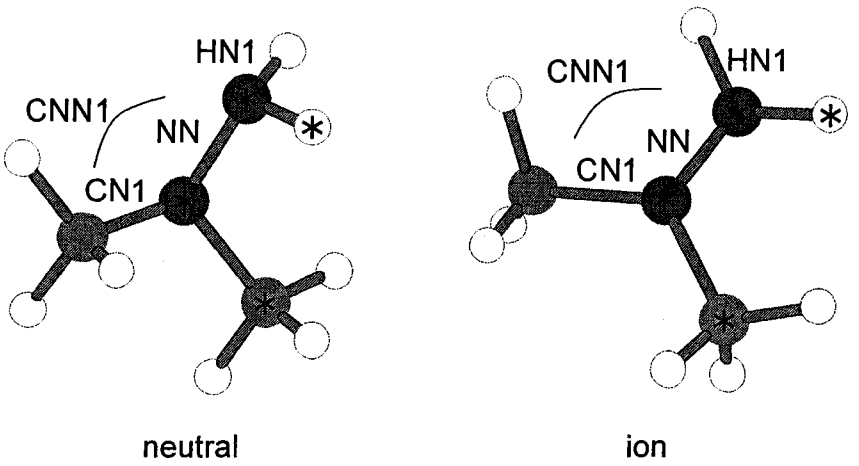

Figure 2.5 – Neutral and ionized 1,1-dimethylhydrazine optimized structures. The nitrogen atoms are dark grey, the carbon atoms are light grey and the hydrogen atoms are white. The asterisks (*) show the four atoms involved in the HNNC dihedral angle (see Table 2.1 for values).

2.4.3 Modified Gaussian theory

A modified G2 (mG2) protocol [96, 97] and a modified G3 (mG3) protocol [98, 99] based on the optimized B3-LYP/6-31+G(d) geometries and scaled B3-LYP ZPE (scaling factor = 0.9806) were used to calculate the enthalpies of formation of all methyl-substituted hydrazine ions and their fragment ions and neutrals [91, 92]. The mG2 and mG3 calculations were done by performing four single point calculations on the optimized structures of interest and by combining them according to the G2 procedure of Curtiss et al. [96] and the G3 procedure of Curtiss et al. [98]:

mG2	mG3
QCISD(T)/6-311G(d,p)	QCISD(T, E4T)/6-31G(d)
MP4/6-311+G(d,p)	MP4/6-31+G(d)
MP4/6-311G(2df,p)	MP4/6-31G(2df,p)
MP2/6-311+G(3df,2p)	MP2(full)/GTlarge

Table 2.1: Optimized Geometric Parameters of Neutral and Ionized 1,1-Dimethylhydrazine

basis set	R_{NN}	R_{CN1}	R_{CN2}	R_{HN1}	R_{HN2}	∠CNN1	∠CNN2	∠HNNC[a]
Neutral 1,1-Dimethylhydrazine								
HF								
6-31G(d)	1.408	1.445	1.445	1.001	1.008	109.3	113.0	-40.2
6-31+G(d)	1.408	1.446	1.447	1.000	1.008	109.3	112.9	-40.3
6-311G(d)	1.406	1.445	1.445	0.997	1.005	109.4	112.9	-40.0
6-311G(d,p)	1.406	1.446	1.446	0.999	1.007	109.4	112.9	-40.8
6-311+G(d,p)	1.406	1.446	1.447	0.999	1.006	109.5	112.9	-40.7
6-311G(df,p)	1.404	1.443	1.444	0.998	1.006	109.6	113.0	-41.4
6-311G(2df,p)	1.405	1.442	1.443	0.999	1.006	109.5	112.9	-41.5
6-311+G(2df,p)	1.404	1.443	1.443	0.998	1.006	109.6	112.9	-41.5
MP2								
6-31G(d)	1.433	1.456	1.457	1.020	1.030	107.3	111.7	-40.2
6-31+G(d)	1.432	1.458	1.460	1.019	1.030	107.7	112.1	-39.5
6-311G(d)	1.426	1.454	1.456	1.013	1.023	107.6	111.7	-39.1
6-311G(d,p)	1.427	1.455	1.457	1.016	1.027	107.4	111.5	-41.0
6-311+G(d,p)	1.426	1.456	1.458	1.016	1.026	107.8	111.8	-40.0
6-311G(df,p)	1.420	1.448	1.451	1.014	1.025	107.7	111.8	-41.3
6-311G(2df,p)	1.427	1.450	1.452	1.016	1.027	107.3	111.5	-41.2
6-311+G(2df,p)	1.426	1.451	1.453	1.016	1.026	107.6	111.7	-40.6
B3-LYP								
6-31G(d)	1.430	1.456	1.457	1.019	1.031	108.4	112.6	-41.4
6-31+G(d)	1.429	1.458	1.460	1.018	1.029	108.7	112.8	-41.1
6-311G(d,p)	1.428	1.456	1.458	1.015	1.027	108.7	112.7	-41.7
6-311+G(d,p)	1.427	1.457	1.459	1.015	1.026	109.0	112.8	-41.1
Ionized 1,1-Dimethylhydrazine								
HF								
6-31G(d)	1.312	1.465	1.465	1.000	1.000	117.9	117.9	-28.0
6-31+G(d)	1.313	1.465	1.465	1.000	1.000	117.9	117.9	-27.9
6-311G(d)	1.311	1.464	1.464	0.996	0.996	117.9	117.9	-28.5
6-311G(d,p)	1.310	1.465	1.465	0.998	0.999	118.0	118.0	-27.0
6-311+G(d,p)	1.311	1.465	1.465	0.999	0.999	118.0	118.0	-27.2
MP2								
6-31G(d)	1.324	1.462	1.462	1.018	1.018	117.0	117.0	-28.7
6-31+G(d)	1.325	1.463	1.463	1.019	1.019	116.8	116.8	-29.5
6-311G(d)	1.319	1.461	1.461	1.013	1.013	117.1	117.1	-29.0
6-311G(d,p)	1.319	1.462	1.462	1.015	1.015	117.2	117.2	-29.0
6-311+G(d,p)	1.320	1.462	1.462	1.015	1.015	117.1	117.1	-29.3
6-311G(df,p)	1.315	1.455	1.455	1.014	1.014	117.3	117.0	-27.5
B3-LYP								
6-31G(d)	1.333	1.464	1.464	1.017	1.017	117.6	117.6	-28.9
6-31+G(d)	1.334	1.465	1.465	1.017	1.017	117.6	117.6	-28.7
6-311G(d,p)	1.330	1.463	1.463	1.014	1.014	117.8	117.8	-26.6
6-311+G(d,p)	1.330	1.463	1.463	1.014	1.014	117.8	117.8	-26.4

[a] The atoms involved in the HNNC dihedral angle are identified by an asterisk (*) in Figure 2.5.

Table 2.2: Comparison of the Absolute and Relative Energies[a] of the Fragment Ions and Neutrals of the 1,1-Dimethylhydrazine Ion[b] at Five Different Levels of Theory (HF, MP2, B3-LYP, mG2 and mG3)[c]

basis set	$(CH_3)_2NNH_2^{+\bullet}$		$(CH_3)(CH_2)NNH_2^+ + H^\bullet$		$(CH_3)_2NNH^+ + H^\bullet$		$CH_3NNH_2^+ + CH_3^\bullet$	
	absolute	relative	absolute	relative	absolute	relative	absolute	relative
HF								
6-31G(d)	-188.902152	0	-188.824145	205	-188.811742	237	-188.825910	200
6-31+G(d)	-188.904294	0	-188.826756	204	-188.813387	239	-188.829297	197
6-311G(d)	-188.941709	0	-188.865275	201	-188.851718	236	-188.867304	195
6-311G(d,p)	-188.958312	0	-188.880293	205	-188.865533	244	-188.884236	194
6-311+G(d,p)	-188.959983	0	-188.881935	205	-188.866928	244	-188.886041	194
MP2								
6-31G(d)	-189.465208	0	-189.395065	184	-189.389121	200	-189.375940	234
6-31+G(d)	-189.472776	0	-189.402854	184	-189.395293	203	-189.384105	233
6-311G(d)	-189.535327	0	-189.465026	185	-189.458419	202	-189.448138	229
6-311G(d,p)	-189.594696	0	-189.518016	201	-189.510232	222	-189.506884	231
6-311+G(d,p)	-189.599093	0	-189.522453	201	-189.514200	223	-189.510844	232
B3-LYP								
6-31G(d)	-190.120277	0	-190.030283	236	-190.018794	266	-190.028875	240
6-31+G(d)	-190.123694	0	-190.034085	235	-190.021522	268	-190.035425	232
6-311G(d,p)	-190.177649	0	-190.089055	233	-190.074061	272	-190.084414	245
6-311+G(d,p)	-190.179472	0	-190.091025	232	-190.075634	273	-190.092264	229
mG2[c]	-189.8479402	0	-189.7686980	208	-189.7561558	241	-189.7604152	230
mG3[c]	-190.034442	0	-189.954131	211	-189.940264	247	-189.946822	230

[a] Absolute energies are in hartrees and relative energies are in kJ mol^{-1}, the energies have been corrected for ZPE. [b] The 1,1-dimethylhydrazine ion, $(CH_3)(CH_2)NNH_2^+$ and $(CH_3)_2NNH^+$ belong to the C_1 point group, $CH_3NNH_2^+$ belongs to the C_s point group and the methyl radical belongs to the D_{3h} point group. [c] Modified G2 [96, 99] and G3 [98, 99] protocols based on optimized B3-LYP/6-31+G(d) geometries and scaled B3-LYP ZPE (scaling factor = 0.9806).

2.4.4 Optimization of potential energy curves

All the potential energy curves [91, 92] were calculated at the B3-LYP/6-31+G(d) level of theory, one for each unimolecular dissociation (e.g. methyl radical or hydrogen atom loss). The first type of potential energy curve corresponds to the loss of a methyl group from the hydrazine backbone, and hence to the cleavage of one N–C bond. The second type of curve corresponds to the loss of a hydrogen atom from a methyl group. The potential energy curves were generated by optimizing the geometry of the dissociating ion by incrementally increasing the bond length by 0.1 Å until the energy reached a plateau at the separated products. For example, in 1,1-dimethylhydrazine ion [92], this meant optimizing structures from the equilibrium bond length $R_{N\text{–}C}$ = 1.46 Å to 6.21 Å for the methyl loss channel and for hydrogen loss, between $R_{H\text{–}C}$ = 1.10 Å and 2.50 Å. The vibrational frequencies and rotational constants were also calculated at each step. To assess the use of the 6-31+G(d) basis set, single-point energy calculations on the B3-LYP/6-31+G(d) geometries were performed with seven other basis sets ranging from 6-31G(d) to 6-311+G(2df,p). The relative energy (compared to the equilibrium structure) of a dissociating ion complex at a particular distance $R_{X\text{–}C}$ did not change as the size of the basis set was increased, as shown in Figure 2.6. Thus the B3-LYP/6-31+G(d) was a good level of theory to describe both unimolecular dissociations of the 1,1-dimethylhydrazine ions and thus the unimolecular dissociations of methyl- and tetramethylhydrazine ions.

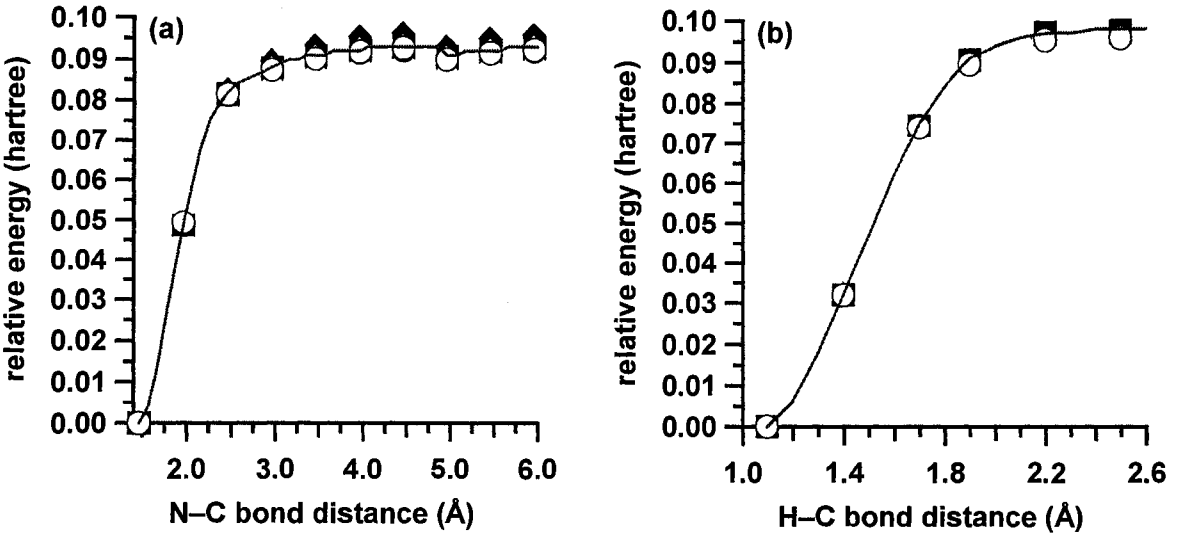

Figure 2.6 – The potential energy curves for the dissociations of the 1,1-dimethylhydrazine ion, at the B3-LYP/6-31+G(d) level of theory, represented by a solid line: (a) methyl radical loss and (b) hydrogen atom loss. The symbols represent the different basis sets used for the energy calculations: ◆ 6-31G(d), ▲ 6-311G(d), ■ 6-311G(d,p), ∗ 6-311+G(d,p), ● 6-311G(df,p), ◇ 6-311G(2df,p) and ○ 6-311+G(2df,p).

The potential energy curves for the dissociations of the 1,1-dimethylhydrazine ion have also been completely optimized at three other levels of theory (HF, MP2 and B3-PW91) using the 6-31+G(d) basis set. Figure 2.7 shows the potential energy curves for the methyl radical and the hydrogen atom losses. The two DFT methods (B3-LYP and B3-PW91) gave similar potential energy curves for both dissociation channels. However, for the methyl radical loss, the HF and MP2 potential energy curves could not be optimized above R_{N-C} = 2.465 Å for HF and above R_{N-C} = 2.663 Å for MP2. The shape of the potential energy curves is also different at the HF and MP2 levels of theory with a shoulder around $R_{N-C} \approx 2.46$ Å.

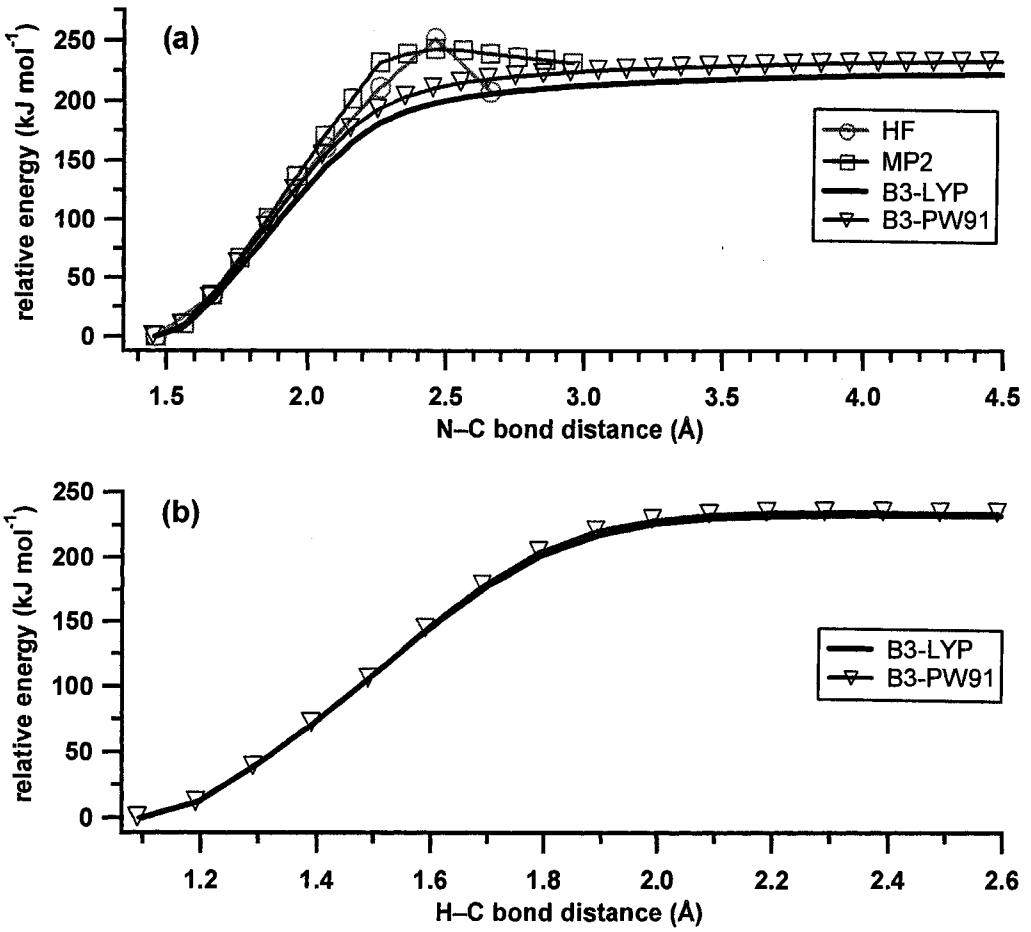

Figure 2.7 – The optimized potential energy curves for (a) the methyl radical loss and (b) the hydrogen atom loss of the 1,1-dimethylhydrazine ion at different levels of theory using the 6-31+G(d) basis set.

2.4.5 Calculations of the sum-of-states and rate constants

To calculate the rate constants ($k(E_{int})$) and the sum-of-states ($N^{\ddagger}$), a rovibrational RRKM approach was used. For each point R_{X-C}, where X = N or H on the potential energy curve, the sum-of-states and rate constants were calculated. This was done by using the rotational constants and the scaled vibrational frequencies of the parent ion (MH, DMH or TMH ion) as well as those of the dissociating complex at the bond distance R_{X-C}. For each methyl-substituted hydrazine ion, an ion internal energy range (E_{min} and E_{max}) was defined corresponding to the experimental TPEPICO internal energy range as well as a 0 K

activation energy (E_0) [91, 92]. For each dissociation channel, a set of rate constants and sum-of-states as a function of internal energy were generated by plotting the sum-of-states as a function of the bond distance R_{X-C}. The effective transition state at a given internal energy was located by finding the molecular configuration along the potential energy curve that gave the minimum rovibrational sum-of-states [91, 92, 100]. As there are obvious limitations in the above approach, it was used only to locate the transition states. The vibrational frequencies of these molecular configurations were used as adjustable parameters in order to obtain a fit to the experimental breakdown curves [91, 92]. The sets of rate constants were constructed by combining the appropriate rate constants corresponding to each transition state [92]. Table 2.3 contains an example of a set of rate constants for the hydrogen atom loss from 1,1-dimethylhydrazine ion. At the B3-LYP/6-31+G(d) level of theory, there are three transition states for the hydrogen atom loss channel of $DMH^{+\bullet}$ in the internal energy range of interest. Each transition state corresponds to a certain internal energy range. For example, $TS(59)_1$ is from E_{int} = 2.992–3.560 eV, $TS(59)_2$ is from E_{int} = 2.527–2.991 eV and $TS(59)_3$ is from E_{int} = 2.424–2.526 eV.

For the rearrangement channels involving methane loss, no potential energy curve was calculated. The transition state properties were estimated using the vibrational frequencies of the methylhydrazine or tetramethylhydrazine ion [91]. The vibrational mode corresponding to the N–C stretch was removed and the five lowest vibrational frequencies were scaled until a good fit was obtained to the experimental curve for *m/z* 30 (for the MH ion) or *m/z* 72 (for the TMH ion). In order to fit the experimental *m/z* 72 breakdown curves for the tetramethylhydrazine ion, a set of two estimated transition states was used. More will be said about this in Chapter 3.

Table 2.3: Example of a Set of Rate Constants for the Hydrogen Loss Channel of 1,1-Dimethylhydrazine Ion[a]

Internal Energy	$TS(59)_1$ (R^* = 2.098 Å)		$TS(59)_2$ (R^* = 2.198 Å)		$TS(59)_3$ (R^* = 2.298 Å)	
(eV)	k(59)	log k(59)	k(59)	log k(59)	k(59)	log k(59)
2.200	0.00E+00	—	0.00E+00	—	0.00E+00	—
2.247	0.00E+00	—	0.00E+00	—	0.00E+00	—
2.294	0.00E+00	—	0.00E+00	—	0.00E+00	—
2.340	0.00E+00	—	0.00E+00	—	0.00E+00	—
2.387	7.24E-04	-3.140	0.00E+00	—	0.00E+00	—
2.434	1.29E-01	-0.890	4.45E-02	-1.352	3.15E-02	-1.501
2.481	9.19E-01	-0.037	5.05E-01	-0.297	4.64E-01	-0.333
2.528	3.93E+00	0.594	2.59E+00	0.413	2.63E+00	0.420
2.574	1.25E+01	1.098	9.23E+00	0.965	9.90E+00	0.995
2.621	3.46E+01	1.539	2.75E+01	1.440	3.06E+01	1.486
2.668	8.46E+01	1.927	7.12E+01	1.853	8.13E+01	1.910
2.715	1.89E+02	2.275	1.66E+02	2.220	1.93E+02	2.286
2.762	3.90E+02	2.591	3.56E+02	2.551	4.22E+02	2.625
2.808	7.49E+02	2.875	7.04E+02	2.848	8.46E+02	2.927
2.855	1.39E+03	3.142	1.34E+03	3.126	1.63E+03	3.211
2.902	2.46E+03	3.390	2.42E+03	3.385	2.98E+03	3.474
2.949	4.19E+03	3.622	4.22E+03	3.625	5.23E+03	3.718
2.996	6.91E+03	3.840	7.08E+03	3.850	8.84E+03	3.947
3.042	1.10E+04	4.040	1.14E+04	4.057	1.43E+04	4.157
3.089	1.71E+04	4.233	1.81E+04	4.257	2.29E+04	4.359
3.136	2.61E+04	4.416	2.79E+04	4.445	3.55E+04	4.550
3.183	3.89E+04	4.590	4.21E+04	4.624	5.39E+04	4.731
3.230	5.70E+04	4.756	6.23E+04	4.794	8.01E+04	4.904
3.276	8.13E+04	4.910	8.98E+04	4.953	1.16E+05	5.064
3.323	1.15E+05	5.061	1.28E+05	5.108	1.66E+05	5.221
3.370	1.60E+05	5.205	1.80E+05	5.256	2.35E+05	5.370
3.417	2.20E+05	5.343	2.50E+05	5.398	3.26E+05	5.514
3.464	2.99E+05	5.476	3.42E+05	5.534	4.48E+05	5.651
3.510	3.99E+05	5.601	4.59E+05	5.662	6.03E+05	5.780
3.557	5.29E+05	5.724	6.13E+05	5.787	8.08E+05	5.907

[a] The highlighted rate constants are the values used to create the set of rate constants for the hydrogen loss channel.

The sum and density of states can be calculated by many different methods [52, 63], the easiest and most accurate one being the direct count method developed by Beyer and Swinehart [101]. In this approach, the state densities are convoluted. If the system under study consists of s harmonic oscillators with vibrational frequencies of $\omega_i = \nu_i / c$ (cm^{-1}), where c is the speed of light, each will have a series of equally spaced states located at $E_i = n\omega_i$ ($n = 0, 1, 2, \ldots$). The ion's zero point energy is the zero of energy ($E_0 = 0$, $n = 0$) and the

ion's internal energy is divided into bins of size 1 meV. The *s* frequencies, expressed in meV units, are rounded off to the nearest meV. The density of vibrational states $\rho(E)$ is given by the following algorithm (in BASIC) [52, 63]:

step	$\rho(I) = [1,0,0,0,\ldots]$	initialize the ρ vector
1	FOR J = 1 TO s	s = the number of oscillators
2	FOR I = ω(J) TO M	M = the maximum energy bin of interest
3	$\rho(I) = \rho(I) + \rho(I - \omega(J))$	
4	NEXT I	
5	NEXT J	

The sum of vibrational states $N(E)$ can be calculated from the direct numerical integration of the density of states or computed directly by using the Beyer-Swinehart (BS) scheme [52, 63]:

step	N(I) = [1,1,1,1,...,1]	initialize the N vector
6	FOR J = 1 TO s	s = the number of oscillators
7	FOR I = ω(J) TO M	M = the maximum energy bin of interest
8	N(I) = N(I) + N(I – ω(J))	
9	NEXT I	
10	NEXT J	

The rovibrational sum and density of states can also be calculated with the BS method. In this case, the initialized $\boldsymbol{\rho}(I)$ vector is replaced with the rotational density of states and all the vibrations are convoluted into the rotational density of states thus producing a rovibrational density of states. The initial rotational density of states vector $\boldsymbol{\rho}_r(I)$ is easily generated from classical mechanics [52]. The rovibrational density of states is then calculated according to the following scheme [52]:

step	$\rho(I)$	initialize as rotational density of states vector
11	FOR J = 1 TO s	s = the number of oscillators
12	FOR I = ω(J) TO M	M = the maximum energy bin of interest
13	$\rho(I) = \rho(I) + \rho(I - \omega(J))$	
14	NEXT I	
15	NEXT J	

The rovibrational sum of states is calculated by first initializing the **N**(I) vector as a rotational sum vector and then by following the steps 11-15 [52].

2.4.6 Fitting of the breakdown curves

In order to fit the experimental breakdown curves, the variational $k(E_{int})$ values for each channel were convoluted with the electron transmission function, the monochromator bandpass and the thermal population distribution of the neutral hydrazine molecule (MH, DMH or TMH). The adjustable parameters in the fitting procedure are the activation energies (E_0) and the five lowest vibrational frequencies of the transition states. These two parameters were slightly modified until a good agreement between the theoretical fits and the experimental breakdown curves was obtained. For each hydrazine ion, three or four good fits were found and are discussed in Chapter 3.

The neutral molecule population, $P(E_{int}, T)$, was calculated up to an internal energy of 0.8 eV for methyl and 1,1-dimethylhydrazine and of 1.0 eV for tetramethylhydrazine and at a temperature of 298 K from equation 2.10:

$$P(E_{\text{int}}, T) = \frac{P(E_{\text{int}})e^{-E_{\text{int}}/k_B T}}{Q(T)} \qquad (2.10)$$

where $P(E_{int})$ is the density of states and $Q(T)$ is the total rovibrational partition function. The neutral molecule population was normalized such that the sum was equal to one. The density of states is calculated using the rovibrational RRKM program (see Appendix A).

The total rovibrational partition function, $Q(T)$, is the product of the molecular rotational and vibrational partition functions [57, 102]:

$$\text{rotational: } Q_{rot} = \frac{1}{\sigma}\left(\frac{k_B T}{hc}\right)^{3/2}\left(\frac{\pi}{ABC}\right)^{1/2} \qquad (2.11)$$

$$\text{vibrational: } Q_{vib} = \prod_{i=1}^{3N-6} \frac{1}{1-e^{-hc\nu_i/k_BT}} \tag{2.12}$$

where σ is the symmetry number and A, B and C are the rotational constants of the molecule or ion. All three methyl-substituted hydrazine ions belong to the C_1 point group and thus σ = 1.

2.4.7 Entropy calculations

The statistical entropy (S) is calculated from the internal energy (E_{int}) of the molecule or ion and the partition functions (Q) [57, 102]:

$$S = \frac{E_{int}}{T} + N_A k_B \ln Q \tag{2.13}$$

$$E_{int} = E_{int}^{rot} + E_{int}^{vib} \tag{2.14.a}$$

$$E_{int} = \frac{3}{2} N_A k_B T + \sum_{i=1}^{3N-6} \frac{N_A hc\nu}{e^{hc\nu_i/k_BT} - 1} \tag{2.14.b}$$

We calculated the rovibrational entropy of activation, $\Delta S^{\ddagger}_{rovib}$, for all dissociation channels (i.e. unimolecular dissociation and rearrangement). For all three hydrazine ions, the absolute entropies (S_{rovib}) and the entropies of activation ($\Delta S^{\ddagger}_{rovib}$) have been calculated using the East and Radom procedure [103] for the computation of third-law entropies. In our procedure, the methyl torsion modes were treated separately first with the harmonic oscillator model (equations 2.15) and second as free rotors (equations 2.16) using the following equations [103]:

$$S(Q_{HO}) = R\left(\frac{\theta_{vib}}{T}\right)\left(e^{\theta_{vib}/T} - 1\right)^{-1} - R\ln\left[1 - e^{-\theta_{vib}/T}\right]$$
$$\theta_{vib} = \frac{h\omega}{k} \tag{2.15}$$

$$S(Q_f) = \frac{1}{2}R\ln\left(\frac{e\pi}{\sigma^2\theta_{rot}}\right) + \frac{1}{2}R\ln T$$
$$\theta_{rot} = \frac{h^2}{8\pi^2 Ik} \tag{2.16}$$

where θ_{vib} is the torsional vibrational temperature constant, ω is the torsional harmonic frequency, σ is the rotor symmetry number, e is the natural log base, θ_{rot} is the rotor rotational temperature constant and I is the rotor's reduced moment of inertia (i.e. methyl free rotor). We assumed that the rotor symmetry number in the free rotor analysis was equal to one. All the other vibrational modes in the hydrazine ions and transition states were calculated using the statistical entropy equation 2.13.

For the free rotor model, the internal moment of inertia was estimated to be between 3.0–3.1 amu Å^2. These values were taken from Table VII in the East and Radom [103] paper, which lists the calculated internal moments of inertia of various single and multiple rotors. In the case of the hydrogen loss channel from methyl- and 1,1-dimethylhydrazine ions, the hydrogen atom comes from one of the methyl groups. The methyl group losing a hydrogen atom was not considered as a free rotor. Therefore, for the methylhydrazine ion [91], the system was treated as having no free rotors in the transition states while in 1,1-dimethylhydrazine ion [92], the system was treated as having only one free rotor which corresponds to the intact methyl group. For the methane loss channel [91] from methylhydrazine ion, the transition state was treated as having no free rotor while for the

same channel from tetramethylhydrazine ion, the transition states were treated as having only two free methyl rotors. The entropies of activation and the absolute entropies of each hydrazine ion will be discussed in more details in Chapter 4.

Chapter 3

RESULTS: UNIMOLECULAR DISSOCIATIONS OF THE METHYL-SUBSTITUTED HYDRAZINE IONS

3.1 Introduction

Hydrazine and five of its methyl substituted hydrazine derivatives were studied almost fifty years ago by Dibeler et al. [48] using electron ionization mass spectrometry. They reported the appearance energies and ionic enthalpies of formation of the observed fragment ions. Their reported $\Delta_f H$ were calculated from the AEs of the fragment ions and from auxillary $\Delta_f H$ values reported by Harshman [42] for the neutral molecules hydrazine, methylhydrazine, 1,1- and 1,2-dimethylhydrazine. However, the enthalpies of formation for trimethylhydrazine and tetramethylhydrazine were estimated using the group equivalents method [104] and were subsequently found to be erroneous [105].

Between 1989 and 1994, three papers [1, 3, 4] were published on $CH_5N_2^+$ ions. In the first, Burgers et al. [1] studied the $CH_5N_2^+$ hydrazyl radicals and cations by mass spectrometry. Four distinct singly charged $CH_5N_2^+$ ions were generated from three different molecular ions, and the $\Delta_f H$ of the $CH_5N_2^+$ cations were determined from their measured AEs. In 1992, the group [4] re-investigated some aspects of the CH_5N_2 potential energy surface based on their previous experimental results [1] and concluded that the reported AEs for the methyl losses from methylhydrazine, 1,1- and 1,2-dimethylhydrazine were not reliable because of interferences from traces of amines. New enthalpies of formation of the $CH_5N_2^+$ fragment ions were also reported as well as proton affinities (PA) for HN=NH, CH_3N=NH and CH_3N=NCH_3. Two years later, Nguyen [3] investigated hydrogen cyanide

loss from $CH_5N_2^+$ cations using *ab initio* molecular orbitals calculations. He also reported enthalpies of formation for the $CH_5N_2^+$ ions along with PA values for diazene and methyldiazene. Recently a book [106] on assigning structures to gas-phase ions was published containing some thermochemistry for $CH_5N_2^+$ (*m/z* 45) and $C_3H_8N_2^{+\bullet}$ (*m/z* 72) fragment ions. No reported structures were available for fragment ions $C_3H_9N_2^+$ (*m/z* 73).

Most of the previously reported $\Delta_f H$ values for NN-containing ions were determined from measurements of onset AEs for the fragment ions. However, when extracting meaningful thermochemical information from AE determinations there are a number of potential problems. First, any rearrangement reaction usually has at least one energetic barrier associated with a transition state which can cause the AE to be higher than the true thermochemical threshold (i.e. there is a reverse energy barrier in the reaction). Secondly, competitive and kinetic shifts can affect the AEs [86]. Thirdly, if the AE measurements were performed using electrons with a broad energy distribution, the true onset can be difficult to determine. As will be shown in the present study, the $\Delta_f H$ values previously determined from AE measurements for a variety of NN-containing ions are found to be inaccurate.

The lowest energy dissociation channels of the three methyl-substituted hydrazine ions studied in this thesis are the loss of a hydrogen atom from a methyl group, the loss of a methyl radical and a rearrangement process leading to the loss of methane. The dissociations of the hydrazine ions were investigated using three different and complementary experimental and theoretical approaches: TPEPICO spectroscopy, in the photon energy range of 8–32 eV, tandem mass spectrometry and variational transition state theory for the modelling of the reaction channels. Our approach was to model the ion decomposition as a

function of internal energy and compare the results with those from TPEPICO spectroscopy. It was necessary in this process to employ a simple VTST treatment to learn about the $\Delta S^{\ddagger}$ for the competing dissociation channels of these ions. The entropy of activation has a significant impact on the dissociation of the parent ion. The large change in $\Delta S^{\ddagger}$ as the internal energy increases also affects the shape of the breakdown curves and their variational fits. $\Delta_f H$s for a series of NN-containing ions were also derived from experiment and calculated at the modified G2 and G3 level of theory: $N_2H_2^{+\bullet}$ *m/z* 30, $NHNH_2^+$ *m/z* 31, $CH_5N_2^+$ *m/z* 45, $C_3H_8N_2^{+\bullet}$ *m/z* 72 and $C_3H_9N_2^+$ *m/z* 73. These values, discussed in Chapter 4, allow us to explore methyl substitution effects on NN-containing ion $\Delta_f H$ as well as to determine the proton affinities of several NN-containing neutral molecules. In this chapter, the reaction mechanisms and the various steps of the fitting procedure will be discussed in detail.

3.2 Reaction mechanisms

The dissociation reactions of the methyl-substituted hydrazine ions were studied first by tandem mass spectrometry which allowed us to record the MIKE and CID mass spectra of the parent ions and their main fragment ions.

3.2.1 1,1-Dimethylhydrazine ion

The MIKE mass spectrum (Figure 3.1.a) of ionized 1,1-dimethylhydrazine in the second FFR shows two peaks at *m/z* 45 and *m/z* 59. These two peaks correspond to the loss of a methyl group to form the ion *m/z* 45 with the empirical formula $CH_5N_2^+$ and to the loss of a hydrogen atom to form the ion *m/z* 59 with the empirical formula $C_2H_7N_2^+$. The CID

mass spectrum of 1,1-dimethylhydrazine ion has also been recorded in the second FFR (Figure 3.1.b). The kinetic energy release has been measured for both fragment ions. The $T_{0.5}$ value associated with fragment ion *m/z* 59 is 118 meV and is 20 meV for fragment ion *m/z* 45, indicating that the reactions are very unlikely to proceed with a large reverse energy barrier. The group of van Garderen et al. [4] reported a $T_{0.5}$ value of 9 meV for the methyl radical loss from 1,1-dimethylhydrazine ion which is lower than our measured value.

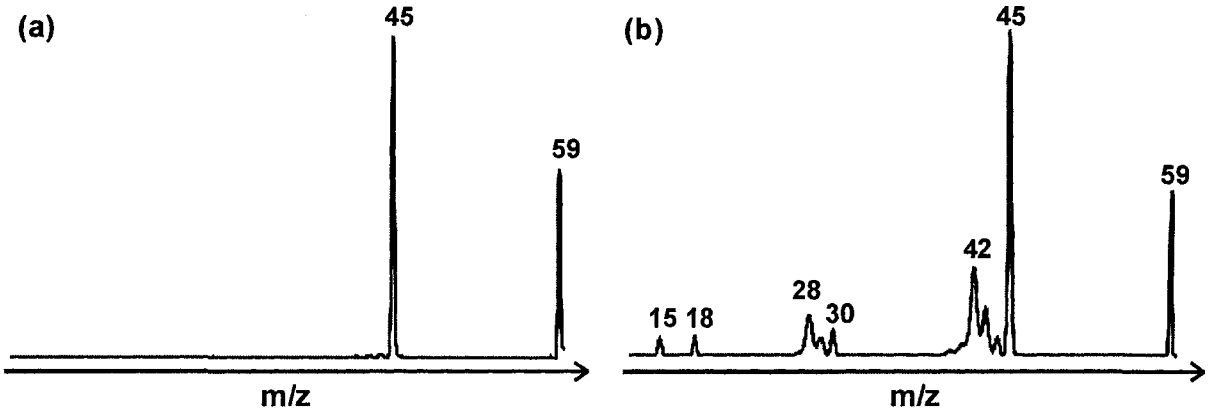

Figure 3.1 – (a) MIKE and (b) CID mass spectra of 1,1-dimethylhydrazine ion *m/z* 60 in the second field-free region.

The CID mass spectra of the metastably generated fragment ions *m/z* 59 and *m/z* 45 were recorded in the third field-free region of the instrument and are shown in Figure 3.2. Fragment ion *m/z* 45 has the methylhydrazyl cation structure $CH_3NNH_2^+$ corresponding to the simple N–C bond cleavage in the parent DMH ion [1, 4]. Fragment ion *m/z* 59 is generated by the loss of a hydrogen atom from its parent DMH ion. There are two possible hydrogen atoms to be lost, from the methyl groups or from the NH_2 moiety to generate the $(CH_3)(CH_2)NNH_2^+$ and $(CH_3)_2NNH^+$ fragment ions, respectively. The structure of the fragment ion *m/z* 59 was confirmed with deuterium labelling experiments. The dissociation of the deuterated parent ion $(CH_3)_2NND_2^{+\bullet}$ was investigated and only hydrogen loss and not

deuterium loss was observed thus confirming the structure of the fragment ion *m/z* 59 to be $(CH_3)(CH_2)NNH_2^+$:

$$(CH_3)_2NNH_2^{+\bullet}\ (m/z\ 60) \rightarrow C_2H_7N_2^+\ (m/z\ 59) + H^\bullet \qquad (3.1.a)$$

$$(CH_3)_2NND_2^{+\bullet}\ (m/z\ 62) \rightarrow C_2H_5D_2N_2^+\ (m/z\ 61) + H^\bullet \qquad (3.1.b)$$

These results, for both fragment ions *m/z* 59 and *m/z* 45, are consistent with previously reported data by Burgers et al. [1] and van Garderen et al. [4].

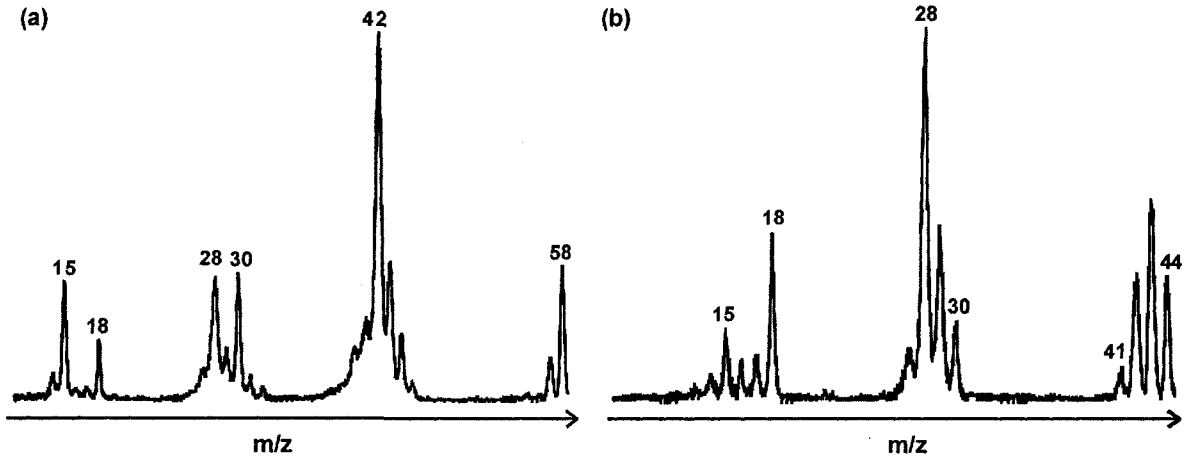

Figure 3.2 – CID mass spectra, in the third field-free region, of the metastably generated (a) fragment ion *m/z* 59, $(CH_3)(CH_2)NNH_2^+$, and (b) fragment ion *m/z* 45, $CH_3NNH_2^+$.

3.2.2 Methylhydrazine

The MIKE mass spectrum, shown in Figure 3.3(a), of ionized methylhydrazine exhibits one peak with *m/z* 45 corresponding to loss of a hydrogen atom and a very low intensity peak at *m/z* 31 corresponding to the loss of a methyl radical. The CID mass spectrum has also been recorded (Figure 3.3(b)). The CID mass spectrum of the metastably generated fragment ion *m/z* 45 is distinct from that of the $CH_3NNH_2^+$ ion generated by methyl loss from metastable 1,1-dimethylhydrazine ions. Its mass spectrum is presented in

Figure 3.4(a) and can be compared to that of $CH_3NNH_2^+$ in Figure 3.2(b). The doubly-charged ion, $CH_2NHNH_2^{2+}$, at *m/z* 22.5 and fragment ion $N_2H_3^+$ at *m/z* 31 are not observed in the CID mass spectrum of $CH_3NNH_2^+$. $CH_3NDND_2^{+\bullet}$ and $(CH_3)_2NND_2^{+\bullet}$, generated by deuterium exchange experiments on methyl- and 1,1-dimethylhydrazine, gave different fragment ions in their MIKE mass spectra, indicating that the structures of the two non-labelled fragment ions with *m/z* 45 ($CH_5N_2^+$) are different:

$$CH_3N\mathbf{D}N\mathbf{D}_2^{+\bullet}\ (m/z\ 49) \rightarrow CH_2\mathbf{D}_3N_2^+\ (m/z\ 48) + H^\bullet \qquad (3.2.a)$$

$$(CH_3)_2NN\mathbf{D}_2^{+\bullet}\ (m/z\ 62) \rightarrow CH_3\mathbf{D}_2N_2^+\ (m/z\ 47) + CH_3^\bullet \qquad (3.2.b)$$

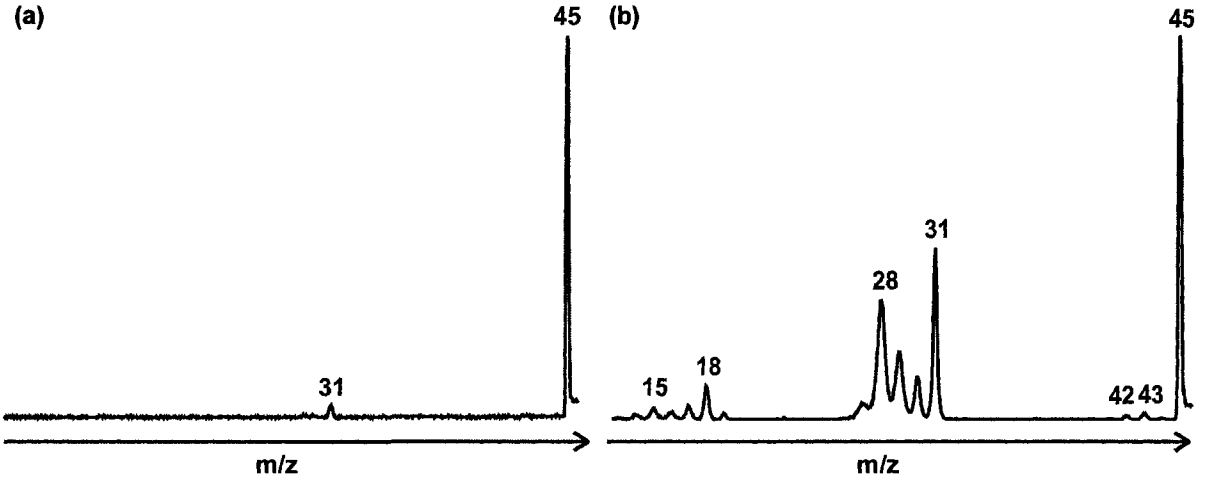

Figure 3.3 – (a) MIKE and (b) CID mass spectra of methylhydrazine ion *m/z* 46 in the second field-free region.

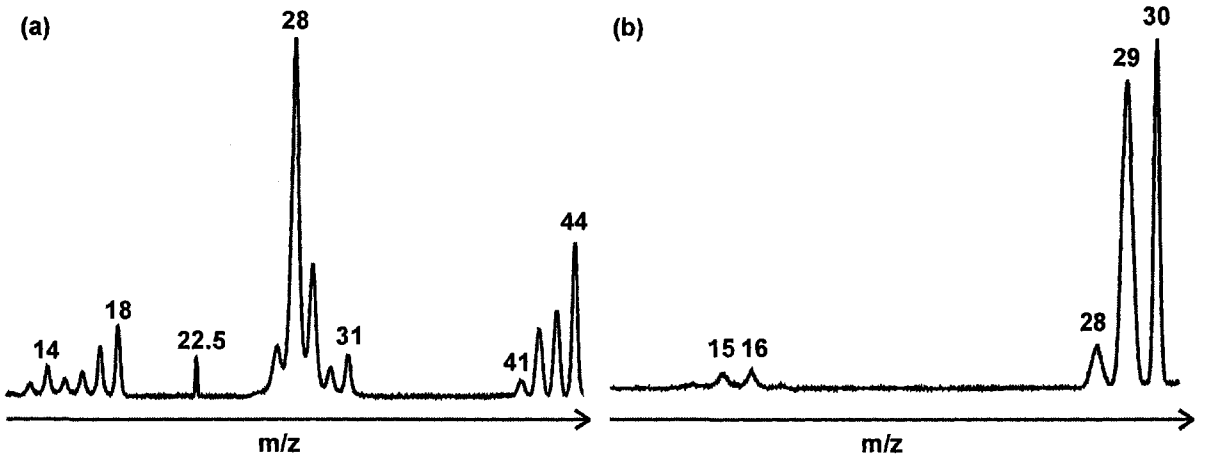

Figure 3.4 – CID mass spectra in the third FFR of the metastably generated (a) fragment ion *m/z* 45, $CH_2NHNH_2^+$ and (b) fragment ion *m/z* 31, $NHNH_2^+$.

There are six possible isomers of the $CH_5N_2^+$ fragment ion [106]: $CH_2NHNH_2^+$, $CH_2NNH_3^+$, $CH_3NNH_2^+$, CH_3NHNH^+, cy-$C(H_2)N(H)N(H_2)$-$^+$ and $[HNC—NH_4]^+$. The isotopic labeling shows that the hydrogen atom is lost from the methyl group of ionized methylhydrazine to form the $CH_2NHNH_2^+$ fragment ion, in agreement with earlier work on the formation of this isomer [1, 4]. Calculations at the B3-LYP/6-31+G(d) level of theory and with the modified G2 and G3 protocols indicate that the formation of $CH_2NHNH_2^+$ is also the most energetically favourable one for the hydrogen loss channel of ionized methylhydrazine. This isomer is approximatively 45 kJ mol^{-1} lower in energy than $CH_3NNH_2^+$ and CH_3NHNH^+ at the mG2 and mG3 levels of theory. The energies for the various isomers are reported in Table 3.1. The $T_{0.5}$ value associated with H loss is 81 meV (van Garderen et al. [4] reported a similar KER, $T_{0.5}$ = 75 meV), indicating that this reaction is unlikely to proceed with a large reverse energy barrier. In the CID mass spectrum of the methylhydrazine ion, fragment ions *m/z* 31 and *m/z* 30 are observed corresponding to $N_2H_3^+$ and $N_2H_2^{+\bullet}$ respectively. These two ions are also observed in the first cross-over region of the TPEPICO breakdown curve of methylhydrazine ions (see Section 3.5.2). Fragment ion

m/z 31 corresponds to the loss of a methyl radical to form $NHNH_2^+$ ($T_{0.5}$ = 63 meV) while fragment ion *m/z* 30 corresponds to a rearrangement leading to the loss of methane. Three isomeric structures are possible for *m/z* 30: iso-diazene ($NNH_2^{+\bullet}$), trans-diazene or cis-diazene ($HNNH^{+\bullet}$). The structure of this fragment ion has been determined from the VTST fits of the methylhydrazine ion breakdown curves (see Section 3.5 Variational fits of the breakdown curves) to be either iso-diazene or trans-diazene. Syage [38], in a paper on the spectroscopy and dynamics of hydrazines, suggested a 1,2-elimination from $CH_3NHNH_2^{+\bullet}$ to form the $HNNH^{+\bullet}$ fragment ions. He also suggested a possible 1,1-elimination process from the hydride-shift ion structure $CH_3NH_2NH^{+\bullet}$ to form the iso-diazene fragment ion $NNH_2^{+\bullet}$.

3.2.3 Tetramethylhydrazine

The tetramethylhydrazine ion has only one peak in its MIKE mass spectrum at *m/z* 73 corresponding to the loss of a methyl radical to form $(CH_3)_2NNCH_3^+$ as shown in Figure 3.5(a). The $T_{0.5}$ value associated with the reaction is 48 meV, indicating that this reaction is unlikely to proceed with a large reverse energy barrier. In the breakdown diagram of the tetramethylhydrazine ion, another fragment ion is observed in the first cross-over region corresponding to fragment ion *m/z* 72 which is due to methane loss. Nine possible isomers (five linear and four cyclic) [106, 107] of fragment ion *m/z* 72 have been considered and are shown in Figure 3.13.

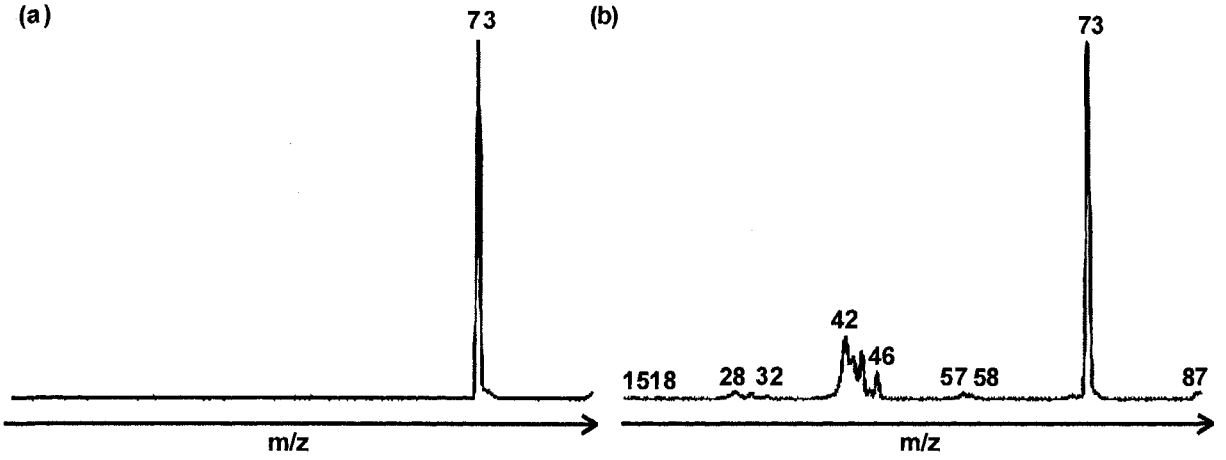

Figure 3.5 – (a) MIKE and (b) CID mass spectra of tetramethylhydrazine ion *m/z* 88 in the second field-free region.

Considerable fragmentation is observed in the CID mass spectrum of TMH (Figure 3.5(b)), in the second field-free region, with low intensity fragment ions with mass-to-charge ratios in the range *m/z* 15-18, *m/z* 28-32, *m/z* 42-46 and *m/z* 57-58. Two very small peaks are also observed at *m/z* 72 and *m/z* 87. The CID mass spectrum of the metastable fragment ion *m/z* 73 was also recorded in the third FFR of the instrument and is presented in Figure 3.6.

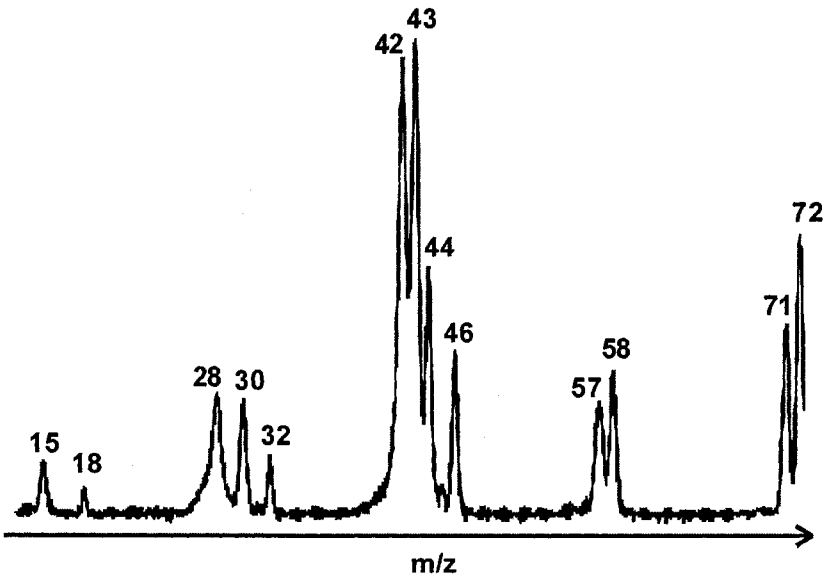

Figure 3.6 – CID mass spectrum, in the third field-free region, of the metastably generated fragment ion *m/z* 73, $(CH_3)_2NNCH_3^+$.

3.3 The potential energy curves for the unimolecular dissociation pathways

The unimolecular dissociation channels were investigated theoretically by calculating and optimizing the potential energy curves for the methyl radical and hydrogen atom losses. 1,1-Dimethylhydrazine ion was studied first and a thorough discussion of its potential energy curves is presented in Section 3.3.1. In Sections 3.3.2 and 3.3.3, a discussion on the methyl- and tetramethylhydrazine ions potential energy curves is presented.

3.3.1 1,1-Dimethylhydrazine

The relative energies of the 1,1-dimethylhydrazine ion and its fragment ions and neutrals have been calculated at the B3-LYP/6-31+G(d) level of theory and with the modified G2 and G3 protocols and are listed in Table 2.2 in Chapter 2. At the B3-LYP/6-

31+G(d) level of theory, the two sets of dissociation products [$CH_3NNH_2^+$ + $CH_3^•$] and [$(CH_3)(CH_2)NNH_2^+$ + $H^•$] have similar energies. However, the hydrogen loss channel is lower by 22 kJ mol^{-1} using the mG2 energies and by 19 kJ mol^{-1} using the mG3 energies. The relative energy of the second possible structure of the ion *m/z* 59 ($(CH_3)_2NNH^+$) was also calculated. However, this dissociation is not energetically favourable since it is 33–36 kJ mol^{-1} higher in energy than hydrogen loss from the methyl group at the mG2 and mG3 levels of theory. The fact that no D loss is observed in the CID mass spectrum of the labelled ion confirms that H loss from the NH_2 moiety does not compete significantly with H loss from CH_3, even for ions with relatively high internal energy. Also the rate constants for the second structure of fragment ion *m/z* 59 are many orders of magnitude smaller than those for the two other sets of dissociation products. This will be discussed in more details in Section 3.5 Variational fits of the breakdown curves.

The potential energy curve for the loss of a methyl group is shown in Figure 3.7 together with the sum-of-states calculated as a function of the N–C bond distance. Figure 3.8 shows the changes in the five lowest vibrational frequencies and the entropy of activation as the N–C bond is elongated. As the 1,1-dimethylhydrazine ion dissociates into the fragment ion $CH_3NNH_2^+$ + $CH_3^•$, six vibrational modes disappear. One mode corresponds to a N–C stretch, the reaction coordinate, and the five other modes correspond to deformation, torsion and scissoring involving a methyl group (either the leaving methyl group or the one in the fragment ion). An inflection point and two distinct local maxima are noticeable in the sum-of-states plot (Figure 3.7, top graph), one at R_{N-C} = 2.16 Å, one at R_{N-C} = 3.56 Å and one around R_{N-C} = 4.86–4.96 Å. The first feature at 2.16 Å is consistent with a sudden change in the H–CH_2 wagging vibrational frequency of the dissociating complex between R_{N-C} =

2.16–2.36 Å (Figure 3.8). The changes in the vibrational frequencies affect the value of the $\Delta S^{\ddagger}$ (in both HO and FR models). At that N–C bond distance, a local maximum (in the HO model) or an inflection point (in the FR model) is observed in the $\Delta S^{\ddagger}$ (Figure 3.8). At R_{N-C} = 3.56 Å there is a local maximum on the plot of $\Delta S^{\ddagger}$ (HO model) even though there is no obvious change in the vibrational frequencies. As the N–CH_3 bond is stretched the two smaller rotational constants slowly decrease from their initial values in the equilibrium geometry and could influence the entropy of activation values. The third local maximum in the sum-of-states, at R_{N-C} = 4.86–4.96 Å, corresponds to a slight dip in energy for this complex. This dip is due to the crossing of the potential energy curve for the loss of methyl with that for the dissociation of a second high energy species having the geometry shown in the last panel of Figure 3.9. As the DMH ion dissociates, the methyl radical leaves the dissociating complex in a linear fashion. The angle defined by the leaving methyl radical (identified as C3 in Figure 3.9) and the two nitrogen atoms (N1 and N2 in Figure 3.9) in the fragment ion backbone barely changes with the elongation of the N–C bond distance, being approximately 117°. At R_{N-C} > 4.86 Å, the geometry of the dissociating complex suddenly changes and the C3N2N1 angle becomes larger (134.4 °) and the methyl group is situated above the $CH_3NNH_2^+$ fragment ion (Figure 3.9). This region of the potential energy curve was thus re-optimized starting at higher values of R_{N-C}; optimizing the geometry at successively shorter bond lengths results in a discontinuity at R_{N-C} = 4.86 Å. However, it was impossible to optimize this structure below R_{N-C} = 4.66 Å. Fortunately, these geometries are found at higher R_{N-C} value than the variational transition states. The geometrical parameters of the dissociating complexes are listed in Table B.5 in Appendix B from the equilibrium geometry up to R_{N-C} = 6.065 Å.

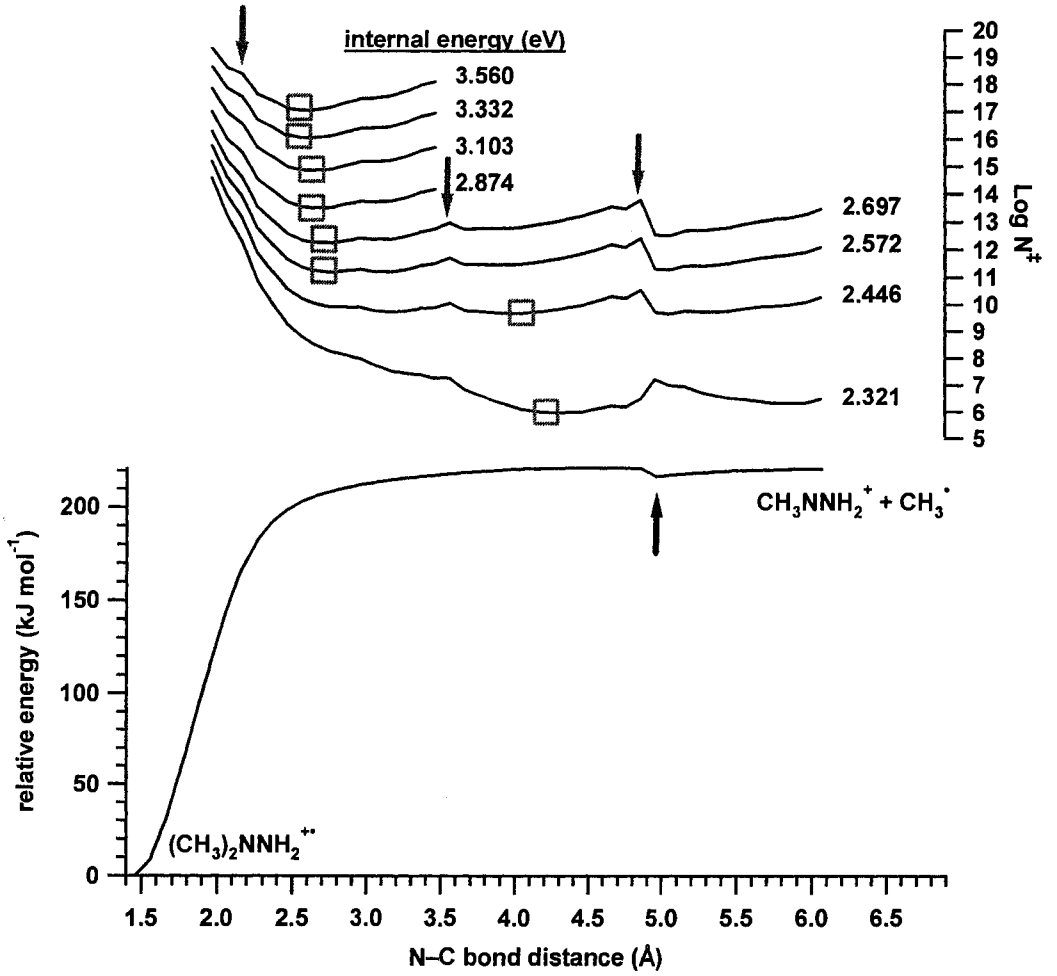

Figure 3.7 – Potential energy curve for the loss of a methyl group from the 1,1-dimethylhydrazine ion and the sum-of-states as a function of the N–C bond distance calculated at the B3-LYP/6-31+G(d) level of theory. The grey arrows pointing down identify the local maxima in the sum-of-states. The variational transition states as a function of ion internal energy are identified by the grey squares and correspond to the minima in $N^{\ddagger}$. The black arrow pointing up identifies the local minimum on the potential energy curve.

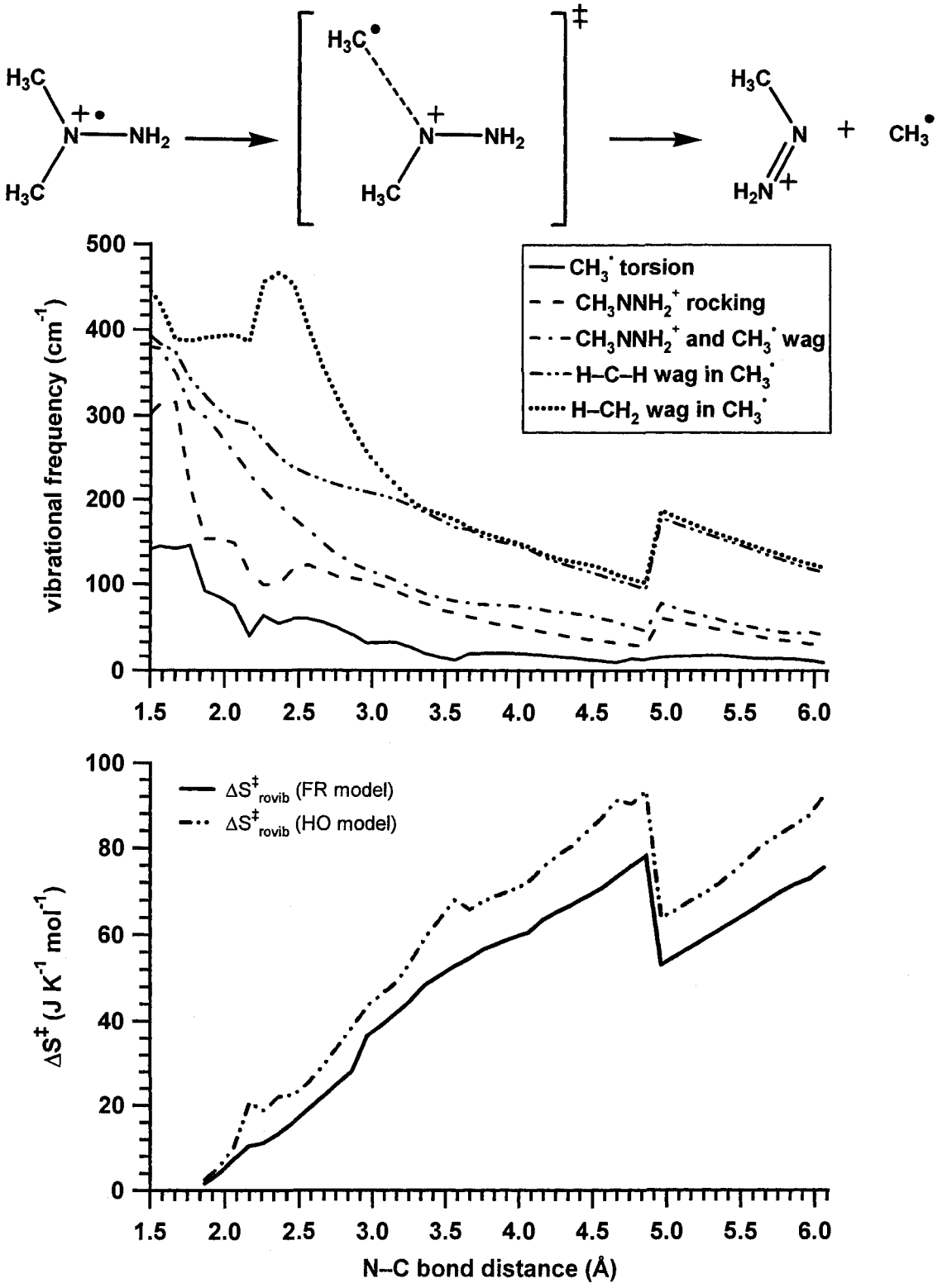

Figure 3.8 – Five lowest vibrational frequencies of the methyl radical loss channel of the DMH ion (top) and the entropy of activation (bottom) as a function of the N–C bond distance.

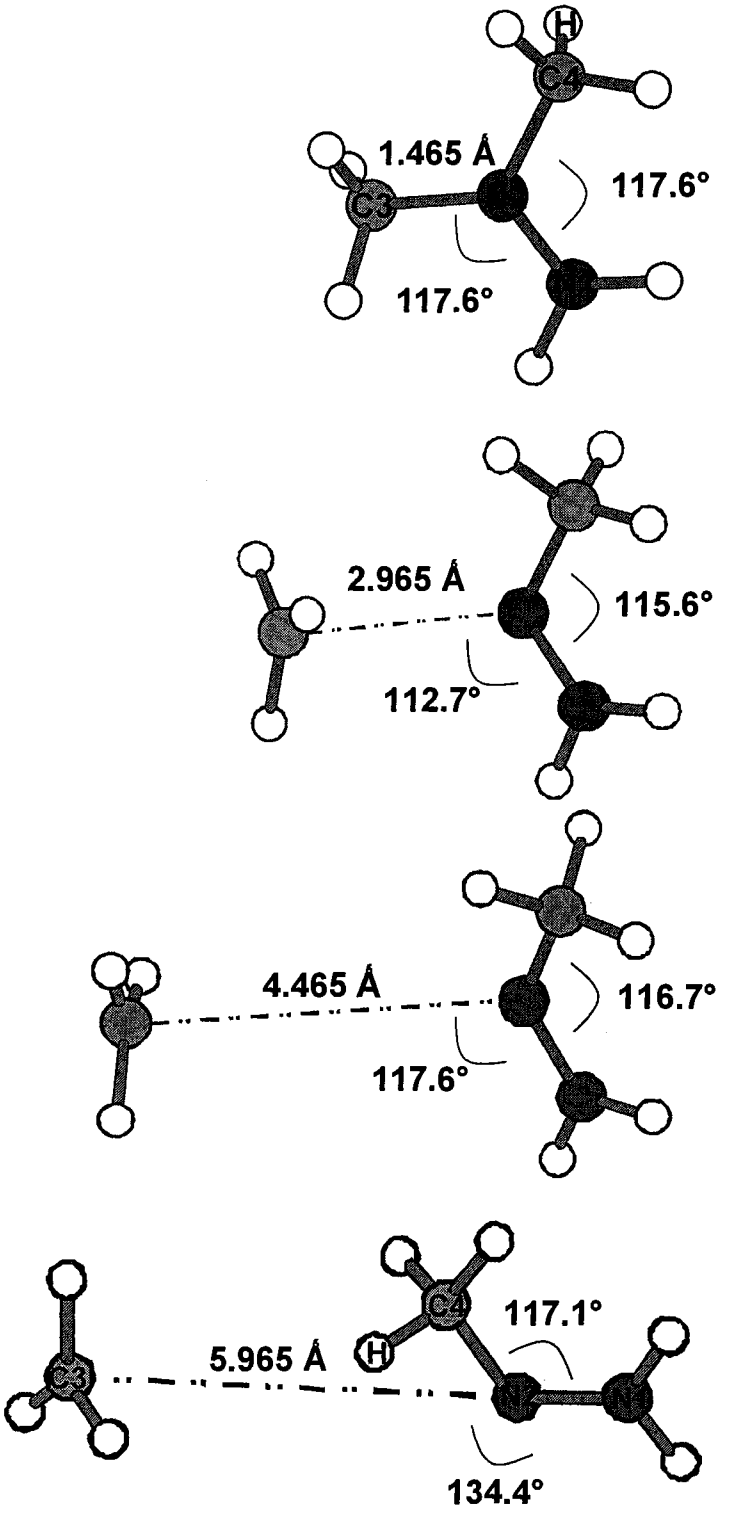

Figure 3.9 – Structures of the 1,1-dimethylhydrazine ion and its dissociating complexes for the loss of a methyl group calculated at the B3-LYP/6-31+G(d) level of theory.

Figure 3.10 shows the potential energy curve and the sum-of-states for the loss of a hydrogen atom from one of the two methyl groups. In this dissociation, three vibrational modes are converted to translational degrees of freedom of the hydrogen atom, one corresponding to the reaction coordinate (H–C stretch) and the two others to H–C scissoring or wag. There are no local maxima in the plot of the sum-of-states for hydrogen loss. The geometrical parameters of the dissociating complexes are listed in Table B.4 in Appendix B.

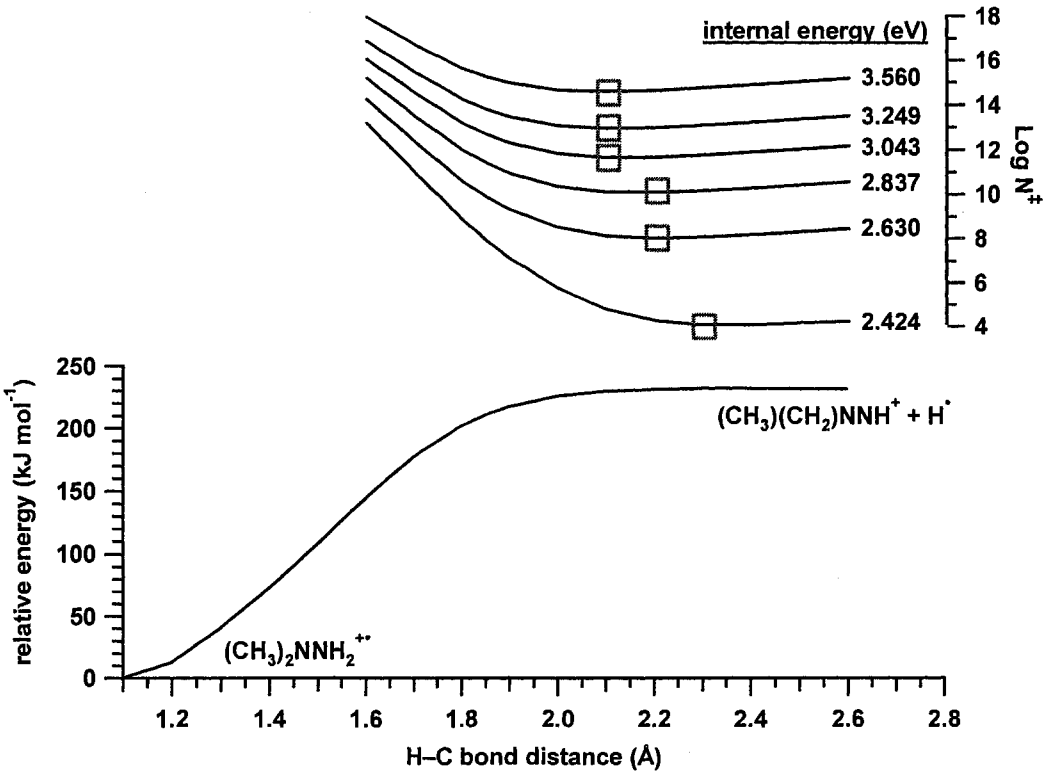

Figure 3.10 – Potential energy curve for the loss of a hydrogen atom from the 1,1-dimethylhydrazine ion and the sum-of-states as a function of the H–C bond distance calculated at the B3-LYP/6-31+G(d) level of theory. The squares correspond to the minimum in $N^{\ddagger}$ and thus to the transition states for the H–C bond cleavage.

The transition states for each channel were located by finding the minima in the sum-of-states as a function of ion internal energy. Table B.1 in Appendix B lists the vibrational

frequencies and the rotational constants for the 1,1-dimethylhydrazine ion, its dissociation products and the various transition states. For the methyl loss reaction, nine transition states are listed in Table B.1, of which six or seven are active for a particular fit of E_0. Likewise, three transition states are listed for the hydrogen loss reaction, of which two or three are active for a particular fit of E_0. For the methyl loss channel at the B3-LYP/6-31+G(d) level of theory, seven transition states were found in the internal energy range of 2.32–3.56 eV. For the hydrogen atom loss channel, three transition states were found in the same energy range. As expected from variational transition state theory, the transition states move to shorter N–C or H–C bond distance as the internal energy of the dissociating complex increases.

3.3.2 Methylhydrazine

The absolute and relative energies of ionized methylhydrazine and its fragment ions and neutrals have been calculated at the B3-LYP/6-31+G(d) level of theory and with the modified G2 and G3 protocols and are listed in Table 3.1. The structures of four $CH_5N_2^+$ isomers of fragment ion *m/z* 45 were optimized. As mentioned previously, the most energetically favourable isomer is $CH_2NHNH_2^+$ generated by the loss of a hydrogen atom from the methyl group. The energies for the three isomers of fragment ion *m/z* 30, $N_2H_2^{+\bullet}$, were also calculated for the rearrangement process leading to the loss of a methane molecule [$N_2H_2^{+\bullet}$ + CH_4] as well as the possible process of a consecutive loss of a methyl radical and a hydrogen atom loss [$N_2H_2^{+\bullet}$ + $CH_3^\bullet$ + $H^\bullet$]. The latter reactions are not expected to occur in the experimental internal energy range studied being not favoured energetically (i.e., the relative energies with respect to the parent ion are ranging from 646 to 672 kJ mol^{-1} at the mG2 and mG3 levels of theory).

The potential energy curves for the two unimolecular dissociations of the methylhydrazine ion have been calculated at the B3-LYP/6-31+G(d) level of theory. Figures 3.11 and 3.12 show the potential energy curves along with the sum-of-states graphs as a function of the C–H and C–N bond distances, respectively. The transition states for each dissociation channel were identified by finding the minimum in the sum-of-states as a function of internal energy. Their vibrational frequencies as well as those of the methylhydrazine ion and its dissociation products are listed in Table B.2 in Appendix B. The optimized geometrical parameters of the methylhydrazine ion and its dissociating complexes, for each unimolecular dissociation, are reported in Tables B.6 and B.7 in Appendix B. In the internal energy range studied for the MH ion ($E_{int} \approx 1.90$–4.00 eV), ten transition states were located for the methyl radical loss channel and four for the hydrogen atom loss channel.

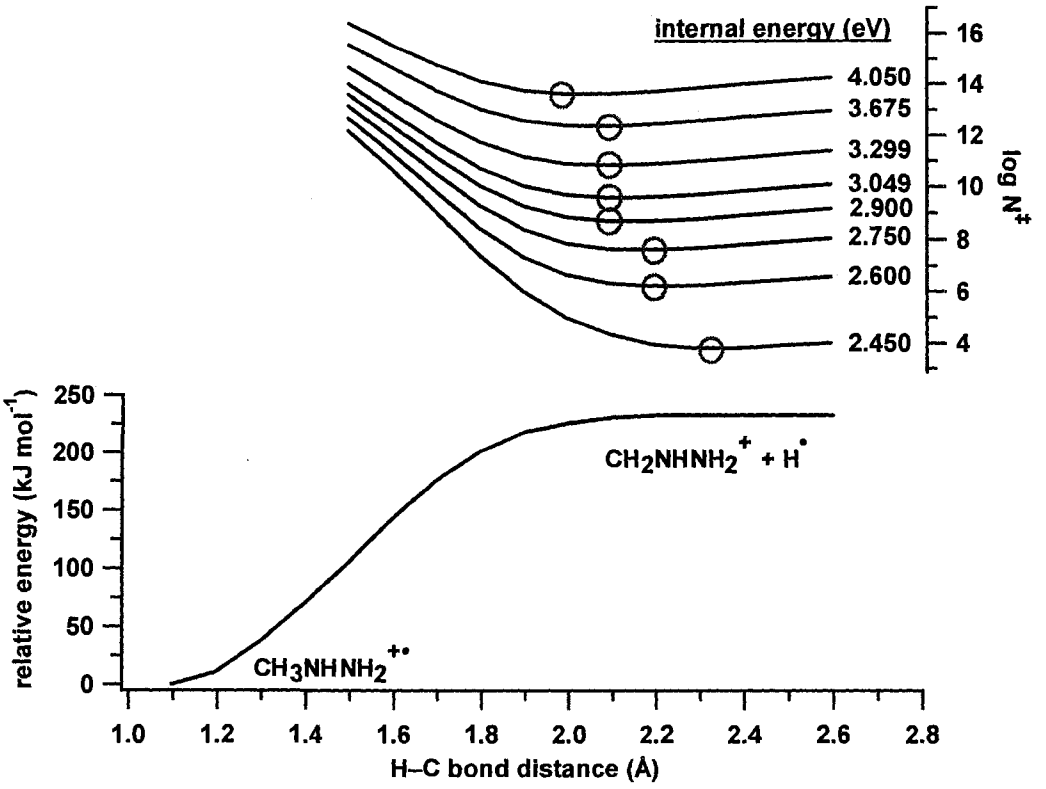

Figure 3.11 – Potential energy curve (bottom), calculated at the B3-LYP/6-31+G(d) level of theory, for the loss of a hydrogen atom from the methylhydrazine ion and the sum-of-states (top) as a function of the H–C bond distance. The transition states are identified by circles and correspond to minima in the sum-of-states ($N^{\ddagger}_{min}$).

Table 3.1: Absolute and Relative Energies[a] of the Fragment Ions and Neutrals of the Methylhydrazine Ion at the B3-LYP/6-31+G(d), mG2[b] and mG3[b] Levels of Theory

Structures[c]	absolute energies (hartrees)			relative energies (eV)			relative energies (kJ mol^{-1})		
	B3-LYP/ 6-31+G(d)	mG2	mG3	B3-LYP/ 6-31+G(d)	mG2	mG3	B3-LYP/ 6-31+G(d)	mG2	mG3
$CH_3NHNH_2^{+\bullet}$	-150.8266743	-150.6149693	-150.7565816	0.000	0.000	0.000	0	0	0
$CH_2NHNH_2^+ + H^\bullet$	-150.7362703	-150.5341055	-150.6742534	2.460	2.200	2.240	237	212	216
$CH_2NNH_3^+ + H^\bullet$	-150.7287432	-150.5277055	-150.6672078	2.665	2.375	2.432	257	229	235
$CH_3NNH_2^+ + H^\bullet$	-150.7223496	-150.5170146	-150.6562740	2.839	2.665	2.730	274	257	263
$CH_3NHNH^+ + H^\bullet$	-150.7173799	-150.5161868	-150.6551809	2.974	2.688	2.759	287	259	266
$NHNH_2^+ + CH_3^\bullet$	-150.7188970	-150.5148290	-150.6569799	2.933	2.703	2.710	283	261	262
$N_2H_2^{+\bullet}$(trans) + CH_4	-150.7409085	-150.5347645	-150.6724733	2.334	2.182	2.289	225	211	221
$N_2H_2^{+\bullet}$(iso) + CH_4	-150.7388647	-150.5318040	-150.6687910	2.389	2.263	2.389	231	218	230
$N_2H_2^{+\bullet}$(cis) + CH_4	-150.7308069	-150.5255079	-150.6633196	2.609	2.434	2.538	252	235	245
$N_2H_2^{+\bullet}$(trans) + $CH_3^\bullet + H^\bullet$	-150.5780558	-150.3688097	-150.5096770	6.765	6.698	6.719	653	646	648
$N_2H_2^{+\bullet}$(iso) + $CH_3^\bullet + H^\bullet$	-150.5760120	-150.3658492	-150.5059947	6.821	6.779	6.819	658	654	658
$N_2H_2^{+\bullet}$(cis) + $CH_3^\bullet + H^\bullet$	-150.5679542	-150.3595531	-150.5005233	7.040	6.950	6.968	679	671	672

[a] The absolute and relative energies have been corrected for ZPE (scaling factor = 0.9806). The present work has been published in Boulanger et al. [91]. [b] Modified G2 and G3 protocols based on optimized B3-LYP/6-31+G(d) geometries and scaled B3-LYP ZPE [96-99]. [c] The methylhydrazine ion, $CH_3NHNH_2^{+\bullet}$, and its fragment ion $CH_2NHNH_2^+$, belong to the C_1 point group. Fragment ions $CH_2NNH_3^+$, $CH_3NNH_2^+$, CH_3NHNH^+, and $HNNH_2^+$ belong to the C_s point group. Cis-diazene and iso-diazene belong to the C_{2v} point group. Trans-diazene belongs to the C_{2h} point group. The methyl radical belongs to the D_{3h} point group and methane belongs to the T_d point group.

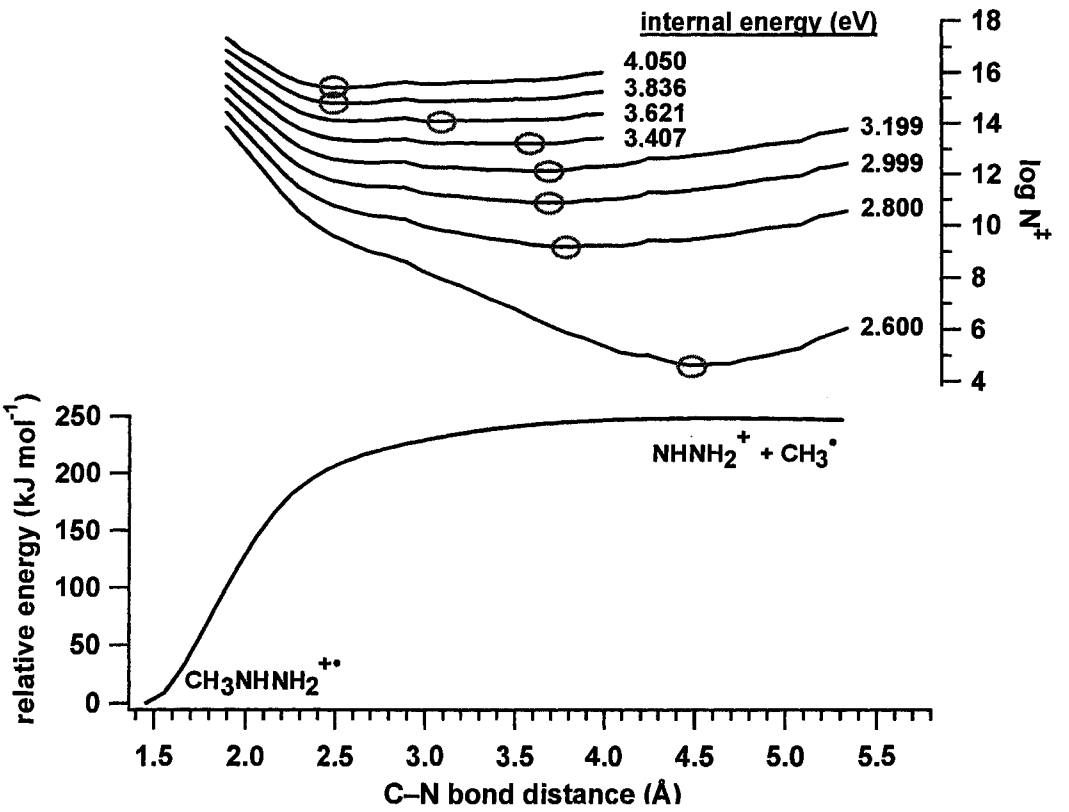

Figure 3.12 – Potential energy curve (bottom), calculated at the B3-LYP/6-31+G(d) level of theory, for the loss of a methyl radical from the methylhydrazine ion and the sum-of-states (top) as a function of the C–N bond distance. The transition states are identified by circles and correspond to minima in the sum-of-states ($N^{\ddagger}_{min}$).

3.3.3 Tetramethylhydrazine

The relative and absolute energies of ionized tetramethylhydrazine and its fragment ions and neutrals are reported in Table 3.2. The tetramethylhydrazine ion has two low energy dissociation channels, the loss of a methyl group to form the trimethylhydrazyl fragment ion *m/z* 73, $(CH_3)_2NNCH_3^+$, and the rearrangement process leading to the loss of methane and the formation of fragment ion *m/z* 72. Nine different isomers of fragment ion *m/z* 72 with the empirical formula $C_3H_8N_2^{+\bullet}$ have been considered and optimized. Their structures are shown in Figure 3.13 below. All of these isomers belong to the C_1 point group

except for isomer IX which belongs to the C_s point group. Isomer I has two possible symmetries, C_1 and C_s.

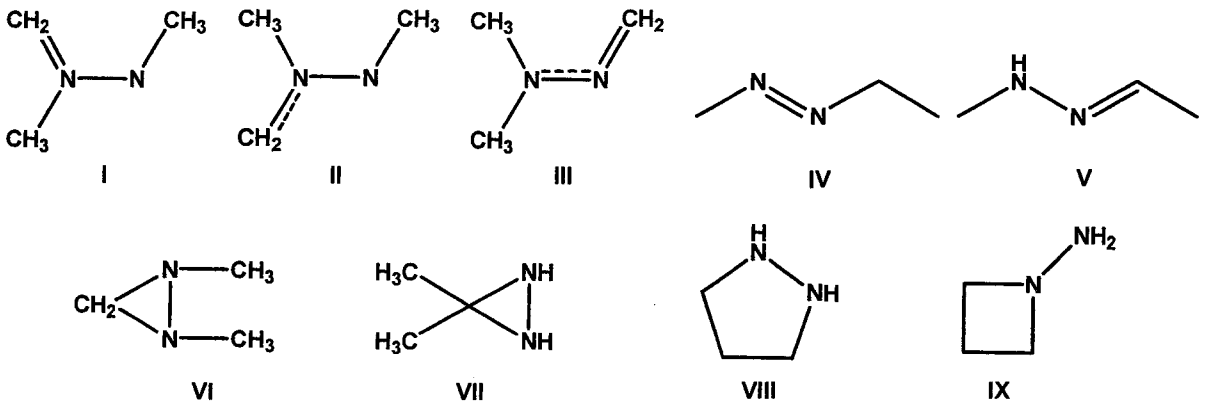

Figure 3.13 – Nine possible isomers of fragment ion *m/z* 72 with the empirical formula $C_3H_8N_2^{+\bullet}$.

A potential energy curve and the sum-of-states in the internal energy range of 1.60–4.00 eV for the methyl loss channel have been calculated at the B3-LYP/6-31+G(d) level of theory from the equilibrium geometry up to a C–N bond distance of 3.266 Å. These two graphs are shown in Figure 3.14. The vibrational frequencies of ionized tetramethylhydrazine, its dissociation products and all the transition states are listed in Table B.3 in Appendix B. The optimized geometrical parameters of the dissociating complexes are also listed in Table B.8 in Appendix B. At the B3-LYP/6-31+G(d) level of theory, four transition states for the methyl radical loss channel were identified in the internal energy range studied.

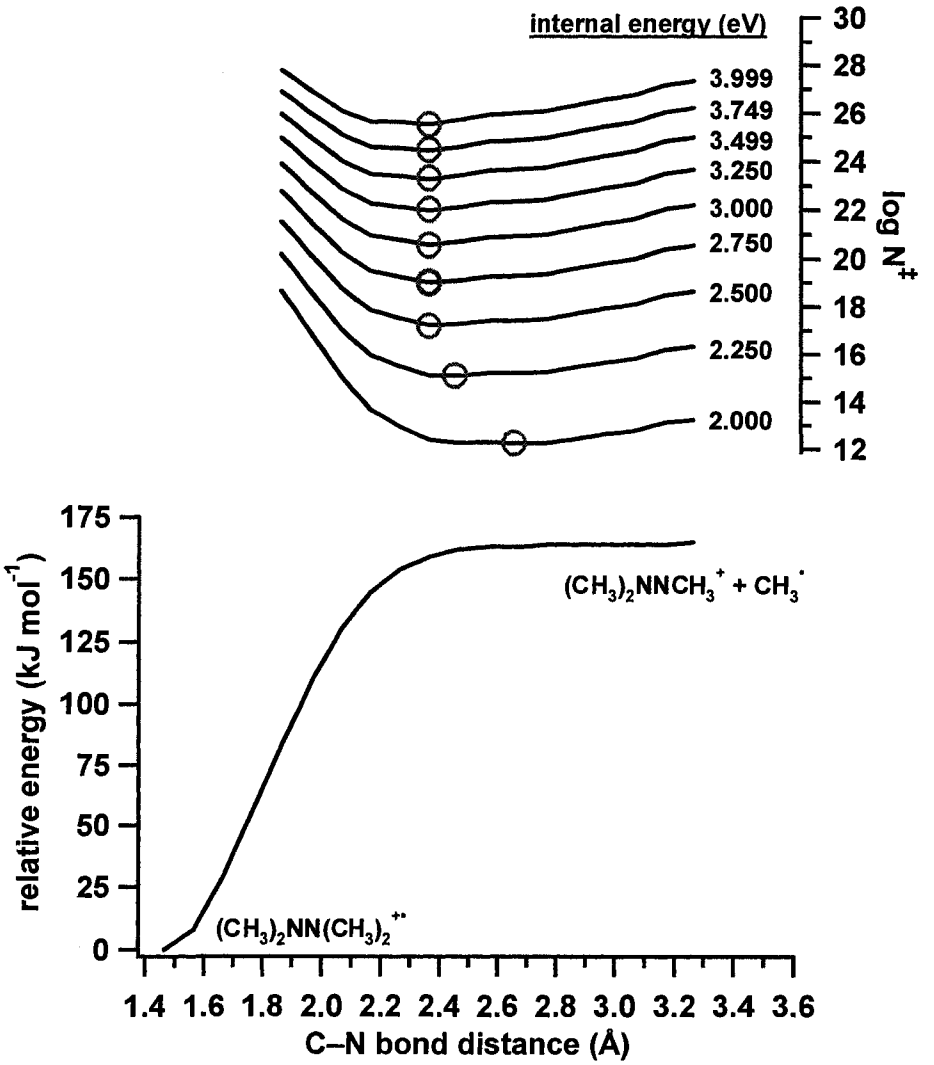

Figure 3.14 – Potential energy curve, calculated at the B3-LYP/6-31+G(d) level of theory, for the loss of a methyl radical from the tetramethylhydrazine ion and the sum-of-states as a function of the C–N bond distance. The transition states are identified by circles and correspond to minima in the sum-of-states ($N^{\ddagger}_{min}$).

Table 3.2: Absolute and Relative Energies[a] of the Fragment Ions and Neutrals of the Tetramethylhydrazine Ion at the B3-LYP/6-31+G(d), mG2[b] and mG3[b] Levels of Theory

Structures[c]	absolute energies (hartrees)			relative energies (eV)			relative energies (kJ mol^{-1})		
	B3-LYP/ 6-31+G(d)	mG2	mG3	B3-LYP/ 6-31+G(d)	mG2	mG3	B3-LYP/ 6-31+G(d)	mG2	mG3
$(CH_3)_2NN(CH_3)_2^{+\bullet}$	-268.7000736	-268.2956570	-268.5731606	0.000	0.000	0.000	0	0	0
$(CH_3)_2NNCH_3^+ + CH_3^\bullet$	-268.6352819[d]	-268.2316527[d]	-268.5085848[d]	1.763[d]	1.742[d]	1.757[d]	170[d]	168[d]	170[d]
	-268.6352030[e]	-268.2315903[e]	-268.5085199[e]	1.765[e]	1.743[e]	1.759[e]	170[e]	168[e]	170[e]
$C_3H_8N_2^{+\bullet}$ isomer I + CH_4	-268.6571618[d]	-268.2494905[d]	-268.5254477[d]	1.168[d]	1.256[d]	1.298[d]	113[d]	121	125[d]
	-268.6572195[e]	-268.2495599[e]	-268.5255170[e]	1.166[e]	1.254[e]	1.296[e]	113[e]	121	125[e]
$C_3H_8N_2^{+\bullet}$ isomer II + CH_4	-268.6591778	-268.2507558	-268.5268281	1.113	1.222	1.261	107	118	122
$C_3H_8N_2^{+\bullet}$ isomer III + CH_4	-268.6713717	-268.2609236	-268.5367966	0.781	0.945	0.990	75	91	95
$C_3H_8N_2^{+\bullet}$ isomer IV + CH_4	-268.6713037	-268.2626679	-268.5417432	0.783	0.898	0.855	76	87	82
$C_3H_8N_2^{+\bullet}$ isomer V + CH_4	-268.6822996	-268.2700415	-268.5465742	0.484	0.697	0.723	47	67	70
$C_3H_8N_2^{+\bullet}$ isomer VI + CH_4	-268.6359898	-268.2280883	-268.5028961	1.744	1.839	1.912	168	177	184
$C_3H_8N_2^{+\bullet}$ isomer VII + CH_4	-268.6382087	-268.2374018	-268.5127544	1.683	1.585	1.644	162	153	159
$C_3H_8N_2^{+\bullet}$ isomer VIII + CH_4	-268.7030893	-268.2994572	-268.5768428	-0.082	-0.103	-0.100	-8	-10	-10
$C_3H_8N_2^{+\bullet}$ isomer IX + CH_4	-268.6739672	-268.2685783	-268.5451725	0.710	0.737	0.762	69	71	73

[a] The absolute and relative energies have been corrected for ZPE (scaling factor = 0.9806). The present work has been published in Boulanger et al. [91]. [b] Modified G2 and G3 protocols based on optimized B3-LYP/6-31+G(d) geometries and scaled B3-LYP ZPE [96-99]. [c] The tetramethylhydrazine ion, $(CH_3)_2NN(CH_3)_2^{+\bullet}$, the trimethylhydrazyl fragment ion $(CH_3)_2NNCH_3^+$ and $C_3H_8N_2^{+\bullet}$ isomers (I to VIII) belong to the C_1 point group. Fragment ion $C_3H_8N_2^{+\bullet}$ isomer IX belongs to the C_s point group. The methyl radical belongs to the D_{3h} point group and methane belongs to the T_d point group. The trimethylhydrazyl fragment ion $(CH_3)_2NNCH_3^+$ and $C_3H_8N_2^{+\bullet}$ isomer I fragment ion can also belong to the C_s point group. [d] Energy when fragment ion belongs to the C_1 point group. [e] Energy when fragment ion belongs to the C_s point group.

3.4 The experimental breakdown curves

The complete breakdown curves of the methyl-substituted hydrazine ions were measured from threshold up to $h\nu \approx 32$ eV. The appearance energies of the observed fragment ions are reported with a brief discussion.

3.4.1 1,1-Dimethylhydrazine

The complete 1,1-dimethylhydrazine ion breakdown curve has been recorded between $h\nu$ = 8.25–31.00 eV, and a total of twenty three fragment ions are observed. Employing the adiabatic ionization energy of 7.29 ± 0.04 eV [108] yields an internal energy range of 0.96–23.71 eV. In a study on the threshold photoelectron spectroscopy of methyl-substituted hydrazines [105], we had determined the adiabatic ionization energy of 1,1-dimethylhydrazine to be 7.78 ± 0.16 eV which was demonstrated to be too high due to the large geometry change upon ionization. Figure 3.15 shows the relative abundances for all the fragment ions as a function of photon energy.

The first two dissociation channels are the loss of a methyl radical and the loss of a hydrogen atom to form the fragment ions *m/z* 45, $CH_3NNH_2^+$ and *m/z* 59, $(CH_3)(CH_2)NNH_2^+$, respectively. The parent ion *m/z* 60 is not observed at photon energies greater than 10.15 eV. Over the next ~ 1.6 eV, the only fragment ions detected are *m/z* 45 and *m/z* 59, and these occur with a constant ratio. Ions *m/z* 44 and 46 have onsets at $h\nu$ = 9.85 and 9.80 eV (E_{int} = 2.56 and 2.51 eV), respectively, but their abundances are low (less than 2%), while the abundances of ions *m/z* 45 and 59 are 55 and 45 %, respectively. One interesting feature in the first cross-over region of the breakdown curve (see Figure 3.19) is that ion *m/z* 59 is more intense than ion *m/z* 45 up to $h\nu$ = 10.05 eV (E_{int} = 2.76 eV) where the two product curves cross. This crossing is also reflected in the rate constants for both

dissociation pathways. It will be discussed in more detail in Section 3.5. At a photon energy of $h\nu$ = 11.75 eV (E_{int} = 4.46 eV), higher energy dissociation products start to appear. The most intense ions are *m/z* 18 (NH_4^+) and *m/z* 42 ($C_2H_4N^+$). MIKE and CID experiments indicate that the NH_4^+ ion is most probably formed from $CH_3NNH_2^+$ while the *m/z* 42 ion is a fragment produced from the decomposition of *m/z* 59. As the photon energy increases further, two other ions, *m/z* 30 ($N_2H_2^+$) from *m/z* 59 and *m/z* 28 (N_2^+ or $HCNH^+$) from *m/z* 45, are progressively forming. Tentative structures or empirical formulae have been assigned to each fragment ion and can be found in Table C.1 in Appendix C. This table also contains the previous experimental appearance energies as well as an indication of the ionization technique used to generate the fragment ions.

3.4.2 Methylhydrazine and tetramethylhydrazine

Eighteen and twenty-five fragment ions have been observed in the breakdown curves of ionized methylhydrazine and tetramethylhydrazine, respectively, from threshold up to $h\nu \approx 32$ eV. Tentative structures or empirical formulae have been assigned to each fragment ion and can be found in Tables C.2 and C.3 in Appendix C. The tables also contain previously reported experimental AEs as well as an indication of the ionization technique used to generate the fragment ions. Figures 3.16 and 3.17 show the relative abundances of all fragment ions of MH and TMH ions respectively, as a function of photon energy.

Figure 3.18 shows portions of the TOF spectra of methylhydrazine recorded at photon energies of 24.45 and 30.95 eV. In the spectrum recorded at 24.45 eV the peaks are well resolved and can be associated with fragments possessing relatively small kinetic energies. An AE of 27.95 eV has been determined for the doubly charged parent ion in the present work.

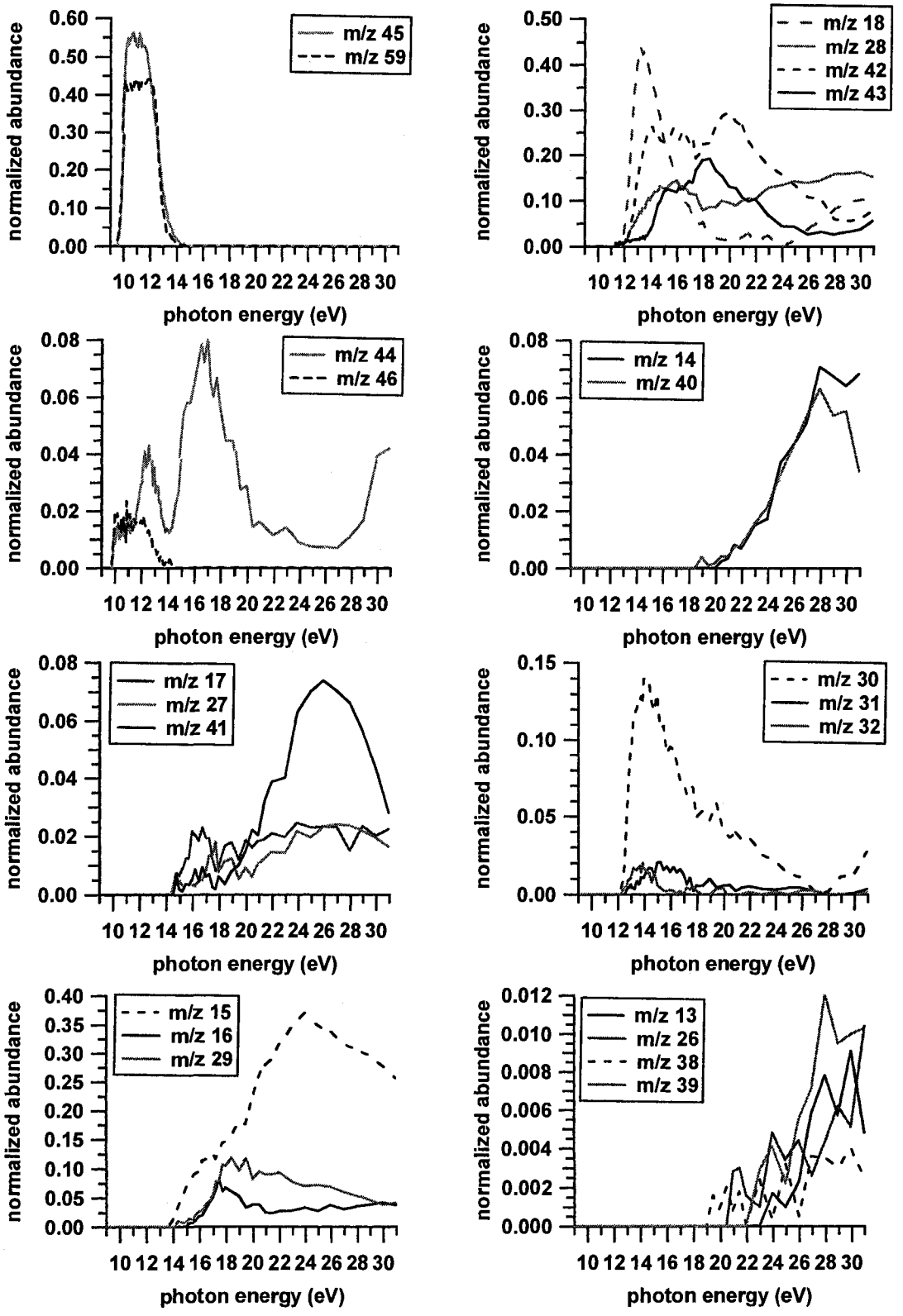

Figure 3.15 – Relative abundances of all fragment ions of 1,1-dimethylhydrazine in the photon energy range 9–31 eV.

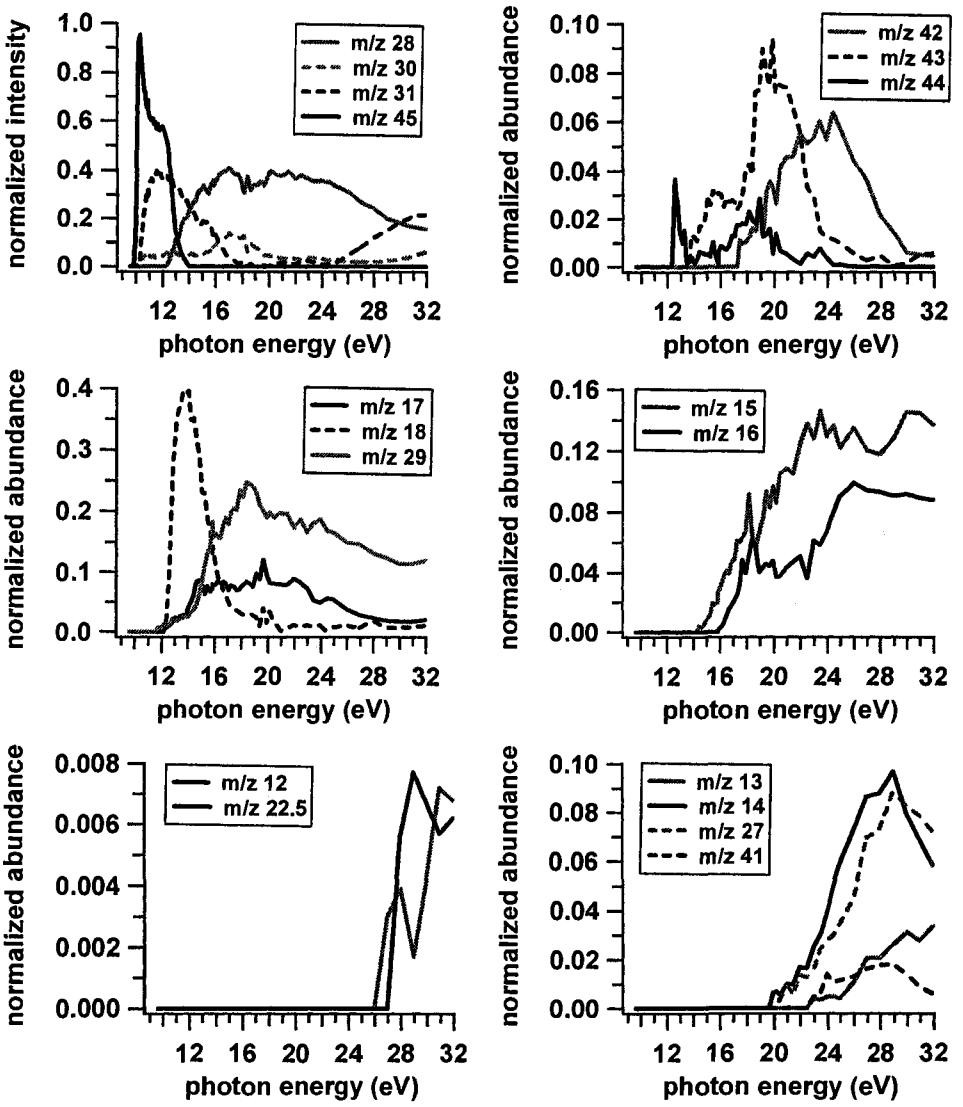

Figure 3.16 – Relative abundances of all fragment ions of methylhydrazine in the photon energy range 9–32 eV.

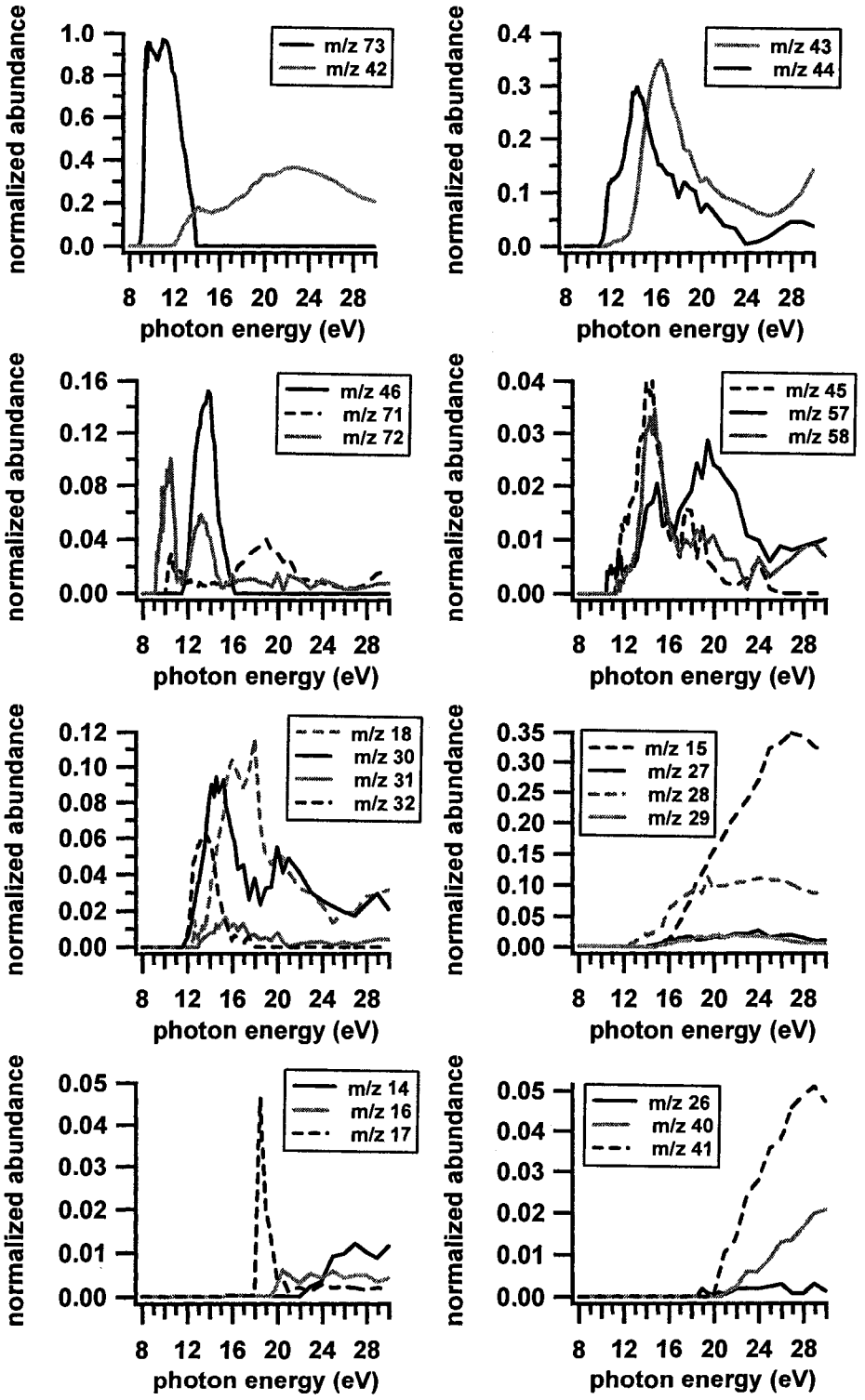

Figure 3.17 – Relative abundances of all fragment ions of tetramethylhydrazine in the photon energy range 8–30 eV.

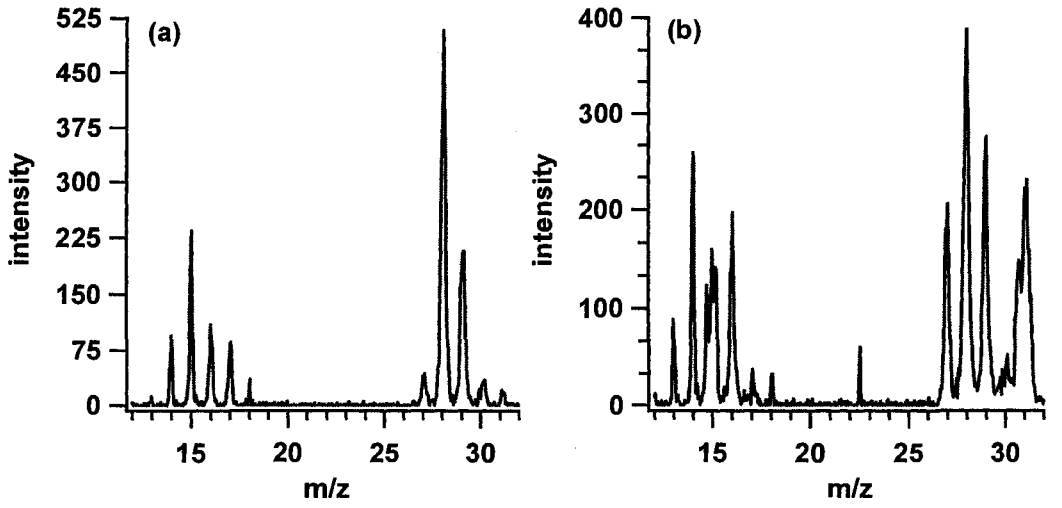

Figure 3.18 – Portions of the TOF mass spectra of methylhydrazine recorded at photon energies of (a) 24.45 eV and (b) 30.95 eV.

The observation of the doubly charged ion (*m/z* 22.5) indicates that at least some of these species have lifetimes greater than the few μs required to reach the detector. In the spectrum recorded at 30.95 eV, which is above the threshold for double ionization, some of the peaks have broadened substantially and must be attributed to fragments possessing significant kinetic energies. This broadening is particularly evident in the peaks corresponding to the CH_3^+ (*m/z* 15) and $NHNH_2^+$ (*m/z* 31) fragments. The large kinetic energy probably results from a charge separation reaction in the doubly charged parent ion yielding two singly charged species. The large kinetic energy is due to a charge separation between the initial ion-pair. A triplet profile is observed in the TOF peak shape for the CH_3^+ fragment in the spectrum recorded at 30.95 eV. The central peak corresponds to fragment ions formed directly with very little kinetic energy. The other two peaks correspond to CH_3^+ fragments formed with large kinetic energies, probably a few eV, via a charge separation, and directed predominantly towards or away from the channelplate detector. Energetic

fragments ejected in directions approximately perpendicular to the spectrometer axis are lost on apertures along the flight path, thereby producing dips in the TOF peak profile.

3.5 Variational fits of the breakdown curves

The theoretical fits of the experimental breakdown curves in the first cross-over region will be discussed. The initial ion studied was 1,1-dimethylhydrazine ion which will be explained first followed by a discussion on methyl- and tetramethylhydrazine ions.

3.5.1 1,1-Dimethylhydrazine

The first cross-over region (E_{int} = 2.30–3.10 eV) of the four experimental breakdown curves of 1,1-dimethylhydrazine ion were fitted with two approaches: with the variational TST and the single transition state approach. The fits were considered to be satisfactory when all four breakdown diagrams were well reproduced with the theoretical parameters (i.e., E_0 and the scaling factor of the five lowest vibrational frequencies of the transition states). The resulting fits are reported in Table 3.3. Fitting the experimental breakdown curves using the calculated VTST $k(E_{int})$ for each channel at the B3-LYP/6-31+G(d) level of theory yielded poor results. There are two reasons why the VTST treatment may not be satisfactory at this level of theory. First, the B3-LYP/6-31+G(d) values for E_0 are certainly in error and secondly the location of the transition states (and hence $\Delta S^{\ddagger}$) may be poorly described with the VTST approach employed herein. As discussed previously in this chapter, at the B3-LYP/6-31+G(d) level of theory, the two sets of dissociation products, $[(CH_3)(CH_2)NNH_2^+ + H^{\bullet}]$ and $[CH_3NNH_2^+ + CH_3^{\bullet}]$ are very close in energy and thus the E_0 values obtained are undoubtedly incorrect. To correct this inaccuracy, we adjusted the B3-

LYP/6-31+G(d) potential energy curves so the plateau (taken at bond distances of $R_{N\text{-}C}$ = 4.56 Å and $R_{H\text{-}C}$ = 2.50 Å) corresponded to the mG3 product energies in order to correct for an inexact E_0. The fit to the experimental data was greatly improved but was still in need of refinement (Figure 3.19). In these two fits, the parameters were not adjusted except for the E_0 values in the second fit (E_0 adjusted to the mG3 product energies).

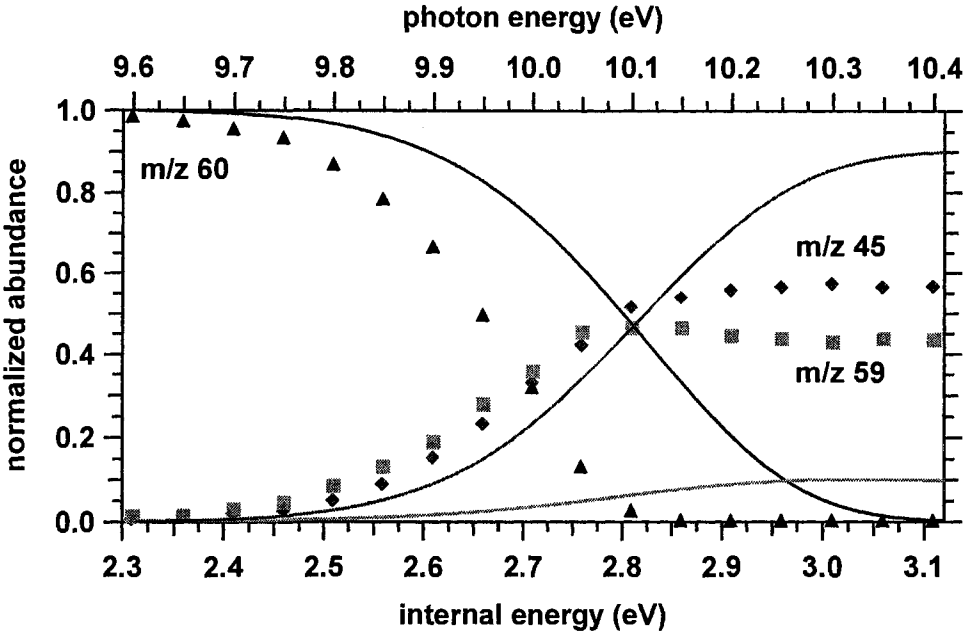

Figure 3.19 – Comparison between the experimental breakdown curve and the theoretical fit at a parent ion residence time of 1.116 μs using the variational transition states at the B3-LYP/6-31+G(d) energies corrected to the mG3 fragment products energies. The parent ion *m/z* 60 is represented by (▲), the fragment ion *m/z* 45 is represented by (♦) and the fragment ion *m/z* 59 is represented by (■). The theoretical fits are represented by the solid lines (black for parent ion *m/z* 60, dark grey for fragment ion *m/z* 45 and light grey for ion *m/z* 59).

In order to get good fits of the breakdown curves, the five lowest vibrational frequencies of the transition states for the hydrogen loss channel were then scaled to change $\Delta S^{\ddagger}$ for this channel from 0.9–7.9 J K^{-1} mol^{-1} to (16-22)–(20-26) J K^{-1} mol^{-1}. The scaling factors that gave good agreement between experiment and theory ranged from 0.52 in fit 1 to 0.62 in fit 3. Due to the large number of transition states for the methyl loss channel, the

vibrational frequencies of these transition states were not scaled and thus the entropy of activation was not adjusted like in the hydrogen atom loss channel. In addition the potential energy curves for the two channels were adjusted up or down to obtain a good fit to the data (Figure 3.20) by altering the activation energies. The results for all of these attempts are summarized in Table 3.3. In the end, only small changes were needed to the energy of the potential energy curves relative to the mG3 results. It is important to note that the value of the adiabatic ionization energy has an effect on the fits of the breakdown curves. When using the calculated mG3 IE_a value of 7.36 eV [105] instead of the reported value of 7.29 ± 0.04 eV by Meot-Ner et al. [108], the values of E_0 for the methyl loss channel did not need to be adjusted in order to fit the experimental breakdown curves (see Table 3.3 for E_0 values of methyl loss channel), only the E_0 values for the hydrogen loss channel had to be changed ($E_0(R_{H\text{-}C} = 2.20$ Å) = 2.122 eV and $E_0(R_{H\text{-}C} = 2.10$ Å) = 2.105 eV). These differences in E_0 are taken into account in the uncertainties of the resulting $\Delta_f H$ values (see Chapter 4 for a discussion on the enthalpies of formation).

There is a large change in the $\Delta S^{\ddagger}$ for the methyl loss channel over the studied internal energy range at the B3-LYP/6-31+G(d) level of theory. $\Delta S^{\ddagger}$ varies from 65 J K^{-1} mol^{-1} at E_{int} = 2.32 eV to 19 J K^{-1} mol^{-1} at E_{int} = 3.56 eV. In the case of the hydrogen loss channel (at the same level of theory), the $\Delta S^{\ddagger}$ values are small (8 to 0.9 J K^{-1} mol^{-1}) and do not vary as much as those for the methyl loss channel. This is also true for the three fits (fits 1, 2 and 3) of the experimental breakdown curves where the entropies of activation vary from 16-22 to 20-26 J K^{-1} mol^{-1} (see Table 3.3). The entropies of activation were calculated using two different approaches (i.e., HO and FR approaches). The complete list is reported in Tables D.1 and D.2 in Appendix D.

Table 3.3: Transition States, Entropies of Activation (600 K) and Energies of Activation (0 K) for the Unimolecular Dissociations of the 1,1-Dimethylhydrazine Ion at the B3-LYP/6-31+G(d) Level of Theory in the Internal Energy Range of 2.32–3.56 eV[a]

Dissociation Channel	$CH_3NNH_2^+ + CH_3^\bullet$							
B3-LYP/6-31+G(d)	ΔE^b = 2.295 eV or 221.5 kJ mol^{-1}							
R^* (Å)	2.565	2.665	2.765	3.165	3.965	4.065	4.265	
$\Delta S^\ddagger$ (J K^{-1} mol^{-1})[c]	19.05	22.15	25.26	41.8	59.39	60.49	65.37	
E_0 (eV)	2.105	2.138	2.162	2.226	2.285	2.289	2.293	
corrected to mG3 product energy	ΔE = 2.391 eV or 230.6 kJ mol^{-1}							
R^* (Å)	2.565	2.665	2.765	3.165	3.965	4.065	4.365	
$\Delta S^\ddagger$ (J K^{-1} mol^{-1})	19.05	22.15	25.26	41.8	59.39	60.49	66.96	
E_0 (eV)	2.200	2.233	2.257	2.322	2.381	2.384	2.390	
fit 1	ΔE = 2.325 eV or 224.4 kJ mol^{-1}							
R^* (Å)	2.565	2.665	2.765	3.165	3.965	4.065	4.265	
$\Delta S^\ddagger$ (J K^{-1} mol^{-1})	19.05	22.15	25.26	41.8	59.39	60.49	65.37	
E_0 (eV)	2.135	2.168	2.192	2.256	2.315	2.319	2.323	
fit 2	ΔE = 2.330 eV or 224.8 kJ mol^{-1}							
R^* (Å)	2.565	2.665	2.765	2.865	3.165	3.965	4.065	4.265
$\Delta S^\ddagger$ (J K^{-1} mol^{-1})	19.05	22.15	25.26	28.16	41.8	59.39	60.49	65.37
E_0 (eV)	2.140	2.173	2.197	2.217	2.261	2.320	2.324	2.328
fitting with one transition state	ΔE = 2.355 eV or 227.2 kJ mol^{-1}							
R^* (Å)	3.46							
$\Delta S^\ddagger$ (J K^{-1} mol^{-1})	43.28							
E_0 (eV)	2.314							
Dissociation Channel	$(CH_3)(CH_2)NNH_2^+ + H^\bullet$							
B3-LYP/6-31+G(d)	ΔE = 2.405 eV or 232.1 kJ mol^{-1}							
R^* (Å)	2.098	2.198	2.298					
$\Delta S^\ddagger$ (J K^{-1} mol^{-1})	0.86	4.46	7.92					
E_0 (eV)	2.385	2.402	2.407					
corrected to mG3 product energy	ΔE = 2.185 eV or 210.9 kJ mol^{-1}							
R^* (Å)	2.098	2.198						
$\Delta S^\ddagger$ (J K^{-1} mol^{-1})	0.86	4.46						
E_0 (eV)	2.165	2.182						
fit 1	ΔE = 2.180 eV or 210.4 kJ mol^{-1}							
R^* (Å)	2.098	2.198						
$\Delta S^\ddagger$ (J K^{-1} mol^{-1})	21.93	25.64						
E_0 (eV)	2.160	2.177						
fit 2	ΔE = 2.155 eV or 208.0 kJ mol^{-1}							
R^* (Å)	2.098	2.198						
$\Delta S^\ddagger$ (J K^{-1} mol^{-1})	18.93	22.63						
E_0 (eV)	2.135	2.152						
fit 3	ΔE = 2.130 eV or 205.6 kJ mol^{-1}							
R^* (Å)	2.098	2.198						
$\Delta S^\ddagger$ (J K^{-1} mol^{-1})	16.19	19.88						
E_0 (eV)	2.110	2.127						
fitting with one transition state	ΔE = 2.155 eV or 208.0 kJ mol^{-1}							
R^* (Å)	2.20							
$\Delta S^\ddagger$ (J K^{-1} mol^{-1})	23.80							
E_0 (eV)	2.152							

[a] The present work has been published in Boulanger et al. [92]. [b] Energy difference between the equilibrium ion and the plateau on the potential energy curve (energy value taken at R_{N-C} = 4.56 Å or R_{H-C} = 2.50 Å). [c] The entropies of activation reported in this table were calculated using the rovibrational FR model of East and Radom [103].

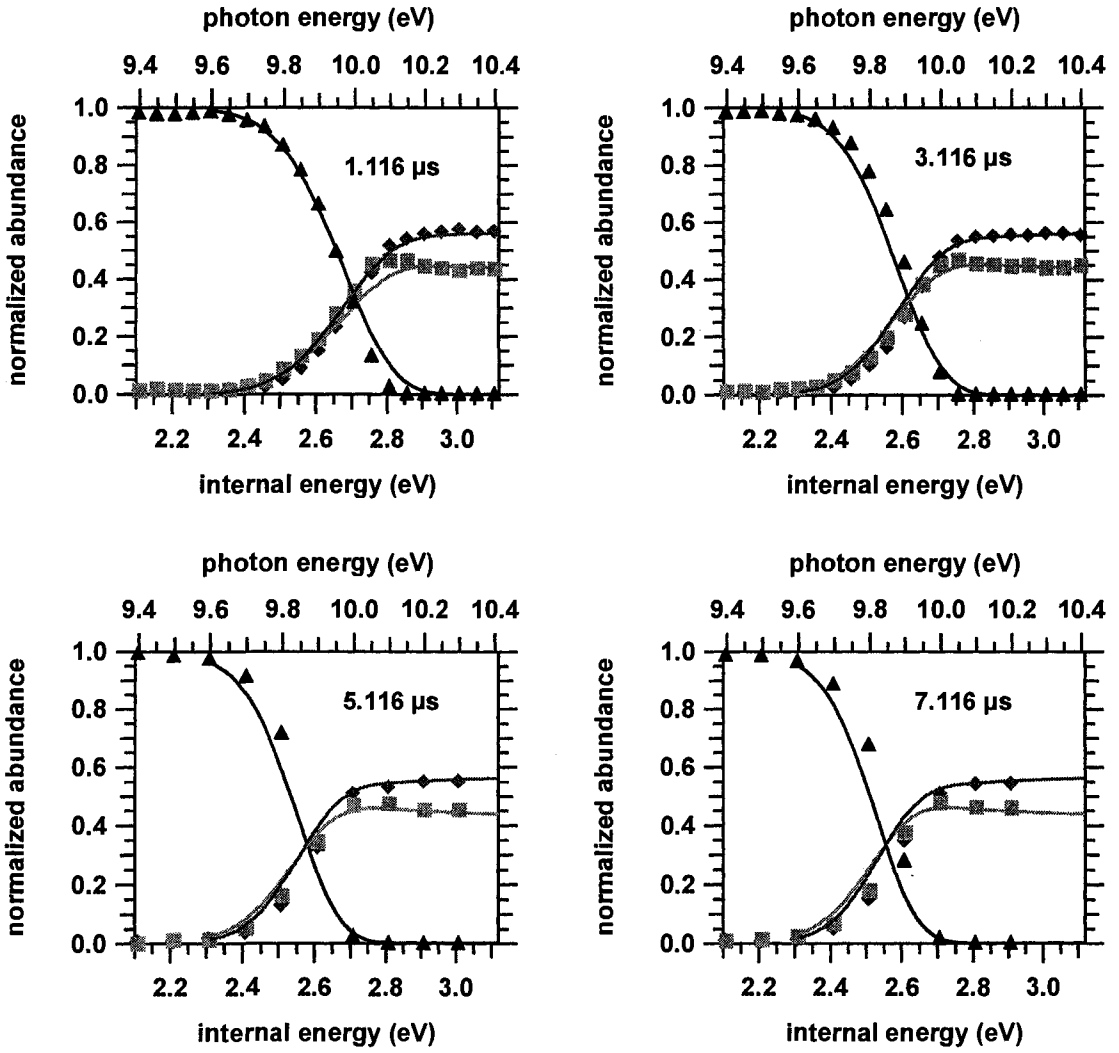

Figure 3.20 – Comparison between the experimental breakdown curves and the theoretical fit (fit 2 for both channels) using seven variational transition states for the methyl loss and two transition states for hydrogen loss. The energy differences between the 1,1-dimethylhydrazine ion and the potential energy curve plateau are: $\Delta E(45) = 2.330$ eV at $R_{N-C} = 4.56$ Å and $\Delta E(59) = 2.155$ eV at $R_{H-C} = 2.50$ Å. The parent ion *m/z* 60 is represented by (▲), the fragment ion *m/z* 45 is represented by (♦) and the fragment ion *m/z* 59 is represented by (■). The theoretical fits are represented by the solid lines (black for parent ion *m/z* 60, dark grey for fragment ion *m/z* 45 and light grey for ion *m/z* 59).

The four breakdown curves of the DMH ion were also fitted without VTST, employing a simple RRKM approach with one transition state for each dissociation channel. In this fit, the transition state for the methyl loss channel was estimated to be at $R_{N-C} = 3.46$

Å and for hydrogen atom loss channel, the transition state was estimated to be at $R_{H-C} = 2.20$ Å. The E_0 and five lowest vibrational frequencies of both channels were changed to find the best agreement with the experimental data. However, it was not possible to find one set of energies and vibrational frequencies that would fit all the experimental data simultaneously. Figure 3.21 shows the best theoretical fit to the 1.116 μs residence time breakdown curve using a single transition state for each dissociation channel. Satisfactory fits to the parent and the total products curves could be obtained but not for the individual product curves. Each product curve (*m/z* 45 and *m/z* 59) could be fitted up to $E_{int} = 2.91$ eV but the plateau above that energy could not be reproduced. Having only one transition state for the methyl loss could not take into account the large change in the $\Delta S^{\ddagger}$ with increasing internal energy observed in the variational analysis.

In all the various fits of the 1,1-dimethylhydrazine ion breakdown diagrams, only the lower energy structure of fragment ion *m/z* 59 was considered. It could be argued that a difference of only 36 kJ mol^{-1} between the two possible structures of fragment ion *m/z* 59 is not enough to prevent a higher energy reaction from occurring at energies somewhat above the higher energy threshold (i.e., above the energy range in which MIKE dissociations occur). Our experimental results tend to show that the lower energy structure $(CH_3)(CH_2)NNH_2^+$ is the correct and more plausible one for that fragment ion. To confirm, a quick fit of the breakdown curve using the higher energy isomer *m/z* 59, $(CH_3)_2NNH^+$, instead of the lower energy one was done and showed that the activation energies of this second ion had to be decreased much more than the activation energies of isomer 1 in order to get a good fit. The results are summarized in Table 3.4. In Figure 3.22, the sets of rate constants for the two possible dissociation pathways of fragment ion *m/z* 59 and the one of

fragment ion *m/z* 45 are shown as a function of ion internal energy. These sets of rate constants have been calculated using the activation energies corrected to the mG3 product energies. From this graph, it is clear that the second isomer of fragment ion *m/z* 59 is not competing with the two other ions at any energy. At the B3-LYP/6-31+G(d) level of theory, the $\Delta S^{\ddagger}(59)_2$ values, for isomer 2 of fragment ion *m/z* 59, are larger than those calculated for isomer 1, ranging from 13 J K^{-1} mol^{-1} to 5 J K^{-1} mol^{-1}. However, the entropies of activation calculated for the crude fit of the breakdown curves (fit A in Table 3.4) are similar to those obtained for isomer 1 (fits 1–3 in Table 3.3).

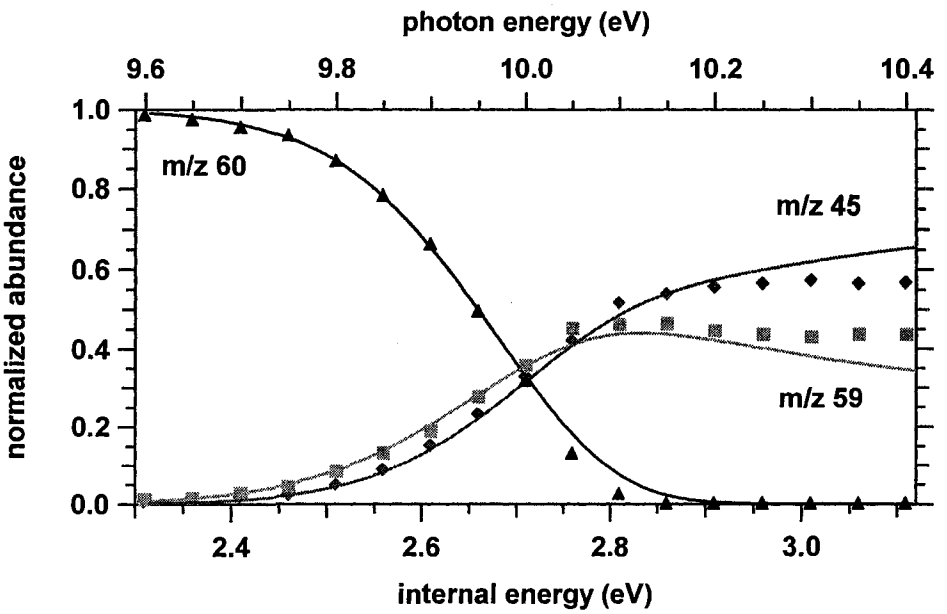

Figure 3.21 – Comparison between the experimental breakdown curve and the theoretical fit at a parent ion residence time of 1.116 μs using one transition state for each dissociation channel ($E_0(45)$ = 2.314 eV and $E_0(59)$ = 2.152 eV). The parent ion *m/z* 60 is represented by (▲), the fragment ion *m/z* 45 is represented by (♦) and the fragment ion *m/z* 59 is represented by (■). The theoretical fits are represented by the solid lines (black for parent ion *m/z* 60, dark grey for fragment ion *m/z* 45 and light grey for ion *m/z* 59).

Table 3.4: Transition States, Entropies of Activation (600 K) and Energies of Activation (0 K) for the Hydrogen Loss Channel from the NH_2 Group of the 1,1-Dimethylhydrazine Ion at the B3-LYP/6-31+G(d) Level of Theory in the Internal Energy Range of 2.32–3.56 eV

Dissociation Channel	$(CH_3)_2NNH^+ + H^\cdot$			
B3-LYP/6-31+G(d)	ΔE^a = 2.740 eV or 264.4 kJ mol^{-1}			
R^* (Å)	2.117	2.217	2.317	2.417
$\Delta S^\ddagger$ (J K^{-1} mol^{-1})	4.89	7.87	10.63	12.99
E_0 (eV)	2.699	2.712	2.720	2.725
corrected to mG3 product energies	ΔE = 2.563 eV or 247.3 kJ mol^{-1}			
R^* (Å)	2.117	2.217	2.317	2.417
$\Delta S^\ddagger$ (J K^{-1} mol^{-1})	4.89	7.87	10.63	12.99
E_0 (eV)	2.522	2.535	2.543	2.548
fit A	ΔE = 2.215 eV or 213.7 kJ mol^{-1}			
R^* (Å)	2.117	2.217	2.317	2.417
$\Delta S^\ddagger$ (J K^{-1} mol^{-1})	13.14	16.49	19.28	21.67
E_0 (eV)	2.174	2.187	2.195	2.200

[a] Energy difference between the equilibrium ion and the plateau on the potential energy curve (energy value taken at R_{H-N} = 3.017 Å).

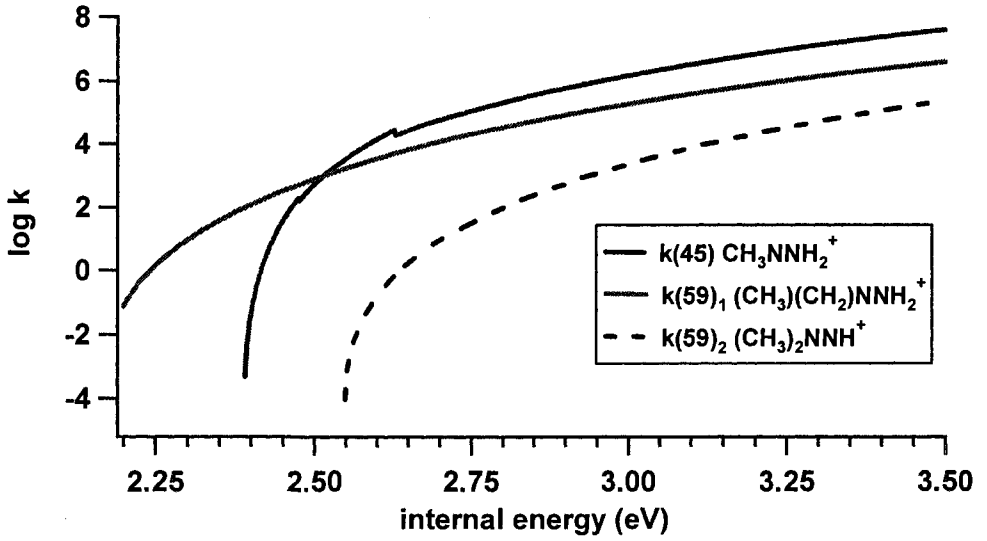

Figure 3.22 – Rate constants for the unimolecular dissociations of the 1,1-dimethylhydrazine ion into the isomer 1 of fragment ion *m/z* 59, $(CH_3)(CH_2)NNH_2^+$, into the isomer 2 $(CH_3)_2NNH^+$ and into fragment ion *m/z* 45 $CH_3NNH_2^+$. The rate constants were calculated using the activation energies from the potential energy curves corrected to the mG3 product energies.

3.5.2 Methylhydrazine

To fit the methylhydrazine ion breakdown curves, the same VTST procedure as described for the fragmentation of 1,1-dimethylhydrazine ions was used. The results for all these fits are summarized in Table 3.5 and one of the resulting fits is shown in Figure 3.23. Only small changes were needed to the energy of the potential energy curves relative to the mG3 results to obtain satisfactory fits.

In all four breakdown curves of ionized methylhydrazine, the hydrogen loss channel has been fitted in the internal energy range of 1.90–2.80 eV. Data for the methyl and methane losses channels were only collected for a parent ion residence time of 1.116 μs and were fitted up to 3.50 eV. At the B3-LYP/6-31+G(d) level of theory, ten transition states were found in the internal energy range of 1.90–4.00 eV for the methyl loss channel. This was reduced to a more practical five to carry out the fitting (Table 3.5) and the quality of the fits has not been affected by that simplification. Because of the transition state switch as the internal energy increases, the values of the entropies of activation vary. The $\Delta S^{\ddagger}(45)_{MH}$ values for the hydrogen loss channel, calculated at the B3-LYP/6-31+G(d) level of theory, ranged from -4 J K^{-1} mol^{-1} at $E_{int} \approx 2.25$ eV to -14 J K^{-1} mol^{-1}at $E_{int} \approx 4.00$ eV. These values are lower than those derived for the hydrogen loss channel of the 1,1-dimethylhydrazine ions [92] at the same level of theory, however the $\Delta S^{\ddagger}$ values decrease similarly with an increase in ion internal energy. For methyl loss, at the B3-LYP/6-31+G(d) level of theory, the $\Delta S^{\ddagger}(31)_{MH}$ ranges from 62 J K^{-1} mol^{-1} at $E_{int} \approx 2.58$ eV to 13 J K^{-1} mol^{-1} at $E_{int} \approx 4.00$ eV. These values are similar to those derived for the methyl loss channel of 1,1-dimethylhydrazine ions at the same level of theory. The entropies of activation will be discussed in more details in Chapter 4.

The methane loss channel was fitted by estimating the transition state vibrational frequencies from the MH ion vibrational frequencies. The five lowest vibrational frequencies were scaled until a good agreement with the experimental breakdown curves was obtained. The rotational constants for this transition state were estimated using the rotational constants of one of the variational transition states of the methyl radical loss channel, $TS_4(31)$ at R^*_{N-C} = 4.061 Å. The rotational constants are also expected to change as the methylhydrazine ion rearranges to form $[N_2H_2^{+\bullet} + CH_4]$ and thus estimating the transition state rotational constants to be different than those of the methylhydrazine ion ones is correct. The $\Delta S^{\ddagger}$ for the methane loss channel of MH ion ranges from 17.3–20.5 J K^{-1} mol^{-1} (depending on the fit used). $\Delta S^{\ddagger}(30)_{MH}$ does not vary with the internal energy since only one estimated transition state was used to fit the experimental curve of *m/z* 30. The complete list of $\Delta S^{\ddagger}$ values is reported in Tables D.3, D.4 and D.6 in Appendix D.

Table 3.5: Transition States, Entropies of Activation (600 K) and Energies of Activation (0 K) for the Unimolecular Dissociations of the Methylhydrazine Ion in the Internal Energy Range of 1.90–4.00 eV[a]

Dissociation Channel		$CH_2NHNH_2^+ + H^{\bullet}$				
B3-LYP/6-31+G(d)		ΔE^b = 2.418 eV or 233.3 kJ mol^{-1}				
R^* (Å)		1.997	2.097	2.197	2.297	
$\Delta S^{\ddagger c}$ (J K^{-1} mol^{-1})	I_{CH3} = 3.0 amu Å^2	-13.56	-10.39	-7.13	-4.01	
	I_{CH3} = 3.1 amu Å^2	-13.70	-10.52	-7.26	-4.14	
E_0 (eV)		2.347	2.392	2.412	2.419	
corrected to mG3 product energy		ΔE = 2.240 eV or 216.2 kJ mol^{-1}				
R^* (Å)		1.997	2.097	2.197	2.297	
$\Delta S^{\ddagger}$ (J K^{-1} mol^{-1})	I_{CH3} = 3.0 amu Å^2	-13.56	-10.39	-7.13	-4.01	
	I_{CH3} = 3.1 amu Å^2	-13.70	-10.52	-7.26	-4.14	
E_0 (eV)		2.169	2.214	2.234	2.241	
fit 1		ΔE = 2.193 eV or 211.6 kJ mol^{-1}				
R^* (Å)		1.997	2.097	2.197	2.297	2.397
$\Delta S^{\ddagger}$ (J K^{-1} mol^{-1})	I_{CH3} = 3.0 amu Å^2	19.72	23.06	26.46	29.69	32.71
	I_{CH3} = 3.1 amu Å^2	19.58	22.93	26.32	29.55	32.58
E_0 (eV)		2.122	2.167	2.187	2.194	2.195
fit 2		ΔE = 2.201 eV or 212.4 kJ mol^{-1}				
R^* (Å)		1.997	2.097	2.197	2.297	
$\Delta S^{\ddagger}$ (J K^{-1} mol^{-1})	I_{CH3} = 3.0 amu Å^2	22.69	26.02	29.42	32.65	
	I_{CH3} = 3.1 amu Å^2	22.56	25.88	29.28	32.52	
E_0 (eV)		2.130	2.175	2.195	2.202	

Table 3.5: continued

Dissociation Channel		$CH_2NHNH_2^+ + H^\cdot$									
fit 3		ΔE = 2.213 eV or 213.5 kJ mol^{-1}									
R^* (Å)		1.997		2.097		2.197		2.297			
$\Delta S^\ddagger$ (J K^{-1} mol^{-1})	I_{CH3} = 3.0 amu Å^2	25.80		29.21		32.61		35.85			
	I_{CH3} = 3.1 amu Å^2	25.66		29.08		32.48		35.72			
E_0 (eV)		2.142		2.187		2.207		2.214			
Dissociation Channel		$NHNH_2^+ + CH_3^\cdot$									
B3-LYP/6-31+G(d)		ΔE^b = 2.578 eV or 248.7 kJ mol^{-1}									
R^* (Å)		2.461	2.561	2.661	3.061	3.561	3.661	3.761	4.061	4.361	4.461
$\Delta S^\ddagger$ (J K^{-1} mol^{-1})		13.32	16.29	19.31	30.65	42.70	44.86	46.98	53.46	60.20	62.21
E_0 (eV)		2.112	2.184	2.241	2.401	2.514	2.529	2.541	2.566	2.576	2.578
corrected to mG3 product energy		ΔE = 2.725 eV or 262.9 kJ mol^{-1}									
R^* (Å)		2.561	2.661	3.061	3.561	3.661	3.761	4.061	4.561		
$\Delta S^\ddagger$ (J K^{-1} mol^{-1})		16.29	19.31	30.65	42.70	44.86	46.98	53.46	64.21		
E_0 (eV)		2.330	2.388	2.548	2.661	2.675	2.687	2.712	2.725		
fit 1[d]		ΔE = 2.528 eV or 243.9 kJ mol^{-1}									
R^* (Å)		2.561	3.061	3.761	4.061	4.461					
$\Delta S^\ddagger$ (J K^{-1} mol^{-1})		17.24	31.64	52.34	58.83	67.62					
E_0 (eV)		2.134	2.351	2.491	2.516	2.528					
fit 2		ΔE = 2.528 eV or 243.9 kJ mol^{-1}									
R^* (Å)		2.561	3.061	3.761	4.061	4.461					
$\Delta S^\ddagger$ (J K^{-1} mol^{-1})		19.25	33.71	53.52	60.01	68.81					
E_0 (eV)		2.134	2.351	2.491	2.516	2.528					
fit 3		ΔE = 2.528 eV or 243.9 kJ mol^{-1}									
R^* (Å)		2.561	3.061	3.761	4.061	4.461					
$\Delta S^\ddagger$ (J K^{-1} mol^{-1})		20.68	35.18	55.17	61.67	70.47					
E_0 (eV)		2.134	2.351	2.491	2.516	2.528					
Dissociation Channel		$N_2H_2^{+\cdot} + CH_4$[e]									
fit 1[d]											
$\Delta S^\ddagger$ (J K^{-1} mol^{-1})		17.26									
E_0 (eV)		2.350									
fit 2											
$\Delta S^\ddagger$ (J K^{-1} mol^{-1})		20.48									
E_0 (eV)		2.350									
fit 3											
$\Delta S^\ddagger$ (J K^{-1} mol^{-1})		20.48									
E_0 (eV)		2.350									

[a] The present work has been published in Boulanger et al. [91] [b] Energy difference between the equilibrium ion and the plateau on the potential energy curve (energy value taken at R_{C-H} = 2.597 Å and R_{C-N} = 4.561 Å). [c] $\Delta S^\ddagger$ calculated using the rovibrational free rotor model from East and Radom procedure [103] on the calculations of the third-law entropies. Two values for the moment of inertia of the methyl group have been used giving slightly different results. [d] Fit 1 for methyl and methane losses corresponds to fit 1 for hydrogen loss, etc. [e] Rearrangement process, transition state estimated, see text for explanations.

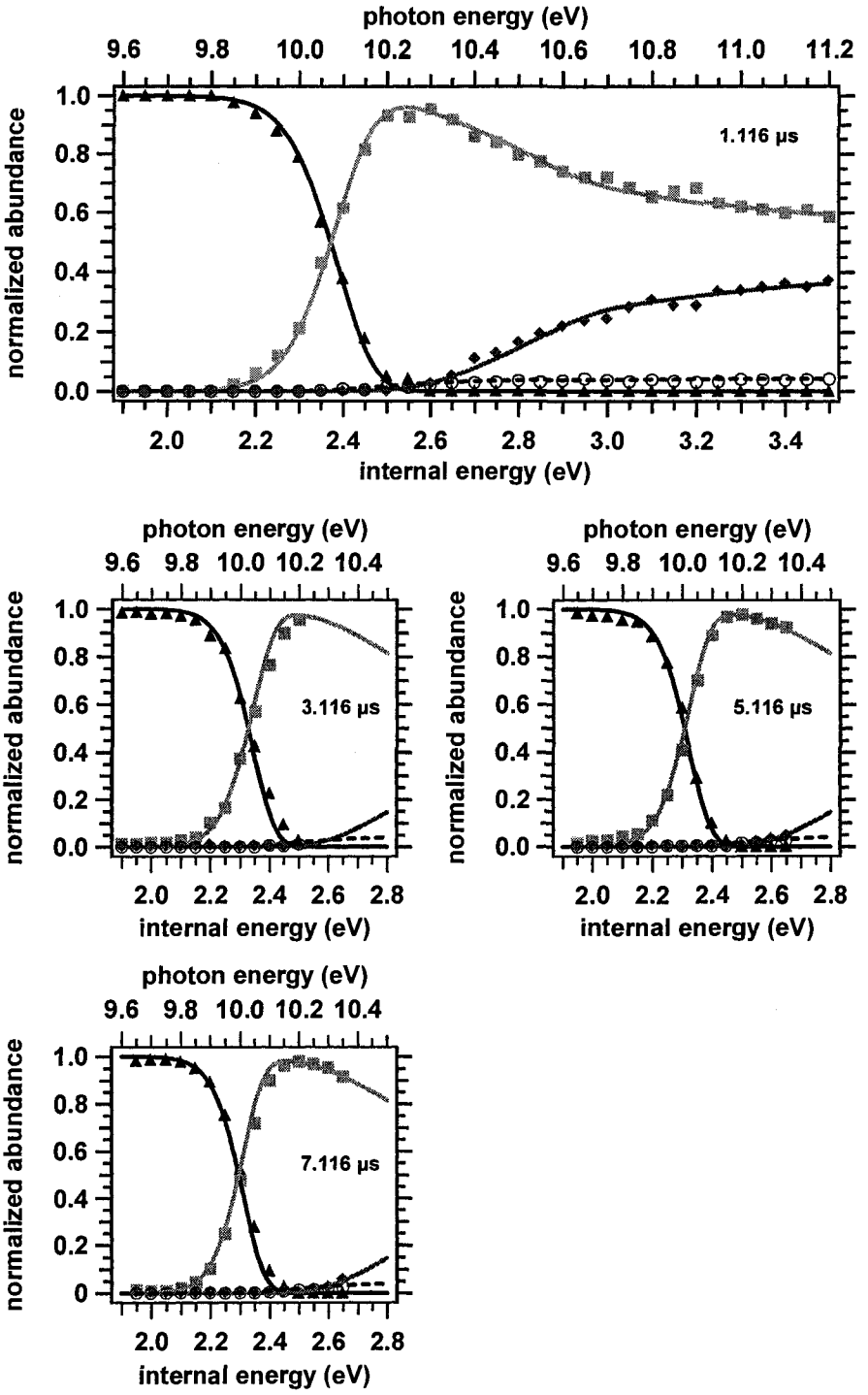

Figure 3.23 – Comparison between the experimental breakdown curve and the theoretical fit (fit 2) using the variational transition states of the hydrogen and methyl losses of the methylhydrazine ion. The parent ion *m/z* 46 is represented by ▲, the fragment ion *m/z* 45 by ■, the fragment ion *m/z* 31 by ♦ and the fragment ion *m/z* 30 is represented by ○. The theoretical fits are represented by the solid lines (black for parent ion *m/z* 46, light grey for fragment ion *m/z* 45 and dark grey for fragment ion *m/z* 31) and by a black dashed line for the fragment ion *m/z* 30.

3.5.3 Tetramethylhydrazine

The value of the adiabatic ionization energy (IE_a) employed to calculate the internal energy range of each breakdown curve was found to have a significant impact on the fit of the breakdown curves and on the values of the enthalpy of formation of the product ions. Meot-Ner et al. [108] have reported experimental IE_a for methylhydrazine and tetramethylhydrazine ions: 7.70 ± 0.15 eV for MH and 6.78 ± 0.04 eV for TMH. Their methylhydrazine IE_a agrees well with our mG3 calculated IE_a of 7.64 eV [109]. However, their value for tetramethylhydrazine is ~ 0.25 eV lower than our calculated mG3 IE_a of 7.02 eV [105]. Depending on the IE_a value used, the internal energy range is shifted by ~ 0.25 eV. We found during our fitting process of the breakdown curves of the TMH ion that the calculated mG3 IE_a produced product ion enthalpies of formation more in line with theory than the experimental IE_a determined by Meot-Ner et al. [108] (see Table 4.5 in Chapter 4). We cannot explain the discrepancy between our calculated mG3 IE_a and the experimental IE_a reported by Meot-Ner et al. [108]. The calculated (mG3) IE_a [105, 109] for methylhydrazine and 1,1-dimethylhydrazine agree with their reported values and gave product ion enthalpies of formation consistent with theory.

The VTST procedure was also used to fit the tetramethylhydrazine ion breakdown curves. Four good fits were found using IE_a = 7.02 eV and are summarized in Table 3.6 and one of the fits is shown in Figure 3.24. Only small changes were needed to the energy of the potential energy curves relative to the mG3 results to obtain satisfactory fits. Four good fits (fits 5–8) were found using the experimental IE_a = 6.78 ± 0.04 eV and are listed in Table 3.7. The same variational transition states were identified for these fits as for fits 1–4, the only difference being in the E_0 values. At the B3-LYP/6-31+G(d) level of theory, at $E_{int} \approx$

1.60 eV, $\Delta S^{\ddagger}(73)_{TMH}$ for the loss of a methyl radical is 18 J K^{-1} mol^{-1} and decreases to 5 J K^{-1} mol^{-1} at E_{int} = 4.00 eV. These $\Delta S^{\ddagger}$ values are much lower than the entropies of activation calculated for the same dissociation channel in methyl- and 1,1-dimethylhydrazine ions. As mentioned previously, the entropies of activation will be discussed in more details in Chapter 4. The complete list of entropies of activation is reported in Tables D.5 and D.6 in Appendix D.

The methane loss channel was fitted by estimating the transition state vibrational frequencies from the TMH ion ones. As for the methane loss channel in MH ion, the rotational constants were also estimated using the ones from the lowest energy variational transition state of the methyl radical loss from TMH ion, $TS(73)_5$ at R^*_{N-C} = 2.766 Å. Since the methane loss reaction necessarily involves a rearrangement, it is curious that two very distinct transition states were needed to obtain a satisfactory fit to the experimental data for this channel. Methane loss is a fairly minor process and so it is possible that the need for two transition states is simply an artefact of the fitting procedure. If it is not, though, it could indicate that the reaction proceeds via two distinct mechanisms depending on the internal energy. For the methane loss channel (fragment ion *m/z* 72), the entropy of activation decreases from 12-14 J K^{-1} mol^{-1} between E_{int} = 1.80 to ~ 3.30 eV to approximately -19 to -25 J K^{-1} mol^{-1} between $E_{int} \approx$ 3.30 to 4.00 eV. From the fits of the breakdown curves, the enthalpy of formation of fragment ion *m/z* 72 was determined and two isomers (i.e., isomers VI and VII) were considered more plausible than the others as it will be explained in Section 4.3 in Chapter 4.

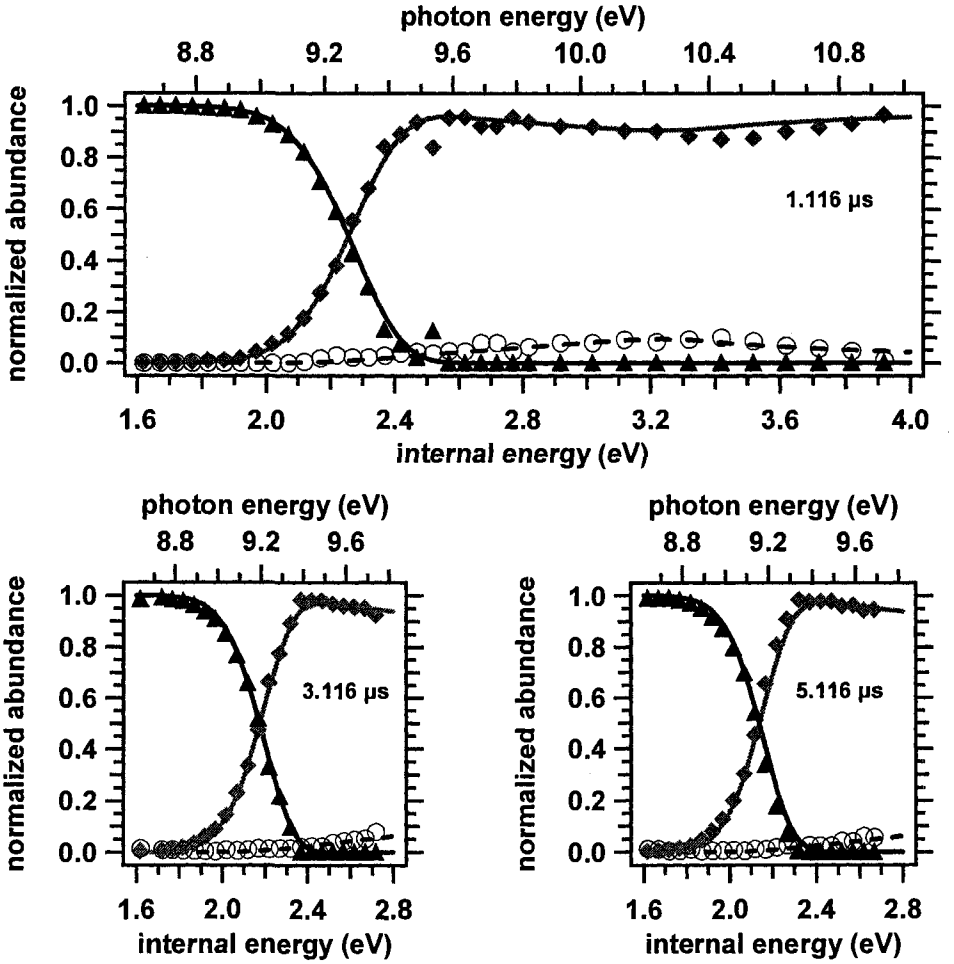

Figure 3.24 – Comparison between the experimental breakdown curves and the theoretical fit (fit 2) using the variational transition states of the methyl loss of the tetramethylhydrazine ion. The parent ion *m/z* 88 is represented by ▲, the fragment ion *m/z* 73 by ♦ and the fragment ion *m/z* 72 by ○. The theoretical fits are represented by the solid lines (black for parent ion *m/z* 88 and dark grey for ion *m/z* 73) and a black dashed line for fragment ion *m/z* 72.

Table 3.6: Transition States, Entropies of Activation (600 K) and Energies of Activation (0 K) for the Unimolecular Dissociations of the Tetramethylhydrazine Ion in the Internal Energy Range of 1.60–4.00 eV[a,b]

Dissociation Channel	$(CH_3)_2NNCH_3^+ + CH_3^\bullet$			
B3-LYP/6-31+G(d)	ΔE^c = 1.706 eV or 165 kJ mol^{-1}			
R^* (Å)	2.366	2.466	2.666	2.766
$\Delta S^{\ddagger}$ [d] (J K^{-1} mol^{-1})	5.12	8.48	14.14	17.52
E_0 (eV)	1.650	1.675	1.694	1.698
corrected to mG3 product energy	ΔE = 1.757 eV or 170 kJ mol^{-1}			
R^* (Å)	2.366	2.466	2.766	
$\Delta S^{\ddagger}$ (J K^{-1} mol^{-1})	5.12	8.48	17.52	
E_0 (eV)	1.701	1.726	1.749	
fit 1[e]	ΔE = 1.816 eV or 175 kJ mol^{-1}			
R^* (Å)	2.366	2.466	2.766	
$\Delta S^{\ddagger}$ (J K^{-1} mol^{-1})	25.10	28.47	37.51	
E_0 (eV)	1.760	1.785	1.808	
fit 2	ΔE = 1.806 eV or 174 kJ mol^{-1}			
R^* (Å)	2.366	2.466	2.766	
$\Delta S^{\ddagger}$ (J K^{-1} mol^{-1})	24.03	27.39	36.44	
E_0 (eV)	1.750	1.775	1.798	
fit 3	ΔE = 1.831 eV or 177 kJ mol^{-1}			
R^* (Å)	2.366	2.466	2.766	
$\Delta S^{\ddagger}$ (J K^{-1} mol^{-1})	26.25	29.61	38.66	
E_0 (eV)	1.775	1.800	1.823	
fit 4	ΔE = 1.791 eV or 173 kJ mol^{-1}			
R^* (Å)	2.366	2.466	2.766	
$\Delta S^{\ddagger}$ (J K^{-1} mol^{-1})	23.02	26.39	35.43	
E_0 (eV)	1.735	1.760	1.783	
Dissociation Channel	$C_3H_8N_2^{+\bullet} + CH_4$			
fit 1[e]				
estimated TS[f]	1	2		
$\Delta S^{\ddagger}$ (J K^{-1} mol^{-1})	14.16	-18.76		
E_0 (eV)	2.000	1.500		
fit 2				
estimated TS	1	2		
$\Delta S^{\ddagger}$ (J K^{-1} mol^{-1})	11.78	-24.62		
E_0 (eV)	2.000	1.400		
fit 3				
estimated TS	1	2		
$\Delta S^{\ddagger}$ (J K^{-1} mol^{-1})	12.94	-23.28		
E_0 (eV)	2.000	1.400		
fit 4				
estimated TS	1	2		
$\Delta S^{\ddagger}$ (J K^{-1} mol^{-1})	11.78	-25.39		
E_0 (eV)	2.000	1.400		

[a] The present work has been published in Boulanger et al. [91]. [b] Internal energy range when IE_a = 7.02 eV [105]. [c] Energy difference between the equilibrium ion and the plateau on the potential energy surface (energy value taken at R_{C-N} = 3.266 Å). [d] $\Delta S^{\ddagger}$ values calculated using the rovibrational FR model of East and Radom [103]. [e] Fit 1 for methyl loss corresponds to fit 1 for methane loss, etc. [f] Estimated TS 1 ranging from E_{int} = 1.60 eV to ~ 3.20–3.40 eV and estimated TS 2 from $E_{int} \approx$ 3.20–3.40 to 4.00 eV.

Table 3.7: Transition States, Entropies of Activation (600 K) and Energies of Activation (0 K) for the Unimolecular Dissociation of the Tetramethylhydrazine Ion at the B3-LYP/6-31+G(d) Level of Theory in the Internal Energy Range of 1.800–4.000 eV using IE_a = 6.78 ± 0.04 eV [108]

Dissociation Channel	$(CH_3)_2NNCH_3^+ + CH_3^\bullet$			
fit 5[a]	ΔE^a = 2.006 eV or 194 kJ mol^{-1}			
R^* (Å)	2.366	2.466	2.766	
$\Delta S^\ddagger$ (J K^{-1} mol^{-1})	28.81	32.18	41.22	
E_0 (eV)	1.950	1.975	1.998	
fit 6	ΔE = 2.016 eV or 195 kJ mol^{-1}			
R^* (Å)	2.366	2.466	2.666	2.766
$\Delta S^\ddagger$ (J K^{-1} mol^{-1})	29.52	32.88	38.55	41.93
E_0 (eV)	1.960	1.985	2.004	2.008
fit 7	ΔE = 2.037 eV or 197 kJ mol^{-1}			
R^* (Å)	2.366	2.466	2.766	
$\Delta S^\ddagger$ (J K^{-1} mol^{-1})	31.03	34.40	43.44	
E_0 (eV)	1.981	2.006	2.029	
fit 8	ΔE = 2.058 eV or 199 kJ mol^{-1}			
R^* (Å)	2.366	2.466	2.566	2.766
$\Delta S^\ddagger$ (J K^{-1} mol^{-1})	32.70	36.06	39.09	45.11
E_0 (eV)	2.002	2.027	2.039	2.050

[a] Energy difference between the equilibrium ion and the plateau on the potential energy surface (energy value taken at R_{C-N} = 3.266 Å).

3.6 Summary

The lowest energy dissociation channels of the methyl-, 1,1-dimethyl- and tetramethylhydrazine ions have been investigated using TPEPICO spectroscopy, tandem mass spectrometry and VTST. The methylhydrazine ion dissociates by losing a hydrogen atom to form fragment ion *m/z* 45, $CH_2NHNH_2^+$, a methyl group to form fragment ion *m/z* 31, $NHNH_2^+$, and by rearranging to lose methane and form fragment ion *m/z* 30, $N_2H_2^{+\bullet}$. The 1,1-dimethylhydrazine ion has two low energy dissociation channels: the loss of a methyl radical to form the fragment ion *m/z* 45, $CH_3NNH_2^+$, and the loss of a hydrogen atom to form the fragment ion *m/z* 59, $(CH_3)(CH_2)NNH_2^+$. The tetramethylhydrazine ion dissociates by losing a methyl radical to form fragment ion *m/z* 73, $(CH_3)_2NNCH_3^+$, and by losing methane to form fragment ion *m/z* 72, $C_3H_8N_2^{+\bullet}$. Variational transition state theory was used

to locate the transition states of the unimolecular dissociation reactions (methyl and hydrogen losses) which were then used to reproduce the TPEPICO breakdown diagrams. The transition states of the rearrangement processes (methane loss) were estimated in the fitting procedure. Only small adjustments were needed to fit the experimental results. In the case of 1,1-dimethylhydrazine ion, it was not possible to reproduce the experimental change in product ion abundance with internal energy employing a single transition state for each channel. In the photon energy range (threshold to ~ 32 eV) used to study the dissociation of the methyl-substituted hydrazine ions, between eighteen and twenty-five fragment ions were observed and their appearance energies have been reported.

Chapter 4

ENTROPIES OF ACTIVATION AND THERMOCHEMISTRY

4.1 Introduction

The fitting of the experimental breakdown curves allowed us to examine the impact that the entropy of activation has on simple dissociation reactions such as bond cleavages. The three methyl-substituted hydrazine ions undergo simple bond cleavage and rearrangement processes ($H^{\bullet}$, $CH_3^{\bullet}$ and/or CH_4 losses) which exhibit significant entropy effects. By modeling the ion decomposition as a function of internal energy with a simple VTST treatment, it was possible to study in depth the impact of $\Delta S^{\ddagger}$ on the competing dissociation channels of the hydrazine ions. The large changes in $\Delta S^{\ddagger}$ with increasing internal energy were found to affect the shape of the breakdown curves and their variational fits. The modeling further permitted the determination of reliable enthalpies of formation for the observed fragment ions. The entropies of activation and the thermochemistry that could be retrieved from the theoretical fits will be discussed in more detail in this chapter.

4.2 Entropies of activation

The entropy of activation, $\Delta S^{\ddagger}$, is simply the difference in entropy between the reactant ion and its transition state and it is a convenient way to describe the nature of a reaction. A loose transition state, typically corresponding to simple bond cleavage, has a positive entropy of activation because the transition state is less ordered than the reactant ion. A tight transition state on the other hand typically goes along with a rearrangement

process and can have a negative entropy of activation because it is often more ordered than the reactant ion. Calculating the entropy of activation is also a convenient method for reducing the large number of vibrational frequencies of the reactant ion and its transition state into a single parameter.

As explained previously in Chapters 1 and 2, the transition states for the unimolecular dissociation reactions have been located using the variational transition state theory approach. The transition state structures were optimized at the B3-LYP/6-31+G(d) level of theory. The vibrational frequencies of these transition states have been used to calculate the entropies of activation discussed below.

4.2.1 Computation of the entropies of activation

The entropies (absolute, S, and of activation, $\Delta S^{\ddagger}$) were computed using the East and Radom procedure [103] as explained in Chapter 2. They proposed two different approaches to calculate the third-law entropies: the harmonic oscillator (HO) and the free rotor (FR) models. In the harmonic oscillator model, all the vibrational modes were considered as harmonic oscillators. The methyl torsion modes which are the lowest vibrational modes in the three hydrazine ions were treated separately and their contribution to the absolute entropy of the ion or transition state was calculated using the torsional vibrational temperature constant θ_{vib} (equation 2.15 in Chapter 2). In the free rotor model, the methyl groups were separately treated as free rotors and thus these torsion modes were calculated using the rotor rotational temperature constant θ_{rot} (equation 2.16 in Chapter 2). The θ_{vib} constant is based on the torsional harmonic frequency of the methyl group while the θ_{rot} constant is based on the methyl rotor's reduced moment of inertia. The HO and FR

approaches will yield different entropy values as shown in Tables 4.1 and 4.2 for hydrogen loss from MH and DMH ions (4.1) and for the methyl radical loss from methylhydrazine ion (4.2). The free rotor ΔS_{rovib} values reported in these two tables are also reported in Tables 3.3, 3.5 and 3.6 as the entropies of activation for the different dissociation channels.

Table 4.1: Comparison of the Entropies of Activation (at 600 K, in J K^{-1} mol^{-1}), at the B3-LYP/6-31+G(d) Level of Theory, for Hydrogen Atom Loss from MH and DMH Ions using Different Methods[a]

Ion	R^*_{H-C} (Å)	harmonic oscillator				free rotor			
		ΔS_{vib}		ΔS_{rovib}		ΔS_{vib}		ΔS_{rovib}	
		A	B	A	B	A	B[b]	A	B[b]
MH	2.297	3.27	3.21	4.16	4.10	3.27	-4.90	4.16	-4.01[c]
							-5.04		-4.14
	2.197	0.30	0.24	1.04	0.98	0.30	-7.87	1.04	-7.13
							-8.00		-7.26
	2.097	-2.82	-2.88	-2.22	-2.28	-2.82	-10.99	-2.22	-10.39
							-11.12		-10.52
	1.997	-5.88	-5.94	-5.40	-5.46	-5.88	-14.04	-5.40	-13.56
							-14.18		-13.70
DMH	2.298	5.37	5.31	5.58	5.53	7.70	-1.63	7.92[c]	-1.41
							-1.76		-1.54
	2.198	2.12	2.06	2.27	2.21	4.31	-5.02	4.46	-4.87
							-5.15		-5.00
	2.098	-1.23	-1.29	-1.13	-1.19	0.76	-8.57	0.86	-8.47
							-8.70		-8.61

[a] In method A, the methyl group losing a H atom in the parent ion and its TS is not considered as a free rotor whereas in method B we considered the methyl groups as free rotors only in the parent ions. The entropies have been calculated using East and Radom [103] procedure for the computation of third-law entropies. [b] The moments of inertia were estimated to be between 3.0 and 3.1 amu $Å^2$ and were taken from Table 7 in East and Radom [103] procedure. In method B, they gave slightly different $\Delta S^{\ddagger}$ values. [c] Same results as those reported in Tables 3.3 and 3.5 in Chapter 3 [91, 92].

The entropies for hydrogen atom loss were calculated with two different methods for each approach (i.e., HO or FR). The leaving hydrogen atom is coming from a methyl group in both parent ions. Thus, that methyl group cannot be considered a free rotor. In method A, the methyl group losing a hydrogen atom in the parent ion (MH or DMH ion) and in the transition state is not considered a free methyl rotor. Its contribution to the entropy is calculated like all the other vibrational modes using the statistical entropy equations

(equations 2.13 and 2.14 in Chapter 2). In method B, the same methyl group losing a hydrogen atom is considered to be a free methyl rotor in the parent ion but not in the TS. It is thus not surprising that method A gives the same entropies of activation for the methylhydrazine ion, ΔS_{vib} and ΔS_{rovib}, in both HO and FR approaches since all the vibrational modes are treated as harmonic oscillators. In method B however, the methyl group is considered as a free rotor only in the parent ion and this has an effect on the ΔS value. Also, the entropies of activation in the FR model are always lower than those obtained with the HO model, by almost 10 J K^{-1} mol^{-1}. For example, ΔS_{rovib} for TS_1 = 2.297 Å is 4.10 J K^{-1} mol^{-1} with the HO approach while it is equal to -4.01 J K^{-1} mol^{-1} with the FR approach. The ΔS_{rovib} values are always larger than the ΔS_{vib} values in both methods. In the 1,1-dimethylhydrazine ion, there are two methyl groups one of which is losing a hydrogen atom. In the harmonic oscillator approach, methods A and B give essentially the same ΔS values. In the free rotor approach though, the method used (A vs B) will yield different values of ΔS.

Table 4.2: Comparison of the Entropies of Activation (at 600 K, in J K^{-1} mol^{-1}), at the B3-LYP/6-31+G(d) Level of Theory, for the Methyl Radical Loss from the MH Ion[a]

R^*_{N-C} (Å)	harmonic oscillator		free rotor	
	ΔS_{vib}	ΔS_{rovib}	ΔS_{vib}	ΔS_{rovib}[b]
4.461	63.60	76.63	49.21	62.24
4.361	61.50	74.25	47.46	60.20
4.061	53.89	65.73	41.62	53.46
3.761	47.94	58.76	36.17	46.98
3.661	46.08	56.54	34.40	44.86
3.561	44.24	54.32	32.61	42.70
3.061	34.64	42.73	22.56	30.65
2.661	23.40	29.72	13.00	19.31
2.561	19.34	25.19	10.44	16.29
2.461	15.07	20.45	7.94	13.32

[a] The two approaches are the harmonic oscillator approach and the free rotor approach which are explained in Chapter 2 and in East and Radom paper [103]. [b] Same results as those reported in Table 3.5 in Chapter 3 [91].

ΔS values for the methyl radical loss for all the hydrazine ions were calculated using both HO and FR approaches. All the methyl groups were treated separately as torsion (in the HO approach) or as a free rotor (in the FR approach).

4.2.2 Changes in $\Delta S^{\ddagger}$ with internal energy

The $\Delta S^{\ddagger}$ values discussed in this section correspond to the values obtained from the three or four good fits of the experimental breakdown curves listed in Tables 3.3, 3.5 and 3.6 in Chapter 3. Some transition state structures for the methyl radical loss channel are shown in Figure 4.1 for the three methyl-substituted hydrazine ions. In the methylhydrazine ion (top panel), the first transition state is found at an N–C bond distance of R^*_{N-C} = 4.461 Å. As the internal energy increases, the TS moves to shorter N–C bond distance; the highest energy transition state (TS_5) is found at R^*_{N-C} = 2.561 Å. At large N–C bond distances, the leaving methyl group ($CH_3^{\bullet}$) can freely rotate about its principal axis of symmetry. The transition state is thus less ordered than the reactant ion and the calculated entropy of activation is large, $\Delta S^{\ddagger}$ = 68-70 J K^{-1} mol^{-1}. At shorter N–C bond distances, the transition state gets more ordered and this is reflected by a decrease in the entropy of activation value: at R^*_{N-C} = 2.561 Å, $\Delta S^{\ddagger}$ = 17-21 J K^{-1} mol^{-1}. The transition states for methyl radical loss from 1,1-dimethylhydrazine ions behave similarly as those found for methylhydrazine ions. The transition states are located essentially at the same N–C bond distances and the values of $\Delta S^{\ddagger}$ are also very similar. For example, in 1,1-dimethylhydrazine ion, the first (low energy) TS is found at an N–C bond distance of R^*_{N-C} = 4.265 Å and the entropy of activation is equal to 65 J K^{-1} mol^{-1} (Figure 4.1, middle panel). As the internal energy

increases, the TS moves to shorter N–C bond distance and the entropy of activation decreases to 19 J K^{-1} mol^{-1} at R^*_{N-C} = 2.565 Å.

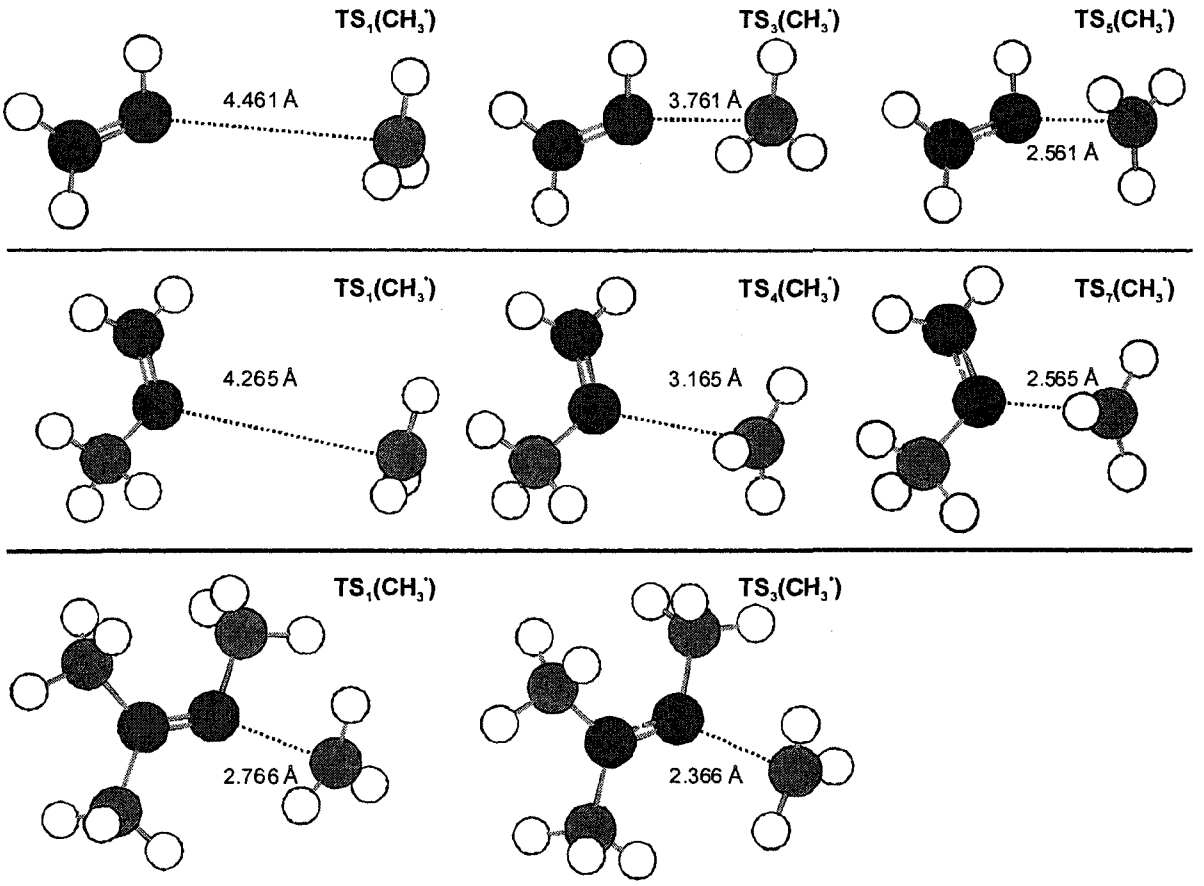

Figure 4.1 – Transition states for the methyl loss channel of methylhydrazine ion (top), 1,1-dimethylhydrazine ion (middle) and tetramethylhydrazine ion (bottom). The nitrogen atoms are dark grey, the carbon atoms are light grey and the hydrogen atoms are white.

In the tetramethylhydrazine ion however, the ensemble of transition states is found to be more ordered than those of the methyl- and 1,1-dimethylhydrazine ions. The TS are found at shorter N–C bond distances between R^*_{N-C} = 2.766 Å and R^*_{N-C} = 2.366 Å (Figure 4.1, bottom panel). In TMH, the values of the entropy of activation are ranging from 35-39 to 23-26 J K^{-1} mol^{-1}. Thus, at a similar N–C bond distance, the entropy of activation of the TMH ion is larger than that of the MH or DMH ions by ~ 10 J K^{-1} mol^{-1}. In the TMH ion, as

one of the methyl groups is pulled away from the ion, the other methyl groups around the hydrazine backbone become freer to rotate which is not the case in methylhydrazine ion nor as important in the 1,1-dimethylhydrazine ion. The changes in the entropies of activation as a function of the N–C bond distance are shown graphically in Figure 4.2(a). As the transition state shifts to shorter N–C bond distances, the $\Delta S^{\ddagger}$ values decrease accordingly.

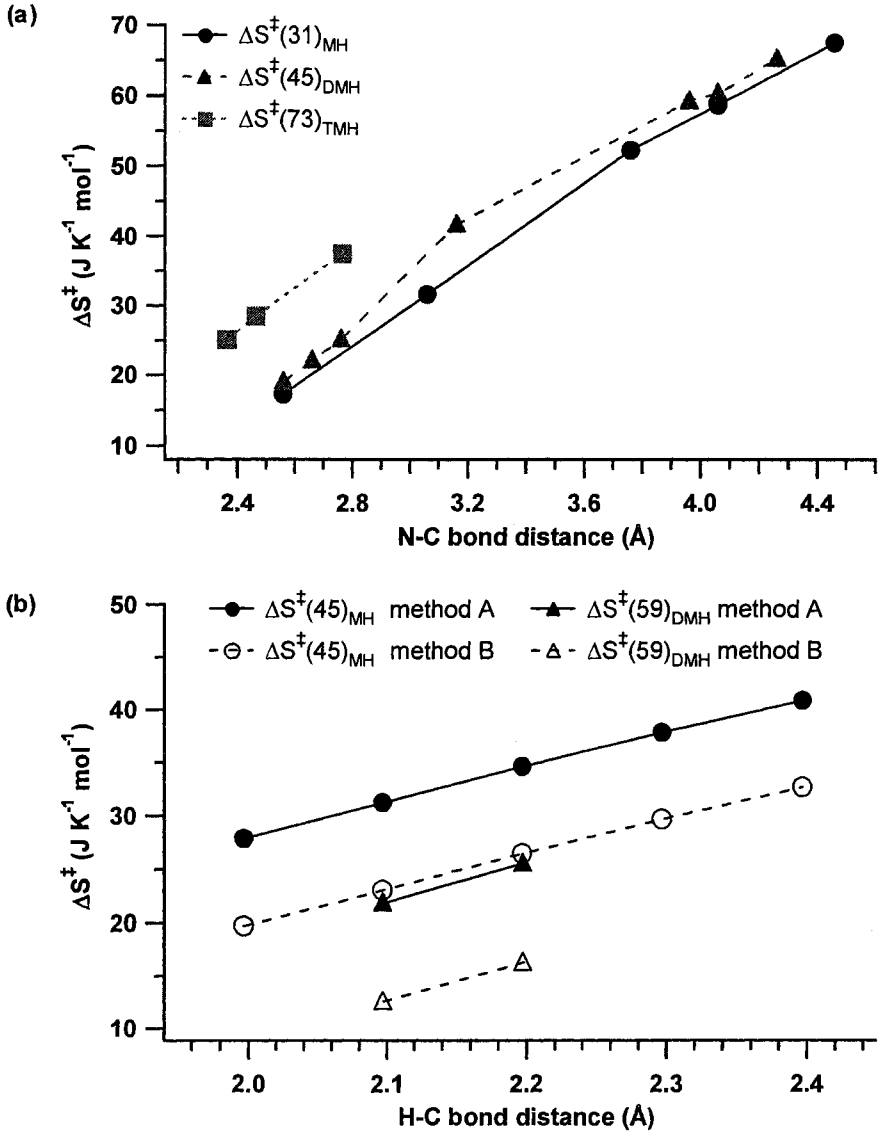

Figure 4.2 – Variation of the entropy of activation as a function of the bond distance for (a) the methyl radical loss channel and (b) the hydrogen atom loss channel. The $\Delta S^{\ddagger}_{rovib}$ values were taken from the first fit of each hydrazine ion. See Tables 3.3, 3.5 and 3.6 for details.

Fewer transition states have been located for the hydrogen atom loss reactions for both methyl- and 1,1-dimethylhydrazine ions over the same internal energy range. Some structures are shown in Figure 4.3 (MH ion in top panel, DMH ion in bottom panel). The entropies of activation for this channel are also much smaller than those calculated for the methyl radical loss channel. For example, in the methylhydrazine ion, the entropies of activation range from 30-36 J K^{-1} mol^{-1} at R^*_{N-C} = 2.297 Å to 20-26 J K^{-1} mol^{-1} at R^*_{N-C} = 1.997 Å, as the internal energy increases (Table 3.5). Moreover, these TS are much more ordered than those of the methyl radical loss channel. The hydrogen is coming from a methyl group and prevents this methyl group from being a true free rotor. Also, the TS structures are very similar to the parent ion structure. In Figure 4.2(b), the variation of $\Delta S^{\ddagger}$ in the MH and DMH ions, as a function of the H–C bond distance, is shown for both methods A and B (see above for explanations).

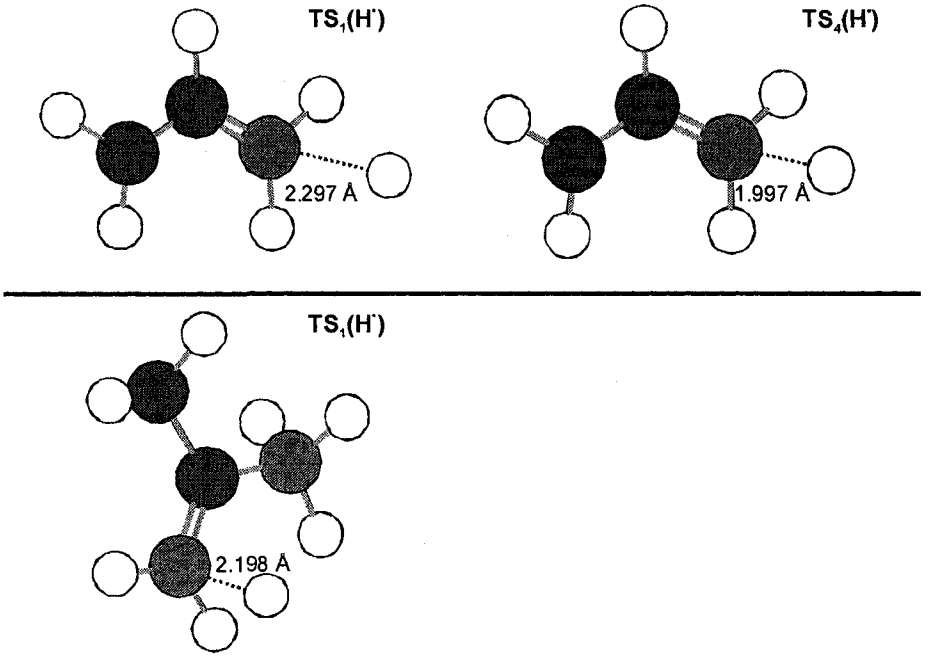

Figure 4.3 – Some transition states for the hydrogen loss channel of methylhydrazine (top) and 1,1-dimethylhydrazine (bottom) ions. The nitrogen atoms are dark grey, the carbon atoms are light grey and the hydrogen atoms are white.

4.2.3 Evaluation of $\Delta S^{\ddagger}$ in the rearrangement processes leading to methane loss

The transition state(s) for the rearrangement processes leading to the loss of a methane molecule in the methyl- and tetramethylhydrazine ions were estimated as explained previously in the preceding chapters. In both processes, the transition state vibrational frequencies were approximated to be the same as those of the parent ion. One vibrational mode, involving a N–C stretch, was removed and considered as the reaction coordinate, and then the five lowest vibrational frequencies were scaled until a good agreement with the experimental fragment curve was obtained. In the dissociation of the methylhydrazine ion into $N_2H_2^{+\bullet}$ + CH_4, there were three possible fragment ions: the cis- and trans-diazene ions, $HNNH^{+\bullet}$, and the iso-diazene ion, $NNH_2^{+\bullet}$. The dissociation process involved some rearrangement where a hydrogen atom moved to the carbon end to form a methane molecule:

$$CH_3NHN\underline{H}_2^{+\bullet} \rightarrow [CH_4\text{—}NHNH^{+\bullet}]^{\ddagger} \rightarrow HNNH^{+\bullet} + CH_4 \qquad (4.1)$$

$$CH_3N\underline{H}NH_2^{+\bullet} \rightarrow [CH_4\text{—}NNH_2^{+\bullet}]^{\ddagger} \rightarrow NNH_2^{+\bullet} + CH_4 \qquad (4.2)$$

In this case, the rearrangement reaction was a minor process, with $\Delta S^{\ddagger}(30)_{MH} \approx 17$–$21$ J K^{-1} mol^{-1}. The entropy of activation for the methane loss channel is lower than the $\Delta S^{\ddagger}$ values calculated for the two unimolecular dissociation pathways thus reflecting a tighter dissociation process which is expected for a rearrangement process: $\Delta S^{\ddagger}(45)_{MH}$ = 20-26 to 30-36 J K^{-1} mol^{-1} and $\Delta S^{\ddagger}(31)_{MH}$ = 17-21 to 68-70 J K^{-1} mol^{-1} (values taken from fits 1–3). The fact that the values are still positive is likely a reflection of the participation of a loosely-bound complex in the dissociation pathway.

Conversely, in the case of the tetramethylhydrazine ion, the rearrangement process could be more complex than in the methylhydrazine ion. Nine different structures for

fragment ion *m/z* 72, $C_3H_8N_2^{+\bullet}$, were considered and are shown in Figure 3.13. Formation of the first three isomers I–III only involve a hydrogen shift reaction just like that for the MH ion dissociation, followed by an N–C bond cleavage. Forming isomers IV and V involves more complex rearrangement with both carbon and hydrogen atom migration. The four cyclic isomers VI–IX would require the most extensive rearrangement, especially in the case of isomer VIII (five-membered ring structure) and isomer IX (four-membered ring structure). During the fitting of the experimental fragment curve *m/z* 72, two estimated transition states had to be used in order to reproduce the experimental data. The entropy of activation was found to vary significantly between the two transition states, $\Delta S^{\ddagger}(72) \approx 12\text{-}14$ J K^{-1} mol^{-1} for TS_1 and $\Delta S^{\ddagger}(72) \approx -19$ to -25 J K^{-1} mol^{-1} for TS_2 (Table 3.7). As explained previously, this need of two TS could be an artefact of the fitting procedure. A thorough computational analysis of the dissociation pathway would be needed to fully understand it. It is important to remember that the entropy of activation depends strongly on the values of the vibrational frequencies of the parent ion and its transition state.

4.3 Enthalpies of formation

The $\Delta_f H$ values for all the observed fragment ions of the methyl-substituted hydrazine ions have been determined from the variational fits of the breakdown curves and from the mG2 and mG3 calculations. The enthalpies of formation have been determined from the following equations [85]:

$$AB + e^- \rightarrow AB^{+\bullet} + 2e^- \qquad (4.3)$$

$$AB^{+\bullet} \rightarrow A^+ + B^\bullet \qquad (4.4)$$

$$\Delta_f H_0(A^+) = E_0(A\text{–}B^{+\bullet}) + \Delta_f H_0(AB^{+\bullet}) - \Delta_f H_0(B^\bullet) \qquad (4.5)$$

The $\Delta_f H_0$ of the parent ion $AB^{+\bullet}$ and neutral fragment $B^{\bullet}$ were taken from our mG3 calculations. To calculate $\Delta_f H_0$ from the VTST results, the E_0 for the transition state found at the lowest internal energy studied was used. This value will technically always be lower than the true thermochemical threshold since the transition states do not sit at products. The uncertainty in the enthalpy of formation takes into account the uncertainties in the IE_a value, the E_0 values and the photon energy. The enthalpies of formation of the various observed fragment ions will be discussed in the following order: those generated from the DMH ion first, followed by those of the MH ion and finally the fragment ions of the TMH ion. The $\Delta_f H$ values are listed in Tables 4.4 (DMH), 4.5 (MH) and 4.6 (TMH) along with previously reported values. The neutral fragment (i.e., $H^{\bullet}$, $CH_3^{\bullet}$ and CH_4) $\Delta_f H$ values are reported in Table 4.3.

The derived $\Delta_f H_0$ of $(CH_3)(CH_2)NNH_2^+$, fragment ion *m/z* 59 from 1,1-dimethylhydrazine ion, compares well with the calculated mG2 and mG3 values, 822 ± 7 vs 820 and 825 kJ mol^{-1}, respectively. All of these values are lower than the 845 kJ mol^{-1} reported by Dibeler et al. [48], based upon electron ionization studies of 1,1-dimethylhydrazine and trimethylhydrazine. Akopyan and Vilesov [110] obtained a value of 820 kJ mol^{-1}. The VTST/experimentally derived $\Delta_f H_0$ value for $CH_3NNH_2^+$, fragment ion *m/z* 45, is 906 ± 6 kJ mol^{-1} and agrees well with the calculated mG2 and mG3 $\Delta_f H_0$ values of 904 and 911 kJ mol^{-1}, respectively. These values are higher than the 883 kJ mol^{-1} reported by Dibeler et al. [48]. The $\Delta_f H$ value of Burgers et al. [1], 768 kJ mol^{-1}, and that of Akopyan and Vilesov [110], 787 kJ mol^{-1}, are more than 100 kJ mol^{-1} lower than our calculated values as their AEs were measured to be more than 1 eV lower than the present results (see Table C.1 in Appendix C for AE values). In a later study, the group of Burgers [4] re-investigated

the appearance energies and enthalpies of formation of the fragment ions of the methyl-substituted hydrazine ions and found that their previous values were erroneous due to contamination from traces of amines. They reported new $\Delta_f H$ values for both fragment ions of 1,1-dimethylhydrazine ion: 820–849 kJ mol^{-1} for $(CH_3)(CH_2)NNH_2^+$ and 883 ± 21 kJ mol^{-1} for $CH_3NNH_2^+$ [4].

The derived $\Delta_f H_0$ of $CH_2NHNH_2^+$, using the mG3 IE_a = 7.64 eV [105, 109] to fit the breakdown curve of ionized methylhydrazine, gave a value of 862 ± 5 kJ mol^{-1} which is in very good agreement with our calculated mG3 value of 864 kJ mol^{-1} and our calculated mG2 value of 859 kJ mol^{-1}. For the fragment ion *m/z* 45 from the methylhydrazine ion, Dibeler et al. [48] reported a $\Delta_f H$ that is 5–10 kJ mol^{-1} lower than our determined values. However, they did not suggest any structure for this ion. Burgers et al. [1] reported a $\Delta_f H_0$ for $CH_2NHNH_2^+$ of 816 kJ mol^{-1} based on its appearance energy from the 2-hydrazinoethanol ion (AE = 9.1 eV) [1] which is 48 kJ mol^{-1} lower than our calculated mG3 enthalpy of formation and 43 kJ mol^{-1} lower than our mG2 $\Delta_f H_0$. The group [4] later reported a revised $\Delta_f H_0$ for $CH_2NHNH_2^+$, 854 ± 21 kJ mol^{-1}, which is only 10 kJ mol^{-1} lower than our mG3 value (or 5 kJ mol^{-1} lower than our mG2 value). Nguyen [3] calculated the $\Delta_f H_{298}$ of $CH_2NHNH_2^+$ to be 860 ± 12 kJ mol^{-1} at the MP4SDTQ/6-311++G(2d,2p) level of theory which is 14 kJ mol^{-1} higher than our calculated 298 K mG3 value of 846 kJ mol^{-1} (and 19 kJ mol^{-1} higher than our calculated 298 K mG2 value of 841 kJ mol^{-1}).

For the fragment ion *m/z* 31 ($NHNH_2^+$), the $\Delta_f H_0$ was calculated from the VTST fits to be 959 ± 5 kJ mol^{-1} which is 18 kJ mol^{-1} lower our calculated mG3 $\Delta_f H_0$ of 976 kJ mol^{-1}. However, this VTST value is in better agreement with our calculated mG2 $\Delta_f H_0$ of 969 kJ mol^{-1}. The discrepancy between the mG2 and mG3 values will be discussed at the end of

this chapter. Dibeler et al. [48] reported a $\Delta_f H$ of 992 kJ mol^{-1} that is 16 to 33 kJ mol^{-1} higher than our $\Delta_f H_0$ values. van Garderen et al. [4] derived the $\Delta_f H_{298}$ of $N_2H_3^+$ from its AE ($CH_3^\bullet$ loss from $CH_3NHNH_2^{+\bullet}$) to be 954 kJ mol^{-1}. Matus et al. [2] calculated the $\Delta_f H_0$ of $N_2H_3^+$ to be 969 kJ mol^{-1} at the CCSD(T) level of theory and their results are in excellent agreement with our own calculated $\Delta_f H$. Nguyen [3] reported a $\Delta_f H_{298}$ for $NHNH_2^+$ of 974 ± 8 kJ mol^{-1} at the MP4SDTQ/6-311++G(2d,2p) level of theory which is 9 kJ mol^{-1} higher than our 298 K mG3 calculated $\Delta_f H$ of 965 kJ mol^{-1} and 16 kJ mol^{-1} higher than our 298 K mG2 calculated $\Delta_f H$ of 958 kJ mol^{-1}. The fragment ion *m/z* 30 ($N_2H_2^{+\bullet}$) has a VTST $\Delta_f H_0$ of 1155 ± 5 kJ mol^{-1}. It is important to note here that the methane loss channel in methylhydrazine has not been treated with the variational approach. However, for consistency, the $\Delta_f H_0$ values determined from the fits are all referred to as "VTST $\Delta_f H_0$". Given the presence of a barrier to this reaction, it is safe to assume that this value is an upper limit to the true value, and hence we can rule out the cis-$HNNH^+$ ion structure. Thus, ion *m/z* 30 could be either the iso-diazene ion ($H_2NN^{+\bullet}$) or the trans-diazene ion ($HNNH^{+\bullet}$). A more thorough computational study of the mechanism would be needed to confirm the ion structure. Dibeler et al. [48] reported a $\Delta_f H$ for this fragment ion (1247 kJ mol^{-1}) which is much higher than our calculated mG2 and mG3 $\Delta_f H_0$ for all three $N_2H_2^{+\bullet}$ isomers.

The adiabatic ionization energy has a direct effect on the value of the enthalpy of formation of the fragment ion as discussed previously in Chapter 3. Using the Meot-Ner et al. [108] IE_a for tetramethylhydrazine gave a $\Delta_f H_0$ of the product ion, $(CH_3)_2NNCH_3^+$, that did not agree with our calculated values (see Table 4.6). Using IE_a = 6.78 ± 0.04 eV [108], the derived $\Delta_f H_0$ of $(CH_3)_2NNCH_3^+$ was 854 ± 7 kJ mol^{-1} which is 25 kJ mol^{-1} higher than our calculated mG3 value of 829 kJ mol^{-1}, and 33 kJ mol^{-1} higher than our calculated mG2

value of 821 kJ mol^{-1}. Again, using our calculated mG3 IE_a of 7.02 eV [105], the $\Delta_f H_0$ of the trimethylhydrazyl ion was found to be 833 ± 5 kJ mol^{-1}. Dibeler et al. [48] reported an experimental $\Delta_f H$ of $(CH_3)_2NNCH_3^+$ that is < 13 kJ mol^{-1} lower than our mG2, mG3 or VTST values.

The $\Delta_f H_0$ for the fragment ion *m/z* 72, $C_3H_8N_2^{+\bullet}$, has been calculated from the VTST fits, the mG2 and mG3 calculations. The VTST derived $\Delta_f H_0$ is 1064 ± 5 kJ mol^{-1} which is 68–124 kJ mol^{-1} higher than the mG2 and mG3 calculated $\Delta_f H_0$ of the five linear isomers of $C_3H_8N_2^{+\bullet}$ (isomers I–V) and 120–203 kJ mol^{-1} higher than the mG2 and mG3 calculated $\Delta_f H_0$ values of the cyclic isomers VIII and IX (see Figure 3.13 in Chapter 3). Cyclic isomers VI and VII have $\Delta_f H_0$ values of 1050 kJ mol^{-1} (mG2), 1055 kJ mol^{-1} (mG3), and 1025 kJ mol^{-1} (mG2), 1029 kJ mol^{-1} (mG3), respectively, which are both in reasonable agreement with our VTST derived value. Obviously, there is a large barrier to methane loss in ionized TMH and the fitting procedure is giving us the height of this barrier and not the true thermochemical threshold to the reaction.

Table 4.3: Enthalpies of Formation of the Neutral Fragments

Neutral	$\Delta_f H$ (kJ mol^{-1})	Method	Reference
CH_4	-66	mG2 calculations (0 K)	present work.
	-74	mG2 calculations (298 K)	present work.
	-62	mG3 calculations (0 K)	present work. [91]
	-70	mG3 calculations (298 K)	present work. [91]
	-65.8	CBS-Q calculations (0 K)	Catoire et al. [34]
	-73.7	CBS-Q calculations (298 K)	Catoire et al. [34]
	-69.5	G2 calculations (0 K)	Catoire et al. [34]
	-77.5	G2 calculations (298 K)	Catoire et al. [34]
	-74.5	experimental value (298 K)	Catoire et al. [34]
	-66.8	experimental value (0 K)	Lias et al. [32]
	-74.5 ± 0.4	experimental value (298 K)	Lias et al. [32]
$CH_3^{\bullet}$	154	mG2 calculations (0 K)	present work.
	151	mG2 calculations (298 K)	present work.
	149	mG3 calculations (0 K)	Boulanger et al. [92]
	146	mG3 calculations (298 K)	Boulanger et al. [92]
	150.4	CBS-Q calculations (0 K)	Catoire et al. [34]
	147.9	CBS-Q calculations (298 K)	Catoire et al. [34]
	149.8	G2 calculations (0 K)	Catoire et al. [34]
	147.2	G2 calculations (298 K)	Catoire et al. [34]
	147.0	experimental value (298 K)	Catoire et al. [34]
	149.0	experimental value (0 K)	Lias et al. [32]
	145.8 ± 1	experimental value (298 K)	Lias et al. [32]
$H^{\bullet}$	216	mG2 calculations (0 K)	present work.
	218	mG2 calculations (298 K)	present work.
	216	mG3 calculations (0 K)	Boulanger et al. [92]
	218	mG3 calculations (298 K)	Boulanger et al. [92]
	216.035	experimental value (0 K)	Lias et al. [32]
	217.999	experimental value (298 K)	Lias et al. [32]

Table 4.4: Enthalpies of Formation of Ionized 1,1-Dimethylhydrazine and its Fragment Ions

m/z	Ion	$\Delta_f H$ (kJ mol^{-1})	Method	Reference
60	$(CH_3)_2NNH_2^{+\bullet}$	828	mG2 calculations (0 K)	present work.
		802	mG2 calculations (298 K)	present work.
		831	mG3 calculations (0 K)	Boulanger et al. [105]
		804	mG3 calculations (298 K)	Boulanger et al. [105]
		786	experimental value (298 K)	Lias et al. [32]
		866	electron ionization	Dibeler et al. [48]
59	$(CH_3)(CH_2)NNH_2^+$	822 ± 7	VTST fit (0 K)	present work. [92]
		823	single TS fit (0 K)	present work.
		820	mG2 calculations (0 K)	present work.
		796	mG2 calculations (298 K)	present work.
		825	mG3 calculations (0 K)	present work. [92]
		801	mG3 calculations (298 K)	present work. [92]
		845	electron ionization	Dibeler et al. [48]
		820	photoionization	Akopyan and Vilesov. [110]
		820–849	electron ionization	van Garderen et al. [4]
	$(CH_3)_2NNH^+$	853	mG2 calculations (0 K)	present work.
		829	mG2 calculations (298 K)	present work.
		862	mG3 calculations (0 K)	present work.
		838	mG3 calculations (298 K)	present work.
45	$CH_3N{=}NH_2^+$	906 ± 6	VTST fit (0 K)	present work. [92]
		905	single TS fit (0 K)	present work.
		904	mG2 calculations (0 K)	present work.
		886	mG2 calculations (298 K)	present work.
		911	mG3 calculations (0 K)	present work. [92]
		893	mG3 calculations (298 K)	present work. [92]
		883	electron ionization	Dibeler et al. [48]
		787	photoionization	Akopyan and Vilesov. [110]
		767.8	electron ionization	Burgers et al. [1]
		883 ± 21	electron ionization	van Garderen et al. [4]

Table 4.5: Enthalpies of Formation of the Methylhydrazine Ion and its Ionic Fragments

m/z	Ion	$\Delta_f H$ (kJ mol^{-1})	Method	Reference
46	$CH_3NHNH_2^{+\bullet}$	863	mG2 calculations (0 K)	present work.
		842	mG2 calculations (298 K)	present work.
		864	mG3 calculations (0 K)	Boulanger et al. [105, 109]
		844	mG3 calculations (298 K)	Boulanger et al. [105, 109]
		856.6	CBS-Q calculations (0 K)	Catoire et al. [34]
		836.5	CBS-Q calculations (298 K)	Catoire et al. [34]
		857.5	G2 calculations (0 K)	Catoire et al. [34]
		837.4	G2 calculations (298 K)	Catoire et al. [34]
		866.1	photoionization	Akopyan and Vilesov. [110]
		835	experimental value (298 K)	Lias et al. [32]
		925	electron ionization	Dibeler et al. [48]
45[a]	$CH_2NHNH_2^+$	862 ± 5	VTST fit (0 K)[b]	present work. [91]
		859	mG2 calculations (0 K)	present work.
		841	mG2 calculations (298 K)	present work.
		864	mG3 calculations (0 K)	present work. [91]
		846	mG3 calculations (298 K)	present work. [91]
		816	electron ionization	Burgers et al. [1]
		854	electron ionization	Dibeler et al. [48]
		860 ± 12	*ab initio* calculations (298 K)	Nguyen. [3]
		854 ± 21	electron ionization	van Garderen et al. [4]

Table 4.5: continued

m/z	Ion	$\Delta_f H$ (kJ mol^{-1})	Method	Reference
45	$CH_2NNH_3^+$	876	mG2 calculations (0 K)	present work.
		858	mG2 calculations (298 K)	present work.
		883	mG3 calculations (0 K)	present work.
		865	mG3 calculations (298 K)	present work.
	CH_3NHNH^+	906	mG2 calculations (0 K)	present work.
		888	mG2 calculations (298 K)	present work.
		914	mG3 calculations (0 K)	present work.
		896	mG3 calculations (298 K)	present work.
31	$HNNH_2^+$	959 ± 5	VTST fit (0 K)[b]	present work. [91]
		969	mG2 calculations (0 K)	present work.
		958	mG2 calculations (298 K)	present work.
		976	mG3 calculations (0 K)	present work. [91]
		965	mG3 calculations (298 K)	present work. [91]
		895	electron ionization	Burgers et al. [1]
		992	electron ionization	Dibeler et al. [48]
		969.0	calculations (0 K)	Matus et al. [2]
		957.7	calculations (298 K)	Matus et al. [2]
		974 ± 8	*ab initio* calculations (298 K)	Nguyen. [3]
		954	experimental	van Garderen et al. [4]
		974.2	CBS-Q calculations (0 K)	Catoire et al. [34]
		962.9	CBS-Q calculations (298 K)	Catoire et al. [34]
		968.2	G2 calculations (0 K)	Catoire et al. [34]
		956.9	G2 calculations (298 K)	Catoire et al. [34]
30	$N_2H_2^{+\bullet}$	1155 ± 5	VTST fit (0 K)[b]	present work. [91]
	trans-$HNNH^{+\bullet}$	1139	mG2 calculations (0 K)	present work.
		1132	mG2 calculations (298 K)	present work.
		1147	mG3 calculations (0 K)	present work. [91]
		1140	mG3 calculations (298 K)	present work. [91]
	iso-$NNH_2^{+\bullet}$	1147	mG2 calculations (0 K)	present work.
		1140	mG2 calculations (298 K)	present work.
		1156	mG3 calculations (0 K)	present work. [91]
		1149	mG3 calculations (298 K)	present work. [91]
	cis-$HNNH^{+\bullet}$	1163	mG2 calculations (0 K)	present work.
		1156	mG2 calculations (298 K)	present work.
		1171	mG3 calculations (0 K)	present work. [91]
		1164	mG3 calculations (298 K)	present work. [91]
		1247	electron ionization	Dibeler et al. [48]

[a] Fragment ion *m/z* 45 $CH_3NNH_2^+$ is listed in Table 4.4 above. [b] $IE_a(MH)$ = 7.64 eV, calculated mG3 value from Boulanger et al. [105, 109].

Table 4.6: Enthalpies of Formation of the Tetramethylhydrazine Ion and its Ionic Fragments

m/z	Ion	$\Delta_f H$ (kJ mol^{-1})	Method	Reference
88	$(CH_3)_2NN(CH_3)_2^{+\bullet}$	806	mG2 calculations (0 K)	present work.
		770	mG2 calculations (298 K)	present work.
		809	mG3 calculations (0 K)	Boulanger et al. [105]
		772	mG3 calculations (298 K)	Boulanger et al. [105]
		732	experimental value (298 K)	Lias et al. [32]
		820	electron ionization	Dibeler et al. [48]
87	$(CH_3)_2NN(CH_2)(CH_3)^+$	813	mG2 calculations (0 K)	present work.
		770	mG2 calculations (298 K)	present work.
		807	mG3 calculations (0 K)	present work.
		776	mG3 calculations (298 K)	present work.

Table 4.6: continued

m/z	Ion	$\Delta_f H$ (kJ mol^{-1})	Method	Reference
73	$(CH_3)_2NNCH_3^+$	833 ± 5	VTST fit (0 K)[a]	present work. [91]
		854 ± 5	VTST fit (0 K)[b]	present work.
		821	mG2 calculations (0 K)	present work.
		791	mG2 calculations (298 K)	present work.
		829	mG3 calculations (0 K)	present work. [91]
		799	mG3 calculations (298 K)	present work. [91]
		820	electron ionization	Dibeler et al. [48]
72	$C_3H_8N_2^{+\bullet}$ [c]	1064 ± 5	VTST fit (0 K)[a]	present work. [91]
	isomer I	993	mG2 calculations (0 K)	present work.
		968	mG2 calculations (298 K)	present work.
		996	mG3 calculations (0 K)	present work. [91]
		970	mG3 calculations (298 K)	present work. [91]
	isomer II	990	mG2 calculations (0 K)	present work.
		964	mG2 calculations (298 K)	present work.
		992	mG3 calculations (0 K)	present work. [91]
		966	mG3 calculations (298 K)	present work. [91]
	isomer III	963	mG2 calculations (0 K)	present work.
		938	mG2 calculations (298 K)	present work.
		966	mG3 calculations (0 K)	present work. [91]
		941	mG3 calculations (298 K)	present work. [91]
	isomer IV	959	mG2 calculations (0 K)	present work.
		934	mG2 calculations (298 K)	present work.
		953	mG3 calculations (0 K)	present work. [91]
		928	mG3 calculations (298 K)	present work. [91]
	isomer V	939	mG2 calculations (0 K)	present work.
		915	mG2 calculations (298 K)	present work.
		940	mG3 calculations (0 K)	present work. [91]
		916	mG3 calculations (298 K)	present work. [91]
	isomer VI	1050	mG2 calculations (0 K)	present work.
		1023	mG2 calculations (298 K)	present work.
		1055	mG3 calculations (0 K)	present work. [91]
		1029	mG3 calculations (298 K)	present work. [91]
		≤ 1152	estimated	Holmes et al. [106]
	isomer VII	1025	mG2 calculations (0 K)	present work.
		998	mG2 calculations (298 K)	present work.
		1029	mG3 calculations (0 K)	present work. [91]
		1002	mG3 calculations (298 K)	present work. [91]
	isomer VIII	862	mG2 calculations (0 K)	present work.
		833	mG2 calculations (298 K)	present work.
		861	mG3 calculations (0 K)	present work. [91]
		832	mG3 calculations (298 K)	present work. [91]
		≤ 1025	estimated	Holmes et al. [106]
	isomer IX	943	mG2 calculations (0 K)	present work.
		915	mG2 calculations (298 K)	present work.
		944	mG3 calculations (0 K)	present work. [91]
		916	mG3 calculations (298 K)	present work. [91]

[a] IE_a(TMH) = 7.02 eV, calculated mG3 value from Boulanger et al. [105]. [b] IE_a(TMH) = 6.78 ± 0.04 eV, experimental value from Meot-Ner et al. [108]. [c] The $C_3H_8N_2^{+\bullet}$ structures are shown in Figure 3.13 in Chapter 3.

As mentioned earlier in this chapter, there is a discrepancy between the mG2 and the mG3 calculated $\Delta_f H$ values. It seems that the two procedures agree well when the enthalpies of formation are calculated for substituted radical cations such as the parent ions. In this case, the discrepancy is less than 3 kJ mol^{-1}. This is not true however for the small N_2-containing ions like the diazene ions for which the two methods give $\Delta_f H$ values that differ by ~ 8 kJ mol^{-1}. The enthalpies of formation of the other fragment ions which are singlet species such as the $CH_5N_2^+$ isomers differ by approximatively 8 kJ mol^{-1}. Even if the absolute $\Delta_f H$ values may not agree perfectly for one particular ion, the relative energies are similar with both composite methods. For example, the methylhydrazine ion undergoes two simple bond dissociations: one N–C and one H–C bond cleavages. At the mG2 level of theory, the relative energies of the dissociation products [$NHNH_2^+ + CH_3^\bullet$] with respect to the MH ion are 261 kJ mol^{-1} and 262 kJ mol^{-1} at the mG3 level of theory. For the second process [$CH_3NHNH_2^{+\bullet} \rightarrow CH_2NHNH_2^+ + H^\bullet$], the relative energies of the dissociation products are slightly different: 212 kJ mol^{-1} at the mG2 level of theory and 216 kJ mol^{-1} at the mG3 level of theory.

4.4 Proton affinity

The proton affinities of some NN-containing neutral molecules have been determined from the following equations [111], using the VTST derived $\Delta_f H_0$ reported in Section 4.3 and compared to reported values in the literature:

$$M + H^+ \rightarrow MH^+ \qquad (4.6)$$

$$PA(M) = -\Delta_{rxn}H = \Delta_f H(M) + \Delta_f H(H^+) - \Delta_f H(MH^+) \qquad (4.7)$$

The PA values are listed in Table 4.7. For $N_2H_3^+$, $CH_2NHNH_2^+$ and $CH_3NNH_2^+$ [91, 92], $\Delta_f H_0$ have been derived from the VTST fits of the breakdown curves. Using these enthalpies of formation, a PA was obtained for each reported $\Delta_f H_0$ of the corresponding neutral molecule. The lowest reported PA [3] of trans-N_2H_2 is 764 ± 8 kJ mol^{-1} which is in good agreement with our determined values (PA ≈ 778 ± 5 kJ mol^{-1} using our VTST $\Delta_f H_0(NHNH_2^+)$, PA = 766 kJ mol^{-1} using the mG2 $\Delta_f H_0$, and PA = 768 kJ mol^{-1} using the mG3 $\Delta_f H_0$). Using the present VTST $\Delta_f H_0$ of $NHNH_2^+$ and the experimental $\Delta_f H_0$ of NNH_2 and cis-HNNH [2, 112] results in average PA values for NNH_2 (i.e. the bare N atom) and cis-HNNH of 890 ± 5 kJ mol^{-1} and ~ 798 ± 5 kJ mol^{-1}, respectively. There have been no previously reported PAs for these two compounds. Our calculated mG2 and mG3 PA agree well with the above values. Methyldiazene (CH_3N=NH) has two sites to accept a proton (its substituted nitrogen atom and its terminal nitrogen atom) and thus two different proton affinities. Hunter and Lias [113] reported the PA of the substituted nitrogen and the terminal nitrogen to be 845 and 841 kJ mol^{-1}, respectively. These values are in good agreement with the PA reported by van Garderen et al. [4] at the SDCI + Pople/6-31G**//6-31G* level of theory: 841 kJ mol^{-1} for the substituted N atom and 845 kJ mol^{-1} for the terminal N atom. However, Nguyen [3] reported a PA for CH_3NNH, at the MP4SDTQ/6-311++G(2d,2p) level of theory, that is ~ 30 kJ mol^{-1} lower than those reported by Hunter and Lias [113] and van Garderen et al. [4]. Nguyen's value [3] is in agreement with our calculated mG2 and mG3 PA of 816 and 818 kJ mol^{-1}, respectively, for the terminal N atom of CH_3NNH which is slightly higher than that of the substituted one (PA(CH_3**N**NH) = 813 or 815 kJ mol^{-1}). The PA of CH_2=NNH_2 has also been calculated to be ~ 857 kJ mol^{-1} at the substituted nitrogen atom. The PA at the terminal nitrogen atom (i.e., CH_2N**N**H_2) is lower, ~ 838 kJ mol^{-1}. The

carbon proton affinity in CH_2=NNH_2 was calculated to be 809 kJ mol^{-1} using the calculated mG3 enthalpies of formation. The calculated PAs of hydrazine, methylhydrazine, 1,1-dimethylhydrazine and tetramethylhydrazine using the mG2 and mG3 procedures are also reported in Table 4.7. Consistent with trends observed for homologous alkylamines, aliphatic alcohols and bromides [111], the PA of the substituted nitrogen atom in the hydrazine derivatives increases with increasing methyl substitution as shown in Figure 4.3. This can be traced to the lowering of the energy of the nitrogen lone pair orbital upon methyl substitution.

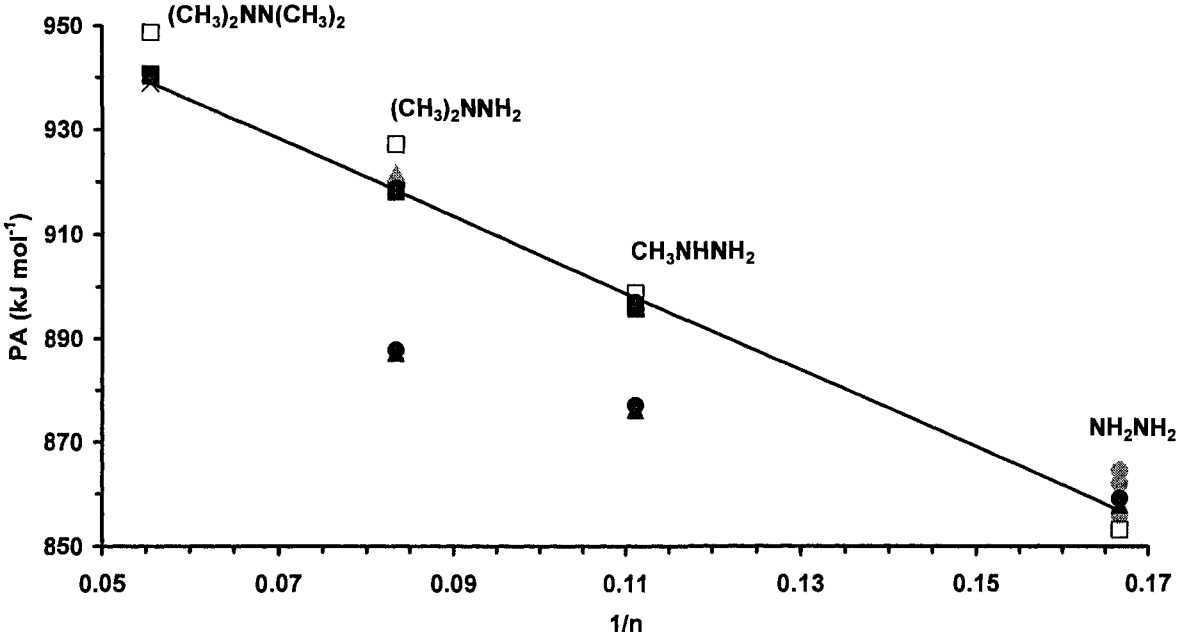

Figure 4.4 – Proton affinity of the methyl-substituted hydrazines as a function of the ion's size. The following symbols correspond to different values: ● calculated mG3 PA, present work [91], ▲ calculated mG2 PA, present work, ● PA from Armstrong et al. [31], ■ PA from Meot-Ner et al. [108], ▲ PA from Hillebrand et al. [114], × PA from Nelsen et al. [115] and □ PA from Hunter and Lias [113]. The points observed below the black line correspond to the proton affinity of the terminal nitrogen in methyl- and 1,1-dimethylhydrazine.

Table 4.7: Proton Affinities of N_2H_2, N_2H_4, CH_4N_2, CH_3NHNH_2, $(CH_3)_2NNH_2$ and $(CH_3)_2NN(CH_3)_2$

neutral molecule (M)	protonated molecule (MH^+)	$\Delta_f H$(M) (kJ mol^{-1})				PA(M) (kJ mol^{-1})		
		reported	mG2[a]	mG3[a]	experimental[b]	mG2[a]	mG3[a]	reported
trans-N_2H_2	$N_2H_3^+$	207.5 [112], 208.8 [2]	207	212	777 ± 5, 778 ± 5	766	768	764 ± 8 [3], 803 [4][c], 782 [4][d]
cis-N_2H_2	$N_2H_3^+$	227.6 [112], 229.7 [2]	227	234	797 ± 5, 799 ± 5	787	789	
iso-NNH_2	$N_2H_3^+$	321.3 [112]	307	312	890 ± 5	866	867	
CH_3NNH	$CH_3NNH_2^+$	196.2 [2], 187 ± 12 [3], 188 ± 8 [3]	191	197	818 ± 6 [2], 809 ± 13 [3], 810 ± 10 [3]	816	818	845 [4, 113], 813 ± 12 [3]
	CH_3NHNH^+					813	815	841 [4, 113]
CH_2=NNH_2	$CH_2NHNH_2^+$	183.0 [34], 188.1 [34]	185	189	851 ± 5, 856 ± 5	855	857	
	$CH_2NNH_3^+$					838	838	
	$CH_3NNH_2^+$					810	809	
N_2H_4	$N_2H_5^+$[e]		116	121		858	859	864.5 [31][f], 862 [31][g], 856 [31][h], 858 [113]
CH_3NHNH_2	$CH_3NH_2NH_2^+$[e]		121	128 [105, 109]		896	897	895.8 [108], 896 [113]
	$CH_3NHNH_3^+$[e]					876	877	
$(CH_3)_2NNH_2$	$(CH_3)_2NHNH_2^+$[e]		114	122 [105]		918	919	918.4 [108], 909.2 [114][i], 921.7 [114][j], 920.1 [114][k], 927.1 [113]
	$(CH_3)_2NNH_3^+$[e]					887	888	882.8 [114][i], 887.4 [114][j]
$(CH_3)_2NN(CH_3)_2$	$(CH_3)_2NHN(CH_3)_2^+$[e]		126	135 [105]		940	940	940.6 [108], 938.9 [115][k], 948.7 [113]

[a] Present work. [b] PA values determined using the $\Delta_f H_0(MH^+)$ obtained from the VTST fit with $\Delta_f H_0(H^+)$ [2] = 1528.1 kJ mol^{-1} and the respective $\Delta_f H$(M) (i.e. $N_2H_2 + H^+ \rightarrow N_2H_3^+$ with $\Delta_f H(N_2H_2)$ = 207.5 kJ mol^{-1} taken from Pople and Curtiss [112] gives a PA(trans-N_2H_2) = 777 ± 5 kJ mol^{-1}) [115]. [c] PA calculated from SDCI + Pople/6-31G**//6-31G** [4]. [d] PA calculated using the CASSCF-Multireference CI procedure [4]. [e] $\Delta_f H_0(N_2H_5^+)$ = 787 kJ mol^{-1} (mG2), 793 kJ mol^{-1} (mG3), $\Delta_f H_0(CH_3NH_2NH_2^+)$ = 754 kJ mol^{-1} (mG2), 763 kJ mol^{-1} (mG3), $\Delta_f H_0(CH_3NHNH_3^+)$ = 774 kJ mol^{-1} (mG2), 783 kJ mol^{-1} (mG3), $\Delta_f H_0((CH_3)_2NHNH_2^+)$ = 724 kJ mol^{-1} (mG2), 734 kJ mol^{-1} (mG3), $\Delta_f H_0((CH_3)_2NNH_3^+)$ = 755 kJ mol^{-1} (mG2), 765 kJ mol^{-1} (mG3), $\Delta_f H_0((CH_3)_2NHN(CH_3)_2^+)$ = 715 kJ mol^{-1} (mG2), 726 kJ mol^{-1} (mG3) from present work. [f] Calculated from the isodesmic reaction 3 in Armstrong et al. [31]. [g] G2(MP2) calculated PA value [31]. [h] Experimental value. [i] PA calculated using M(I) method [114]. [j] PA calculated using M(II) method [114]. [k] PA calculated at 550 K.

4.5 Bond dissociation enthalpies

Bond strengths are important thermochemical values to know in order to understand the chemical properties of molecules. The bond dissociation enthalpy (DH) of a molecule AB is defined as the enthalpy of the homolytic bond cleavage reaction of the molecule AB and is calculated according to the equations written below [116]:

$$AB \rightarrow A + B \tag{4.8}$$

$$\Delta_{rxn}H = \Delta_f H(A) + \Delta_f H(B) - \Delta_f H(AB) = DH(A\text{–}B) \tag{4.9}$$

Table 4.8: N–C and H–C Bond Dissociation Enthalpies (in kJ mol^{-1}) in the Neutral and Ionized Hydrazine Derivatives

	$DH_0(N\text{–}CH_3)$				$DH_0(H_2C\text{–}H)$			
	mG2	mG3	VTST	reported	mG2	mG3	VTST	reported
neutral								
methylhydrazine	274[a]	262[a]		274.9 [45]	386	380		390.8 [45]
1,1-dimethylhydrazine	273	262			390	383		
tetramethylhydrazine	268	257			387	381		
ion								
methylhydrazine	261	262	244		212	216	214	
1,1-dimethylhydrazine	230	230	225		208	211	207	
tetramethylhydrazine	168	170	174		217	220	—	

[a] using the G2 $\Delta_f H_0$ taken from Catoire et al. [34].

Table 4.9: Enthalpies of Formation of the Methyl-Substituted Hydrazyl Radicals

	$\Delta_f H_0$ (kJ mol^{-1})			$\Delta_f H_{298}$ (kJ mol^{-1})		
	mG2	mG3	reported	mG2	mG3	reported
$NHNH_2^{\bullet}$	—	—	240.7[a], 239.6[b], 231.4 ± 1.3[c]	—	—	230.0[a], 228.9[b]
$CH_2NHNH_2^{\bullet}$	291	292	293.5[a], 295.7[b]	274	275	276.3[a], 278.3[b]
$CH_3NNH_2^{\bullet}$	233	234	229.3[a], 229.9[b]	215	217	212.2[a], 212.7[b]
$(CH_3)(CH_2)NNH_2^{\bullet}$	288	289		265	266	
$(CH_3)_2NNCH_3^{\bullet}$	240	243		211	213	
$(CH_3)_2NN(CH_3)(CH_2)^{\bullet}$	297	299		262	264	

[a] G2 $\Delta_f H_0$ taken from Catoire et al. [34]. [b] CBS-Q $\Delta_f H_0$ taken from Catoire et al. [34]. [c] experimental $\Delta_f H_0$ from Ruscic and Berkowitz [22].

The three methyl-substituted hydrazine ions dissociate by either losing a methyl radical or a hydrogen atom or both. The N–C or H–C bond dissociation enthalpies in the neutral and ionic hydrazines were derived from the VTST $\Delta_f H_0$ of the product ions and from

the calculated mG2 and mG3 $\Delta_f H_0$, and are listed in Table 4.8. The enthalpies of formation of the hydrazine radicals, used to calculate the DH_0 values, are listed in Table 4.9. The N–C bond dissociation enthalpies in the neutral hydrazine derivatives are constant as the methyl substitution increases on the hydrazine backbone showing that the effect of methyl substitution on the stability of the radicals formed from the homolytic bond cleavage reaction is similar to that for the neutral molecules. However, in the radical cations, the N–C bond dissociation enthalpy decreases with methyl substitution. The mG3 calculated DH_0(N–CH_3) decreases from 262 kJ mol^{-1} in the $MH^{+\bullet}$ to 230 kJ mol^{-1} in $DMH^{+\bullet}$ and to 170 kJ mol^{-1} in $TMH^{+\bullet}$. When the nitrogen-carbon bond is cleaved in the parent radical cation, a singlet fragment ion is formed:

$$(CH_3)_2NN(CH_3)_2^{+\bullet} \rightarrow (CH_3)_2NNCH_3^{+} + CH_3^{\bullet} \qquad (4.10)$$

So we can conclude that the positive charge is better stabilized in the fragment ion than in the parent radical cation as the methyl substitution increases on the hydrazine backbone. The H–C bond dissociation enthalpies were also calculated in the neutral and ionic hydrazine derivatives. In the neutral hydrazines, the loss of a hydrogen atom creates a carbon-centered radical which is not the case in the ion:

$$(CH_3)_2NN(CH_3)_2 \rightarrow (CH_3)_2NNCH_2^{\bullet}(CH_3) + H^{\bullet} \qquad (4.11)$$

$$(CH_3)_2NN(CH_3)_2^{+\bullet} \rightarrow (CH_3)_2NN^{+}{=}CH_2(CH_3) + H^{\bullet} \qquad (4.12)$$

We calculated the $DH_0(H_2C–H)$ in all three neutral hydrazines to be ~ 381 kJ mol^{-1} and ~ 216 kJ mol^{-1} in the ions. The bond dissociation enthalpies in the neutrals and ions stay constant as the methyl substitution increases. No extra methyl stabilization is expected in the fragment ions compared to the parent radical cation since the charge is still solely located on one of the two nitrogen atoms.

A discussion similar to the one about the calculated ionic mG2 and mG3 $\Delta_f H$ can be made about the calculated mG2 and mG3 enthalpies of formation of the neutral hydrazine derivatives and their respective hydrazyl radicals. The neutral hydrazine molecules are singlet species. Their calculated $\Delta_f H$ values differ by 6–9 kJ mol^{-1} between the two methods. However, their respective hydrazyl radicals have enthalpies of formation that agree very well, $\Delta(\Delta_f H) \leq 3$ kJ mol^{-1}. Just like the relative energies for the unimolecular dissociations of the parent ions, the mG2 and mG3 derived proton affinities and bond dissociation enthalpies agree excellently, $\Delta(\text{PA}) \leq 2$ kJ mol^{-1} and $\Delta(\text{DH}) \leq 3$ kJ mol^{-1}, except for the bond dissociation enthalpies in the neutral hydrazine derivatives where the difference is large being ~ 9 kJ mol^{-1} which is directly related to the discrepancy of the neutral enthalpies of formation.

4.6 Summary

The entropies of activation for the two unimolecular dissociation reactions of the hydrazine ions, namely the H–C and the N–C bond cleavages, vary significantly as the internal energy of the ions is raised. These large changes affect the shape of the breakdown curves and can be used to explain the competition between the two dissociation pathways. The entropies of activation can also be used to compare similar reactions amongst the three hydrazine ions.

Enthalpies of formation of all the observed fragment ions (*m/z* 73, *m/z* 72, *m/z* 59, *m/z* 45, *m/z* 31 and *m/z* 30) were determined from the VTST fits to the TPEPICO data and compared with those from mG2 and mG3 calculations. Excellent agreement was found for all fragment ions except for fragment ion *m/z* 31, $NHNH_2^+$, for which the VTST derived

enthalpy of formation was lower than the mG3 calculated one. Two plausible structures of fragment ion *m/z* 72 have been proposed (i.e. isomers VI and VII). From the derived and calculated $\Delta_f H_0$ of the fragment ions, the proton affinity of small neutral molecules (N_2H_2 and CH_4N_2) were determined as well as the N–C and H–C bond dissociation enthalpies in the three hydrazine derivatives.

Chapter 5

CONCLUSIONS

5.1 Entropies of activation

The experimental and theoretical investigations of the unimolecular dissociation reactions of the three methyl-substituted hydrazine ions studied in this thesis showed that the entropy of activation has a profound impact on these dissociation reactions. The low energy dissociation pathways of the hydrazine ions corresponded to simple bond cleavage reactions, either an N–C and/or an H–C bond, and to a rearrangement process leading to the loss of methane. The two simple bond cleavage reactions were studied with variational transition state theory.

For the methyl radical loss channel, up to ten transition states were identified in the internal energy range studied. The transition states for the methyl- and 1,1-dimethylhydrazine ions were located at similar N–C bond distances, the lowest energy transition state being found at $R^*_{N-C} \approx 4.4$ Å and the highest energy transition state at $R^*_{N-C} \approx 2.5$ Å. The methyl radical loss transition states for ionized tetramethylhydrazine were located at much shorter N–C bond distances compared to those of ionized MH and DMH, between $R^*_{N-C} = 2.4–2.8$ Å. The entropies of activation derived for the methyl radical loss channel reflect the shift in the TS location with internal energy, especially for MH and DMH ions for which the switch is large ($\Delta R_{N-C} \approx 2$ Å). In ionized MH and DMH, the entropies of activation vary from approximately 65-70 J K^{-1} mol^{-1} at low internal energies to 17-21 J K^{-1} mol^{-1} at high internal energies. In TMH ion, the entropies of activation vary slightly with increasing internal energy, $\Delta S^{\ddagger}$ decreasing from 35-39 J K^{-1} mol^{-1} to 23-26 J K^{-1} mol^{-1}.

These $\Delta S^{\ddagger}$ values are higher than those of MH and DMH ions as shown graphically in Figure 4.2(a). As one of the methyl groups is pulled from the TMH ion, the three other methyl groups become freer to rotate.

For the hydrogen atom loss channel, fewer transition states were located in the same internal energy ranges for ionized MH and DMH. The transition states were located in both parent ions between R^*_{H-C} = 2.0–2.4 Å. Because of the small shift in the TS location, the $\Delta S^{\ddagger}$ values did not vary significantly with internal energy, $\Delta S^{\ddagger}(MH)_{45}$ = 30-36 J K^{-1} mol^{-1}, at low internal energies, and 20-26 J K^{-1} mol^{-1}, at high internal energies and $\Delta S^{\ddagger}(DMH)_{59}$ = 20-26 J K^{-1} mol^{-1}, at low internal energies, and 16-22 J K^{-1} mol^{-1}, at high internal energies. For the rearrangement process leading to the loss of methane in MH and TMH ions, the transition state(s) were estimated from the parent ion vibrational frequencies. One transition state was necessary to fit theoretically the breakdown curve of the MH ion while two transition states were needed for the TMH ions. The entropies of activation for this dissociation channel in both ions are lower than those of the bond cleavages, however the $\Delta S^{\ddagger}$ values are positive indicating the participation of loosely bound complex in the dissociation: $\Delta S^{\ddagger}(MH)_{30}$ = 17–21 J K^{-1} mol^{-1} and $\Delta S^{\ddagger}(TMH, TS_1)_{72}$ = 12-14 J K^{-1} mol^{-1} and $\Delta S^{\ddagger}(TMH, TS_2)_{72}$ = -19 to -25 J K^{-1} mol^{-1}.

5.2 Thermochemistry

From the VTST fits of the experimental breakdown curves, the enthalpies of formation of all the observed fragment ions (*m/z* 73, *m/z* 72, *m/z* 59, *m/z* 45, *m/z* 31 and *m/z* 30) were derived. The $\Delta_f H_0$ have been determined from the 0 K activation energies (E_0) obtained from the fitting procedure: $\Delta_f H_0[(CH_3)_2NNCH_3^+]$ = 833 ± 5 kJ mol^{-1}, $\Delta_f H_0$

$[C_3H_8N_2^{+\bullet}]$ = 1064 ± 5 kJ mol^{-1}, $\Delta_fH_0[(CH_3)(CH_2)NNH^+]$ = 822 ± 7 kJ mol^{-1}, $\Delta_fH_0[CH_3NNH_2^+]$ = 906 ± 6 kJ mol^{-1}, $\Delta_fH_0[CH_2NHNH_2^+]$ = 862 ± 5 kJ mol^{-1}, $\Delta_fH_0[NHNH_2^+]$ = 959 ± 5 kJ mol^{-1} and $\Delta_fH_0[N_2H_2^{+\bullet}]$ = 1155 ± 5 kJ mol^{-1}. These were compared to the calculated mG2 and mG3 values and were found to be in excellent agreement except for the VTST Δ_fH_0 value of fragment ion *m/z* 31, $NHNH_2^+$ which is lower than the calculated enthalpies of formation. The enthalpies of formation of nine isomers of fragment ion *m/z* 72, $C_3H_8N_2^{+\bullet}$, were calculated and two of them agreed well with the derived VTST enthalpy of formation.

The proton affinity of some small neutral molecules (N_2H_2 and CH_4N_2) have been determined from the VTST and calculated Δ_fH_0 values. The proton affinity of the methyl-substituted hydrazine derivatives were also determined and found to agree with previously reported data.

The N–C and H–C bond dissociation enthalpies of the neutral and ionic hydrazine derivatives were calculated and derived from the above enthalpies of formation. The determined $DH_0(N–CH_3)$ values in the neutral hydrazine derivatives are constant with increasing methyl substitution indicating that a similar effect of methyl substitution on the stability of the hydrazyl radicals and their neutral molecules. However, the $DH_0(N–CH_3)$ values in the ionic hydrazine derivatives decrease with increasing methyl substitution indicating a better stabilization of the positive charge in the fragment ion than in the parent radical cation. In the case of the H–C bond dissociation, the determined $DH_0(H–C)$ values are constant in both the neutral and ionic hydrazine derivatives indicating no extra methyl stabilization in the hydrazyl radicals or ions.

These bond dissociation enthalpies are important values to know in order to understand the hydrazine atmospheric chemistry and improve the models presently developed. As explained in the introductory chapter, the methyl-substituted hydrazine compounds are used, among other things, as fuel in rocket and satellite thrusters. A considerable amount of these hydrazine derivatives is released in the atmosphere in an unburned state and these compounds can then undergo chemical reactions with other atmospheric species. It is thus useful to have precise and accurate thermochemical data about these compounds to properly model their atmospheric chemistry.

Claims to Original Research

1. The lowest energy unimolecular dissociation pathways of three methyl-substituted hydrazine ions (i.e., methyl-, 1,1-dimethyl- and tetramethylhydrazine) have been investigated using tandem mass spectrometry, TPEPICO spectroscopy and variational transition state theory.
2. The experimental breakdown curves of these hydrazine ions have been recorded on a TPEPICO mass spectrometer connected to a 5m normal incidence monochromator at the Daresbury Laboratory Synchrotron Radiation Source in Daresbury, UK. The breakdown curves in the threshold region were collected at four different parent ion residence times. The complete breakdown diagrams at the minimum parent ion residence time were also recorded from threshold up to a photon energy of ~ 32 eV.
3. The unimolecular dissociations of the methyl-substituted hydrazine ions studied were modeled by optimizing the corresponding potential energy curves. These curves were calculated in the following manner: the geometry of the dissociating ion complexes was optimized from the equilibrium geometry of the parent ion up to the plateau corresponding to the separated products every 0.1 Å.
4. A simple VTST treatment was employed to locate the transition states of the unimolecular dissociation reactions as a function of the ion's internal energy. In the internal energy ranges studied, up to ten transition states were identified for the methyl radical loss channel and up to four transition states for the hydrogen atom loss channel. These transition states were then used in the calculations of the rate constants. The

transition state(s) for the rearrangement channel leading to the loss of methane were estimated using the parent ion vibrational frequencies.

5. The four experimental breakdown curves in the first cross-over region have been reproduced theoretically using the variational transition states mentioned above. Only small adjustement were needed to obtain satisfactory fits of the breakdown diagrams.

6. The VTST investigation of the unimolecular dissociations of the methyl-substituted hydrazine ions through the fits of their breakdown curves improved our understanding of the impact of the entropy of activation on simple bond dissociation reactions. It was found that the entropy of activation vary significantly with an increase in the ion's internal energy and that change in $\Delta S^{\ddagger}$ is found to have a profound impact on the shape of the breakdown curves. A systematic study of the entropies of activation for each dissociation pathway also permitted a thorough comparison of the dissociation processes undergone by the hydrazine ions.

7. The thermochemistry of many N_2-containing ions and molecules was determined from this project. Enthalpies of formation for all the observed fragment ions were derived from the VTST fits of the breakdown curves. Proton affinities of small N_2-containing molecules were determined as well as N–C and H–C bond dissociation energies.

8. Most of the results reported in this thesis have already been published in two papers. The first paper concerned the 1,1-dimethylhydrazine ion while the second one concerned the methyl- and tetramethylhydrazine ions. The complete references for the two papers are listed below:

a. Boulanger, A.-M., Rennie, E. E., Holland, D. M. P., Shaw, D. A., Mayer, P. M., *Entropy Effects in the Fragmentation of 1,1-Dimethylhydrazine Ions*. J. Phys. Chem. A, 2007. 111: p. 5388-5398.

b. Boulanger, A.-M., Rennie, E. E., Holland, D. M. P., Shaw, D. A., Mayer, P. M., *Thermochemistry of N-N Containing Ions: A TPEPICO Study of Ionized Methyl- and Tetramethylhydrazine*. J. Phys. Chem. A, 2008. 112: p. 866-879.

References

1. Burgers, P.C., T. Drewello, H. Schwarz, and J.K. Terlouw, *CH_5N_2 Hydrazyl Radicals, Cations and Dication Radicals Studied by Mass Spectrometry. Is the N-Protonated Formaldehyde Hydrazon Cation $^+CH_2$---NH---NH_2 a Bridged Species?* Int. J. Mass Spectrom. Ion Proc., 1989. **95**: p. 157-169.
2. Matus, M.H., A.J.I. Arduengo, and D.A. Dixon, *The Heats of Formation of Diazene, Hydrazine, $N_2H_3^+$, $N_2H_5^+$, N_2H, and N_2H_3 and the Methyl Derivatives CH_3NNH, CH_3NNCH_3, and $CH_3HNNHCH_3$.* J. Phys. Chem. A, 2006. **110**: p. 10116-10121.
3. Nguyen, M.T., *Hydrogen cyanide loss from [CH5N2]+ cations: 1,2-elimination versus Beckmann rearrangement.* Int. J. Mass Spectrom. Ion Proc., 1994. **136**: p. 45-53.
4. van Garderen, H.F., P.J.A. Ruttink, P.C. Burgers, G.A. McGibbon, and J.K. Terlouw, *Aspects of the CH_5N_2 potential energy surface: ions CH_3NHNH^+, $CH_3NNH_2^+$ and $CH_2NHNH_2^+$ and radicals CH_2NHNH_2 studied by theory and experiment.* Int. J. Mass Spectrom. Ion Proc., 1992. **121**: p. 159-182.
5. Kimura, K., S. Katsumata, Y. Achiba, T. Yamazaki, and S. Iwata, *Handbook of HeI Photoelectron Spectra of Fundamental Organic Molecules.* 1981, Tokyo: Japan Scientific Societies Press.
6. Houk, K.N., *Photoelectron Spectroscopy of Azo Compounds.* J. Am. Chem. Soc., 1975. **97**(7): p. 1824-1832.
7. Boyd, R.J., J.C. Bunzli, J.P. Snyder, and M.L. Heyman, *Photoelectron Spectra of 2,3-Diazabicyclo[2.2.n]alk-2-enes (n = 1, 2, 3, 4).* J. Am. Chem. Soc., 1973. **95**(19): p. 6478-6480.
8. Bock, H., K. Wittel, M. Veith, and N. Wiberg, *Photoelectron Spectra and Molecular Properties. L. On the Blue Color of Bis(trimethylsilyl)diimine.* J. Am. Chem. Soc., 1976. **98**: p. 109-114.
9. Dyke, J., N. Jonathan, E. Lee, A. Morris, and M. Winter, *Vacuum Ultraviolet Photoelectron Spectroscopy of Transient Species: Part 8, the t-Butyl Radical.* Physica Scripta, 1977. **16**: p. 197-201.
10. Koenig, T., T. Balle, and W. Snell, *Helium(I) Photoelectron Spectra of Organic Radicals.* J. Am. Chem. Soc., 1975. **97**: p. 662-663.
11. Frost, D.C., S.T. Lee, C.A. McDowell, and N.P.C. Westwood, *The photoelectron spectra of diazene, diazene-d_2, and trans-methyldiazene.* J. Chem. Phys., 1976. **64**: p. 4719-4729.
12. von Niessen, W., W. Domcke, L.S. Cederbaum, and W.P. Kraemer, *Ionization potentials and vibrational structure in photoelectron spectra by a Green's function method: trans-HNNH, cis-HNNH, and 1,1-dihydrodiazine (H_2NN).* J. Chem. Phys., 1977. **67**: p. 44-51.
13. Schmidt, H., A. Schweig, B.M. Trost, H.B. Neubold, and P.H. Scudder, *Influence of Geometry on Cyclopropyl Participation in the Thermolysis of Azo Compounds. A Photoelectron Spectroscopic Rationalization.* J. Am. Chem. Soc., 1974. **96**: p. 622-624.
14. Kobayashi, T., K. Yokota, and S. Nagakura, *Photoelectron spectra of trans-azobenzene and benzalaniline.* J. Electron Spectrosc., 1975. **6**: p. 167-170.

15. Robin, M.B., C.R. Brundle, N.A. Kuebler, G.B. Ellison, and K.B. Wiberg, *Photoelectron Spectra of Small Rings. IV. The Unsaturated Three-Membered Rings.* J. Chem. Phys., 1972. **57**: p. 1758-1763.
16. Haselbach, E. and A. Schmelzer, *On the Correlation between Photoelectron and Electronic Spectra in trans-Azomethane.* Helv. Chim. Acta, 1971. **54**: p. 1575-1580.
17. Haselbach, E., A. Mannschreck, and W. Seitz, *'Lone pair' Electronic Structure, Conformation and Oxidation Behaviour of Diaziridines.* Helv. Chim. Acta, 1973. **56**: p. 1614-1620.
18. Brogli, F., W. Eberbach, E. Haselbach, E. Heilbronner, V. Hornung, and D.M. Lemal, *Die Photoelectronen-Spektren des Tricyclo[4.2.1.0]nonadiens und seines 3,4-Diaza-Analogons. Ein Beitrag zur Kenntnis der Wechselwirkung zwischen den einsamen Electronenpaaren der cis-konfigurierten Azogruppe.* Helv. Chim. Acta, 1973. **56**: p. 1933-1944.
19. Haselbach, E., J.A. Hashmall, E. Heilbronner, and V. Hornung, *The Interaction between the Lone Pairs in Azomethane.* Angew. Chem. Internat. Edit., 1969. **8**: p. 878.
20. Haselbach, E., E. Heilbronner, A. Mannschreck, and W. Seitz, *Lone Pair Interaction in 3,3-Dimethyldiazirine.* Angew. Chem. Internat. Edit., 1970. **9**: p. 902-903.
21. Frost, D.C., S.T. Lee, C.A. McDowell, and N.P.C. Westwood, *The photoelectron spectrum of diazene (diimine).* Chem. Phys. Lett., 1975. **30**: p. 26-27.
22. Ruscic, B. and J. Berkowitz, *Photoionization mass spectrometric study of N_2H_2 and N_2H_3: N-H, N=N bond energies and proton affinity of N_2.* J. Chem. Phys., 1991. **95**: p. 4378-4384.
23. Carlotti, M., J.W.C. Johns, and A. Trombetti, *The ν_5 Fundamental Bands of N_2H_2 and N_2D_2.* Can. J. Chem., 1974. **52**: p. 340-344.
24. Tjebbes, J., *The Heats of Combustion and Formation of the Three Diazines and their Resonance Energies.* Acta Chem. Scand., 1962. **16**: p. 916-921.
25. Ahlrichs, R. and V. Staemmler, *An Ab Initio Study of the Electronic Structure of Diimide.* Chem. Phys. Lett., 1976. **37**: p. 77-81.
26. Miller, C.E., J. Chem. Ed., 1965. **42**: p. 254.
27. Barney, B.M., T.-C. Yang, R.Y. Igarashi, P.C. Dos Santos, M. Laryukhin, H.-I. Lee, B.M. Hoffman, D.R. Dean, and L.C. Seefeldt, *Intermediates Trapped during Nitrogenase Reduction of NN, CH_3-N=NH, and H_2N-NH_2.* J. Am. Chem. Soc., 2005. **127**: p. 14960-14961.
28. Dance, I., *Elucidating the Coordination Chemistry and Mechanism of Biological Nitrogen Fixation.* Chem. Asian J., 2007. **2**: p. 936–946.
29. Levy, J. and B.K.W. Copeland, *The Thermal Decomposition of 2,2'-Azoisobutane.* J. Am. Chem. Soc., 1960. **82**: p. 5314-5318.
30. Engel, P.S., J.L. Wood, J.A. Sweet, and J.L. Margrave, *Thermochemistry of Azoalkanes.* J. Am. Chem. Soc., 1974. **96**: p. 2381-2387.
31. Armstrong, D.A., D. Yu, and A. Rauk, *Gas Phase and Aqueous Thermochemistry of Hydrazine and Related Radicals and the Energy Profiles of Reactions with H and OH: An ab Initio Study.* J. Phys. Chem. A, 1997. **101**: p. 4761-4769.
32. Lias, S.G., J.E. Bartmess, J.F. Liebman, J.L. Holmes, R.D. Levin, and W.G. Mallard, *Gas-Phase Ion and Neutral Thermochemistry.* J. Phys. Chem. Ref. Data, 1988. **17**(Suppl. 1).

33. Custer, T.G., S. Kato, V.M. Bierbaum, C.J. Howard, and G.C. Morrison, *Gas-Phase Kinetics and Mechanism of the Reactions of Protonated Hydrazine with Carbonyl Compounds. Gas-phase Hydrazone Formation: Kinetics and Mechanism.* J. Am. Chem. Soc., 2004. **126**: p. 2744-2754.
34. Catoire, L. and M.T. Swihart, *Thermochemistry of Species Produced from Monomethylhydrazine in Propulsion and Space-Related Applications.* J. Prop. Power, 2002. **18**: p. 1242-1253.
35. Lee, R.T. and G.B. Stringfellow, *Pyrolysis of Monomethylhydrazine for Organometallic Vapor-Phase Epitaxy (OMVPE) Growth.* J. Crystal Growth, 1999. **204**: p. 247-255.
36. Uesugi, K. and L. Suemune, *MetalOrganic Molecular Beam Epitaxy of GaNAs Alloys on (001) GaAs.* J. Crystal Growth, 1998. **189-190**: p. 490-495.
37. Takahashi, N., J. Ogasawara, and A. Koukitu, *Vapor Phase Epitaxy of GaNAs Alloys on (001) GaAs.* J. Crystal Growth, 1997. **172**: p. 298-302.
38. Syage, J.A., *Spectroscopy and dynamics of jet-cooled hydrazines and ammonia. II. Electron-impact dissociative ionization.* J. Chem. Phys., 1992. **97**: p. 6085-107.
39. Syage, J.A., R.B. Cohen, and J. Steadman, *Spectroscopy and dynamics of jet-cooled hydrazines and ammonia. I. Single-photon absorption and ionization spectra.* J. Chem. Phys., 1992. **97**: p. 6072-6084.
40. Rahimi, S., D. Hasan, and A. Peretz, *Development of Laboratory-Scale Gel-Propulsion Technology.* J. Prop. Power, 2004. **20**: p. 93-100.
41. Palaszewski, B. and R. Powell, *Launch Vehicule Performance Using Metallized Propellants.* Journal of Propulsion and Power, 1994. **10**: p. 828-833.
42. Harshman, R.C., Jet Propulsion, 1957. **27**: p. 398.
43. Bohn, M.A. and T.M. Klapötke, *DFT and G2MP2 Calculations of the N-N Bond Dissociation Enthalpies and Enthalpies of Formation of Hydrazine, Monomethylhydrazine and Symmetrical and Unsymmetrical Dimethylhydrazine.* Z. Naturforsch., 2004. **59b**: p. 148-152.
44. Nonnenberg, C., I. Frank, and T.M. Klapötke, *Ultrafast Cold Reactions in the Bipropellant Monomethylhydrazine/Nitrogen Tetroxide: CPMD Simulations.* Angew. Chem. internat. Edit., 2004. **43**: p. 4586-4589.
45. Sun, H. and C.K. Law, *Thermochemical and Kinetic Analysis of the Thermal Decomposition of Monomethylhydrazine: an Elementary Reaction Mechanism.* J. Phys. Chem. A, 2007. **111**: p. 3748-3760.
46. Feng, W.Y., V. Aviyente, T. Varnali, and C. Lifshitz, *Structures, Energetics, and Reactions of Proton-Bound Hydrazine Clusters.* J. Phys. Chem., 1995. **99**: p. 1776-85.
47. Oiestad, A.M.L. and E. Uggerud, *Loss of H_2 from $CH_2NH_2^+$ and $NHNH_2^+$. Reaction mechanisms and dynamics from observation of metastable ion fragmentations and ab initio calculations.* Int. J. Mass Spectrom. Ion Proc., 1997. **167/168**: p. 117-126.
48. Dibeler, V.H., J.L. Franklin, and R.M. Reese, *Electron Impact Studies of Hydrazine and the Methyl-substituted Hydrazines.* J. Am. Chem. Soc., 1959. **81**: p. 68-73.
49. Gardner, J.A., R.A. Dressler, and R.H. Salter, *Methylhydrazine Reactions with O^+ and Other Ions at Hyperthermal Collision Energies.* J. Phys. Chem., 1994. **98**: p. 11630-11636.

50. Holland, D.M.P., D.A. Shaw, I. Sumner, M.A. Hayes, R.A. Mackie, B. Wannberg, L.G. Shpinkova, E.E. Rennie, L. Cooper, C.A.F. Johnson, and J.E. Parker, *The design and performance of a threshold-photoelectron-photoion coincidence spectrometer for the study of unimolecular decomposition in polyatomic ions.* Nucl. Instr. Meth. Phys. Res. B, 2001. **179**: p. 436-454.
51. Baer, T., *The Dissociation Dynamics of Energy-Selected Ions*, in *Advances in Chemical Physics*, I. Prigogine and S.A. Rice, Editors. 1986, John Wiley & Sons: Toronto. p. 111-202.
52. Baer, T. and W.L. Hase, *Unimolecular Reactions Dynamics - Theory and Experiments*. 1996, New York: Oxford University Press.
53. Stockbauer, R., *Threshold electron-photoion coincidence mass spectrometric study of CH_4, CD_4, C_2H_6 and C_2D_6.* J. Chem. Phys., 1973. **58**: p. 3800-3815.
54. Stockbauer, R., *A Threshold Photoelectron-Photoion Coincidence Mass Spectrometer for Measuring Ion Kinetic Energy Release on Fragmentation.* Int. J. Mass Spectrom. Ion Phys., 1977. **25**: p. 89-101.
55. *IUPAC Compendium of Chemical Terminology*, A.D. McNaught and A. Wilkinson, Editors. 1997, IUPAC. p. http://www.iupac.org/publications/compendium/index.html.
56. Ng, C.-Y., *Vacuum Ultraviolet Spectroscopy and Chemistry by Photoionization and Photoelectron Methods.* Annu. Rev. Phys. Chem., 2002. **53**: p. 101-140.
57. Atkins, P.W., *Physical Chemistry*. 6th ed. 1998, New York: W. H. Freeman and Company.
58. Schmidt, V., *Electron Spectrometry of Atoms using Synchrotron Radiation.* 1997, Cambridge: Cambridge University Press.
59. Truhlar, D. and B.C. Garrett, *Variational Transition-State Theory.* Acc. Chem. Res., 1980. **13**: p. 440-448.
60. Hinshelwood, C.N., *The theory of unimolecular reactions.* Proc. Roy. Soc. London Ser. A, 1926. **113**: p. 230-233.
61. Marcus, R.A., *Unimolecular Dissociations and Free Radical Recombination Reactions.* J. Chem. Phys., 1952. **20**: p. 359-364.
62. Marcus, R.A., *Dissociation and Isomerization of Vibrationally Excited Species. III.* J. Chem. Phys., 1965. **43**: p. 2658-2661.
63. Baer, T. and P.M. Mayer, *Statistical Rice-Ramsperger-Kassel-Marcus Quasiequilibrium Theory Calculations in Mass Spectrometry.* J. Am. Soc. Mass Spectrom., 1997. **8**: p. 103-115.
64. Pechukas, P., *Transition State Theory.* Ann. Rev. Phys. Chem., 1981. **32**: p. 159-177.
65. Chesnavich, W.J. and M.T. Bowers, *Statistical methods in reaction dynamics*, in *Gas Phase Ion Chemistry*, M.T. Bowers, Editor. 1979, Academic Press, Inc.: New York. p. 119-151.
66. Wigner, E., *The transition-state method.* Trans. Faraday Soc., 1938. **34**: p. 29-41.
67. Miller, W.H., *Importance of Nonseparability in Quantum Mechanical Transition-State Theory.* Acc. Chem. Res., 1976. **9**: p. 306-312.
68. Miller, W.H., *Unified statistical model for "complex" and "direct" reaction mechanisms.* J. Chem. Phys., 1976. **65**: p. 2216-2223.

69. Chesnavich, W.J., L. Bass, T. Su, and M.T. Bowers, *Multiple transition states in unimolecular reactions: a transition state switching model. Application to the $C_4H_8^+$ system.* J. Chem. Phys., 1981. **74**: p. 2228-2246.
70. Oomens, J., B.G. Sartakov, G. Meijer, and G. von Helden, *Gas-phase infrared multiple photon dissociation spectroscopy of mass-selected molecular ions.* Int. J. Mass Spectrom., 2006. **254**: p. 1-19.
71. Riveros, J.M., *Infrared Photodissociation*, in *The Encyclopedia of Mass Spectrometry - Theory and Ion Chemistry*, M.L. Gross, Editor. 2003, Elsevier Ltd.: Oxford. p. 262-271.
72. Baer, T. and R. Kury, *Random Energy Flow in the Dissociation of Energy Selected Bromobenzene and Bromobenzene-d_5 Ions.* Chem. Phys. Lett., 1982. **92**: p. 659-6622.
73. Baer, T., B.P. Tsai, D. Smith, and P.T. Murray, *Absolute unimolecular decay rates of energy selected metastable halobenzene ions.* J. Chem. Phys., 1976. **64**: p. 2460-2465.
74. Lifshitz, C., Adv. Mass Spectrom., 1978. **7A**: p. 3.
75. Klippenstein, S.J., Y.-C. Yang, V. Ryzhov, and R.C. Dunbar, *Theory and modeling of ion–molecule radiative association kinetics.* J. Chem. Phys., 1996. **104**: p. 4502-4516.
76. Klippenstein, S.J., *Implementation of RRKM theory for highly flexible transition states with a bond length as the reaction coordinate.* Chem. Phys. Lett., 1990. **170**: p. 71-77.
77. Harding, L.B., Y. Georgievskiia, and S.J. Klippenstein, *Predictive Theory for Hydrogen Atom-Hydrocarbon Radical Association Kinetics.* J. Phys. Chem. A, 2005. **109**: p. 4646-4656.
78. Klippenstein, S.J. and L.B. Harding, *A Summary of "A Direct Transition State Theory Based Study of Methyl Radical Recombination Kinetics".* J. Phys. Chem. A, 2000. **104**: p. 2351-2354.
79. Klippenstein, S.J. and L.B. Harding, *A Direct Transition State Theory Based Study of Methyl Radical Recombination Kinetics.* J. Phys. Chem. A, 1999. **103**: p. 9388-9398.
80. Klippenstein, S.J., Y. Georgievskiia, and L.B. Hardingb, *Predictive theory for the combination kinetics of two alkyl radicals.* Phys. Chem. Chem. Phys., 2006. **8**: p. 1133-1147.
81. Garrett, B.C. and D. Truhlar, *Criterion of minimum state density in the transition state theory of bimolecular reactions.* J. Chem. Phys., 1979. **70**: p. 1593-1598.
82. Georgievskiia, Y. and S.J. Klippenstein, *Long-range transition state theory.* J. Chem. Phys., 2005. **122**: p. 194103.
83. Keck, J.C., *Variational Theory of Chemical Reaction Rates Applied to Three-Body Recombinations.* J. Chem. Phys., 1960. **32**: p. 1032-1050.
84. Lifshitz, C., F. Louage, and V. Aviyente, *Transition-State Switchings for Single Potential Well Ionic Dissociations.* J. Phys. Chem., 1991. **95**: p. 9298-9302.
85. Holmes, J.L. and P.M. Mayer, *A Combined Mass Spectrometric and Thermochemical Examination of the C_2H_2N Family of Cations and Radicals.* J. Phys. Chem., 1995. **99**: p. 1366-1370.
86. Cooks, R.G., J.H. Beynon, R.M. Caprioli, and G.R. Lester, *Metastable Ions.* 1973, Amsterdam: Elsevier.

87. Holmes, J.L., *Instrumentation*, in *The Encyclopedia of Mass Spectrometry - Theory and Ion Chemistry*, M.L. Gross and R.M. Caprioli, Editors. 2003, Elsevier Inc.: San Diego. p. 91-98.
88. Holland, D.M.P., J.B. West, A.A. Macdowell, I.H. Munro, and A.G. Beckett, *The performance of a 5 metre normal incidence monochromator at the Daresbury Laboratory Synchrotron Radiation Source.* Nucl. Instr. Meth. Phys. Res. B, 1989. **44**: p. 233-241.
89. Wiley, W.C. and I.H. McLaren, *Time-of-Flight Mass Spectrometer with Improved Resolution.* Rev. Sci. Instrum., 1955. **26**: p. 1150-1157.
90. Rennie, E.E., L. Cooper, C.A.F. Johnson, J.E. Parker, R.A. Mackie, L.G. Shpinkova, D.M.P. Holland, D.A. Shaw, and M.A. Hayes, *A study of the unimolecular decomposition of internal-energy-selected furan molecular ions by threshold-photoelectron-photoion coincidence spectroscopy.* Chem. Phys., 2001. **263**: p. 149-165.
91. Boulanger, A.-M., E.E. Rennie, D.M.P. Holland, D.A. Shaw, and P.M. Mayer, *Thermochemistry of N-N Containing Ions: A TPEPICO Study of Ionized Methyl- and Tetramethylhydrazine.* J. Phys. Chem. A, 2008. **112**: p. 866-879.
92. Boulanger, A.-M., E.E. Rennie, D.M.P. Holland, D.A. Shaw, and P.M. Mayer, *Entropy Effects in the Fragmentation of 1,1-Dimethylhydrazine Ions.* J. Phys. Chem. A, 2007. **111**: p. 5388-5398.
93. Butler, J.J., D.M.P. Holland, A.C. Parr, R. Stockbauer, and R. Buff, *Automation of the NBS threshold photoelectron-photoion coincidence mass spectrometer.* J. Phys. E, 1985. **18**: p. 286-289.
94. Chupka, W.A., *Effects of Unimolecular Decay Kinetics on the Interpretation of Appearance Potentials.* J. Chem. Phys., 1959. **30**: p. 191-211.
95. Frisch, M.J., G.W. Trucks, H.B. Schlegel, G.E. Scuseria, M.A. Robb, J.R. Cheeseman, V.G. Zakrzewski, J.A. Montgomery, R.E. Stratmann, J.C. Burant, S. Dapprich, J.M. Millam, A.D. Daniels, K.N. Kudin, M.C. Strain, O. Farkas, J. Tomasi, V. Barone, M. Cossi, R. Cammi, B. Mennucci, C. Pomelli, C. Adamo, S. Clifford, J. Ochterski, G.A. Petersson, P.Y. Ayala, Q. Cui, K. Morokuma, D.K. Malick, A.D. Rabuck, K. Raghavachari, J.B. Foresman, J. Cioslowski, J.V. Ortiz, B.B. Stefanov, G. Liu, A. Liashenko, P. Piskorz, I. Komaromi, R. Gomperts, R.L. Martin, D.J. Fox, T. Keith, M.A. Al-Laham, C.Y. Peng, A. Nanayakkara, C. Gonzalez, M. Challacombe, P.M.W. Gill, B. Johnson, W. Chen, M.W. Wong, J.L. Andres, C. Gonzalez, M. Head-Gordon, E.S. Replogle, and J.A. Pople, *GAUSSIAN 98 Rev. A.6*, in *GAUSSIAN 98 Rev. A.6*. 1998, Gaussian Inc.: Pittsburgh PA.
96. Curtiss, L.A., K. Raghavachari, G.W. Trucks, and J.A. Pople, *Gaussian-2 theory for molecular energies of first- and second-row compounds.* J. Chem. Phys., 1991. **94**: p. 7221-7230.
97. Pople, J.A., *Gaussian-1 theory: A general procedure for prediction of molecular energies.* J. Chem. Phys., 1989. **90**: p. 5622-5629.
98. Curtiss, L.A., K. Raghavachari, P.C. Redfern, V. Rassolov, and J.A. Pople, *Gaussian-3 (G3) theory for molecules containing first and second-row atoms.* J. Chem. Phys., 1998. **109**: p. 7764-7776.

99. Nicolaides, A., A. Rauk, M.N. Glukhovtsev, and L. Radom, *Heats of Formation from G2, G2(MP2), and G2(MP2,SVP) Total Energies.* J. Phys. Chem., 1996. **100**: p. 17460-17464.
100. Baer, T. and W.L. Hase, *Unimolecular Reaction Dynamics, Theory and Experiments.* 1996, New York: Oxford University Press.
101. Beyer, T. and D.R. Swinehart, *Algorithm 448 Number of Multiply-Restricted Partitions.* ACM Commun., 1973. **16**: p. 379.
102. Engel, T. and P. Reid, *Physical Chemistry.* 2006, San Franscico: Pearson Education, Inc.
103. East, A.L.L. and L. Radom, *Ab initio statistical thermodynamical models for the computation of third-law entropies.* J. Chem. Phys., 1997. **106**: p. 6655-6674.
104. Franklin, J.L., *Prediction of Heat and Free Energies of Organic Compounds.* Ind. Eng. Chem., 1949. **41**: p. 1070-1076.
105. Boulanger, A.-M., E.E. Rennie, D.M.P. Holland, D.A. Shaw, and P.M. Mayer, *Threshold-Photoelectron Spectroscopic Study of Methyl-Substituted Hydrazine Compounds.* J. Phys. Chem. A, 2006. **110**: p. 8563-8571.
106. Holmes, J.L., C. Aubry, and P.M. Mayer, *Assigning structures to ions in mass spectrometry.* 2007, Boca Raton: CRC Press.
107. *NIST Chemistry WebBook, NIST Standard Reference Database Number 69*, W.G. Mallard and P.J. Linstrom, Editors. 2000, National Institute of Standards and Technology: Gaithersburg MD.
108. Meot-Ner, M., S.F. Nelsen, M.R. Willi, and T.B. Frigo, *Special Effects of an Unusually Large Neutral to Radical Cation Geometry Change. Adiabatic Ionization Energies and Proton Affinities of Alkylhydrazines.* J. Am. Chem. Soc., 1984. **106**: p. 7384-7389.
109. Boulanger, A.-M., E.E. Rennie, D.M.P. Holland, D.A. Shaw, and P.M. Mayer, *Threshold-Photoelectron Spectroscopic Study of Methyl-Substituted Hydrazine Compounds (Addition/Correction).* J. Chem. Phys. A, 2007. **111**: p. 10884-10885.
110. Akopyan, M.E. and F.I. Vilesov, *Decay of the Molecular Ions Formed in Photoionization of Hydrazine and some of its Alkyl Derivatives.* Kinetica i Kataliz, 1963. **4**: p. 39.
111. Holmes, J.L., *The Correlation of Thermochemical Data*, in *The Encyclopedia of Mass Spectrometry*, M.L. Gross, Editor. 2003, Elsevier Inc.: San Diego. p. 434-440.
112. Pople, J.A. and L.A. Curtiss, *The energy of the diazene molecule (N_2H_2) and related compounds.* J. Chem. Phys., 1991. **95**: p. 4385-4388.
113. Hunter, E.P. and S.G. Lias, *Evaluated Gas Phase Basicities and Proton Affinities of Molecules: An Update.* J. Phys. Chem. Ref. Data, 1998. **27**: p. 413.
114. Hillebrand, C., M. Klessinger, M. Eckert-Maksic, and Z.B. Maksic, *Theoretical Model Calculations of the Proton Affinities of Aminoalkanes, Aniline, and Pyridine.* J. Phys. Chem., 1996. **100**: p. 9698-9702.
115. Nelsen, S.F., D.T. Rumack, L.W. Sieck, and M. Meot-Ner, *Proton Affinities and pK_a Values of Tetraalkylhydrazines.* J. Am. Chem. Soc., 1988. **110**: p. 6303-6308.
116. Blanskby, S.J. and G.B. Ellison, *Bond Dissociation Energies of Organic Molecules.* Acc. Chem. Res., 2003. **36**: p. 255-263.
117. Foner, S.N. and R.L. Hudson, *Mass spectrometry of inorganic free radicals.* Advan. Chem. Ser., 1962. **36**: p. 34.

118. Foner, S.N. and R.L. Hudson, *Mass spectrometric studies of atom-molecule reactions using high-intensity crossed molecular beams.* J. Chem. Phys., 1970. **53**: p. 4377-4386.
119. Fisher, I.P. and E. Henderson, *Mass spectrometry of free radicals.* J. Chem. Soc. Faraday Trans., 1967. **63**: p. 1342-1348.
120. Gowenlock, B.G., P.P. Jones, and J.R. Majer, *Bond Dissociation Energies in Some Molecules Containing Alkyl Substituted CH_3, NH_2 and OH.* Trans. Faraday Soc., 1961. **57**: p. 23-27.

Appendix A

PROGRAMS

A1. Program for calculating the sum and densities of states

This program was used to calculate the sum and densities of states using the direct count method developed by Beyer and Swinehart.

```
* calculation of Density and Sum of States and Unimolecular Rate Constants
* with the use of the Beyer-Swinehart scheme for Direct Count
*
* This FORTRAN program was adapted from the BASIC version quoted in
* P.M. Mayer and T. Baer, J. Am. Soc. Mass Spectrom. 1997, 8, 103-115.
*  by Paul M. Mayer (Chem Dept, U of Ottawa, Ottawa, Canada K1N 6N5)
*   25/7/97
*
* The variables:
* Eo   the activation energy
* MIN and IMIN are the minimum energy for which you want a k printed
* MAX and IMAX are the maximum energy for which you want a k calc and print
* NUM and INUM is the interval you want the k printed at
* Nfreq is the number of vibrational frequencies for both ion and ts
* w(100) is the array into which freqs are put
* p(32000) is the density of states vector in which densities are put
* N(32000) is the sum of states vector in which sums are put
* RATE(32000) is the rate constant vector into which k's are put
* LOGRATE(32000) is the vector into which is put log10(k)
* QMolc, QTs are the ion and ts partition functions at 600K
* UMolc, UTs are the ion and ts internal energies at 600K
*
* The constants:
*  H=3.3364E-11 is Planck's constant in cm-1 sec
*  Kb=1.3807E-23 in Boltzman's constant in J/K
*  Na=6.022E23 is Avogadro's number
*  HJ=6.6262E-34 is Planck's constant in Jsec
*  c=2.9979E10 is the speed of light in cm/sec
*  T is temperature in Kelvin
*
* STEP 1. Variable declaration:
*
```

```
      INTEGER IEo,Nfreq,IMIN,INCR,IMAX,ITMAX,J,I,T,v(1000),Nrot
      REAL w(1000),rB(10),LOGRATE(480000), m(1000)
      DOUBLE PRECISION p(480000)
      DOUBLE PRECISION N(480000)
      DOUBLE PRECISION RATE(480000)
      REAL Eo,MAX,MIN,NUM,QMolc,UMolc,QTs,UTs,Sts
      REAL H,Kb,Na,HJ,c,Sigma,BA,BC, L
      CHARACTER Title*80,Name*6
*
* STEP 2. Reading in the stuff
*
      WRITE (*,'("input file name")')
      READ (*,'(a6)') Name
      OPEN (UNIT=8, FILE=Name, STATUS='OLD')
      READ (8,'(a80)') Title
      READ (8,*) Eo,MIN,MAX,NUM,Sigma
      READ (8,*) BA,BC
      READ (8,*) Nfreq
      READ (8,*) (w(I),I=1,Nfreq)
      READ (8,*) Nrot
      READ (8,*) (rb(I),I=1,Nrot)
*
* STEP 3. Converting input energies to integral units of 0.1 meV
*
      Eo=Eo*10000.0        !converting to units of 0.1 meV
      IEo=NINT(Eo)       ! converting to an integer
      MAX=MAX*10000.0      ! converting to units of 0.1 meV
      IMAX=NINT(MAX)     ! converting to an integer
      ITMAX=IMAX-IEo     ! defining transition state maximum energy
      MIN=MIN*10000.0
      IMIN=NINT(MIN)
*
*     Converting input frequencies to integers
*
      DO 20 J=1,Nfreq,1
      m(J)=w(J)*1.24
      v(J)=NINT(m(J))
20    CONTINUE
*
*     Converting rotational constants (GHz) to units of 0.1 meV
*
      Kb=1.3807E-23;Na=6.022E23;HJ=6.6262E-34;c=2.9979E10;T=600
      L=4.136E-11
*
      BA=BA*1.0E9*L
      BC=BC*1.0E9*L
```

```
*
    DO 30 J=1,Nrot,1
    rB(J)=rB(J)*(1.0E9)*L
30   CONTINUE
*
* STEP 4. Initializing p and N vectors
*
    DO 40 J=1,480000,1
      p(J)=0
      N(J)=0
40   CONTINUE
*
* STEP 4a. Adding to p an N vectors the internal rotor densities
*
    DO 50 J=1,480000,1
       DO 45 I=1,Nrot,1
        p(J)=p(J)+SQRT(1/(rB(I)*J))
45   CONTINUE
50   CONTINUE
*
* STEP 4b. Adding to p an N vectors the molecular rotational densities
*
    DO 60 J=1,480000,1
        p(J)=p(J)+(2*J**(0.5))/(BA*SQRT(BC))
60   CONTINUE
*
* STEP 5. Convoluting in the vibrational density of states
*
    DO 200 J=1,Nfreq,1
      DO 100 I=v(J),IMAX,1
       IF ((I-v(J)) .EQ. 0) THEN
         p(I)=p(I)+0
       ELSE
       p(I) = p(I) + p(I - v(J))
       END IF
100    CONTINUE
200  CONTINUE
*
* STEP 6. Calculating ion partition function and internal energy
*
    QMolc=1; UMolc=0
    DO 250 I=1,Nfreq,1
      QMolc=QMolc*(1/(1-EXP(-w(I)/417.0)))    !calcing molc partion fcn
      UMolc=UMolc + (w(I)/(EXP(w(I)/417.0)-1)) ! calcing molc int nrg
250  CONTINUE
*
```

```
* STEP 7. Calculating sum of states of transition state
*
    READ (8,*) BA,BC
    READ (8,*) Nfreq
    READ (8,*) (w(I),I=1,Nfreq)
    READ (8,*) Nrot
    READ (8,*) (rB(I),I=1,Nrot)
*
* making TS frequencies integers
*
    DO 270 J=1,Nfreq,1
    m(J)=w(J)*1.24
    v(J)=NINT(m(J))
270  CONTINUE
*
* converting rotational constants to units of 0.1 meV from GHz
*
    BA=BA*1.0E9*L
    BC=BC*1.0E9*L
*
    DO 275 J=1,Nrot,1
      rB(J)=rB(J)*(1.0E9*L)
275  CONTINUE
*
* STEP 7a. Adding to N vector the internal rotor sums
*
    DO 285 J=1,480000,1
       DO 280 I=1,Nrot,1
       N(J)=N(J)+2*SQRT(J/rB(I))
280  CONTINUE
285  CONTINUE
*
* STEP 7b. Adding to N vector the molecular rotational sums
*
    DO 290 J=1,480000,1
        N(J)=N(J)+(4/3)*(J**(1.5))/(BA*SQRT(BC))
290  CONTINUE
*
* STEP 7c.  Convoluting in the vibrational sums
*
    DO 400 J=1,Nfreq,1
      DO 300 I=v(J),ITMAX,1
        N(I) = N(I) + N(I-v(J))
300     CONTINUE
400  CONTINUE
*
```

```
* STEP 8. Calculating ts partition function and internal energy at 600K
*
    QTs=1; UTs=0
    DO 450 I=1,Nfreq,1
      QTs=QTs*(1/(1-EXP(-w(I)/417.0)))     !calcing molc partion fcn
      UTs=UTs + (w(I)/(EXP(w(I)/417.0)-1)) ! calcing molc int nrg
450   CONTINUE
*
* STEP 9. Calculating rate constant at specific intervals
*
    H=3.3364E-11
    DO 500 J=1,ITMAX,1
    RATE(J)=(Sigma*N(J))/(H*p(J+IEo))
    LOGRATE(J) = LOG10(RATE(J))
500   CONTINUE
*
* STEP 10. Calculating entropy of activation at 600K
*
    Sts= ((Kb*LOG(Qts/QMolc)) + (HJ*c*(UTs-UMolc))/T)*Na
*
* STEP 8. Printing it off
*
    PRINT '("RRKM k(E) vs E using the Direct Count method")'
    PRINT 550, Title
550   FORMAT (1X,A80)
    PRINT 560, Sts
560   FORMAT ('entropy of activation (J/K/mol) at 600K is', 1PG15.7E2)
    PRINT 600
600   FORMAT (' E       RATE       Log10RATE       p       N')
*
    INCR=INT((IMAX-IMIN)/(NUM-1))
    DO 800 J=IMIN-IEo,IMAX-IEo,INCR
    PRINT 700, (J+IEo)/10000.0, RATE(J), LOGRATE(J), p(J+IEo), N(J)
700   FORMAT (1PG10.4E2,E15.7E2,1PG13.4E2,E20.7E3,E20.7E3)
800   CONTINUE
*
    DO 950 J=IMIN-IEo,IMAX-IEo,10
    WRITE (9,900) (J+IEo)/10000.0, RATE(J)
900   FORMAT (1PG10.4E2,E20.7E2)
*
950   CONTINUE
    DO 1050 J=IMIN-IEo,IMAX-IEo,10
    WRITE (10,1000) (J+IEo)/10000.0, p(J+IEo)
1000  FORMAT (1PG10.4E2,E20.7E3)
1050  CONTINUE
    END
```

A2. Program for fitting the breakdown diagrams

This is the program used to fit the experimental breakdown curves. This version of the program can be used to fit simultaneously three fragment ions.

```
      Program main
c     Calculate breakdown curve. Convolute breakdown curve with P(E',T) then with
electfunc
c     k needs to go at least number of points in electfunc below 1st
c     required k'
c     ek energy(eV)
c
        integer i,j,l,m
      real ek(2000),k(2000),ep(2000),p(2000),el(2000)
      real eel(2000),Pk(2000,10),Dk1(2000,10),Pkpe(2000,10)
      real Dkpe1(2000,10),Dkpe2(2000,10),Dkpe3(2000,10),delay(10)
      real Pkp(2000,10)
      real sum,tot,psum,k1(2000),k2(2000),k3(2000),Dk2(2000,10)
      real Dk3(2000,10),pa(2000)
      real sum1,sum2,sum3,tot1,tot2,tot3,Dkp1(2000,10),Dkp2(2000,10)
      real Dkp3(2000,10)
      real res,sig,dum,gauss(2000)
      real Pg(2000,10),Dg1(2000,10),Dg2(2000,10),Dg3(2000,10)
      real ela(2000),esum


      do 1,i=1,2000
       k1(i)=0.0
       k2(i)=0.0
       k3(i)=0.0
1     continue


        open (unit=3, file= 'k45.dat',status='unknown')
      i=1
5       read(3,*,err=10) ek(i),k1(i)
      i=i+1
      goto 5
10    nptsk=i-1

        open (unit=17, file= 'k31.dat',status='unknown')
      i=1
6       read(17,*,err=11) ek(i),k2(i)
      i=i+1
      goto 6
```

```
11    nptsk=i-1

        open (unit=27, file= 'k30.dat',status='unknown')
      i=1
55    read(27,*,err=60) ek(i),k3(i)
      i=i+1
      goto 55
60    nptsk=i-1


c     Generate a slope function K rises to 5000000in ~300meV
c     do 10 i=1,400
c      ek(i)=i*0.004
c      k(i)=(i-200)*70000.0
c      if (i.le.200) k(i)=0.0
c10    continue
c     nptsk=400

      print *,nptsk
      psum=0.0
      open (unit=4, file= 'p.dat',status='unknown')
      i=1
15    read(4,*,err=20) ep(i),pa(i)
      psum=psum+pa(i)
      i=i+1
      goto 15
20    nptsp=i-1
      print *,nptsp
      do 21 i=1,nptsp
       p(i)=pa(i)/psum
21    continue



      open (unit=15, file= 'electfunc3.dat',status='unknown')
      i=1
      esum=0.0
25    read(15,*,err=30) eel(i),ela(i)
      esum=esum+ela(i)
      i=i+1
      go to 25
30    nptsel=i-1
      print *,nptsel
      do 26 i=1,nptsel
       el(i)=ela(i)/esum
26    continue
```

```
      open (unit=16, file= 'delay.dat',status='unknown')
      read(16,*) nptsd
      do 31 i=1,nptsd
       read(16,*) delay(i)
       print*, delay(i)
31     continue

c     Gaussian 1/sig*sqrt(2Pi) exp(0.5((x-ave)/sig)**2)
      do 33 i=1,31
c       res=FWHM mono in meV
       res=8
      sig=res/2.3548
      dum=(i-16)/sig
      dum2=dum**2
      gauss(i)=(1/(sig*2.5066))*exp(-0.5*dum2)
33     continue

      close (unit=3)
      close (unit=4)
      close (unit=15)
      close (unit=16)
      close (unit=17)
      close (unit=27)

c     Calc breakdown from k(e)
      do 32 i=1,nptsk
      do 32 j=1,nptsd
      k(i)=k1(i)+k2(i)+k3(i)
      if(k(i).LE.0) k(i)=.00001
        Pk(i,j)=exp(-delay(j)*1e-6*(k1(i)+k2(i)+k3(i)))
        Dk1(i,j)=(k1(i)/k(i))*(1-Pk(i,j))
      Dk2(i,j)=(k2(i)/k(i))*(1-Pk(i,j))
      Dk3(i,j)=(k3(i)/k(i))*(1-Pk(i,j))
32     continue

c     Gaussian convolution
      do 34 l=1,nptsd
      do 34 i=1,nptsk
       Pg(i,l)=0.0
       Dg1(i,l)=0.0
       Dg2(i,l)=0.0
       Dg3(i,l)=0.0
34     continue
      do 35 l=1,nptsd
      do 35 i=1,nptsk
```

```
      sum=0
      sum1=0.0
      sum2=0.0
      sum3=0.0
      tot=0
      tot1=0.0
      tot2=0.0
      tot3=0.0
     do 35 j=1,31
      if(i+j-1 .ge .nptsk) goto 35
      tot=Pk((i+j-1),l)*gauss(j)
      tot1=Dk1((i+j-1),l)*gauss(j)
      tot2=Dk2((i+j-1),l)*gauss(j)
      tot3=Dk3((i+j-1),l)*gauss(j)
      sum=sum+tot
      sum1=sum1+tot1
      sum2=sum2+tot2
      sum3=sum3+tot3
      m=i+16-1
      Pg(m,l)=sum
      Dg1(m,l)=sum1
      Dg2(m,l)=sum2
      Dg3(m,l)=sum3
35    continue

c     Convolution P(e)
     do 40 l=1,nptsd
     do 40 i=16,nptsk
      sum=0
      sum1=0.0
      sum2=0.0
      sum3=0.0
      tot=0
      tot1=0.0
      tot2=0.0
      tot3=0.0
      do 40 j=1,nptsp
       if(i+j-1 .ge .nptsk) goto 40
c        print*,i,j,l,p(j),Pg((i+j-l),l)
       tot=Pg((i+j-1),l)*p(j)
       tot1=Dg1((i+j-1),l)*p(j)
       tot2=Dg2((i+j-1),l)*p(j)
       tot3=Dg3((i+j-1),l)*p(j)
       sum=sum+tot
       sum1=sum1+tot1
       sum2=sum2+tot2
```

```
        sum3=sum3+tot3
        Pkp(i,l)=sum
        Dkp1(i,l)=sum1
        Dkp2(i,l)=sum2
        Dkp3(i,l)=sum3
 40    continue

c      convolution with electfunc
       do 41 i=1,2000
       do 41 j=1,10
        Pkpe(i,j)=0.0
        Dkpe1(i,j)=0.0
        Dkpe2(i,j)=0.0
        Dkpe3(i,j)=0.0
41      continue

       do 50 l=1,nptsd
       do 50 i=16,nptsk
         sum=0.0
         sum1=0.0
         sum2=0.0
         sum3=0.0
         tot=0.0
         tot1=0.0
         tot2=0.0
         tot3=0.0
         do 50 j=1,nptsel
          if(i+j-1 .ge .nptsk) goto 50
          tot=Pkp((i+j-1),l)*el(j)
          tot1=Dkp1((i+j-1),l)*el(j)
          tot2=Dkp2((i+j-1),l)*el(j)
          tot3=Dkp3((i+j-1),l)*el(j)
          sum=sum+tot
          sum1=sum1+tot1
          sum2=sum2+tot2
          sum3=sum3+tot3
          m=i+nptsel-1
          Pkpe(m,l)=sum
          Dkpe1(m,l)=sum1
          Dkpe2(m,l)=sum2
          Dkpe3(m,l)=sum3
50     continue

       open(unit=8 ,file='breakfrag.dat', status='unknown')
       open(unit=9 ,file='breakfragconv.dat', status='unknown')
       open(unit=10 ,file='breakfraggauss.dat', status='unknown')
```

```
      write(8,96)(delay(i),i=1,nptsd)
      write(9,96)(delay(i),i=1,nptsd)
96     format(5x,'E',4x,'delay',4(f8.4,10x))

      do 200 i=nptsel+15,nptsk-16
      write(8,100)ek(i),(Pk(i,j),Dk1(i,j),Dk2(i,j),Dk3(i,j),j=1,nptsd)
c     the next statement goes over two physical lines
      write(9,100)ek(i),
     + (Pkpe(i,j),Dkpe1(i,j),Dkpe2(i,j),Dkpe3(i,j),j=1,nptsd)
c     the next statement goes over two physical lines
      write(10,100)ek(i),
     + (Pg(i,j),Dg1(i,j),Dg2(i,j),Dg3(i,j),j=1,nptsd)
100    format(1x,f8.4,12(f7.4))
200    continue

      close (unit=8)
      close (unit=9)


      end
```

Appendix B

VIBRATIONAL FREQUENCIES AND GEOMETRICAL PARAMETERS

B1. Vibrational frequencies

The vibrational frequencies of the three methyl-substituted hydrazine ions, their dissociation products and various transition states are listed in Tables B.1–B.3. The vibrational frequencies of the methyl radical ($CH_3^{\bullet}$) and methane (CH_4) are only listed in Tables B.1 and B.2, respectively. These sets of vibrational frequencies were used to fit theoretically the experimental breakdown curves of the hydrazine ions. These vibrational frequencies have been scaled with the correction factor of 0.9614. The theoretical fits were obtained by scaling the five lowest vibrational frequencies of the transition states by another scaling factor, usually less than one, until a good agreement was obtained with the experimental breakdown curves. These "scaled" vibrational frequencies are not listed in the following tables except for the methane loss channel (see Tables B.2 and B.3 for explanations).

Table B.1: Calculated Vibrational Frequencies and Rotational Constants for the 1,1-Dimethylhydrazine Ion, its Transition States and Dissociation Products[a]

	harmonic frequencies (cm^{-1})[b] and rotational constants (GHz)
$(CH_3)_2NNH_2^{+\bullet}$	111, 139, 296, 382, 398, 453, 555, 772, 992, 1051, 1074, 1098, 1121, 1345, 1379, 1404, 1422, 1428, 1443, 1446, 1478, 1617, 2939, 2943, 3027, 3027, 3064, 3069, 3377, 3499, 4.7 GHz, 8.4 GHz, 9.4 GHz
$CH_3NNH_2^+$	225, 482, 694, 906, 945, 1086, 1102, 1313, 1335, 1377, 1441, 1568, 1682, 2910, 2973, 3020, 3183, 3355, 9.3 GHz, 10.5 GHz, 54.7 GHz
$(CH_3)(CH_2)NNH_2^+$	152, 265, 441, 471, 498, 666, 727, 822, 957, 1036, 1082, 1118, 1208, 1345, 1407, 1432, 1438, 1466, 1637, 1677, 2974, 3057, 3074, 3094, 3190, 3368, 3476, 5.1 GHz, 9.3 GHz, 10.1 GHz
$(CH_3)_2NNH^+$	74, 166, 404, 461, 537, 758, 860, 917, 1103, 1136, 1143, 1143, 1380, 1392, 1406, 1407, 1427, 1436, 1453, 1670, 2959, 2968, 3040, 3048, 3075, 3098, 3237, 5.0 GHz, 8.7 GHz, 10.3 GHz

Table B.1: continued

	harmonic frequencies (cm^{-1})[b] and rotational constants (GHz)
$CH_3^{\bullet}$	500, 1370, 1370, 3011, 3178, 3178, 142.2 GHz, 284.5 GHz, 284.5 GHz
transition states for methyl loss	
$TS(45)_1$ (R^* = 2.565 Å)	60, 122, 162, 230, 400, 416, 484, 633, 734, 889, 906, 1062, 1090, 1282, 1361, 1374, 1382, 1397, 1442, 1455, 1642 2913, 2982, 3015, 3069, 3189, 3196, 3255, 3428, 3.3 GHz, 4.6 GHz, 9.2 GHz
$TS(45)_2$ (R^* = 2.665 Å)	56, 115, 147, 223, 356, 366, 486, 643, 764, 872, 889, 1064, 1091, 1286, 1359, 1374, 1381, 1395, 1446, 1461, 1645, 2912, 2982, 3015, 3065, 3188, 3195, 3245, 3420, 3.2 GHz, 4.4 GHz, 9.2 GHz
$TS(45)_3$ (R^* = 2.765 Å)	50, 109, 134, 217, 318, 325, 486, 651, 786, 843, 889, 1066, 1092, 1290, 1356, 1374, 1380, 1393, 1447, 1470, 1648, 2912, 2983, 3014, 3060, 3187, 3194, 3237, 3413, 3.1 GHz, 4.2 GHz, 9.2 GHz
$TS(45)_4$ (R^* = 2.865 Å)	42, 106, 124, 212, 284, 293, 487, 656, 803, 819, 890, 1068, 1093, 1292, 1354, 1373, 1379, 1392, 1447, 1478, 1650, 2912, 2985, 3014, 3055, 3187, 3193, 3231, 3408, 3.0 GHz, 4.0 GHz, 9.2 GHz
$TS(45)_5$ (R^* = 3.165 Å)	33, 91, 104, 200, 216, 233, 486, 665, 765, 839, 893, 1071, 1095, 1298, 1348, 1373, 1377, 1389, 1446, 1495, 1654, 2913, 2987, 3014, 3041, 3185, 3191, 3218, 3397, 2.6 GHz, 3.4 GHz, 9.2 GHz
$TS(45)_6$ (R^* = 3.965 Å)	20, 51, 74, 146, 149, 203, 484, 671, 709, 859, 900, 1074, 1097, 1302, 1343, 1374, 1374, 1387, 1443, 1504, 1657, 2915, 2988, 3016, 3019, 3188, 3191, 3209, 3389, 1.9 GHz, 2.3 GHz, 9.3 GHz
$TS(45)_7$ (R^* = 4.065 Å)	19, 48, 72, 140, 143, 203, 484, 671, 707, 858, 901, 1073, 1097, 1302, 1343, 1374, 1374, 1387, 1443, 1504, 1657, 2915, 2987, 3017, 3018, 3189, 3191, 3209, 3389, 2.2 GHz, 2.2 GHz, 9.3 GHz
$TS(45)_8$ (R^* = 4.265 Å)	17, 42, 68, 125, 129, 200, 484, 671, 704, 856, 903, 1073, 1097, 1301, 1343, 1374, 1375, 1387, 1443, 1503, 1657, 2914, 2986, 3016, 3017, 3190, 3191, 3209, 3390, 1.7 GHz, 2.0 GHz, 9.3 GHz
$TS(45)_9$ (R^* = 4.365 Å)	15, 39, 66, 120, 126, 198, 484, 671, 705, 855, 903, 1073, 1097, 1301, 1343, 1374, 1375, 1387, 1443, 1503, 1657, 2914, 2985, 3015, 3017, 3191, 3192, 3210, 3391, 1.6 GHz, 1.9 GHz, 9.3 GHz
transition states for hydrogen loss	
$TS(59)_1$ (R^* = 2.098 Å)	141, 253, 311, 349, 438, 492, 509, 671, 768, 825, 946, 1042, 1080, 1113, 1188, 1348, 1406, 1428, 1428, 1437, 1462, 1589, 1636, 2967, 3048, 3075, 3092, 3192, 3369, 3481, 4.8 GHz, 8.4 GHz, 9.0 GHz
$TS(59)_2$ (R^* = 2.198 Å)	145, 233, 273, 285, 439, 487, 498, 680, 753, 824, 942, 1039, 1081, 1115, 1195, 1346, 1407, 1429, 1438, 1463, 1614, 1638, 2969, 3050, 3075, 3092, 3192, 3367, 3478, 4.8 GHz, 8.4 GHz, 8.9 GHz
$TS(59)_3$ (R^* = 2.298 Å)	147, 198, 231, 262, 439, 482, 496, 683, 745, 824, 941, 1037, 1081, 1116, 1200, 1346, 1407, 1430, 1438, 1463, 1630, 1642, 2970, 3052, 3076, 3092, 3193, 3367, 3476, 4.8 GHz, 8.3 GHz, 8.9 GHz

[a] The present work has been published in Boulanger et al. [92] [b] Vibrational frequencies calculated at the B3-LYP/6-31+G(d) level of theory, scaled by 0.9614.

Table B.2: Calculated Vibrational Frequencies and Rotational Constants for the Methylhydrazine Ion, its Transition States and Dissociation Products[a]

	harmonic frequencies (cm^{-1})[b] and rotational constants (GHz)
$CH_3NHNH_2^{+\bullet}$	121, 332, 423, 479, 574, 899, 1061, 1080, 1246, 1356, 1414, 1433, 1443, 1511, 1619, 2943, 3025, 3068, 3376, 3415, 3502, 44.7 GHz, 9.5 GHz, 8.3 GHz
$CH_2NHNH_2^+$	280, 496, 644, 683, 950, 976, 1021, 1129, 1328, 1411, 1471, 1636, 1684, 3071, 3188, 3367, 3372, 3482, 58.0 GHz, 10.5 GHz, 9.0 GHz
$CH_2NNH_3^+$	175, 491, 697, 757, 1051, 1056, 1113, 1167, 1419, 1488, 1599, 1622, 1664, 2989, 3120, 3198, 3306, 3326, 51.2 GHz, 10.3 GHz, 9.0 GHz

Table B.2: continued

	harmonic frequencies (cm^{-1})[b] and rotational constants (GHz)
CH_3NHNH^+	179, 510, 685, 864, 1112, 1113, 1143, 1354, 1378, 1412, 1420, 1502, 1684, 2947, 3022, 3087, 3195, 3243, 53.9 GHz, 10.2 GHz, 9.1 GHz
$NHNH_2^+$	1036, 1160, 1212, 1434, 1582, 1714, 3185, 3221, 3315, 210.1 GHz, 35.4 GHz, 30.3 GHz
$N_2H_2^{+\bullet}$ (cis)	835, 880, 940, 2027, 3002, 3059, 458.1 GHz, 39.8 GHz, 36.6 GHz
$N_2H_2^{+\bullet}$ (iso)	948, 1056, 1489, 1693, 3036, 3129, 311.2 GHz, 39.9 GHz, 35.4 GHz
$N_2H_2^{+\bullet}$ (trans)	887, 971, 1188, 1932, 3102, 3112, 449.2 GHz, 39.8 GHz, 36.5 GHz
CH_4	1314, 1314, 1314, 1522, 1522, 2926, 3028, 3028, 3028, 157.0 GHz, 157.0 GHz, 157.0 GHz
transition states for hydrogen loss	
$TS(45)_1$ (R^* = 2.397 Å)	179, 221, 299, 497, 659, 692, 931, 960, 1017, 1126, 1327, 1403, 1466, 1637, 1661, 3075, 3193, 3367, 3378, 3479, 35.9 GHz, 9.1 GHz, 8.3 GHz
$TS(45)_2$ (R^* = 2.297 Å)	214, 242, 324, 496, 666, 689, 926, 958, 1017, 1125, 1327, 1399, 1464, 1637, 1651, 3075, 3193, 3368, 3380, 3480, 36.8 GHz, 9.1 GHz, 8.4 GHz
$TS(45)_3$ (R^* = 2.197 Å)	241, 277, 367, 496, 675, 683, 921, 956, 1018, 1124, 1326, 1393, 1461, 1634, 1639, 3075, 3193, 3369, 3382, 3481, 37.8 GHz, 9.2 GHz, 8.4 GHz
$TS(45)_4$ (R^* = 2.097 Å)	257, 334, 431, 495, 670, 688, 912, 956, 1019, 1121, 1326, 1383, 1456, 1617, 1636, 3073, 3192, 3370, 3385, 3484, 38.8 GHz, 9.2 GHz, 8.4 GHz
$TS(45)_5$ (R^* = 1.997 Å)	274, 400, 488, 525, 648, 706, 899, 962, 1023, 1116, 1325, 1367, 1449, 1595, 1633, 3072, 3191, 3373, 3389, 3489, 39.7 GHz, 9.3 GHz, 8.4 GHz
transition states for methyl loss	
$TS(31)_1$ (R^* = 4.661 Å)	20, 64, 91, 101, 109, 834, 840, 1073, 1145, 1377, 1378, 1407, 1486, 1668, 3019, 3199, 3199, 3258, 3262, 3403, 43.2 GHz,1.8 GHz, 1.7 GHz
$TS(31)_2$ (R^* = 4.461 Å)	21, 71, 99, 113, 122, 835, 843, 1075, 1146, 1377, 1378, 1407, 1486, 1668, 3019, 3199, 3199, 3258, 3262, 3402, 41.6 GHz, 1.9 GHz, 1.9 GHz
$TS(31)_3$ (R^* = 4.361 Å)	22, 75, 103, 120, 129, 835, 844, 1076, 1146, 1378, 1378, 1407, 1486, 1668, 3019, 3198, 3199, 3257, 3261, 3401, 41.0 GHz, 2.0 GHz, 2.0 GHz
$TS(31)_4$ (R^* = 4.061 Å)	28, 87, 121, 147, 154, 838, 849, 1079, 1146, 1377, 1378, 1407, 1487, 1669, 3019, 3197, 3199, 3256, 3261, 3400, 39.3 GHz, 2.3 GHz, 2.2 GHz
$TS(31)_5$ (R^* = 3.761 Å)	29, 102, 140, 176, 184, 844, 852, 1080, 1146, 1377, 1378, 1406, 1487, 1668, 3018, 3196, 3199, 3256, 3261, 3399, 38.2 GHz, 2.6 GHz, 2.6 GHz
$TS(31)_6$ (R^* = 3.661 Å)	30, 107, 147, 187, 194, 846, 853, 1079, 1146, 1377, 1378, 1406, 1486, 1668, 3018, 3196, 3199, 3256, 3261, 3400, 37.9 GHz, 2.8 GHz, 2.7 GHz
$TS(31)_7$ (R^* = 3.561 Å)	30, 113, 154, 198, 206, 847, 854, 1078, 1145, 1377, 1378, 1405, 1486, 1668, 3018, 3196, 3199, 3257, 3262, 3400, 37.6 GHz, 2.9 GHz, 2.8 GHz
$TS(31)_8$ (R^* = 3.061 Å)	28, 151, 211, 274, 279, 829, 887, 1066, 1144, 1376, 1380, 1399, 1478, 1665, 3016, 3193, 3201, 3265, 3267, 3407, 36.6 GHz, 3.8 GHz, 3.6 GHz
$TS(31)_9$ (R^* = 2.661 Å)	35, 193, 281, 387, 400, 769, 949, 1037, 1143, 1373, 1379, 1383, 1459, 1657, 3016, 3193, 3201, 3278, 3284, 3426, 36.4 GHz, 4.7 GHz, 4.5 GHz
$TS(31)_{10}$ (R^* = 2.561 Å)	41, 206, 302, 430, 449, 740, 974, 1022, 1142, 1369, 1374, 1384, 1451, 1654, 3016, 3193, 3202, 3284, 3292, 3433, 36.4 GHz, 5.0 GHz, 4.7 GHz
$TS(31)_{11}$ (R^* = 2.461 Å)	51, 221, 322, 484, 507, 700, 1000, 1004, 1140, 1356, 1374, 1385, 1442, 1649, 3016, 3193, 3202, 3291, 3302, 3443, 36.5 GHz, 5.3 GHz, 5.0 GHz
estimated transition states for methane loss[c,d]	
$TS(30)_1$ (fit 1)	45, 123, 157, 177, 212, 39.3 GHz, 2.3 GHz, 2.2 GHz
$TS(30)_2$ (fit 2)	42, 116, 148, 168, 201, 39.3 GHz, 2.3 GHz, 2.2 GHz
$TS(30)_3$ (fit 3)	40, 109, 140, 158, 189, 39.3 GHz, 2.3 GHz, 2.2 GHz

[a] The present work has been published in Boulanger et al. [91] [b] Vibrational frequencies calculated at the B3-LYP/6-31+G(d) level of theory, scaled by 0.9614. [c] Only the five lowest vibrational frequencies were scaled to get a good fit of the breakdown curves. The transition states were estimated using the methylhydrazine ion vibrational frequencies, see Chapter 3 for details. [d] Rotational constants estimated from $TS(31)_4$ (R^* = 4.061 Å).

Table B.3: Calculated Vibrational Frequencies and Rotational Constants for the Tetramethylhydrazine Ion, its Transition States and Dissociation Products[a]

	harmonic frequencies (cm^{-1})[b] and rotational constants (GHz)
$(CH_3)_2NN(CH_3)_2^{+\bullet}$	76, 85, 112, 151, 151, 156, 179, 322, 404, 443, 484, 678, 855, 1018, 1028, 1057, 1068, 1077, 1084, 1102, 1163, 1204, 1313, 1397, 1402, 1417, 1420, 1438, 1442, 1442, 1442, 1460, 1460, 1465, 1466, 1504, 2940, 2941, 2943, 2944, 3025, 3026, 3030, 3030, 3059, 3062, 3064, 3066, 4.4GHZ, 3.3GHz, 2.0 GHz
$(CH_3)_2NN(CH_2)(CH_3)^+$	90, 161, 224, 246, 305, 348, 435, 464, 511, 529, 685, 717, 876, 913, 1000, 1014, 1076, 1080, 1115, 1127, 1204, 1225, 1313, 1401, 1408, 1425, 1437, 1441, 1451, 1457, 1465, 1471, 1490, 1617, 2906, 2932, 2986, 3001, 3041, 3060, 3072, 3076, 3090, 3105, 3215, 4.8 GHz, 3.4 GHz, 2.2 GHz
$(CH_3)_2NNCH_3^+$ (C_1)	85, 135, 188, 274, 327, 409, 468, 556, 721, 950, 967, 1002, 1075, 1118, 1133, 1151, 1233, 1356, 1386, 1395, 1406, 1424, 1432, 1436, 1453, 1464, 1641, 2936, 2962, 2972, 2990, 3039, 3055, 3060, 3090, 3097, 8.4 GHz, 4.0 GHz, 2.9 GHz
$(CH_3)_2NNCH_3^+$ (C_s)	84, 147, 195, 278, 328, 410, 470, 557, 721, 950, 968, 1003, 1076, 1118, 1135, 1151, 1233, 1356, 1387, 1395, 1406, 1424, 1434, 1437, 1454, 1465, 1640, 2936, 2962, 2972, 2990, 3040, 3054, 3062, 3090, 3096, 8.5 GHz, 4.0 GHz, 2.9 GHz
$C_3H_8N_2^{+\bullet}$ isomer I (C_1)	78, 120, 166, 330, 447, 454, 534, 548, 802, 858, 918, 953, 1041, 1068, 1115, 1135, 1238, 1341, 1362, 1409, 1430, 1435, 1439, 1453, 1496, 2892, 2950, 2987, 3067, 3078, 3085, 3094, 3203, 9.7 GHz, 4.0 GHz, 3.0 GHz
$C_3H_8N_2^{+\bullet}$ isomer I (C_s)	81, 109, 163, 328, 445, 453, 534, 547, 801, 858, 918, 952, 1040, 1067, 1115, 1133, 1237, 1341, 1361, 1409, 1430, 1434, 1438, 1453, 1495, 2891, 2949, 2987, 3067, 3079, 3084, 3094, 3203, 9.7GHz, 4.0 GHz, 3.0 GHz
$C_3H_8N_2^{+\bullet}$ isomer II	18, 174, 208, 323, 463, 469, 544,588, 753, 864, 939, 958, 1037, 1097, 1100, 1128, 1229, 1348, 1367,1400, 1425, 1432, 1449, 1461, 1494, 2895, 2950, 2981, 3065, 3067, 3075, 3091, 3205, 8.8 GHz, 4.4 GHz, 3.0 GHz
$C_3H_8N_2^{+\bullet}$ isomer III	77, 109, 120, 248, 338, 385, 468, 662, 739, 992, 999, 1016, 1030, 1094, 1115, 1215,1271, 1390, 1392, 1418, 1422, 1433, 1441, 1452, 1535, 2929, 2939, 3008, 3012, 3024, 3071, 3082, 3140, 8.4 GHz, 4.3 GHz, 3.0 GHz
$C_3H_8N_2^{+\bullet}$ isomer IV	77, 151, 156, 183, 270, 324, 567, 736, 750, 867, 921, 1045, 1057, 1108, 1109, 1237, 1296, 1367, 1375, 1398, 1411, 1425, 1439, 1453, 1889, 2954, 2955, 2962, 2998, 3029, 3039, 3048, 3063, 15.5 GHz, 2.6 GHz, 2.3 GHz
$C_3H_8N_2^{+\bullet}$ isomer V	34, 126, 167, 186, 297, 433, 488, 607, 845, 866, 937, 1054, 1069, 1114, 1129, 1184, 1334, 1368, 1401, 1417, 1419, 1427, 1432, 1468, 1678, 2933, 2942, 2983, 3000, 3030, 3057, 3070, 3349, 21.3 GHz, 2.3 GHz, 2.2 GHz
$C_3H_8N_2^{+\bullet}$ isomer VI	123, 144, 190, 269, 314, 430, 645, 774, 922, 983, 1051, 1059, 1096, 1117, 1126, 1174, 1174, 1382, 1387, 1417, 1420, 1435, 1438, 1449, 1515, 2927, 2927, 3016, 3030, 3031, 3074, 3075, 3142, 7.8 GHz, 4.9 GHz, 3.4 GHz
$C_3H_8N_2^{+\bullet}$ isomer VII	144, 195, 340, 351, 404, 407, 555, 690, 771, 801, 926, 963, 967, 1043, 1071, 1194, 1208, 1287, 1345, 1384, 1393, 1423, 1434, 1448, 1463, 2942, 2957, 3006, 3025, 3025, 3053, 3302, 3321, 6.6 GHz, 5.5 GHz, 3.8 GHz
$C_3H_8N_2^{+\bullet}$ isomer VIII	157, 208, 312, 458, 616, 751, 822, 858, 885, 887, 932, 1013, 1084, 1160, 1195, 1204, 1240, 1293, 1296, 1313, 1441, 1451, 1457, 1468, 1484, 2950, 2956, 2990, 3024, 3035, 3051, 3422, 3447, 7.2 GHz, 7.2 GHz, 3.9 GHz
$C_3H_8N_2^{+\bullet}$ isomer IX	106, 230, 329, 371, 582, 633, 750, 778, 847, 910, 942, 948, 1074, 1088, 1168, 1182, 1222, 1250, 1288, 1345, 1407, 1435, 1442, 1471, 1601, 2957, 2961, 3015, 3016, 3017, 3074, 3362, 3482, 10.7 GHz, 4.5 GHz, 3.4 GHz
transition states for methyl loss	
$TS(73)_1$ (R^* = 2.366 Å)	63, 80, 112, 141, 177, 205, 267, 321, 402, 420, 485, 512, 550, 743, 916, 955, 991, 1014, 1064, 1089, 1119, 1155, 1236, 1368, 1376, 1385, 1386, 1396, 1423, 1433, 1437, 1444, 1452, 1458, 1500, 2928, 2953, 2957, 2992, 3016, 3025, 3030, 3072, 3078, 3087, 3182, 3193, 3.8GHz, 2.7 GHz, 1.9 GHz

Table B.3: continued

transition states for methyl loss	
$TS(73)_2$ (R^* = 2.466 Å)	54, 81, 101, 129, 171, 191, 268, 321, 400, 406, 422, 465, 551, 743, 866, 953, 988, 1008, 1065, 1089, 1121, 1157, 1235, 1370, 1375, 1383, 1386, 1394, 1422, 1432, 1436, 1443, 1452, 1458, 1516, 2926, 2954, 2958, 2992, 3015, 3027, 3033, 3075, 3080, 3089, 3181, 3193, 3.8 GHz, 2.6 GHz, 1.8 GHz
$TS(73)_3$ (R^* = 2.566 Å)	45, 85, 92, 113, 167, 181, 267, 321, 349, 368, 409, 456, 553, 743, 824, 953, 985, 1005, 1066, 1090, 1124, 1159, 1234, 1370, 1374, 1381, 1388, 1393, 1421, 1431, 1435, 1442, 1452, 1459, 1533, 2924, 2955, 2959, 2993, 3014, 3029, 3035, 3077, 3081, 3090, 3180, 3191, 3.7 GHz, 2.5 GHz, 1.8 GHz
$TS(73)_4$ (R^* = 2.666 Å)	54, 82, 95, 101, 165, 174, 266, 305, 318, 326, 408, 458, 555, 742, 789, 952, 983, 1003, 1067, 1091, 1125, 1160, 1234, 1370, 1373, 1380, 1389, 1392, 1420, 1431, 1435, 1440, 1453, 1460, 1549, 2923, 2956, 2960, 2995, 3013, 3031, 3038, 3078, 3082, 3092, 3179, 3190, 3.7 GHz, 2.4 GHz, 1.8 GHz
$TS(73)_5$ (R^* = 2.766 Å)	62, 74, 92, 98, 163, 172, 261, 276, 287, 325, 408, 460, 556, 741, 760, 951, 981, 1001, 1067, 1092, 1127, 1161, 1233, 1369, 1373, 1379, 1389, 1392, 1419, 1430, 1434, 1440, 1453, 1462, 1562, 2921, 2957, 2961, 2997, 3012, 3032, 3040, 3078, 3083, 3093, 3178, 3189, 3.6 GHz, 2.4 GHz, 1.7 GHz
estimated transition states for methane loss[c,d]	
$TS(72)_1$ (fit 1)	15,17, 22, 30, 30, 3.6 GHz, 2.4 GHz, 1.7 GHz
$TS(72)_2$ (fit 1)	57, 64, 84, 113, 113 , 3.6 GHz, 2.4 GHz, 1.7 GHz
$TS(72)_3$ (fit 2)	17, 19, 25, 33, 33, 3.6 GHz, 2.4 GHz, 1.7 GHz
$TS(72)_4$ (fit 2)	72, 81, 106, 143, 144, 3.6 GHz, 2.4 GHz, 1.7 GHz
$TS(72)_5$ (fit 3)	16, 18, 23, 32, 32, 3.6 GHz, 2.4 GHz, 1.7 GHz
$TS(72)_6$ (fit 3)	68, 77, 101, 136, 136, 3.6 GHz, 2.4 GHz, 1.7 GHz
$TS(72)_7$ (fit 4)	17, 19, 25, 33, 33, 3.6 GHz, 2.4 GHz, 1.7 GHz
$TS(72)_8$ (fit 4)	75, 84, 110, 148, 148, 3.6 GHz, 2.4 GHz, 1.7 GHz

[a] The present work has been published in Boulanger et al. [91] [b] Vibrational frequencies calculated at the B3-LYP/6-31+G(d) level of theory, scaled by 0.9614. [c] Only the five lowest vibrational frequencies were scaled to get a good fit of the breakdown curves. The transition states were estimated using the tetramethylhydrazine ion vibrational frequencies, see Chapter 3 for details. [d] Rotational constants estimated from $TS(73)_5$ (R^* = 2.766 Å).

B2. Optimized geometrical parameters

In Tables B.4–B.8, the geometrical parameters of the dissociating complexes of the three methyl-substituted hydrazine ions are listed at each optimized point of the potential energy curves shown in Chapter 3. The main bond lengths and angles are listed from the equilibrium geometry of the parent ion up to the plateau of the potential energy curve. Figures B.1–B.3 show the equilibrium structure of the three parent ions with the main geometrical parameters identified.

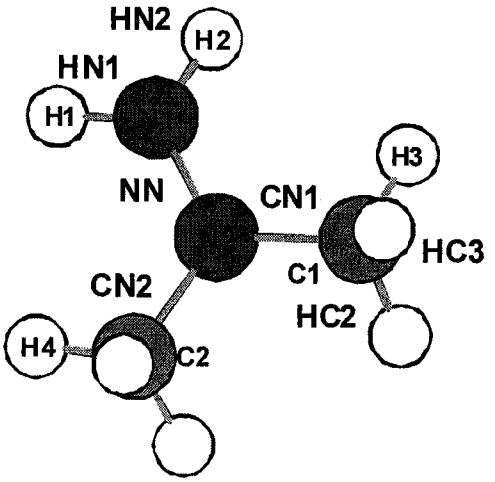

Figure B.1 – Optimized structure of the 1,1-dimethylhydrazine ion at the B3-LYP/6-31+G(d) level of theory.

Table B.4 : Geometrical Parameters (R in Å and, A and D in °) of the Dissociating Complexes of 1,1-Dimethylhydrazine Ion for the Loss of a Hydrogen Atom (Dissociating Bond is R_{HC1})

R_{HC1} [a]	R_{NN}	R_{NC1}	R_{NC2}	R_{HN1}	R_{HN2}	R_{HC2}	R_{HC3}	A_{CNN1} [b]	A_{CNN2} [c]	D_{HCNN} [d]
1.098	1.334	1.465	1.465	1.017	1.017	1.091	1.093	117.6	117.6	-81.9
1.198	1.333	1.461	1.465	1.017	1.017	1.089	1.096	117.4	117.7	-46.8
1.298	1.333	1.455	1.465	1.017	1.017	1.088	1.095	117.4	118.1	-60.3
1.398	1.334	1.438	1.464	1.016	1.017	1.088	1.090	118.9	118.6	-90.9
1.498	1.335	1.425	1.466	1.016	1.017	1.087	1.089	119.2	118.1	-91.8
1.598	1.335	1.407	1.467	1.016	1.016	1.085	1.088	119.6	117.4	-89.1
1.698	1.340	1.384	1.470	1.016	1.016	1.084	1.087	120.4	116.7	-90.9
1.798	1.348	1.356	1.472	1.017	1.017	1.083	1.086	121.3	115.9	-92.5
1.848	1.352	1.343	1.474	1.017	1.017	1.083	1.086	121.7	115.5	-93.2
1.898	1.357	1.332	1.475	1.017	1.017	1.083	1.086	122.0	115.1	-93.7
1.998	1.364	1.315	1.477	1.017	1.017	1.083	1.085	122.5	114.5	-94.4
2.098	1.369	1.304	1.479	1.018	1.017	1.083	1.085	122.8	114.1	-94.8
2.198	1.372	1.298	1.480	1.018	1.018	1.083	1.085	123.0	113.8	-95.0
2.298	1.374	1.294	1.481	1.018	1.018	1.083	1.085	123.1	113.7	-95.0
2.398	1.375	1.292	1.481	1.018	1.018	1.083	1.085	123.2	113.6	-95.0
2.498	1.376	1.290	1.482	1.018	1.018	1.083	1.085	123.2	113.5	-95.1

[a] The dissociating bond HC1 is defined by the atoms H3 and C1. [b] The angle CNN1 is defined by the atoms C1, N2, N1. [c] The angle CNN2 is defined by the atoms C2, N2, N1. [d] The dihedral angle is defined by the atoms H3, C2, N2, N1.

Table B.5: Geometrical Parameters (R in Å, A and D in °) of the Dissociating Complexes of 1,1-Dimethylhydrazine Ion for the Loss of $CH_3^{\bullet}$ (Dissociating Bond is R_{NC1})

R_{NC1} [a]	R_{NN}	R_{NC2}	R_{HN1}	R_{HN2}	A_{CNN1} [b]	A_{CNN2} [c]	D_{NNCH} [d]
1.465	1.334	1.465	1.017	1.017	117.6	117.6	81.9
1.565	1.331	1.461	1.018	1.017	116.5	118.1	40.5
1.665	1.330	1.459	1.019	1.017	115.6	118.3	42.4

Table B.5: continued

R_{NC1}[a]	R_{NN}	R_{NC2}	R_{HN1}	R_{HN2}	A_{CNN1}[b]	A_{CNN2}[c]	D_{NNCH}[d]
1.765	1.329	1.458	1.019	1.017	114.8	118.3	44.8
1.865	1.328	1.457	1.020	1.017	114.1	118.1	46.4
1.965	1.325	1.456	1.020	1.017	113.6	117.6	48.1
2.065	1.319	1.457	1.020	1.016	113.4	116.8	50.5
2.165	1.303	1.460	1.021	1.016	114.5	115.5	55.9
2.265	1.290	1.461	1.023	1.017	114.9	114.7	66.8
2.365	1.280	1.460	1.025	1.019	114.4	114.5	80.5
2.465	1.273	1.458	1.027	1.020	113.8	114.6	89.7
2.565	1.267	1.456	1.028	1.020	113.5	114.7	94.6
2.665	1.263	1.454	1.029	1.021	113.2	115.0	98.6
2.765	1.260	1.453	1.029	1.022	112.9	115.2	102.3
2.865	1.257	1.451	1.030	1.022	112.7	115.4	105.5
2.965	1.255	1.449	1.030	1.023	112.7	115.6	108.0
3.065	1.253	1.448	1.031	1.023	112.6	115.8	110.1
3.165	1.251	1.447	1.031	1.023	112.6	116.0	111.9
3.265	1.250	1.446	1.031	1.023	112.6	116.2	113.6
3.365	1.249	1.445	1.032	1.024	112.7	116.3	115.1
3.465	1.249	1.444	1.032	1.024	112.9	116.4	116.5
3.565	1.248	1.443	1.032	1.024	113.0	116.5	117.6
3.665	1.248	1.443	1.032	1.024	113.3	116.5	118.7
3.765	1.248	1.442	1.032	1.024	113.6	116.6	119.4
3.865	1.248	1.442	1.032	1.024	114.0	116.6	120.0
3.965	1.248	1.442	1.032	1.024	114.4	116.6	120.5
4.065	1.248	1.441	1.032	1.024	114.9	116.7	120.9
4.165	1.248	1.441	1.032	1.024	115.4	116.7	121.2
4.265	1.249	1.441	1.032	1.024	116.0	116.7	121.6
4.365	1.249	1.441	1.032	1.024	116.8	116.7	121.9
4.465	1.249	1.441	1.032	1.024	117.6	116.7	122.1
4.565	1.249	1.441	1.032	1.024	118.5	116.7	122.4
4.665	1.250	1.441	1.032	1.024	119.3	116.7	122.6
4.765	1.250	1.440	1.032	1.023	120.4	116.7	122.9
4.865	1.250	1.440	1.032	1.023	121.6	116.7	123.1
4.965	1.247	1.433	1.032	1.024	127.3	117.4	130.0
5.065	1.247	1.434	1.032	1.024	127.7	117.4	129.3
5.165	1.247	1.434	1.032	1.024	128.2	117.3	128.7
5.265	1.247	1.435	1.032	1.024	128.7	117.3	128.1
5.365	1.247	1.435	1.032	1.024	129.2	117.3	127.5
5.465	1.247	1.436	1.032	1.024	129.8	117.3	127.0
5.565	1.247	1.436	1.032	1.024	130.4	117.2	126.4
5.665	1.248	1.436	1.032	1.024	131.0	117.2	126.1
5.765	1.248	1.436	1.032	1.024	131.9	117.2	125.6
5.865	1.248	1.437	1.032	1.024	132.9	117.1	125.3
5.965	1.249	1.437	1.032	1.024	134.4	117.1	124.9
6.065	1.249	1.437	1.032	1.024	135.4	117.1	124.6

[a] The dissociating bond NC1 is defined by the atoms C1 and N2. [b] The angle CNN1 is defined by the atoms C1, N2, N1. [c] The angle CNN2 is defined by the atoms C2, N2, N1. [d] The dihedral angle NNCH is defined by the atoms N1, N2, C1, H4.

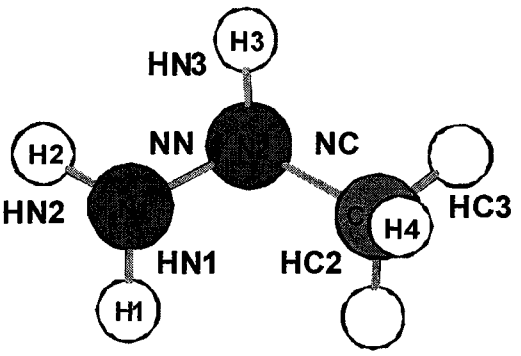

Figure B.2 – Optimized structure of the methylhydrazine ion at the B3-LYP/6-31+G(d) level of theory.

Table B.6: Geometrical Parameters (R in Å and, A and D in °) of the Dissociating Complexes of Methylhydrazine Ion for the Loss of a Hydrogen Atom (Dissociating Bond is R_{HC1})

R_{HC1} [a]	R_{NN}	R_{NC}	R_{HN1}	R_{HN2}	R_{HN3}	R_{HC2}	R_{HC3}	A_{NNC}	A_{HCN} [b]	D_{HCNN} [c]
1.097	1.325	1.461	1.018	1.018	1.019	1.093	1.091	121.4	110.1	-74.0
1.197	1.326	1.454	1.018	1.018	1.019	1.092	1.090	121.5	109.9	-75.2
1.297	1.326	1.446	1.018	1.017	1.019	1.091	1.089	121.8	109.7	-76.2
1.397	1.327	1.435	1.018	1.017	1.019	1.090	1.088	122.1	109.4	-77.2
1.497	1.329	1.422	1.018	1.017	1.019	1.089	1.087	122.5	109.1	-78.1
1.597	1.331	1.406	1.018	1.017	1.020	1.088	1.086	123.1	108.6	-79.0
1.697	1.336	1.383	1.017	1.017	1.020	1.087	1.085	123.9	107.9	-79.8
1.797	1.343	1.356	1.017	1.017	1.020	1.086	1.084	124.9	107.2	-80.2
1.897	1.352	1.331	1.018	1.017	1.021	1.086	1.084	125.8	106.5	-80.3
1.997	1.359	1.314	1.018	1.017	1.021	1.085	1.084	126.4	106.1	-80.2
2.097	1.364	1.304	1.018	1.018	1.022	1.085	1.084	126.8	106.0	-80.2
2.197	1.366	1.297	1.018	1.018	1.022	1.085	1.084	127.1	106.0	-80.2
2.297	1.367	1.294	1.018	1.018	1.022	1.085	1.084	127.3	106.3	-80.3
2.397	1.368	1.291	1.018	1.018	1.022	1.086	1.084	127.4	106.5	-80.3
2.497	1.368	1.290	1.018	1.018	1.023	1.086	1.084	127.5	106.8	-80.4

[a] The dissociating bond HC1 is by the atoms H4 and C. [b] The angle HCN is defined as by the atoms H4, C and N2. [c] The dihedral angle HCNN is defined by the atoms H4, C, N2 and N1.

Table B.7 : Geometrical Parameters (R in Å, A and D in °) of the Dissociating Complexes of Methylhydrazine Ion for the Loss of $CH_3^{\bullet}$ (Dissociating Bond is R_{NC})

R_{NC}	R_{NN}	R_{HN1}	R_{HN2}	R_{HN3}	A_{NNC}	A_{NNH1} [a]	A_{HCN} [b]	D_{HNNC} [c]
1.461	1.325	1.018	1.018	1.019	121.4	117.4	120.2	-176.9
1.561	1.323	1.018	1.018	1.019	120.4	117.4	119.2	-179.3
1.661	1.322	1.018	1.019	1.020	119.6	117.4	118.1	177.6
1.761	1.321	1.018	1.019	1.021	118.9	117.3	116.9	173.7
1.861	1.321	1.017	1.020	1.021	118.3	117.3	115.5	168.8
1.961	1.319	1.017	1.020	1.022	117.9	117.4	113.9	161.9
2.061	1.313	1.017	1.020	1.023	117.9	117.7	111.6	150.8
2.161	1.303	1.017	1.020	1.025	118.6	118.1	108.3	134.7

Table B.7: continued

R_{NC}	R_{NN}	R_{HN1}	R_{HN2}	R_{HN3}	A_{NNC}	A_{NNH1} [a]	A_{HCN} [b]	D_{HNNC} [c]
2.261	1.293	1.018	1.022	1.026	119.2	117.9	104.8	123.2
2.361	1.285	1.019	1.023	1.028	119.6	117.7	101.7	116.2
2.461	1.278	1.020	1.024	1.029	119.9	117.6	99.0	111.5
2.561	1.273	1.021	1.025	1.029	120.4	117.5	96.7	108.3
2.661	1.269	1.022	1.026	1.030	120.8	117.4	94.8	106.0
2.761	1.266	1.022	1.026	1.030	121.2	117.4	93.2	104.3
2.861	1.264	1.023	1.027	1.031	121.6	117.3	92.2	103.4
2.961	1.262	1.023	1.027	1.031	122.2	117.3	91.2	102.7
3.061	1.260	1.023	1.027	1.031	122.9	117.3	90.4	102.2
3.161	1.259	1.024	1.028	1.031	123.5	117.3	89.8	102.0
3.261	1.258	1.024	1.028	1.031	124.1	117.3	89.5	102.1
3.361	1.258	1.024	1.028	1.031	124.8	117.3	89.4	102.5
3.461	1.257	1.024	1.028	1.032	125.5	117.3	89.6	103.2
3.561	1.257	1.024	1.028	1.032	126.2	117.3	89.8	104.0
3.661	1.257	1.024	1.028	1.032	126.9	117.3	90.2	105.1
3.761	1.257	1.024	1.028	1.032	127.7	117.3	90.8	106.4
3.861	1.257	1.024	1.028	1.032	128.4	117.3	91.4	107.9
3.961	1.257	1.024	1.028	1.032	129.2	117.3	92.3	109.7
4.061	1.257	1.024	1.028	1.032	130.1	117.3	93.0	111.5
4.161	1.257	1.024	1.028	1.032	131.0	117.3	94.0	113.7
4.211	1.257	1.024	1.028	1.032	131.6	117.3	94.5	114.7
4.361	1.258	1.024	1.028	1.032	133.1	117.3	95.9	118.5
4.461	1.258	1.024	1.028	1.032	134.2	117.3	96.7	121.0
4.561	1.258	1.024	1.028	1.031	135.4	117.3	97.6	123.6
4.661	1.258	1.024	1.028	1.031	136.5	117.3	98.4	126.6
4.761	1.258	1.024	1.028	1.031	137.6	117.3	99.3	129.8
4.861	1.259	1.024	1.028	1.031	138.7	117.3	100.1	133.0
4.961	1.259	1.023	1.028	1.031	139.8	117.3	100.7	136.2
5.061	1.259	1.023	1.028	1.031	140.8	117.3	101.2	139.4
5.161	1.259	1.023	1.028	1.031	141.4	117.3	101.8	142.0
5.211	1.259	1.023	1.028	1.031	142.2	117.3	102.0	144.1
5.311	1.259	1.023	1.028	1.031	143.0	117.3	102.3	147.3

[a] The angle NNH1 is defined by the atoms H1, N1, N2. [b] The angle HCN is defined by the atoms H3, N2, C. [c] The dihedral angle is defined by the atoms H2, N1, N2, C.

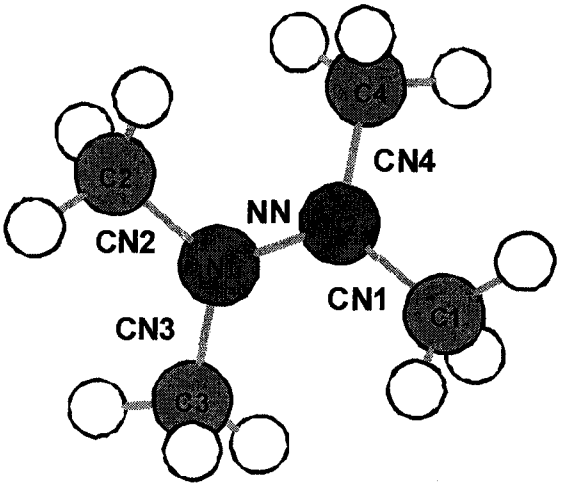

Figure B.3 – Optimized structure of the tetramethylhydrazine ion at the B3-LYP/6-31+G(d) level of theory.

Table B.8 : Geometrical Parameters (R in Å, A and D in °) of the Dissociating Complexes of Tetramethylhydrazine Ion for the Loss of $CH_3^{\bullet}$ (Dissociating Bond is R_{NC1})

R_{CN1} [a]	R_{NN}	R_{CN2}	R_{CN3}	R_{CN4}	A_{CNN1} [b]	A_{CNN2} [c]	D_{CNNC} [d]
1.466	1.343	1.466	1.466	1.466	120.2	120.2	163.8
1.566	1.346	1.470	1.470	1.466	117.8	118.8	175.3
1.666	1.343	1.470	1.470	1.463	117.0	118.9	170.8
1.766	1.340	1.470	1.469	1.462	116.2	119.3	163.8
1.866	1.330	1.468	1.468	1.460	115.9	122.1	142.0
1.966	1.321	1.469	1.467	1.460	115.5	123.1	134.6
2.066	1.308	1.472	1.467	1.461	115.3	123.9	125.7
2.166	1.295	1.475	1.468	1.462	115.1	124.3	117.7
2.266	1.283	1.477	1.470	1.462	114.6	124.8	113.3
2.366	1.274	1.479	1.471	1.462	114.2	125.1	110.9
2.466	1.267	1.480	1.473	1.462	113.9	125.3	109.4
2.566	1.261	1.482	1.474	1.461	113.4	125.5	108.4
2.666	1.257	1.483	1.475	1.459	112.9	125.5	107.7
2.766	1.254	1.484	1.476	1.458	112.3	125.6	107.1
2.866	1.251	1.484	1.477	1.458	111.7	125.6	106.4
2.966	1.249	1.485	1.477	1.456	111.1	125.6	105.7
3.066	1.247	1.486	1.478	1.455	110.1	125.7	104.9
3.166	1.245	1.487	1.478	1.454	108.4	125.7	103.9
3.266	1.244	1.488	1.479	1.453	106.1	125.8	102.4

[a] The dissociating bond CN1 is defined by the atoms C1 and N2. [b] The angle CNN1 is defined by the atoms C1, N2, N1. [c] The angle CNN2 is defined by the atoms C2, N1, N2. [d] The dihedral angle CNNC is defined by the atoms C1, N2, N1, C2.

Appendix C

APPEARANCE ENERGIES OF THE OBSERVED FRAGMENT IONS

C1. Introduction

Up to twenty-five fragment ions were observed in the dissociation of the methyl-substituted hydrazine ions as the photon energy was increased from the ionization threshold to $h\nu \approx 32$ eV. The appearance energies of some of these fragments have been reported previously using electron ionization or photoionization techniques, and Tables C.1 (DMH), C.2 (MH) and C.3 (TMH) provide a summary of the results with empirical formulae and/or tentative structures. It should be borne in mind that experimentally determined AEs may be subject to kinetic and competitive shifts and/or reverse energy barriers [86], and therefore should be regarded as upper limits to the thermochemical thresholds. The relative abundances for all the fragment ions as a function of photon energy are shown in Figures 3.15–17 in Chapter 3.

C2. 1,1-Dimethylhydrazine ion

The AEs of the fragment ion *m/z* 59 reported by Foner and Hudson [117, 118] and by Dibeler et al. [48] are ~ 0.5 eV higher than our value. In these studies [48, 117, 118], the $(CH_3)_2NNH^+$ structure was proposed for this ion. However, the results of our mG3 calculations show that this ion is actually 36 kJ mol^{-1} higher in energy than $(CH_3)(CH_2)NNH_2^+$.

The various AEs for the fragment ion *m/z* 45 differ considerably from one another. The value reported by Dibeler et al. [48] (9.7 ± 0.2 eV) is in accord with our AE of 9.65 ± 0.05 eV. However, Akopyan and Vilesov [110] and Burgers et al. [1] give values which are more than 1 eV lower. The group of Burgers et al. [4] found that contamination from traces of amines had affected the measurements of the AEs of the fragment ions in their study on the $CH_5N_2^+$ cation [1, 4]. Akopyan and Vilesov [110] have also reported an AE of 11.2 ± 0.2 eV for another possible structure of *m/z* 45, $(CH_3)_2NH^+$. All previous AEs for the fragment ion *m/z* 44 lie 0.6–1.0 eV higher than our value of 9.85 ± 0.05 eV, except that measured by Akopyan and Vilesov [110], which is 0.85 eV lower. Fisher and Henderson [119] have proposed a structure of $(CH_3)_2N^+$ for the *m/z* 44 ion, although $CH_3NHCH_2^+$ may be more favourable. Previous AEs for the fragment ion *m/z* 43 differ significantly from our experimental result of 11.35 ± 0.05 eV. Dibeler et al. [48] reported two AEs (12.5 ± 0.2 and 13.5 ± 0.2 eV) for this ion, as did Akopyan and Vilesov [110] (8.8 ± 0.1 and 10.9 ± 0.2 eV). For *m/z* 42, Dibeler et al. [48] give an AE of 12.8 ± 0.2 eV, compared to our value of 11.65 ± 0.05 eV, and suggest that the fragment ion is $(CH_2)_2N^+$. Our appearance energies for the fragment ions *m/z* 30 ($N_2H_2^+$) and *m/z* 29 (N_2H^+) are in good agreement with those measured by Dibeler et al. [48], but the AE reported by Akopyan and Vilesov [110] for the *m/z* 30 fragment ion differs considerably.

Our AE for the N_2^+ fragment is lower by ~ 1.4 eV than that given by Dibeler et al. [48]. Fragment ion *m/z* 16, corresponding to NH_2^+, has an AE of 15.20 ± 0.25 eV, which is higher than that reported by Gowenlock et al. [120], and finally, the methyl cation, CH_3^+, has an AE of 13.75 ± 0.10 eV, which is close to that determined by Dibeler et al. [48].

No AEs are available for the other fragment ions observed in the present work. Akopyan and Vilesov [110] report an AE of 9.5 ± 0.1 eV for the fragment ion *m/z* 58, but we did not observed this ion, pointing to possible contamination of their sample. The *m/z* 58 ion is observed in our MIKE and CID mass spectra of $(CH_3)(CH_2)NNH_2^+$, *m/z* 59.

C3. Methylhydrazine ion

The reported AEs for fragment ion *m/z* 45, $CH_5N_2^+$, from Dibeler et al. [48] and Foner and Hudson [118] are higher by 0.35 eV than our reported value of 9.85 ± 0.05 eV while Akopyan and Vilesov [110] reported an AE lower by 0.65 eV. They did not report any specific structure for that ion. Syage [38] reported an AE of 10 eV for the ion $CH_3NNH_2^+$ which is not the most energetically favourable $CH_5N_2^+$ ion to be formed from ionized methylhydrazine according to our calculations (see Table 3.1 in Chapter 3). For the fragment ions *m/z* 41–44, the reported values are all lower than our experimental AE values except for the second AE value reported by Dibeler et al. [48] for fragment ion *m/z* 43 (14.8 ± 0.3 eV) which is ~ 1 eV higher. Dibeler et al. [48] reported two AEs for fragment ion *m/z* 43 suggesting different neutral losses.

Five AEs have been reported for fragment ion *m/z* 31. Dibeler et al. [48] reported an AE that is 0.45 eV higher than our experimental value of 10.25 ± 0.05 eV. Burger et al. [1] reported an AE of 9.82 eV for the $N_2H_3^+$ fragment ion. Akopyan and Vilesov [110] reported two values (9.5 ± 0.1 eV and 11.3 ± 0.1 eV) for ion *m/z* 31, their second AE corresponding to the CH_5N^+ ion. Syage [38] reported an AE of 11 eV which is 0.75 eV higher than our reported AE value. For the fragment ion *m/z* 30, two AEs have been reported, one corresponding to the $N_2H_2^{+\bullet}$ ion (11.2 ± 0.2 eV [48]) and the other to the $CH_2NH_2^+$ ion (11.5

eV [38]). These two values are higher than our experimental AE by > 1 eV. According to our experimental results and to calculations, this fragment ion should be iso-diazene, $H_2NN^{+\bullet}$, or trans-diazene, $HNNH^{+\bullet}$. Fragment ion *m/z* 29 could either be CH_3N^+ or N_2H^+. Our experimental AE value is 0.85–1.65 eV lower than the reported values by Syage [38] ($CHNH_2^+$) and Dibeler et al. [48] (HN_2^+). Fragment ion *m/z* 28 has an AE of 12.35 ± 0.10 eV which is slightly higher than the reported value of Syage [38] (AE = 12 eV, $CHNH^+$). Dibeler et al. [48] reported an AE of 13.2 ± 0.3 eV corresponding to the N_2^+ fragment ion.

AEs have been reported by Syage [38] for all the remaining fragment ions, *m/z* 12–27. His reported AE values higher for fragment ions *m/z* 12–14, 22.5 and 27. For fragment ions *m/z* 15, 16 and 18, his reported AEs are 0.45–1.75 eV lower than our measured values. For fragment ion *m/z* 15, Dibeler et al. [48] also reported an AE value of 14.1 ± 0.3 eV which is 0.35 eV lower than our experimental AE of 14.45 ± 0.20 eV. For fragment ion *m/z* 17, Syage's AE value [38] (12 eV) is in agreement with our reported value of 11.95 ± 0.10 eV. In the breakdown curve of methylhydrazine, a fragment ion was observed at *m/z* 32. Since this ion was not observed in the MIKE and CID mass spectra of $CH_3NHNH_2^{+\bullet}$, it was assumed to be due to an impurity and its AE has not been reported in Table C.2.

C4. Tetramethylhydrazine ion

In the breakdown diagram of tetramethylhydrazine ion, we observed fragment ions at *m/z* 86 and *m/z* 87 corresponding to H losses, but it was not feasible to determine reliable AEs for these ions from the TPEPICO data. An ion at *m/z* 74 was also observed, but was attributed to a decomposition by-product. AEs for the fragment ions of tetramethylhydrazine have been reported by Dibeler et al. [48] for most of the fragment ions observed in our

breakdown curve. We measured an AE of 8.79 ± 0.05 eV for fragment ion *m/z* 73. This value is 0.3 eV lower than the AE reported by Dibeler et al. [48]. Our AE for fragment ion *m/z* 72 is in agreement with the one reported by Dibeler et al. [48] being 0.24 eV lower. For fragment ions *m/z* 57, *m/z* 58 and *m/z* 71, the reported AEs by Dibeler et al. [48] are all higher than our measured AEs except for the first AE of fragment ion *m/z* 58 measured by Dibeler et al. [48] which is ~ 0.94 eV lower than our reported value. For fragment ion *m/z* 58, Dibeler et al. [48] reported two AEs with different neutral losses, the lower AE corresponding to ethane loss and the second value corresponding to two methyl radical losses.

We report two AEs for fragment ion *m/z* 47, 11.44 ± 0.10 eV and 17.94 ± 0.50 eV. This ion disappears around 15.94 eV and reappears 2 eV higher. For fragment ion *m/z* 46, our reported AE is ~ 0.64 eV lower than the first AE reported by Dibeler et al. [48]. They also reported a second AE at 12.3 ± 0.2 eV for this ion without any indication about the neutral loss or ion molecular formula. We observed the apparition of fragment ion *m/z* 45 1.64 eV higher than Dibeler et al. [48]. We suggested two ion molecular formulae but think that $C_2H_7N^+$ is probably more plausible for this ion. Our AE of fragment ion *m/z* 44 is in excellent agreement with the reported values by Dibeler et al. [48] and Gowenlock et al. [120], this ion probably having the $(CH_3)_2N^+$ structure. Our determined AE for fragment ion *m/z* 43 is in-between the two AEs reported by Dibeler et al. [48] for the s-$C_3H_7^+$ ion. Our AE of fragment ion *m/z* 42 is lower by ~ 0.7 eV than the one reported by Dibeler et al. [48]. For fragment ion *m/z* 41, our experimental AE is approximatively 7 eV higher than the reported value by Dibeler et al. [48]. Our reported AE for fragment ion *m/z* 32 is ~ 0.66 eV lower than the one reported by Dibeler et al. [48]. We have again an agreement between our AE

and the one reported by Dibeler et al. [48] for fragment ion *m/z* 30, our value being < 0.3 eV lower. There is a one electron-Volt difference between our experimental AE and Dibeler et al. [48] value for fragment ion *m/z* 28, corresponding most probably to the N_2^+ ion. We have an excellent agreement for the fragment ion *m/z* 15 AE with Dibeler et al. [48]. For all the other fragment ions, no reported AEs have been found in the literature.

Table C.1: Appearance Energies for the Fragment Ions from 1,1-Dimethylhydrazine

m/z	ion fragment	AE (eV)	Ionization Technique	Reference
59	$(CH_3)(CH_2)NNH_2^+$	9.65 ± 0.05	TPEPICO	present work. [92]
		8.7 ± 0.2	photoionization	Akopyan and Vilesov. [110]
		10.08 ± 0.1	electron ionization	Foner and Hudson. [118]
		10.2 ± 0.2	electron ionization	Dibeler et al. [48]
		10.0 ± 0.3	electron ionization	Foner and Hudson. [117]
58	$C_2H_6N_2^+$	9.5 ± 0.1	photoionization	Akopyan and Vilesov. [110]
46	$CH_6N_2^+$ or $C_2H_8N^+$	9.80 ± 0.05	TPEPICO	present work. [92]
45	$CH_3NNH_2^+$	9.65 ± 0.05	TPEPICO	present work. [92]
		8.4 ± 0.1	photoionization	Akopyan and Vilesov. [110]
		8.60	electron ionization	Burgers et al. [1]
		9.7 ± 0.2	electron ionization	Dibeler et al. [48]
	$(CH_3)_2NH^+$	11.2 ± 0.2	photoionization	Akopyan and Vilesov. [110]
44	$C_2H_6N^+$	9.85 ± 0.05	TPEPICO	present work. [92]
		9.0 ± 0.2	photoionization	Akopyan and Vilesov. [110]
		11.2 ± 0.2	photoionization	Akopyan and Vilesov. [110]
		10.45 ± 0.05	electron ionization	Fisher and Henderson. [119]
		10.7 ± 0.1	electron ionization	Gowenlock et al. [120]
		10.9 ± 0.2	electron ionization	Dibeler et al. [48]
43	$C_2H_5N^+$	11.35 ± 0.05	TPEPICO	present work. [92]
		8.8 ± 0.1	photoionization	Akopyan and Vilesov. [110]
		10.9 ± 0.2	photoionization	Akopyan and Vilesov. [110]
		12.5 ± 0.2	electron ionization	Dibeler et al. [48]
		13.5 ± 0.2	electron ionization	Dibeler et al. [48]
42	$C_2H_4N^+$	11.65 ± 0.10	TPEPICO	present work. [92]
		12.8 ± 0.2	electron ionization	Dibeler et al. [48]
41	$C_2H_3N^+$	14.75 ± 0.20	TPEPICO	present work. [92]
40	$C_2H_2N^+$	18.95 ± 0.50	TPEPICO	present work. [92]
39	C_2HN^+	22.95 ± 1.00	TPEPICO	present work. [92]
38	C_2N^+	19.45 ± 0.50	TPEPICO	present work. [92]
32	$N_2H_4^+$	12.35 ± 0.10	TPEPICO	present work. [92]
31	$N_2H_3^+$	12.65 ± 0.10	TPEPICO	present work. [92]
30	$N_2H_2^+$	12.25 ± 0.10	TPEPICO	present work. [92]
		8.6 ± 0.1	photoionization	Akopyan and Vilesov. [110]
		12.9 ± 0.1	electron ionization	Dibeler et al. [48]
29	N_2H^+ or $CH_2{=}NH^+$	14.35 ± 0.20	TPEPICO	present work. [92]
		14.2 ± 0.5	electron ionization	Dibeler et al. [48]
28	N_2^+ or $HCNH^+$	11.85 ± 0.10	TPEPICO	present work. [92]
		13.2 ± 0.1	electron ionization	Dibeler et al. [48]
27	HCN^+	14.55 ± 0.20	TPEPICO	present work. [92]

Table C.1: continued

26	CN^+	20.95 ± 0.50	TPEPICO	present work. [92]
18	NH_4^+	11.75 ± 0.10	TPEPICO	present work. [92]
17	NH_3^+	14.55 ± 0.20	TPEPICO	present work. [92]
16	NH_2^+	15.20 ± 0.25	TPEPICO	present work. [92]
		13.3 ± 0.1	electron ionization	Gowenlock et al. [120]
15	CH_3^+	13.75 ± 0.10	TPEPICO	present work. [92]
		14.5 ± 0.3	electron ionization	Dibeler et al. [48]
14	CH_2^+	20.45 ± 0.50	TPEPICO	present work. [92]
13	CH^+	23.95 ± 1.00	TPEPICO	present work. [92]

Table C.2: Appearance Energies for the Fragment Ions from Methylhydrazine

m/z	Fragment Ion	AE (eV)	Ionization Technique	Reference
45	$CH_2NHNH_2^+$	9.85 ± 0.05	TPEPICO	present work. [91]
	$CH_5N_2^+$	10.2 ± 0.1	electron ionization	Dibeler et al. [48]
		10.18 ± 0.1	electron ionization	Foner and Hudson. [118]
		9.2 ± 0.1	photoionization	Akopyan and Vilesov. [110]
	$CH_3NNH_2^+$	10	electron ionization	Syage. [38]
44	$CH_4N_2^+$	12.45 ± 0.10	TPEPICO	present work. [91]
		10.4 ± 0.2	electron ionization	Dibeler et al. [48]
		10.5	electron ionization	Syage. [38]
		9.92 ± 0.1	electron ionization	Foner and Hudson. [118]
		9.4 ± 0.1	photoionization	Akopyan and Vilesov. [110]
	$CH_3N_2H^+$	10.5	electron ionization	Syage. [38]
43	$CH_3N_2^+$	13.85 ± 0.20	TPEPICO	present work. [91]
		11.9 ± 0.3	electron ionization	Dibeler et al. [48]
		14.8 ± 0.3	electron ionization	Dibeler et al. [48]
		9.2 ± 0.2	photoionization	Akopyan and Vilesov. [110]
		11.5	electron ionization	Syage. [38]
42	$CH_2N_2^+$	17.45 ± 0.20	TPEPICO	present work. [91]
		15.2 ± 0.2	electron ionization	Dibeler et al. [48]
		16.5	electron ionization	Syage. [38]
41	CHN_2^+	22.95 ± 0.50	TPEPICO	present work. [91]
		28	electron ionization	Syage. [38]
31	$H_3N_2^+$	10.25 ± 0.05	TPEPICO	present work. [91]
		10.7 ± 0.3	electron ionization	Dibeler et al. [48]
		11	electron ionization	Syage. [38]
		9.82	electron ionization	Burgers et al. [1]
		9.5 ± 0.1	photoionization	Akopyan and Vilesov. [110]
	CH_5N^+	11.3 ± 0.1	photoionization	Akopyan and Vilesov. [110]
30	$H_2N_2^+$	10.05 ± 0.05	TPEPICO	present work. [91]
		11.2 ± 0.2	electron ionization	Dibeler et al. [48]
	$CH_2NH_2^+$	11.5	electron ionization	Syage. [38]
29	CH_3N^+ or N_2H^+	11.65 ± 0.10	TPEPICO	present work. [91]
	HN_2^+	13.3 ± 0.3	electron ionization	Dibeler et al. [48]
	$CHNH_2^+$	12.5	electron ionization	Syage. [38]
28	CH_2N^+ or N_2^+	12.35 ± 0.10	TPEPICO	present work. [91]
		13.2 ± 0.3	electron ionization	Dibeler et al. [48]
	$CHNH^+$	12	electron ionization	Syage. [38]
27	CHN^+	20.45 ± 0.40	TPEPICO	present work. [91]
		24	electron ionization	Syage. [38]
22.5	$CH_5N_2^{2+}$	27.95 ± 1.00	TPEPICO	present work. [91]
		36	electron ionization	Syage. [38]
18	NH_4^+	12.25 ± 0.10	TPEPICO	present work. [91]
		10.5	electron ionization	Syage. [38]

Table C.2: continued

17	NH_3^+	11.95 ± 0.10	TPEPICO	present work. [91]
		12	electron ionization	Syage. [38]
16	CH_4^+ or NH_2^+	15.85 ± 0.20	TPEPICO	present work. [91]
	NH_2^+	14.5	electron ionization	Syage. [38]
15	CH_3^+ or NH^+	14.45 ± 0.20	TPEPICO	present work. [91]
		14.1 ± 0.3	electron ionization	Dibeler et al. [48]
		14	electron ionization	Syage. [38]
14	CH_2^+ or N^+	19.90 ± 0.25	TPEPICO	present work. [91]
	CH_2^+	22	electron ionization	Syage. [38]
13	CH^+	22.95 ± 0.50	TPEPICO	present work. [91]
		24	electron ionization	Syage. [38]
12	C^+	26.95 ± 1.00	TPEPICO	present work. [91]
		33	electron ionization	Syage. [38]

Table C.3: Appearance Energies for the Fragment Ions from Tetramethylhydrazine

m/z	Fragment Ion	AE (eV)	Ionization Technique	Reference
87	$C_4H_{11}N_2^+$	—	TPEPICO	present work. [91]
86	$C_4H_{10}N_2^+$	—	TPEPICO	present work. [91]
73	$C_3H_9N_2^+$	8.79 ± 0.05	TPEPICO	present work. [91]
		9.1 ± 0.1	electron ionization	Dibeler et al. [48]
72	$C_3H_8N_2^+$	9.14 ± 0.05	TPEPICO	present work. [91]
		8.9 ± 0.1	electron ionization	Dibeler et al. [48]
71	$C_3H_7N_2^+$	10.04 ± 0.05	TPEPICO	present work. [91]
		10.7 ± 0.1	electron ionization	Dibeler et al. [48]
58	$C_2H_6N_2^+$	11.44 ± 0.10	TPEPICO	present work. [91]
		10.5 ± 0.1	electron ionization	Dibeler et al. [48]
		13.3 ± 0.5	electron ionization	Dibeler et al. [48]
57	$C_2H_5N_2^+$	10.54 ± 0.10	TPEPICO	present work. [91]
		12.4 ± 0.2	electron ionization	Dibeler et al. [48]
47	$CH_7N_2^+$ or $C_2H_9N^+$	11.54 ± 0.10	TPEPICO	present work. [91]
		17.94 ± 0.50	TPEPICO	present work. [91]
46	$CH_6N_2^+$ or $C_2H_8N^+$	11.54 ± 0.10	TPEPICO	present work. [91]
		10.9 ± 0.2	electron ionization	Dibeler et al. [48]
		12.3 ± 0.2	electron ionization	Dibeler et al. [48]
45	$CH_5N_2^+$ or $C_2H_7N^+$	11.34 ± 0.10	TPEPICO	present work. [91]
		9.7 ± 0.2	electron ionization	Dibeler et al. [48]
44	$CH_4N_2^+$ or $C_2H_6N^+$	11.04 ± 0.10	TPEPICO	present work. [91]
		11.2 ± 0.2	electron ionization	Dibeler et al. [48]
		11.2 ± 0.1	electron ionization	Gowenlock et al. [120]
43	$CH_3N_2^+$, $C_2H_5N^+$ or	11.54 ± 0.10	TPEPICO	present work. [91]
	s-$C_3H_7^+$	10.9 ± 0.2	electron ionization	Dibeler et al. [48]
		13.2 ± 0.3	electron ionization	Dibeler et al. [48]
42	$CH_2N_2^+$ or $C_2H_4N^+$	11.54 ± 0.10	TPEPICO	present work. [91]
		12.2 ± 0.2	electron ionization	Dibeler et al. [48]
41	CHN_2^+ or $C_2H_3N^+$	20.44 ± 0.50	TPEPICO	present work. [91]
		~ 13	electron ionization	Dibeler et al. [48]
40	CN_2^+ or $C_2H_2N^+$	20.94 ± 0.50	TPEPICO	present work. [91]
39	C_2HN^+	—	TPEPICO	present work. [91]
32	$H_4N_2^+$	11.64 ± 0.10	TPEPICO	present work. [91]
		12.3 ± 0.1	electron ionization	Dibeler et al. [48]
31	$H_3N_2^+$	13.04 ± 0.10	TPEPICO	present work. [91]
30	$H_2N_2^+$	11.64 ± 0.10	TPEPICO	present work. [91]
		11.9 ± 0.2	electron ionization	Dibeler et al. [48]

Table C.3: continued

29	CH_3N^+ or N_2H^+	14.94 ± 0.20	TPEPICO	present work. [91]
28	CH_2N^+ or N_2^+	12.14 ± 0.10	TPEPICO	present work. [91]
		13.1 ± 0.2	electron ionization	Dibeler et al. [48]
27	CHN^+	14.54 ± 0.20	TPEPICO	present work. [91]
26	CN^+ or $C_2H_2^+$	18.94 ± 0.50	TPEPICO	present work. [91]
18	NH_4^+	12.24 ± 0.10	TPEPICO	present work. [91]
17	NH_3^+	17.94 ± 0.50	TPEPICO	present work. [91]
16	CH_4^+ or NH_2^+	19.94 ± 0.50	TPEPICO	present work. [91]
15	CH_3^+ or NH^+	14.14 ± 0.20	TPEPICO	present work. [91]
		14 ± 1	electron ionization	Dibeler et al. [48]
14	CH_2^+ or N^+	22.94 ± 0.50	TPEPICO	present work. [91]

Appendix D

ENTROPIES OF ACTIVATION

D1. Introduction

The entropies of activation have been calculated using the harmonic oscillator and the free rotor models of East and Radom [103], as explained in Chapter 2. These methods yield different $\Delta S^{\ddagger}$ values. In Tables 3.3, 3.5 and 3.6, only the $\Delta S^{\ddagger}$ values calculated using the rovibrational FR approach are reported. In this appendix, the vibrational and rovibrational entropies of activation for both approaches (HO and FR) are reported. In the case of the hydrogen loss atom from MH and DMH ions, the $\Delta S^{\ddagger}$ values for methods A and B are also reported (see Chapter 4 for explanations).

D2. 1,1-Dimethylhydrazine

Table D.1: Comparison of the Entropies of Activation (at 600 K, in J K^{-1} mol^{-1}) for the Methyl Radical Loss from 1,1-Dimethylhydrazine Ion using Two Approaches[a]

R^*_{N-C} (Å)	harmonic oscillator		free rotor	
	ΔS_{vib}	ΔS_{rovib}	ΔS_{vib}	ΔS_{rovib}[b]
2.565	21.19	25.22	15.02	19.05
2.665	24.97	29.38	17.74	22.15
2.765	29.16	33.96	20.46	25.26
2.865	33.36	38.54	22.98	28.16
3.165	42.55	48.90	35.45	41.80
3.965	61.13	70.44	50.07	59.39
4.065	62.94	71.90	51.53	60.49
4.265	67.82	78.15	55.04	65.37
4.365	69.92	80.57	56.31	66.96

[a] The two approaches are the harmonic oscillator approach and the free rotor approach which are explained in Chapter 2 and in East and Radom paper [103]. [b] Same results as those reported in Table 3.3 in Chapter 3 and in Boulanger et al. [92].

Table D.2: Comparison of the Entropies of Activation (at 600 K, in J K^{-1} mol^{-1}) for the Hydrogen Atom Loss from 1,1-Dimethylhydrazine Ion using Different Methods[a]

Fit	R^*_{C-H} (Å)	harmonic oscillator[b]				free rotor[b]			
		ΔS_{vib}		ΔS_{rovib}		ΔS_{vib}		ΔS_{rovib}	
		A	B	A	B	A	B	A[c]	B
1	2.098	25.27	25.22	25.37	25.31	21.84	12.51	21.93	12.60
							12.37		12.47
	2.198	28.72	28.66	28.87	28.82	25.49	16.16	25.64	16.31
							16.02		16.18
2	2.098	21.51	21.45	21.60	21.54	18.83	9.51	18.93	9.60
							9.37		9.46
	2.198	24.95	24.89	25.10	25.04	22.48	13.15	22.63	13.30
							13.01		13.17
3	2.098	18.07	18.01	18.16	18.10	16.09	6.76	16.19	6.86
							6.63		6.72
	2.198	21.50	21.44	21.65	21.59	19.73	10.40	19.88	10.55
							10.26		10.42

[a] In method A, we considered that DMH ion and its TS had only one free methyl rotor whereas in method B we considered that DMH ion had two free methyl rotors and only one in its TS. The entropies have been calculated using East and Radom [103] procedure for the computation of third-law entropies. [b] The moments of inertia were estimated to be between 3.0 and 3.1 amu $Å^2$ and were taken from Table 7 in East and Radom [103] procedure. In method B, they gave slightly different $\Delta S^{\ddagger}$ values. [c] Same results as those reported in Table 3.3 in Chapter 3 and in Boulanger et al. [92].

D3. Methylhydrazine

Table D.3: Comparison of the Entropies of Activation (at 600 K, in J K^{-1} mol^{-1}) for the Methyl Radical Loss from Methylhydrazine Ion using Two Approaches[a]

Fit[b]	R^*_{N-C} (Å)	harmonic oscillator		free rotor	
		ΔS_{vib}	ΔS_{rovib}	ΔS_{vib}	ΔS_{rovib}
Fit 1	2.561	20.55	26.40	11.39	17.24
	3.061	35.88	43.97	23.55	31.64
	3.761	54.65	65.47	41.52	52.34
	4.061	60.62	72.45	46.99	58.83
	4.461	70.34	83.36	54.59	67.62
Fit 2	2.561	23.09	28.94	13.40	19.25
	3.061	38.49	46.58	25.62	33.71
	3.761	56.13	66.95	42.70	53.52
	4.061	62.11	73.94	48.18	60.01
	4.461	71.83	84.86	55.78	68.81
Fit 3	2.561	24.89	30.74	14.83	20.68
	3.061	40.33	48.42	27.09	35.18
	3.761	58.20	69.02	44.36	55.17
	4.061	64.18	76.01	49.83	61.67
	4.461	73.91	86.93	57.44	70.47

[a] The two approaches are the harmonic oscillator approach and the free rotor approach which are explained in Chapter 2 and in East and Radom paper [103]. [b] Same results as those reported in Table 3.5 in Chapter 3 [91].

Table D.4: Comparison of the Entropies of Activation (at 600 K, in J K^{-1} mol^{-1}) for the Hydrogen Atom Loss from Methylhydrazine Ion using Different Methods[a]

Fit	R^*_{C-H} (Å)	harmonic oscillator[b]				free rotor[b]			
		ΔS_{vib}		ΔS_{rovib}		ΔS_{vib}		ΔS_{rovib}	
		A	B	A	B	A	B	A	B[c]
1	2.397	39.83	39.77	40.88	40.82	39.83	31.66	40.88	32.71
							31.53		32.58
	2.297	36.97	36.90	37.86	37.80	36.97	28.80	37.86	29.69
							28.66		29.55
	2.197	33.89	33.83	34.63	34.56	33.89	25.72	34.63	26.46
							25.58		26.32
	2.097	30.63	30.57	31.23	31.17	30.63	22.46	31.23	23.06
							22.33		22.93
	1.997	27.40	27.34	27.88	27.82	27.40	19.24	27.88	19.72
							19.10		19.58
2	2.297	39.93	39.87	40.82	40.76	39.93	31.76	40.82	32.65
							31.63		32.52
	2.197	36.84	36.78	37.58	37.52	36.84	28.68	37.58	29.42
							28.54		29.28
	2.097	33.58	33.52	34.19	34.13	33.58	25.42	34.19	26.02
							25.28		25.88
	1.997	30.38	30.32	30.86	30.80	30.38	22.21	30.86	22.69
							22.08		22.56
3	2.297	43.13	43.07	44.02	43.96	43.13	34.96	44.02	35.85
							34.83		35.72
	2.197	40.04	39.98	40.78	40.72	40.04	31.88	40.78	32.61
							31.74		32.48
	2.097	36.78	36.72	37.38	37.32	36.78	28.61	37.38	29.21
							28.47		29.08
	1.997	33.48	33.42	33.97	33.90	33.48	25.32	33.97	25.80
							25.18		25.66

[a] In method A, we considered that MH ion and its TS had no free methyl rotor whereas in method B we considered that MH ion had one free methyl rotor and none in its TS. The entropies have been calculated using East and Radom[103] procedure for the computation of third-law entropies. [b] The moments of inertia were estimated to be between 3.0 and 3.1 amu $Å^2$ and were taken from Table 7 in East and Radom [103] procedure. In method B, they gave slightly different $\Delta S^{\ddagger}$ values. [c] Same results as those reported in Table 3.5 in Chapter 3 [92].

D4. Tetramethylhydrazine

Table D.5: Comparison of the Entropies of Activation (at 600 K, in J K^{-1} mol^{-1}) for the Methyl Radical Loss from Tetramethylhydrazine Ion using Two Approaches[a]

Fit	R^*_{N-C} (Å)	harmonic oscillator		free rotor	
		ΔS_{vib}	ΔS_{rovib}	ΔS_{vib}	ΔS_{rovib}[b]
B3-LYP	2.366	5.14	6.95	3.31	5.12
	2.466	11.21	13.25	6.43	8.48
	2.666	19.40	21.94	11.60	14.14
	2.766	21.79	24.58	14.73	17.52

Table D.5: continued

Fit	R^*_{N-C} (Å)	harmonic oscillator		free rotor	
		ΔS_{vib}	ΔS_{rovib}	ΔS_{vib}	ΔS_{rovib} [b]
Fit 1	2.366	55.16	56.96	23.30	25.10
	2.466	61.24	63.28	26.43	28.47
	2.766	71.84	74.63	34.72	37.51
Fit 2	2.366	52.47	54.28	22.23	24.03
	2.466	58.56	60.60	25.35	27.39
	2.766	69.15	71.94	33.65	36.44
Fit 3	2.366	58.03	59.84	24.45	26.25
	2.466	64.11	66.16	27.57	29.61
	2.766	74.71	77.50	35.87	38.66
Fit 4	2.366	49.95	51.75	21.22	23.02
	2.466	56.03	58.07	24.35	26.39
	2.766	66.63	69.42	32.64	35.43

[a] The two approaches are the harmonic oscillator approach and the free rotor approach which are explained in Chapter 2 and in East and Radom paper [103]. [b] Same results as those reported in Table 3.6 in Chapter 3 [91].

D5. $\Delta S^{\ddagger}$ for the rearrangement processes leading to the loss of methane

Table D.6: Comparison of the Entropies of Activation (at 600 K, in J K^{-1} mol^{-1}) for the Methane Loss from Methyl- and Tetramethylhydrazine Ions using Two Approaches[a]

Fit	TS	harmonic oscillator		free rotor	
		ΔS_{vib}	ΔS_{rovib}	ΔS_{vib}	ΔS_{rovib} [b]
MH					
Fit 1	1	13.53	25.36	5.42	17.26
Fits 2,3	1	16.75	28.59	8.65	20.48
TMH					
Fit 1	1	63.11	65.90	11.37	14.16
	2	8.16	10.95	-21.55	-18.76
Fit 2	1	59.14	61.93	8.99	11.78
	2	-1.63	1.16	-27.41	-24.62
Fit 3	1	61.08	63.87	10.15	12.94
	2	0.60	3.40	-26.07	-23.28
Fit 4	1	59.14	61.93	8.99	11.78
	2	-2.92	-0.13	-28.18	-25.39

[a] The two approaches are the harmonic oscillator approach and the free rotor approach which are explained in Chapter 2 and in East and Radom paper [103]. [b] Same results as those reported in Tables 3.5 and 3.6 in Chapter 3 [91].